

P 231

30-kW Ammonia Arcjet Technology

Final Report

July 1986–December 1989

W. D. Deininger
A. Chopra
T. J. Pivrotto
K. D. Goodfellow
J. W. Barnett

(NASA-CR-186850) THE 30-KW AMMONIA ARCJET
TECHNOLOGY Final Report, Jul. 1986 - Dec.
1989 (JPL) 231 p CSCL 21H

N90-25100

Unclass

G3/20 0293536

February 15 1990



National Aeronautics and
Space Administration

Jet Propulsion Laboratory
California Institute of Technology
Pasadena, California

1. Report No. JPL Pub. 90-4		2. Government Accession No.		3. Recipient's Catalog No.	
4. Title and Subtitle 30-kW Ammonia Arcjet Technology Final Report July 1986-December 1989				5. Report Date February 15, 1990	
				6. Performing Organization Code	
7. Author(s) W.D. Deininger, A. Chopra, T.J. Pivrotto, K.D. Goodfellow, J.W. Barnett				8. Performing Organization Report No.	
9. Performing Organization Name and Address JET PROPULSION LABORATORY California Institute of Technology 4800 Oak Grove Drive Pasadena, California 91109				10. Work Unit No.	
				11. Contract or Grant No. NAS7-918	
				13. Type of Report and Period Covered	
12. Sponsoring Agency Name and Address NATIONAL AERONAUTICS AND SPACE ADMINISTRATION Washington, D.C. 20546				14. Sponsoring Agency Code RE 238 PX-644-11-X2-00-01	
15. Supplementary Notes					
16. Abstract This report summarizes the technical results of a 30-kW class ammonia-propellant arcjet technology program that extended over 3 1/2 years. Evaluation of previous arcjet thruster performance, including materials analysis of used thruster components, led to the design of an arcjet with improved performance and thermal characteristics. Tests of the new engine demonstrated that engine performance is relatively insensitive to cathode tip geometry. Other data suggested a maximum sustainable arc length for a given thruster configuration, beyond which the arc may reconfigure in a destructive manner. A flow controller calibration error was identified. This error caused previously reported values of specific impulse and thrust efficiency to be 20-percent higher than the real values. Corrected arcjet performance data are given in the report. Duration tests of 413 and 252 hours, and several tests 100 hours in duration, were performed. The cathode tip erosion rate increased with increasing arc current. Elimination of power source ripple did not affect cathode tip whisker growth. Results of arcjet modeling, diagnostic development and mission analyses are also discussed. The 30-kW ammonia arcjet may now be considered ready for development for a flight demonstration, but widespread application of 30-kW class arcjet will require improved efficiency and lifetime.					
17. Key Words (Selected by Author(s)) Spacecraft Propulsion and Power; Logistics; Electric Propulsion				18. Distribution Statement	
19. Security Classif. (of this report) Unclassified		20. Security Classif. (of this page) Unclassified		21. No. of Pages 227	
				22. Price	

30-kW Ammonia Arcjet Technology

Final Report

July 1986–December 1989

W. D. Deininger

A. Chopra

T. J. Pivrotto

K. D. Goodfellow

J. W. Barnett

February 15, 1990



National Aeronautics and
Space Administration

Jet Propulsion Laboratory
California Institute of Technology
Pasadena, California

The research described in this publication was carried out by the Jet Propulsion Laboratory, California Institute of Technology, under a contract with the National Aeronautics and Space Administration.

Reference herein to any specific commercial product, process, or service by trade name, trademark, manufacturer, or otherwise, does not constitute or imply its endorsement by the United States Government or the Jet Propulsion Laboratory, California Institute of Technology.

ABSTRACT

This report summarizes the technical results of a 30-kW class ammonia-propellant arcjet technology program which extended over 3 1/2 years. Evaluation of previous arcjet thruster performance, including materials analysis of used thruster components, led to the design of an arcjet with improved performance and thermal characteristics. Tests of the new engine demonstrated that engine performance is relatively insensitive to cathode tip geometry. Other data suggested a maximum sustainable arc length for a given thruster configuration, beyond which the arc may reconfigure in a destructive manner. A flow controller calibration error was identified. This error caused previously reported values of specific impulse and thrust efficiency to be 20-percent higher than the real values. Corrected arcjet performance data are given in this report. Duration tests of 413 and 252 hours, and several tests 100 hours in duration, were performed. The cathode tip erosion rate increased with increasing arc current. Elimination of power source ripple did not affect cathode tip whisker growth. Results of arcjet modeling, diagnostic development and mission analyses are also discussed. The 30-kW ammonia arcjet may now be considered ready for development for a flight demonstration, but widespread application of 30-kW class arcjet technology will require improved efficiency and lifetime.

FOREWORD

This report describes the results of an arcjet technology program focused on 30-kW ammonia-propellant engines. The program consisted of eight primary technical tasks: (1) preparation of the facility and instrumentation, (2) arcjet engine design, (3) materials analysis and evaluation, (4) arcjet performance testing, (5) arcjet endurance testing, (6) modeling, (7) diagnostics development and application, and (8) mission and system analysis.

The results of the technical tasks are discussed in Chapters 2 through 10. The program conclusions and recommendations for future work are presented in Chapter 11. Many sections of this report are condensed from publications written under this program. A complete list of program-supported publications is given in Section 12.0.

This work led to the initiation of several other programs and collaborative efforts. Efforts to define the baseline mission and spacecraft configuration for the SP-100 flight experiments were started early in the program and led to the start of the "Arcjet Propulsion System Definition Studies," which were funded by the SDIO-Key Technologies (KT) Office and managed by JPL. Two competitive contracts to industry were conducted to define a preliminary breadboard arcjet propulsion system suitable for use as a power system load on the SP-100 flight experiment. In addition, an SDIO/KT-sponsored Materials Technology Program, managed by NASA Lewis Research Center, has begun at Texas Tech University as an outgrowth of the materials analysis and cathode erosion testing conducted at JPL. An optical diagnostics program with the Aerospace Engineering Department at the University of Southern California was conducted with support from a California Institute of Technology President's Fund Grant. Finally, a collaboration involving advanced neutron and photogrammetric diagnostics was initiated between JPL and Rolls Royce, plc, Bristol, England.

ACKNOWLEDGEMENTS

The research described in this report was carried out by the Jet Propulsion Laboratory (JPL), California Institute of Technology, and was sponsored by the Strategic Defense Initiative Organization, Innovative Science and Technology (SDIO/IST) Office, and by the National Aeronautics and Space Administration (NASA). The work was performed as part of JPL's Innovative Space Technology Center, managed by Dr. Carl K. Kukkonen. The contract was monitored by Dr. L. H. Caveny of SDIO/IST with support from Dr. R. J. Vondra of W. J. Schafer, Associates.

The authors thank W. R. Thogmartin, A. G. Owens and R. L. Toomath for facilities and electronics support along with C. Garner, Dr. D. King, and L. Shiraishi for assistance in performing after-hours facilities and engine checks during the endurance tests. W. R. Thogmartin also provided the initial flat-face cathode design. The authors appreciated Dr. D. G. Elliott's contribution to understanding sources of error in the flow controller. Thanks are expressed to C. Andrews, J. Cassady, Dr. L. Caveny, Dr. F. Curran, Dr. J. Heberlein, Dr. D. King, Dr. J. Lawless, Dr. V. Subramaniam, and Dr. R. J. Vondra for many helpful and interesting discussions.

The efforts to resolve the discrepancy in performance data taken at the Jet Propulsion Laboratory-Caltech (JPL) and Rocket Research Company (RRC) of the Olin Defense Systems Group benefitted from close cooperation between JPL, RRC, and the Astronautics Laboratory (AL) of the Air Force Space Command. C. Andrews (AL), R. Cassady (RRC), P. Lichon (RRC) and Dr. D. King (RRC) played key roles in resolving the performance differences. Thanks are given to Dr. D. Erwin and G. Pham-Van-Diep, of the University of Southern California for their help in conducting the Laser-Induced Fluorescence (LIF) experiments, and the Caltech President's Fund for enabling their participation. The majority of the LIF work was done by G. Pham-Van-Diep.

Rolls Royce, plc, of Bristol, England, the University of Bristol, England, and the Rutherford Appleton Laboratories, Chilton, England, enabled the neutron analysis work to take place. The efforts of Dr. P. Stewart, Dr. J. Roger, Dr. P. Fowler, and Dr. A. Taylor are appreciated.

Particular thanks are expressed to Dr. R. J. Vondra for his support and assistance in conducting the mission and systems analyses. All the orbital analysis calculations were done by Dr. Vondra.

Finally, the authors would like to thank D. J. Carter, T. D. Williams, and P. South for their assistance in preparing this manuscript.

NOMENCLATURE

Abbreviations and Acronyms

AFSC	Air Force Space Command
AL	Astronautics Laboratory (AFSC)
ATD	Advanced Technology Development
AVCO	Avco Corporation
DACS	Data Acquisition and Control System
DACU	Data Acquisition/Control Unit
ELITE	Electric Insertion Transfer Experiment
IEPC	International Electric Propulsion Conference
JPC	Joint Propulsion Conference
JPL	Jet Propulsion Laboratory
LVDT	Linear Variable Differential Transformer
MFC	Mass Flow Controller
MFM	Mass Flow Meter
NASA	National Aeronautics and Space Administration
RRC	Rocket Research Company
SDI	Strategic Defense Initiative
SNAP	Space Nuclear Reactor Program of the 1960s
SP-100	SRPS at 100 kW
SRPS	Space Reactor Power System

Variables and Constants

A_c	cathode cross-sectional area
A_R	Richardson coefficient
A_s	cathode surface radial area
C_p	specific heat at constant pressure
d	gas density
D	diameter
ΔP	pressure difference
e	electron charge
E	electric field
F	measured thrust
g_0	mass-to-force conversion constant
i	total arc current
I_{sp}	specific impulse
j	current density
J	normalized current density
k_b	Boltzmann constant
k_T	thermal conductivity
K	gas K-factor: $K=N/dC_p$
L	length
L_D	Debye length
m	mass flow rate
m	particle mass
n	number density
N	molecular structure correction factor

η_F	thrust efficiency
P	power input to engine
q	heat flux
Q	heat generation or loss
r_o	local constricted arc radius
r	radial space variable
T	temperature
T_B	measured brightness temperature
\underline{u}	particle energy
U	normalized particle energy
v	velocity
V	electric potential
Vol	volume
x,y	position

Greek

γ	normalized electric field
ϵ_i	ionization energy
ϵ_o	electrical permittivity of free space
ϵ_T	thermal emissivity
ζ	normalized position
η	normalized electric potential
μ	magnetic permeability
v	normalized ion density
ρ^c	electric charge density
σ	Stefan-Boltzmann constant
χ	material work function

Subscripts

a	anode (environment) value
b	thermionic (beam) electrons
$base$	base of cathode
$cath$	cathode
$cond$	conduction
$conv$	convection
c	value at the cathode surface
e	plasma electron
eff	effective value
$evap$	evaporation
i	ion
in	input to surface
l	liquid
$melt$	melting
o	reference value (sheath edge)
ohm	ohmic heating
out	output from surface
r	radial
rad	radiation

s	solid
tip	tip of cathode
tot	total

Arcjet Designators

Baseline	JPL 30-kW ammonia arcjet (1986)
Baseline	JPL 30-kW ammonia arcjet (1988)
D-1E	Rocket Research Company 30-kW ammonia arcjet (1986)
MOD I	JPL 30-kW ammonia arcjet with a bell-shaped nozzle (1986)
MOD II	JPL 30-kW ammonia arcjet with a modified cathode design (1987)
MOD III	JPL 30-kW ammonia arcjet with a high-emissivity coating (1987)

CONTENTS

EXECUTIVE SUMMARY	ES-1
1.0 INTRODUCTION.	1-1
2.0 THE EXPERIMENTAL FACILITY AND INSTRUMENTATION	2-1
2.1 Vacuum Subsystem	2-1
2.2 Data Acquisition and Control Subsystem	2-1
2.3 Instrumentation	2-2
2.4 Power Subsystem	2-3
2.5 Propellant Feed Subsystem	2-4
3.0 ARCJET ENGINE DESIGN	3-1
3.1 Baseline Engine	3-2
3.2 Baseline MOD-I	3-3
3.3 Baseline MOD-II	3-4
3.4 Baseline MOD-III	3-4
3.5 D-1E Engine	3-5
3.5.1 Design	3-7
3.5.2 Materials	3-8
3.5.3 Radiative Design	3-9
3.5.4 Cathode Tip Shapes	3-10

CONTENTS (Continued)

4.0	MATERIALS ANALYSIS	4-1
4.1	Analysis of Used Arcjet Components	4-1
4.1.1	Cathode	4-1
4.1.2	Anode/Nozzle Analysis	4-7
4.1.3	Injector	4-9
4.2	Materials Evaluation	4-11
4.2.1	Electrode Materials	4-11
4.2.2	Insulator Materials	4-13
5.0	PERFORMANCE TESTING	5-1
5.1	Experimental Procedures	5-1
5.2	Cathode Variation Effects	5-2
5.2.1	Performance	5-3
5.2.2	Electrical Characteristics	5-4
5.2.2.1	Geometric Arc length	5-5
5.3	Engine Radiative Design Comparison	5-11
5.3.1	High Emissivity Coatings	5-11
5.3.1.1	Electrical characteristics	5-11
5.3.1.2	Nozzle Temperature Reduction Tests	5-12
5.3.2	Verification of D-1E Engine Thermal Design . . .	5-14
5.3.2.1	Electrical Characteristics	5-15
5.3.2.2	Thermal Design Results	5-16

CONTENTS (Continued)

5.4	Nozzle Effects	5-18
5.4.1	Flow Characteristics	5-18
5.4.2	Nozzle Profile Definition	5-19
5.4.3	Conical/Bell Comparison	5-20
5.4.4	Detailed Performance with a Bell Nozzle	5-23
5.5	D-1E Performance	5-27
5.6	Identification and Resolution of a Performance Discrepancy	5-28
5.6.1	Performance Discrepancy Identification	5-28
5.6.2	Experiments to Resolve the Discrepancy	5-30
5.6.3	Discussion	5-36
5.6.3.1	Sierra Instruments Mass Flow Controller (MFC) Operation	5-37
5.6.3.2	Micromotion Mass Flow Meter (MFM) Operation	5-37
5.6.3.3	Sources of MFC Error	5-39
5.6.4	Corrections of Published Data	5-40
5.7	Direct Start Testing	5-43
6.0	ENDURANCE TESTING	6-1
6.1	Tests with Unfiltered Power	6-2
6.1.1	Test Events	6-5
6.1.2	Performance	6-5

CONTENTS (Continued)

6.2	Tests with Filtered Power	6-6
6.2.1	Test Events	6-6
6.2.2	Performance	6-7
6.3	Long-Term Tests (with Filtered Power)	6-10
6.3.1	Test Events	6-10
6.3.1.1	413-Hour Test	6-10
6.3.1.2	252-Hour Test	6-13
6.3.2	Performance	6-13
7.0	DISCUSSION OF ENDURANCE TEST RESULTS	7-1
7.1	Effect of Electrical Filtering.	7-2
7.2	413-Hour Endurance Test	7-6
7.2.1	Electric Characteristics	7-6
7.2.2	Performance	7-7
7.2.3	Component Conditions	7-7
7.2.3.1	Cathode	7-8
7.2.3.2	Nozzle	7-10
7.2.3.3	Injector	7-10
7.3	252-Hour Endurance Test	7-11
7.3.1	Electrical Characteristics	7-11
7.3.2	Performance	7-12
7.3.3	Component Conditions	7-12

CONTENTS (Continued)

7.3.3.1	Cathode	7-12
7.3.3.2	Nozzle	7-14
7.3.3.3	Injector	7-16
7.4	Cathode Erosion	7-16
8.0	MODELING	8-1
8.1	Plasma Sheath Model	8-1
8.2	Heat Transfer Model	8-6
8.3	Combined Model	8-7
8.4	Preliminary Results	8-7
9.0	DIAGNOSTICS	9-1
9.1	Known Exhaust Plume Properties	9-1
9.1.1	Particle Effluxes	9-1
9.1.2	Field Effluxes	9-2
9.2	Emission Spectroscopy	9-3
9.2.1	Optical Setup	9-3
9.2.2	Representative Results	9-5
9.3	Laser-Induced Fluorescence	9-10
9.3.1	LIF Technique	9-11
9.3.2	Results and Discussion	9-13
9.4	Neutron Analysis	9-14

CONTENTS (Continued)

9.4.1	Neutron Techniques	9-14
9.4.1.1	Cold or Subthermal Neutrons	9-15
9.4.1.2	'Thermal' Neutrons	9-15
9.4.1.3	Epithermal Neutrons	9-15
9.4.2	Facilities and Instrumentation	9-17
9.4.3	Feasibility Experiments	9-17
10.0	MISSION AND SYSTEMS ANALYSIS	10-1
10.1	Arcjet Mission Capabilities	10-2
10.1.1	Arcjet Propulsion System Parameters	10-2
10.2	SP-100 Flight Experiment Definition	10-3
10.2.1	System Definition	10-5
10.2.1.1	100-kWe Spacecraft Concept	10-6
10.2.1.2	30-kW Baseline Spacecraft	10-8
10.2.2	Mission Analysis	10-8
10.2.2.1	100-kW Spacecraft	10-8
10.2.2.2	30-kW Spacecraft	10-12
10.3	Constellation Deployment	10-13
10.3.1	Constraints and Assumptions	10-13
10.3.2	Platform Mass Considerations	10-14
10.3.3	Effect of Launch Rate	10-17
10.3.4	Effect of Constellation Size	10-17

CONTENTS (Continued)

10.4	Defensive Maneuvering	10-19
10.4.1	Constraints and Assumptions	10-19
10.4.2	Power Included in Payload	10-21
10.4.3	Power as Part of the Electric Propulsion System	10-22
11.0	CONCLUSIONS AND RECOMMENDATIONS	11-1
11.1	Program Highlights	11-1
11.1.1	Facilities and Instrumentation	11-1
11.1.2	Engine Design	11-2
11.1.3	Materials Analysis	11-4
11.1.4	Performance Testing	11-5
11.1.5	Endurance Testing	11-10
11.1.6	Modeling	11-10
11.1.7	Diagnostics	11-12
11.1.8	Mission and System Analysis	11-14
11.2	Recommendations	11-18
11.2.1	Engine Technology	11-18
11.2.2	Mission and System Design and Evaluation	11-20
12.0	LIST OF PROGRAM-SUPPORTED PUBLICATIONS	12-1
13.0	REFERENCES	13-1

CONTENTS (Continued)

Figures

ES-1.	Schematic of an Arcjet Thruster	ES-1
ES-2.	The D-1E Engine	ES-4
ES-3.	Summary of Endurance Tests	ES-6
ES-4.	Axial Velocity Profile in a 14-kW Arcjet	ES-7
ES-5.	Arcjet NEP System Block Diagram	ES-8
1-1.	General Schematic of Arcjet Operation	1-1
1-2.	Program Work Breakdown	1-3
2-1.	Arcjet Power Subsystem with L-C Filter.	2-4
2-2.	Propellant Subsystem Schematic	2-5
3-1.	Schematic of the Baseline Arcjet Engine	3-2
3-2.	Schematic of the Baseline MOD I Engine	3-4
3-3.	Schematic of the Baseline MOD II Engine	3-5
3-4.	Schematic of the Baseline MOD III Engine	3-6
3-5.	Schematic of the D-1E Arcjet Engine	3-6
3-6.	Results of Heat Transfer Calculations in the Nozzle Block of a 30-kW Arcjet	3-10
3-7.	Normal Emissivity of Tungsten	3-11
3-8.	Cathode Tip Shapes	3-12
4-1.	Before and After Photographs of the Cathode Tip (573-Hour Test)	4-2
4-2.	Oblique View of Cathode Tip (375-hour test)	4-3
4-3.	Cathode Tip Cross Section (573-Hour Test)	4-4
4-4.	Possible Cause of Cathode Tip Cratering	4-5
4-5.	End View of Cathode Tip (573-hour test)	4-6

CONTENTS (Continued)

4-6.	Cathode Tip Microspots (573-Hour Test, 750 x Magnification)	4-7
4-7.	Cross-Section of the Anode (573-Hour Test)	4-8
4-8.	Photographs of Unused and Eroded Injectors	4-10
5-1.	Thrust vs. \dot{m} (Baseline MOD I and Baseline MOD II)	5-3
5-2.	Arc Potential vs. \dot{m} (Baseline MOD I and Baseline MOD II)	5-4
5-3.	Nozzle Temperature vs. \dot{m} (Baseline MOD I and Baseline MOD II)	5-5
5-4.	D-1E Electrical Characteristics (Baseline Cathode)	5-6
5-5.	D-1E Electrical Characteristics (45° Red. Radius Cathode)	5-7
5-6.	D-1E Electrical Characteristics (Dimpled Cathode)	5-8
5-7.	D-1E Electrical Characteristics (Flat-Face Cathode)	5-8
5-8.	Voltage vs. Current as a Function of \dot{m} at One GAL.	5-9
5-9.	Definition of GAL	5-9
5-10.	Current vs. GAL	5-10
5-11.	Baseline Engine Voltage-Current Characteristics	5-11
5-12.	Nozzle Brightness Temperature as a Function of Power for a mass flow rate of 0.25 g/s With and Without ZrB ₂ Coating.	5-12
5-13.	Nozzle Brightness Temperature as a Function of Power for a mass flow rate of 0.30 g/s With and Without the ZrB ₂ Coating.	5-13
5-14.	Location of Thermocouples on the D-1E Arcjet	5-14

CONTENTS (Continued)

5-15.	D-1E Engine Voltage - Current Characteristics	5-15
5-16.	D-1E Exterior Engine Temperature as a Function of Input Power	5-16
5-17.	D-1E Exterior Engine Temperature as a Function of Specific Power	5-18
5-18.	Optimum Inviscid Expansion Nozzle Contour	5-20
5-19.	Thrust as a Function of P, \dot{m} (Baseline, Baseline, MOD I Engines)	5-21
5-20.	I_{sp} as a Function of P, \dot{m} (Baseline, Baseline, MOD I Engines)	5-22
5-21.	Efficiency as a Function of P, \dot{m} (Baseline, Baseline, MOD I Engines)	5-22
5-22.	Thrust as a Function of P, \dot{m} (Contoured Nozzle)	5-24
5-23.	Current vs. Power (Contoured Nozzle)	5-24
5-24.	Voltage vs. Power (Contoured Nozzle)	5-25
5-25.	V-I Characteristics (Contoured Nozzle)	5-26
5-26.	Nozzle Brightness Temperature as a Function of P, \dot{m}	5-26
5-27.	Nozzle Brightness Temperature as a Function of \dot{m}	5-27
5-28.	I_{sp} vs. P/\dot{m} (JPL and RRC Test Results)	5-29
5-29.	Schematic of RRC Engine	5-30
5-30.	Thruster Voltage vs. Vacuum Chamber Pressure	5-32
5-31.	Mass Flow Controller Test Plumbing at RRC	5-32
5-32.	Results of Mass Flow Controller Comparison	5-33
5-33.	Results of Further Calibration Check	5-34
5-34.	Propellant Feed Setup (Tests 1-4)	5-34

CONTENTS (Continued)

5-35.	Propellant Feed Setup (Tests 5, 6)	5-35
5-36.	Indicated Thrust Comparison with Corrected Flow	5-35
5-37.	I_{sp} vs. P/\dot{m} Comparison with Corrected Flow	5-36
5-38.	Schematic of Sierra MFC	5-38
5-39.	Schematic of Micromotion MFM	5-39
5-40.	Variation of the Product of Density and Specific Heat for Ammonia at Various Pressures	5-41
6-1.	Voltage vs. Time (Unfiltered Power Tests)	6-2
6-2.	Current vs. Time (Unfiltered Power Tests)	6-3
6-3.	Impedance vs. Time (Unfiltered Power Tests)	6-3
6-4.	V-I Characteristic (Unfiltered Power Tests)	6-4
6-5.	Nozzle Brightness Temperature vs. Time (Unfiltered Power Tests)	6-4
6-6.	Voltage vs. Time (Filtered Power Tests)	6-7
6-7.	Current vs. Time (Filtered Power Tests)	6-8
6-8.	Impedance vs. Time (Filtered Power Tests)	6-8
6-9.	V-I Characteristic (Filtered Power Tests)	6-9
6-10.	Nozzle Brightness Temperature (Filtered Power Tests)	6-9
6-11.	Thrust vs. Time (Filtered Power Tests)	6-10
6-12.	Long-Term Test Timeline	6-12
6-13.	Voltage vs. Time (Long-Term Tests)	6-14
6-14.	Current vs. Time (Long-Term Tests)	6-14
6-15.	Impedance vs. Time (Long-Term Tests)	6-15
6-16.	V-I Characteristic (Long-Term Tests)	6-15

CONTENTS (Continued)

6-17.	Nozzle Brightness Temperature (Long-Term Tests)	6-16
6-18.	Thrust vs. Time (Long-Term Test)	6-16
7-1.	Arc Voltage Variations Over 100 Hours	7-1
7-2.	Tips of Cathodes 22 and 24 After 100 Hours of Operation	7-3
7-3.	Filtered and Unfiltered Current Ripple	7-4
7-4.	Tip of Flat Face Cathode 17 After 100 Hours of Operation	7-4
7-5.	Tip of Cathode 4 After 100 Hours of Operation	7-5
7-6.	Tip of Cathode 15 After 21 Hours of Operation	7-5
7-7.	Operating Power as a Function of Time (413-Hour Test)	7-7
7-8.	D-1E Arcjet After 413 Hours at 30 kW	7-9
7-9.	Cathode After 413 Hours of Operation and 8 Restart Attempts	7-9
7-10.	Nozzle After 413 Hours of Operation at 30 kW	7-10
7-11.	Injector After 413 Hours of Operation at 30 kW	7-11
7-12.	Thrust - Current Correlation Over 24 Hours	7-12
7-13.	Cathode 25 After 252 Hours	7-13
7-14.	Engine Nozzle After 252-Hour Test	7-15
7-15.	Effect of Arc Current on Cathode Erosion	7-17
7-16.	Increase of Flat-Face Cathode Erosion Rate with Time	7-17
8-1.	Schematic of Cathode Tip/Plasma Sheath Interactions	8-1
8-2.	Cathode Heat Transfer Model	8-6
9-1.	Fabry-Perot Spectroscopic System	9-4

CONTENTS (Continued)

9-2.	Scan of Standard Lamp Output at 6563 \AA	9-6
9-3.	Scan of Arcjet Plume Output at 6563 \AA	9-6
9-4.	Intensity Distribution Measured Perpendicular to the Axis	9-7
9-5.	Intensity Distribution Measured at an Angle of 78.4°	9-8
9-6.	Azimuthal Velocity Distribution	9-9
9-7.	Axial Velocity Distribution	9-10
9-8.	LIF Experimental Setup	9-12
9-9.	LIF Signal Intensity vs. Wavelength	9-13
9-10.	Axial Velocity vs. Radial Position	9-14
9-11.	Calibration Results for Tungsten Resonance	9-16
9-12.	Schematic Diagram of Beam Line and Detector System	9-18
9-13.	Measured Neutron Transmission vs. Time of Flight	9-19
10-1.	Arcjet SRPS Payload Capability as a Function of Orbital Altitude and Inclination	10-4
10-2.	Arcjet SRPS Trip Time as a Function of Orbital Altitude and Inclination	10-4
10-3.	Arcjet NEP System Block Diagram	10-6
10-4.	Proposed Spacecraft Configuration for the SP-100 Flight Experiment (100-kW Spacecraft)	10-7
10-5.	Schematic of Modular Arcjet Propulsion Subsystem Component String	10-9
10-6.	Proposed Spacecraft Configuration for the SP-100 Flight Experiment (30-kW Spacecraft)	10-9
10-7.	Effect of Platform Payload Mass on the Number of Launch Vehicles Needed for Constellation Deployment . . .	10-15

CONTENTS (Continued)

10-8.	Effect of Platform Payload Mass on the Total Constellation Deployment Time	10-16
10-9.	Total Constellation Deployment Time as a Function of the Time Between Launches	10-17
10-10.	Effect of Platform Number on Constellation Deployment Time	10-18
10-11.	Initial Platform Mass as a Function of the Number of Maneuvers. Power Included in Payload	10-19
10-12.	Initial Payload Power Required to Enable Electric Propulsion Maneuvering as a Function of the Number of Maneuvers	10-22
10-13.	Initial Platform Mass as a Function of the Number of Maneuvers. Power Part of Electric Propulsion System	10-23
10-14.	Initial Electric Propulsion System Power Required for Maneuvering as a Function of the Number of Maneuvers	10-24
11-1.	The D-1E Arcjet Engine	11-3
11-2.	Pattern of Erosion on a Tungsten Cathode Tip	11-5
11-3.	Arc Current as a Function of Arc Length	11-7
11-4.	Thrust Efficiency as a Function of Input Power.	11-7
11-5.	Performance of the Bell-Shaped Nozzle	11-8
11-6.	Summary of Endurance Tests	11-11
11-7.	Increase of Flat-Face Cathode Erosion Rate with Time	11-11
11-8.	The Hydrogen Balmer Line in a 20-kW Arcjet	11-13
11-9.	Axial Velocity Profile in a 14-kW Arcjet	11-13
11-10.	Epithermal Neutron Transmission Through a Mo-Re-W Material Sandwich	11-14

CONTENTS (Continued)

11-11.	Arcjet NEP System Block Diagram	11-15
11-12.	Total Constellation Deployment Time as a Function of the Total Time Between Launches	11-17
11-13.	Initial Platform Mass as a Function of Number of Maneuvers. Power Included in Payload	11-18

Tables

ES-1.	Comparison of AVCO (1964) and JPL (1986) Arcjet Performance Data	ES-2
ES-2.	Summary of Reported 30-kW Ammonia Arcjet Performance Data.	ES-5
1-1.	Comparison of AVCO (1964) and JPL (1986) Arcjet Performance Data	1-3
3-1.	Design Parameters and Essential Dimensions of the Test Engines	3-1
5-1.	D-1E Performance Data	5-28
5-2.	30-kW Duration Test Performance at JPL	5-37
5-3.	Sierra MFC Calibration History	5-42
5-4.	Summary of Data Correction Procedure	5-43
6-1.	Summary of Endurance Tests	6-1
8-1.	Model Parameters and Assumptions	8-8
9-1.	Epithermal Neutron Resonances for Some Arcjet-Compatible Materials	9-16
10-1.	Assumed Arcjet Performance Characteristics.	10-2
10-2.	Assumed Mass Summary for the 100-kW _e Arcjet Spacecraft	10-3

CONTENTS (Continued)

10-3.	Projected Mass Summary for the 100-kW _e SRPS SOA Arcjet Flight Experiment Spacecraft	10-8
10-4.	Projected Mass Summary for the 30-kW _e SRPS SOA Arcjet Flight Experiment Spacecraft	10-10
10-5.	Assumed Arcjet Performance Characteristics (100-kW Study)	10-11
10-6.	Launch Vehicle and Orbit Assumptions	10-11
10-7.	Summary of Arcjet Throttling Orbital Analysis (100-kW Study)	10-12
10-8.	Propulsion System Parameters (Constellation Deployment Study)	10-14
10-9.	Propulsion System Parameters (Defensive Maneuvering Study)	10-20
11-1.	Summary of Reported 30-kW Ammonia Arcjet Performance Data.	11-9

EXECUTIVE SUMMARY

This report describes the results of a program designed to validate 30-kW ammonia arcjet technology for use in the SP-100 flight experiment. The program consisted of an experimental component that included performance testing, endurance testing, and diagnostics development, and an analytical component that included electrode modeling and mission analyses. In this summary, the history of arcjet development is first reviewed, and the program which is the subject of this report is defined. The technical highlights of the program are then discussed. Finally, the primary conclusions and recommendations of the program are given.

HISTORICAL OVERVIEW AND PROGRAM DEFINITION

A schematic of a typical arcjet engine configuration is shown in Fig. ES-1. Propellant gas is fed into a plenum chamber and is heated by passing through and around a stationary electric arc. The heated propellant is expanded in a supersonic nozzle to produce thrust.

Thermal arcjet research began in the late 1950s, and continued until the mid-1960s.^{86,118} During that period, arcjet engines were developed for primary propulsion applications to be powered by Space Reactor Power Systems (SRPS). Engines operating on one kilowatt to more than 200 kW of electrical power were examined. Arcjet research was terminated in the late 1960s, following the cancellation of the SNAP SRPS programs, because no adequate power source was being developed.

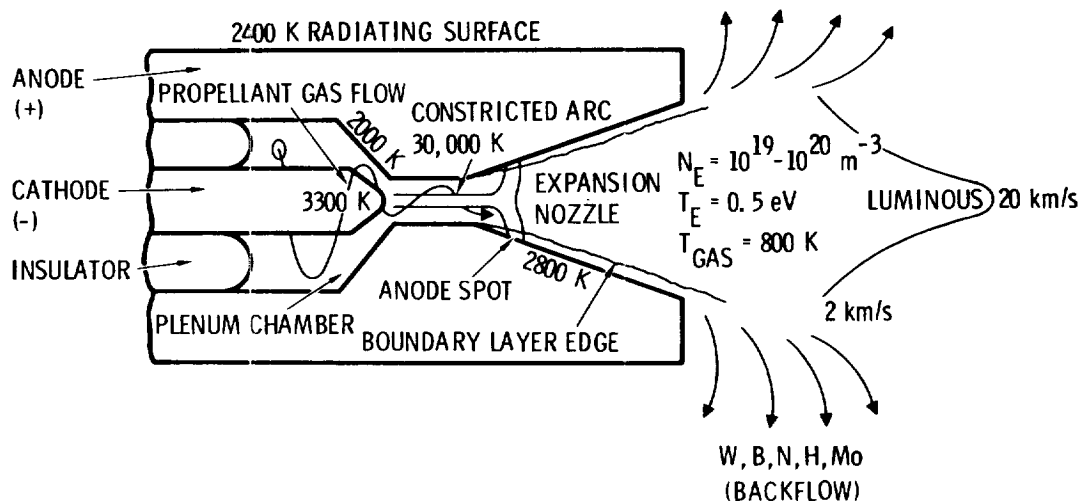


Figure ES-1. Schematic of an arcjet thruster.

Development of both high-power solar and nuclear space power systems has renewed interest in electric propulsion for primary and auxiliary propulsion functions. Arcjet engines operating at power levels of 10-30 kW are considered for a variety of missions, including orbit-raising. An arcjet propulsion system using 30-kW arcjets is baselined as the active load for the SP-100 flight experiment, a flight test of an SRPS planned for the late 1990s. An Air Force arcjet Advanced Technology Development (ATD) program⁹⁸ and a proposed joint Air Force/NASA/SDI technology demonstration flight, called ELITE, may provide additional flight test opportunities.^{71,91,96}

Renewed development of 30-kW ammonia propellant arcjets began in 1985 through the Air Force-sponsored endurance test at the Jet Propulsion Laboratory (JPL).^{80,84,85} In this program, ammonia is of interest as a propellant because of its demonstrated performance as a propellant and its storability. In 1986, an ammonia arcjet was operated at 25 kW for 573 hours; the arcjet design was based on an AVCO design for which interesting performance was reported in 1964. Other tests in 1986 showed the same indicated performance as the 1964 tests (see Table ES-1).

Table ES-1. Comparison of AVCO (1964) and JPL (1986)
Arcjet Performance Data

ENGINE	R-3 ⁵	BASELINE ⁸⁵
Date	1964	1986
Laboratory	AVCO	JPL
Power, kW	30.0	30.5
Thrust, N	2.50	2.45
Specific Impulse, s	978	967*
Efficiency	0.38	0.37*
Mass Flow, g/s	0.25	0.25*

* Uncorrected for mass flow error discovered in subsequent tests; see discussion under Performance Testing section below.

The program described in this report, begun in 1986, was designed to continue development of a 30-kW ammonia arcjet thruster and to validate this technology for use in the SP-100 Flight Experiment. The program was divided into eight technical tasks: (1) facility and instrumentation; (2) arcjet engine design; (3) materials analysis and evaluation; (4) arcjet performance and testing; (5) arcjet endurance testing; (6) modeling; (7) diagnostics development and application; and (8) mission and system analysis. Technical highlights from these tasks are presented in the next section.

TECHNICAL HIGHLIGHTS

Facility and Instrumentation

The goal of this part of the program was to develop a facility capable of prolonged (up to 1500-hour) arcjet operation at power levels up to 30 kW. The facility was composed of data acquisition and control power, and cooling water subsystems. The data acquisition and control system supported automated collection of data during periods of unattended operation, while a series of interlocks and programmed operational tolerances protected the experimental apparatus and laboratory from possible catastrophic failure of some part of the experiment.

Arcjet Engine Design

A number of design modifications to the initial baseline engine were tested, and the results were applied to the design of a new engine. Modifications included the addition of a high-emissivity coating to the radiating surfaces, and redesign of the nozzle contour. A ZrB_2 coating increased the engine surface emissivity by 30 percent, resulting in a lower operating temperature and improved operating power margin. The new bell-shaped nozzle provided up to a 10-percent increase in thrust when compared with the baseline conical nozzle at the same operating conditions.

A new engine, called the D-1E engine, is shown in Fig. ES-2. The D-1E engine incorporated ZrB_2 coating and a bell-shaped nozzle, along with other simplifications designed to simplify assembly and improve operation. Regenerative cooling of the cathode drastically decreased the temperature of the cathode feedthrough into the D-1E engine.

Materials Analysis

The cathode, anode and injector of a 30-kW class arcjet, operated under a previous Air Force-sponsored program at JPL, were analyzed. Cathode erosion led to the formation on the cathode tip of a hemispherical depression, surrounded by thread-like tungsten formations called whiskers. Energy-dispersive X-ray analysis (EDAX) showed that the crater on the tip of the thoriated tungsten cathode was depleted of thorium. The central region of the crater showed evidence that it was molten during operation. Additional materials analysis identified alternative high-temperature materials which could decrease cathode erosion and improve cathode lifetime. These materials include other tungsten-based materials, borides of rare-earth materials, and carbides.

ORIGINAL PAGE
BLACK AND WHITE PHOTOGRAPH



Figure ES-2. The D-1E engine.

Nozzle and propellant injector erosion was studied. The nozzle eroded in the region of the constrictor outlet, but no erosion was seen in the plenum chamber. The propellant injector was badly eroded; the injection holes increased in size by a factor of 2.25. Excessive local temperatures are believed to have caused the observed nozzle and injector erosion.

Performance Testing

Tests of different cathode tip geometries in otherwise identical engines indicated that engine performance is relatively insensitive to cathode shape and spacing. Additional experiments suggested that, as the cathode tip erodes and the arc must flow over a longer distance between the electrodes, there is a maximum sustainable arc length. If continuing cathode erosion acts to increase the length of the arc once the maximum length is approached, the anode arc attachment may pull back from the anode nozzle into the constrictor. This reconfiguration is likely to be destructive, leading to disruption of thruster operation.

Comparative testing of two arcjets, which differed only in nozzle contour, was performed. One nozzle was conical and the second nozzle, bell-shaped. The bell-shaped nozzle was found to improve thrust by up to 10 percent.

A series of experiments was conducted in 1989 to examine differences in performance reported by JPL and the Rocket Research Company (RRC). RRC performance data were seen to be different from JPL data as early as 1986 (see Table ES-2), but the discrepancy was attributed to differences in thruster design and facilities. In 1988, performance of the D-1E engine was evaluated at JPL; these data are shown in the fourth column of Table ES-2. A series of tests of a similar engine in RRC facilities in 1989 showed that the earlier performance discrepancies did not result from design differences. A calibration error in the flow controller used by JPL was found to explain the performance discrepancies. The error caused JPL mass flow measurements to be 20-percent low, leading to calculations of specific impulse and thrust efficiency which were 20-percent high. Previously published data which are affected by this error have been identified, and correction procedures specified for those cases where correction is possible (see Section 5.6 of this report). The tests leading to the discovery of this error also demonstrated that the thrust stands used at JPL and RRC agree to within 2 percent, and that a gas-dynamic diffuser used at JPL has negligible effect on engine electrical and performance characteristics. Table ES-2 summarizes 30-kW ammonia arcjet performance; the fifth column shows a typical JPL 30 kW operating point corrected for the mass flow calibration error. The lower values of the corrected specific impulse and thrust efficiency indicate the need for further 30-kW class arcjet development, including the use of alternate propellants (e.g., hydrazine or hydrogen).

Table ES-2. Summary of Reported 30-kW Ammonia Arcjet Performance

ENGINE	R-3 ⁵	BASE- LINE ⁸⁵	RRC-2 ¹⁰⁵	D-1E ³⁰	D-1E ⁺
Date	1964	1986	1986	1988	1989
Laboratory	AVCO	JPL	RRC	JPL	JPL
Power, kW	30.0	30.5	29.9	30.5	30.3
Thrust, N	2.50	2.45	2.0	2.50	2.42
Specific Impulse, s	978	967*	850	1018*	754
Efficiency	0.38	0.37*	0.28	0.41*	0.29
Mass Flow, g/s	0.25	0.25*	0.25	0.25*	0.33


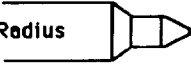

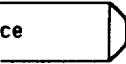
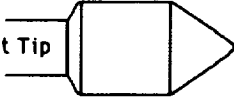
* Uncorrected for mass flow error; see Section 5.6.

+ Corrected typical 30-kW operating point.

Endurance Testing

A series of long-duration tests was performed (Fig. ES-3). One hundred-hour tests were run to determine the effect of cathode tip configuration on cathode erosion. The tip configuration did not appear to significantly affect erosion; the tip erosion rate did appear to increase with emitted arc current. The average cathode erosion rate over 100 hours of operation doubled when the engine current increased from 235 A to 285 A. The data suggest that the erosion rate may increase with time. The input power to the thruster was filtered to determine the effect of input power ripple on cathode tip whisker growth. These tests showed that elimination of normal input power ripple did not significantly affect whisker growth.

Four hundred thirteen-hour and 252-hour endurance tests were performed using the D-1E engine. The 413-hour test was voluntarily terminated due to facility problems. The nozzle and propellant injector were in excellent condition after the test. The average mass loss of the cathode was 5.2 mg/hr.

	TEST DURATION (hrs)	INPUT CURRENT RIPPLE	GEOMETRIC ARC LENGTH* (cm)	WHISKER GROWTH?	EROSION RATE (mg/hr)	ARC CURRENT (A)
 Baseline	# 13 53	3 %	1.11	yes	1.5	265-281
	# 14 100	3 %	1.11	yes	4.0	289-303
	# 22 100	0.2 %	1.11	yes	3.1	264-289
 45° Reduced Radius	# 4 100	3 %	1.43	?	2.1	238-252
 Dimpled	# 15 21	0.2 %	1.81	yes	6.2	243-247
 Flat Face	# 20 28	0.2 %	1.47	no	1.4	234-252
	# 20 413	0.2 %	1.47	yes	5.2	215-251
	# 17 100	0.2 %	1.47	no	2.0	246-257
	# 25 252	0.2 %	1.44	yes	4.1	229-208
 Fat Tip	# 24 100	3 %	1.14	yes	3.3	244-277

* AT START OF TEST

Figure ES-3. Summary of endurance tests.

Modeling

A modeling effort was performed to quantify the cathode tip heating phenomena. The model combined a three-species model of the plasma sheath region with a one-dimensional heat transfer model. A test case yielded results which were consistent with experimental results.

Diagnostics

Three non-intrusive diagnostic techniques were demonstrated for their applicability to arcjet thrusters. Emission spectroscopy was used to estimate the azimuthal and axial velocity distributions in the arcjet plume. Laser-induced fluorescence (LIF) was used to measure the axial velocity profile in the plume (Fig. ES-4); this technique allows accurate point measurements and procedural simplification. Finally, epithermal neutron analysis was shown to provide accurate non-intrusive temperature measurements in samples of materials used for arcjet components.

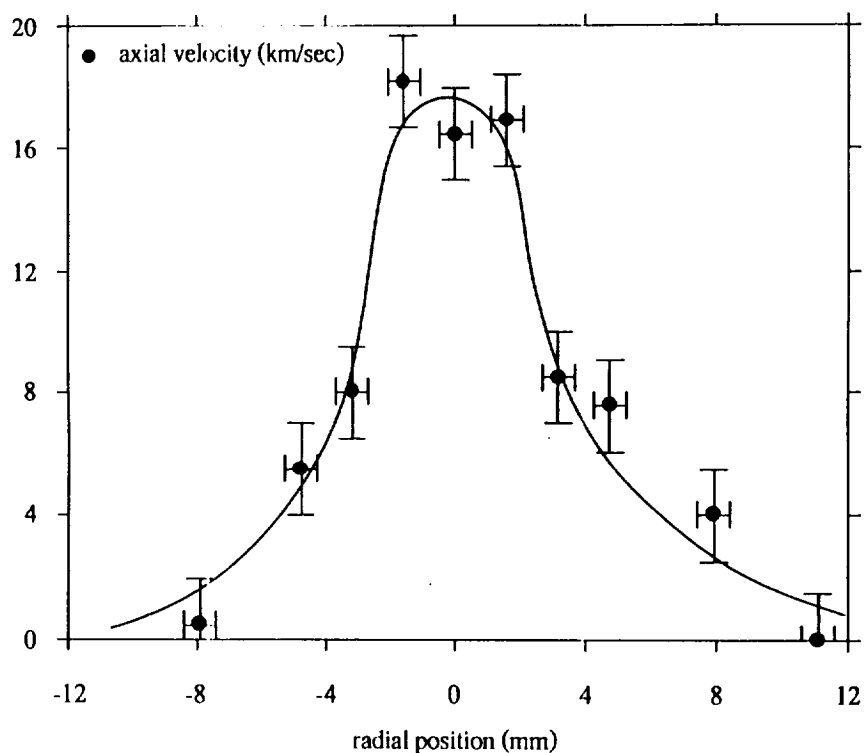


Figure ES-4. Axial velocity profile in a 14-kW arcjet.

Mission and System Analysis

The design and performance characteristics of an arcjet Nuclear Electric Propulsion (NEP) spacecraft suitable for conducting the SP-100 Flight Experiment were determined. A block diagram of an arcjet NEP system is shown in Fig. ES-5. Orbital analysis was conducted to evaluate the spacecraft performance. Analysis showed that the vehicle is capable of mission delta-Vs of approximately 6000 m/s.

Additional analysis of the SP-100 mission verified that a 30-kWe flight demonstration with arcjet propulsion can be accomplished using Titan 4, Titan 3 or Atlas 2AS launch vehicles. An attractive flight demonstration with the Atlas 2AS would involve lifting a modest payload (e.g., 1400 kg) to a 10,000-km altitude in a relatively brief period (a few months).

The use of arcjets for SDI constellation deployment and defensive maneuvering was analyzed. For typically-sized SDI constellations and reasonable assumed launch rates of ground launch systems, the use of arcjet propulsion upper stages can significantly reduce the number of launches and deployment time compared to those achievable with advanced chemical upper stages. Continuous defensive maneuvering using electric propulsion systems can enable lower initial platform masses than chemical maneuvering systems.

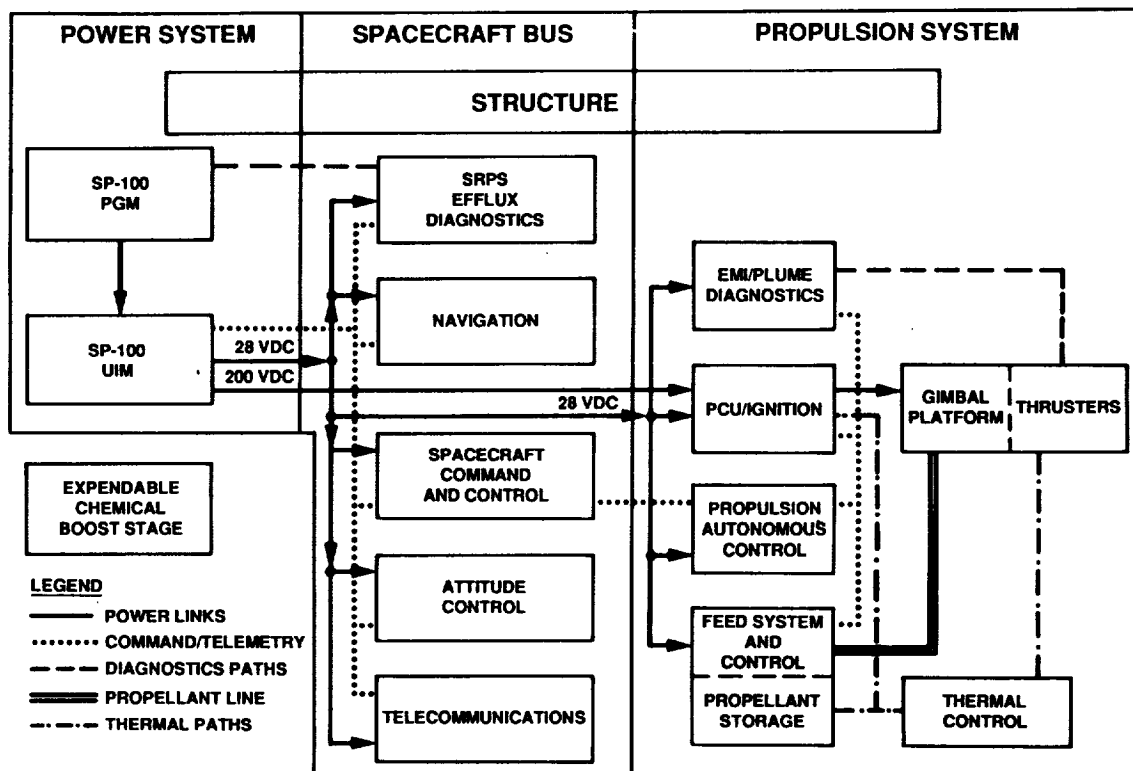


Figure ES-5. Arcjet NEP system block diagram.

RECOMMENDATIONS

Recommendations in the areas of engine technology, facilities, and mission and system design are summarized in this section.

Engine Technology

The issue of cathode erosion is of central importance. Some data from this program suggests that the erosion rate may increase with time. This tendency should be confirmed, and then analyzed. Alternate materials that promise to prolong cathode lifetime should be tested. In particular, the effect of lowered cathode material work function should be explored.

The effect of propellant swirl on engine operation and performance should be determined. Also, further examination of nozzle geometry effects would aid in the selection of an optimal thruster geometry. The geometric conditions which could cause destructive reconfiguration of the arc geometry, brought about, for example, by cathode erosion, should be identified. The geometric boundaries of stable thruster operation should be determined.

Since the 30-kW ammonia arcjet is now known to produce less than 800 s specific impulse and 30-percent thrust efficiency, further development is necessary before the technology can be broadly applied. Performance improvements may result from the recommended investigations cited above; in addition, it may be necessary to employ another propellant, such as hydrogen or hydrazine.

Missions and Systems

An endurance test involving engineering model hardware, including the arcjet engine, power-conditioning unit and propellant feed system should be conducted to ensure that no subsystem-level show-stopper issues will prevent the application of this technology.

System-level components which require development include a suitable power feed for the thruster gimbals; a switching mechanism that would allow spare thrusters to be switched in; and flow control hardware that would enable throttling.

A flight test of a 30-kW class arcjet propulsion system should be conducted to validate this technology. Such a flight test should demonstrate the required attributes of an arcjet propulsion system: appropriate delta-V; the on-off cycling needed for a solar-powered mission; adequate lifetime; EMI characteristics; and particulate contamination levels.

1.0

INTRODUCTION

Arcjet engines employ electrothermal effects to produce thrust. A schematic of a typical arcjet engine configuration is shown in Fig. 1-1. It consists of a single piece which forms the plenum chamber, constrictor, and expansion nozzle, and which also serves as the discharge anode. The cathode is a conically tipped rod centrally located in the plenum chamber, with its tip near the constrictor entrance. An insulator holds the cathode in place and isolates the two electrodes. The propellant gas is fed into the plenum chamber tangentially, is heated by passing through and around an arc discharge and is then expanded in a diverging nozzle to produce thrust. When the engine starts, a constricted arc extends from the conical tip of the cathode through the constrictor and attaches to the nozzle as shown in Fig. 1-1. The conical tip of the cathode provides a high-temperature region for thermionic emission of electrons. The arc is blown downstream through the constrictor channel by the propellant gas pressure in the plenum chamber. The attachment point in the nozzle must be either diffuse or, if concentrated, must move very rapidly within the nozzle to prevent anode surface melting. The propellant receives the bulk of the thermal energy in a thin cylinder along the center line of the constrictor.

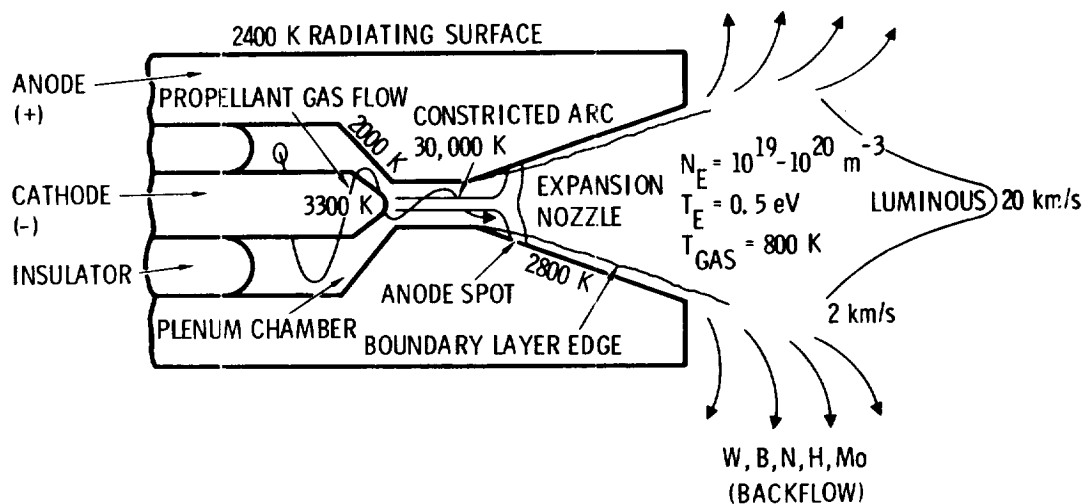


Figure 1-1. General schematic of arcjet operation.

Active research on thermal arcjet thrusters, begun during the late 1950s and continued until the mid-1960s, is reviewed in Refs. 86 and 118. During that period, arcjet engines were developed for primary propulsion applications powered by Space Reactor Power Systems (SRPS). Engines requiring from one kilowatt to more than 200 kW of input power were examined. A variety of propellant gases was investigated, including H₂, He, Li, NH₃, N₂H₄, Ne and Ar. Arcjet research was terminated in the mid-1960s following the cancellation of the SNAP SRPS programs, because no other adequate power source was being developed.

Development of both high-power solar and nuclear space power systems has renewed interest in using electric propulsion for primary propulsion functions and has led to the renewed development of the 30-kW arcjet engine. Arcjet engines are being investigated for applications in the near-Earth environment, specifically station-keeping (1-5 kW) and orbit-raising (10-30 kW). An arcjet propulsion system using 30-kW arcjets is baselined as the active load for the SP-100 Flight Experiment, a flight test of an SRPS planned for the late 1990s. Additional flight opportunities for 30-kW class arcjets include an Air Force arcjet Advanced Technology Development (ATD) Program⁹⁸ and a proposed joint Air Force/NASA/SDI technology demonstration flight called ELITE.^{71,91,96}

Renewed development of 30-kW ammonia-propellant arcjets began in 1985 through an Air Force-sponsored endurance test at JPL.^{80,84,85} During this test, an ammonia arcjet of a baseline design was operated at a nominal power of 25 kW for 573 hours, before cathode tip whisker growth caused a low voltage condition which terminated the test. The engine was based on the AVCO R-3 design originally tested for 50 hours in 1964.^{1,118} Performance characterization tests with the baseline engine design showed the same indicated performance reported for the AVCO R-3 engine, as shown in Table 1-1.^{17,18,19} Subsequent work at the Jet Propulsion Laboratory under Strategic Defense Initiative Organization (SDIO) sponsorship, based on the baseline engine design and test results, culminated in the D-1E arcjet which has a more robust thermal design and improved indicated performance.

This report describes the results of the SDIO-sponsored arcjet technology program focusing on 30-kW ammonia-propellant engines. The program can be broken down into eight major technical tasks: (1) facility preparation and maintenance; (2) arcjet engine design; (3) materials analysis and evaluation; (4) arcjet performance testing; (5) arcjet endurance testing; (6) modeling; (7) diagnostics development and application; and (8) mission and system analysis. This program focused mainly on Tasks 4 and 5. An approximate breakdown of the program focus over the 3 1/2 year period of performance is shown in Fig. 1-2.

Table 1-1. Comparison of AVCO (1964) and JPL (1986)
Arcjet Performance Data

ENGINE	R-3 ⁵	BASELINE ⁸⁵
Date	1964	1986
Laboratory	AVCO	JPL
Power, kW	30.0	30.5
Thrust, N	2.50	2.45
Specific Impulse, s	978	967*
Efficiency	0.38	0.37*
Mass Flow, g/s	0.25	0.25*

* Uncorrected for mass flow error; see Section 5.6.

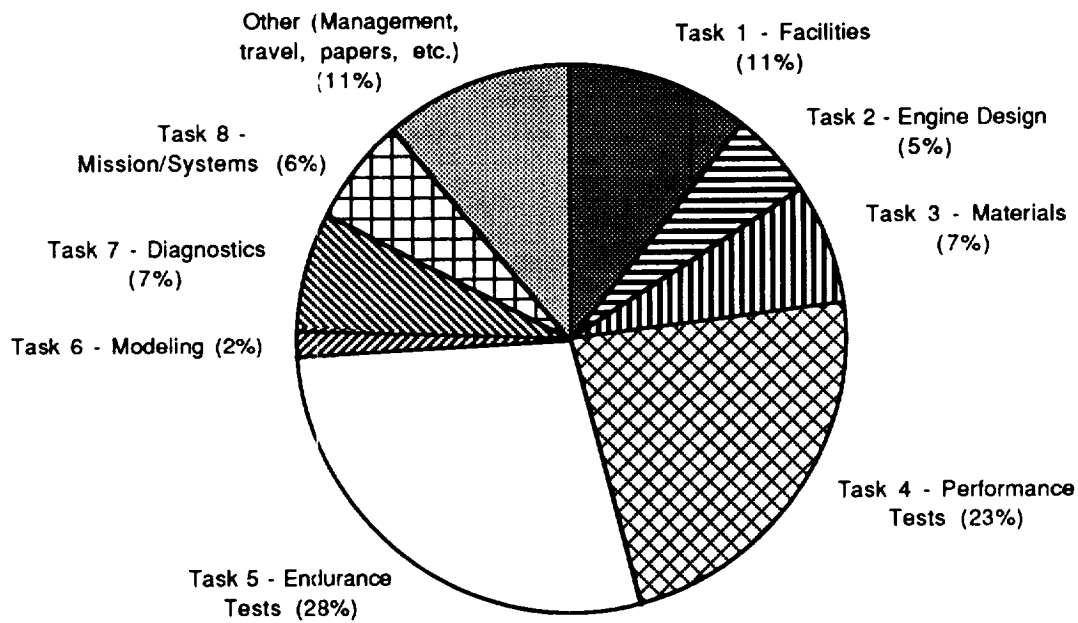


Figure 1-2. Program work breakdown.

2.0 THE EXPERIMENTAL FACILITY AND INSTRUMENTATION

The details of the original JPL arcjet facility are documented in Ref. 85, the final report for the Air Force-sponsored arcjet test program conducted from December 1984 to November 1986. These facilities were moved to a new location between May 1987 and May 1988. Reference 20 contains a description of the relocated facility and updates specifications given in Ref. 85. The facility consists of the vacuum subsystem (vacuum tank pumps and exhaust line), data acquisition and control subsystem, instrumentation (voltage and current meters, facility pressure and temperatures, and engine thrust measurement), power subsystem, and the propellant storage and feed subsystem. The specifications of the relocated facility subsystems are given in Refs. 20 and 85 and are summarized below.

2.1 VACUUM SUBSYSTEM

The arcjet was run in a water-cooled, stainless-steel vacuum tank with an internal diameter of 1.2 m and a centerline length of 2.1 m. One tank end cap and eleven smaller ports opened to provide access to the experiment. The exhaust plume of the arcjet was collected by a water-cooled diffuser, 0.16 m in diameter and pumped by a high capacity vacuum pumping plant. This pumping plant consisted of a 6320 l/s Roots blower, backed by a 610 l/s Roots blower and a 140 l/s Stokes mechanical vacuum pump. The first stage was powered by a 50-horsepower motor and was capable of continuous operation with an inlet pressure as high as 0.5 torr. All of the pumps were water-cooled. With zero propellant flow, the vacuum tank pressure could reach about 0.002 torr. With an ammonia flow rate of 0.32 g/s, the tank pressure increased to about 0.035 torr with the engine off. The exhaust gases are vented to the atmosphere through a dilution stack.

2.2 DATA ACQUISITION AND AUTONOMOUS CONTROL SUBSYSTEM

The test facility and engine were monitored autonomously using a Hewlett-Packard 3421A Data Acquisition/Control Unit (DACU) and an HP 9836 computer. The DACU had 16 input data channels and 4 output relays for active facility control. The built-in digital voltmeter of the DACU had automatic range and zeroing capability with a maximum sensitivity of $1\mu\text{V}$ (DC). The maximum DC input voltage was 300 V with an input impedance of $10^7\Omega \pm 1$ percent to $> 10^{10}\Omega$. Input data to the DACU included arc voltage, arc current, ammonia propellant flow rate and pressure, tank pressure, and various facility component temperatures (e.g., cooling lines).

The arcjet test facility had the ability to acquire and store data at user-specified intervals between 1 and 300 seconds. In the event of anomalous behavior, the computer would terminate engine operation and shut down all facility subsystems (except data acquisition) in an orderly manner. This ability to detect anomalous behavior was defined by the operator, who input acceptable ranges of voltage, current, pressures, and engine and facility temperatures against which the computer compared the real-time input. In addition, the data acquisition subsystem allowed remote monitoring of the

facility and engine via computer modem. In the event of a computer-directed test termination, the computer saved the sampled data for five minutes before and five minutes after the shutdown, when the sample interval was less than 5 s, so that the failure sequence was known. A more detailed description of operation was given in Appendix C of Ref. 85.

2.3 INSTRUMENTATION

Arc voltage was measured near the anode and the cathode to minimize corrections for resistive drops. Arc voltage was measured with a 10-to-1 precision metal film resistor divider. The measurement was corrected for the small 0.0025 Ω resistance between the measuring point and the engine. Accuracy was ± 0.02 percent.

Arc current was determined by measuring the voltage across a 0.000504 Ω (± 0.2 percent) low inductance coaxial shunt. This shunt was calibrated prior to the start of the tests in February 1988 at 50.00 A and 100.00 A at an ambient temperature of 23°C. The shunt was cooled by a fan. The accuracy of the current measurement was ± 0.10 percent of full-scale.

Tank pressure was measured with a variable-capacitance type gage. This transducer was capable of measuring the pressure of any gas and/or vapor mixture with an accuracy of ± 0.5 percent of the reading. The gage had a range of 0 to 10 torr.

Engine temperature was measured with a Raytek infrared remote sensing pyrometer. The pyrometer was located outside of the vacuum tank and senses through a 1.9 cm thick glass window. A GE ribbon filament standard lamp was used to calibrate this system. The lamp was located inside the vacuum tank at the position occupied by the engine during the testing. The known lamp brightness temperature was then used to correct the pyrometer data with a systematic uncertainty of $\pm 6^\circ\text{C}$.

Facility temperatures were measured using E-type thermocouples referenced to an electronic ice-point within the DACU. The accuracy of the temperature measurements was equal to or better than 0.095 percent of full-scale.

The arcjet engine was hung from a cantilevered hollow beam. The thrust produced by the engine was measured by detecting the amount of deflection in the beam during engine operation. The beam, made of 321 stainless steel with a 1.27 cm outer diameter and 0.17 cm wall thickness, was also part of the propellant feed system. The beam deflects about 1 mm for 2 N of thrust. The amount of deflection was measured with a Linear Voltage Displacement Transducer (LVDT) that had an operation range of ± 0.25 cm. The body of the LVDT was held in a housing located at the bottom end of a second cantilevered beam. Both pieces of steel were fully annealed. The LVDT core was attached to the hollow beam with an adapter. The housing for the LVDT body had six adjusting screws so that the attitude of the body relative to the core could be adjusted in three translational and three rotational degrees of freedom. This fine degree of adjustment was necessary to keep the LVDT body and core from touching throughout the range of movement of the thrust beam. This

method of measurement of beam deflection did not affect the stiffness of the thrust beam nor did it add hysteresis to the measuring system. Power was fed to the engine through coaxial mercury pools to eliminate power lead effects on thrust. Both beams were attached to a 321 stainless-steel plate with feed-through fittings. The thrust stand and engine attachment fixture were shielded from the hot engine and low-density circulating gases by a water-cooled copper jacket. The engine attachment fixture was designed so that engines with various mass distributions could be mounted with their center-of-gravity underneath the thrust beam.

The device used to remotely calibrate the thrust stand while under vacuum was described and pictured in Appendix A of Ref. 85. The calibration was based on simulating the position of the engine at different thrust levels by applying known loads to the upstream end of the arcjet, using a pulley and weight system, and equating the change in position with the LVDT output voltage. The thrust stand sensitivity was found to be 925 mV/N.

2.4 POWER SUBSYSTEM

The power to the arcjet was supplied by a Linde PHC-401 DC arc-welding power supply. This power supply has a continuous duty capacity of 400 A at a load voltage of 215 V and 50-percent duty capacity of 500 A at 180 V. A 0.3Ω forced-air-cooled ballast resistor reduced the power supply ripple to about 3 percent at 30 kW and protected the power supply from a short circuit at the arcjet.

The capacitor-inductor bank (L-C filter) used during some of the long tests consists of 8 inductors of $2.3\ \mu\text{H}$ each and 8 sets of 4 capacitors, with a capacitance of $9600\ \mu\text{F}$ per set. This gives a total of $76,800\ \mu\text{F}$ capacitance and $18.4\ \mu\text{H}$ inductance for the bank. The effect of the capacitor-inductor bank was to reduce current ripple from 3.0 percent to 0.2 percent. Figure 2-1 shows the power subsystem circuit with the L-C filter installed.

Coaxially-configured water-cooled pools of mercury were used to transfer power to the engine while maintaining mechanical isolation between the engine and heavy power leads so that thrust can be measured. The coaxial current feed system is described in detail and pictured in Appendix B of Ref. 85.

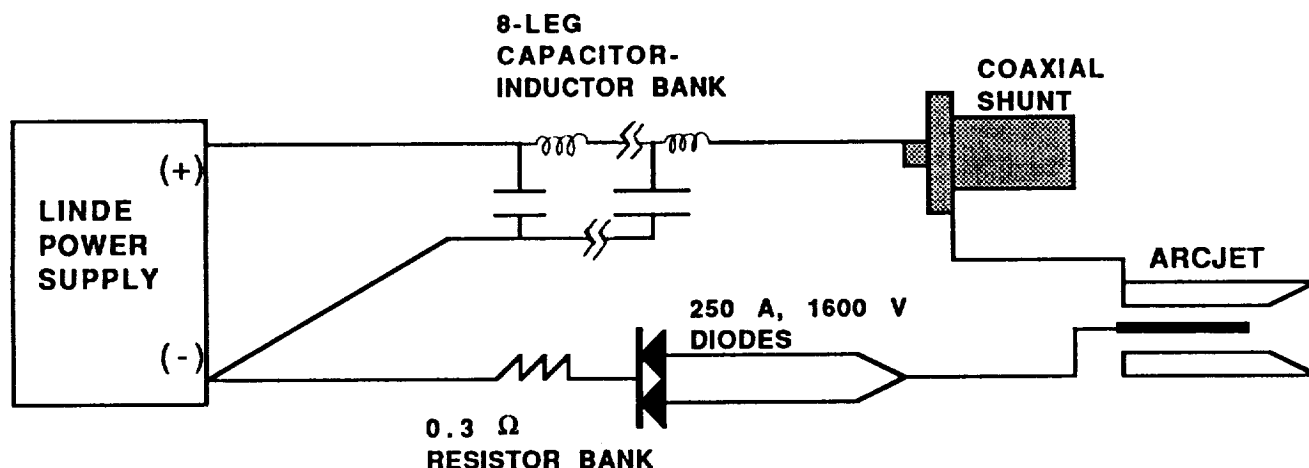


Figure 2-1. Arcjet power subsystem with L-C filter.

2.5 PROPELLANT FEED SUBSYSTEM

Figure 2-2 shows a schematic of the propellant subsystem. The most significant difference between the original facility and the relocated facility is that the ammonia storage tank is now located at a higher level than the vacuum test chamber and the heated air from the ballast resistor no longer can be used to keep the ammonia storage tank warm. This storage tank relocation required the use of a large diameter six-foot vertical rise in the propellant line with a line heater directly outside of the ammonia tank outlet to prevent liquid ammonia from reaching the arcjet engine. In addition, during overnight arcjet operation on cool or rainy evenings, the supply pressure of the ammonia tank drops. If the pressure dropped to within the regulated pressure, the ammonia flow controllers would not have sufficient pressure for stable flow control. This situation did not occur very often and was partly remedied by the addition of a water-proof tent cover over the tank to minimize cooling and heating lamps to maintain the supply pressure. Ammonia propellant mass flow rate was measured and controlled with a Sierra Instruments Side-Trak Model No. 830 flow controller. This flow controller has been calibrated for ammonia vapor to measure flow rates from 0 to 30.0 standard liters per minute (0 to 36 g/s). Section 5.6 describes the discovery of a source of error in the calibration procedure used by the manufacturer and the effect of this error on reported performance data.

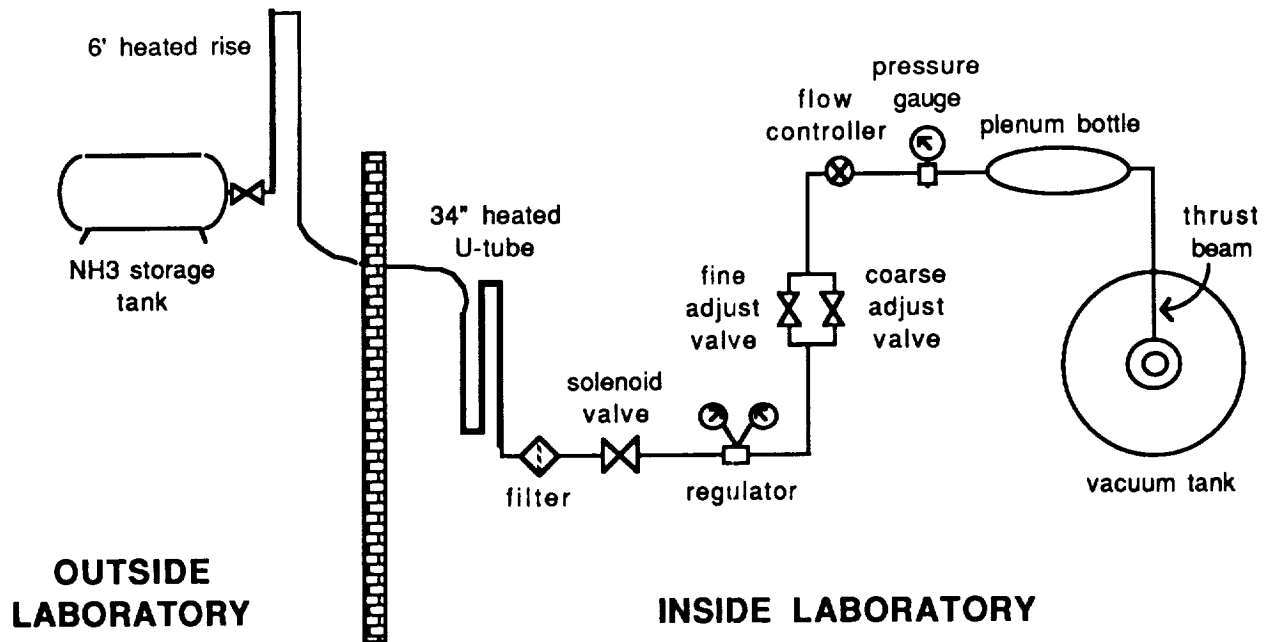


Figure 2-2. Propellant subsystem schematic.

A stainless-steel pressure regulator was used to reduce the supply pressure to 30 psi as required by the flow controllers. Stainless-steel lines and gauges were used to route ammonia vapor to the thrust stand thrust beam. The ammonia propellant was introduced into the engine through the thrust beam. The propellant pressure was measured at the top end of the thrust beam (outside of the tank) and downstream of the flow controllers using a strain-gauge type pressure transducer. The range of this gauge is 0 to 500 cm-Hg and its accuracy was ± 1 percent of full scale.

3.0

ARCJET ENGINE DESIGN

Several arcjet engine designs were evaluated during the course of this program. The essential dimensions and critical parameters of these engines are summarized in Table 3-1. The "baseline" engine was identical to the engine used in the earlier Air Force-sponsored 573-hour duration test program. The "baseline MOD I" engine utilized a bell-shaped nozzle in the baseline design. The "baseline MOD II" engine incorporated a modified cathode design into the baseline MOD I engine. The "baseline MOD-III" engine added a high-emissivity coating on the nozzle radiating surface of the baseline engine. The "D-1E" engine is a new design with fewer seals and improved regenerative cooling compared to the baseline engine designs. The D-1E engine has a bell-shaped nozzle and uses a high-emissivity coating.

Table 3-1. Design Parameters and Essential Dimensions
of the Test Engines

PARAMETER	BASELINE ENGINE	MOD I ENGINE	MOD II ENGINE	MOD III ENGINE	D-1E ENGINE
Constrictor Length, cm	1.07	1.08	1.08	1.07	1.05
Constrictor Diameter, cm	0.51	0.51	0.51	0.51	0.50
Nozzle Exit Diameter, cm	2.41	2.93	2.93	2.41	2.93
Exit Area Ratio ⁺	23	33	33	23	33
Nozzle Type	38° cone	bell	bell	38° cone	bell
Outer Nozzle Surface Material	W	W	W	ZrB ₂	ZrB ₂
Plenum Chamber Diameter, cm	2.03	2.03	2.03	2.03	2.03
Plenum Half Angle Taper at Constrictor End	50°	49.5°	49.5°	50°	49.5°
Cathode Diameter, cm	0.95	0.95	0.70	0.95	0.95
Minor Cathode Diameter [#] , cm	0.95	0.95	0.70	0.95	0.95
Cathode Tip Included Angle	60°	60°	45°	60°	60°
Cathode Tip Radius, cm	0.15	0.15	0.05	0.15	0.15
Electrode Gap*, cm	0.21	0.21	0.21	0.21	0.21
Propellant Injection Angle	30°	30°	30°	30°	30°
Nominal Engine Diameter, cm	5.08	5.08	5.08	5.08	5.08
Nominal Engine Length, cm	16.4	14.7	14.7	16.4	15.0

+ Ratio of constrictor area to nozzle exit area.

Diameter of cathode immediately behind tip cone.

* Axial gap between the cathode cone and corner of the constrictor entrance.

3.1

BASELINE ENGINE

A schematic drawing of the baseline arcjet engine used for these experiments is shown in Fig. 3-1. Summarized here are those features important to its thermal behavior. Additional details can be found in Refs. 80, 84 and 85. The plenum chamber-constrictor-supersonic nozzle was turned from a single piece of 2-percent thoriated tungsten. The plenum chamber has a diameter of 2.03 cm with a 50° half-angle taper on the downstream end. The constrictor has a diameter of 0.51 cm and a length of 1.07 cm. The nozzle has an area ratio of 22 and takes the form of a 19° half-angle cone. The nozzle block has a 7° taper along its back edge and is fitted into a cylindrical molybdenum body, as shown in Fig. 3-1. Lapping these parts together at the 7° taper effects a gas-tight seal between the engine body and nozzle block.

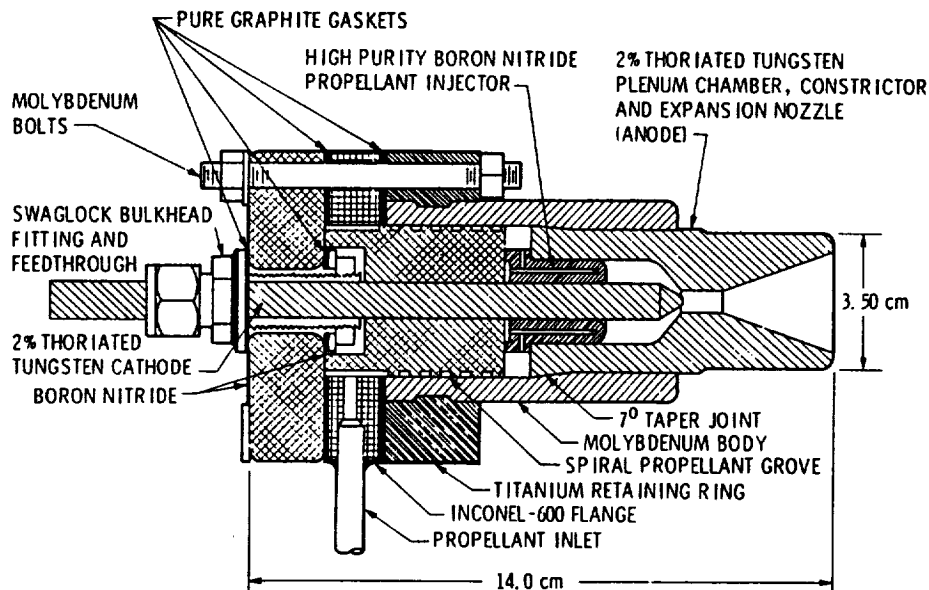


Figure 3-1. Schematic of the baseline arcjet engine.

The ammonia propellant is fed into the engine through a stainless-steel tube welded into a flange made of Inconel 600 on the side of the engine body, as shown in Fig. 3-1. A cylinder of boron nitride with a square, helical groove machined in its outer surface forces the incoming propellant to flow along the hot inner surface of the molybdenum body to reduce the heat flow to the seals at the rear of the engine. A small amount of propellant also flows between the boron nitride cylinder and the cathode.

The back end of the engine is closed with a 1.91 cm thick disk of boron nitride. A standard swagelock bulkhead fitting/feedthrough seals the cathode at the boron nitride disk. A 2.54 cm diameter by 0.25 cm thick stainless-steel washer is welded to the fitting, as shown in Fig. 3-1, to increase the bearing surface on the boron nitride.

A split ring of titanium engages the molybdenum body through a matching groove machined into the molybdenum as is shown in Fig. 3-1. Eight 0.64 cm diameter threaded molybdenum rods running through the boron nitride disk, Inconel flange and titanium retaining ring hold the engine together. Gaskets of 0.08 cm thick pure graphite are used as seals in four places as shown. The steel nuts on the eight rods required tightening after each run since the boron nitride, Inconel, and titanium expanded more than the molybdenum rods/steel nuts, causing the nuts to creep and the joints to become loose after the engine cools.

3.2 BASELINE MOD-I

The important features of the Baseline MOD I engine are shown in Fig. 3-2. Table 3-1 also includes design parameters for this engine. This engine is identical to the Baseline engine except that it has a bell-shaped, contoured nozzle. This nozzle shape was developed in an effort to improve arcjet efficiency and is discussed in Section 5.4 below.¹¹ The nozzle contour is not optimized since no techniques have been developed to optimize nozzle flow for the flow conditions in the arcjet. This nozzle has an area ratio of 33 and a cord length which is 80 percent that of the baseline conical nozzle.

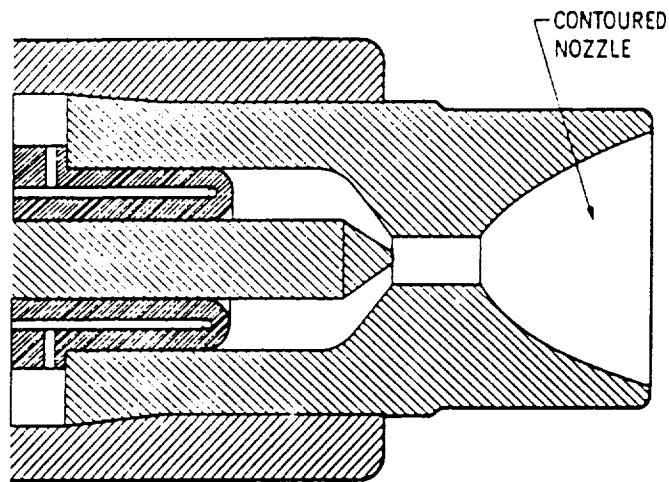


Figure 3-2. Schematic of the baseline MOD I engine.

3.3 BASELINE MOD-II

The Baseline MOD II engine, shown in Fig. 3-3, is identical to the Baseline MOD I engine except for the cathode tip design. This engine was described in Refs. 28, 32 and 34. The design parameters are summarized in Table 3-1. In the baseline cathode design, heat conduction away from the tip is thought to be enough to force the arc to concentrate onto a small spot in order to maintain sufficiently high local temperatures to support thermionic emission. This results in the formation of a small molten pool of tungsten. The evaporation of this molten pool is believed to result in cathode tip erosion. The modified tip design forces the entire tip region to a higher temperature by increasing ohmic heating and reducing rearward thermal conduction. An increased overall tip temperature should allow an expansion of the thermionic emission zone thereby reducing the peak tip temperature of the cathode material. If the peak tip temperature is reduced below the melting point of tungsten, cathode tip erosion should decrease markedly.

3.4 BASELINE MOD-III

The baseline MOD III engine is identical to the baseline engine (Fig. 3-4) except that it was plasma-spray-coated with 325 mesh size ZrB_2 on the outer nozzle and body surfaces as shown in Fig. 3-4.³⁸ See Table 3-1 for the design parameters and dimensions of this engine. The coating had a thickness of 0.025 cm and had a mat grey appearance at room temperature. Emissivities ranging from 0.50 to 0.95 are reported in the literature for

ZrB₂.⁴⁹ Increased surface emissivity should enable higher power operation because the engine can radiate heat more efficiently.

3.5 D-1E ENGINE

The D-1E arcjet engine is shown schematically in Fig. 3-5. The critical dimensions and essential parameters are also summarized in Table 3-1. The letter designations A, A1, B, etc., in the following paragraphs refer to labels of parts or locations shown in Fig. 3-5. More detailed descriptions of the D-1E arcjet engine, along with its assembly and operating characteristics, are given in Refs. 19, 20, 27 and 38.

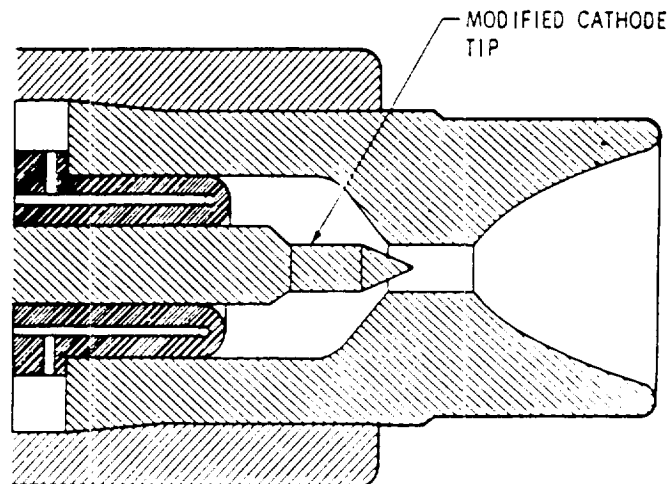


Figure 3-3. Schematic of the baseline MOD II engine.

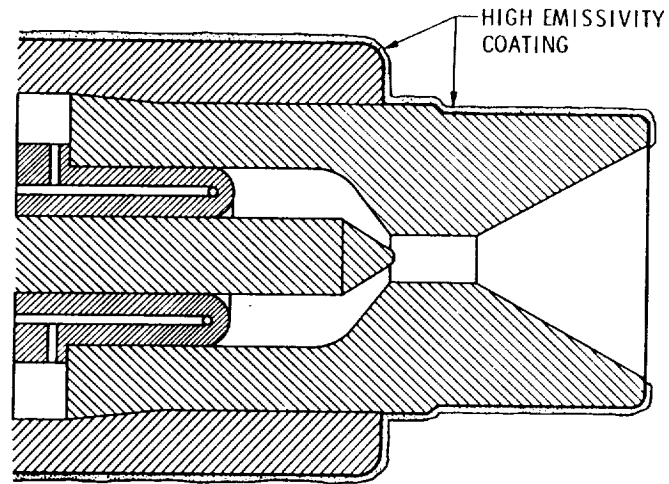


Figure 3-4. Schematic of the baseline MOD-III engine.

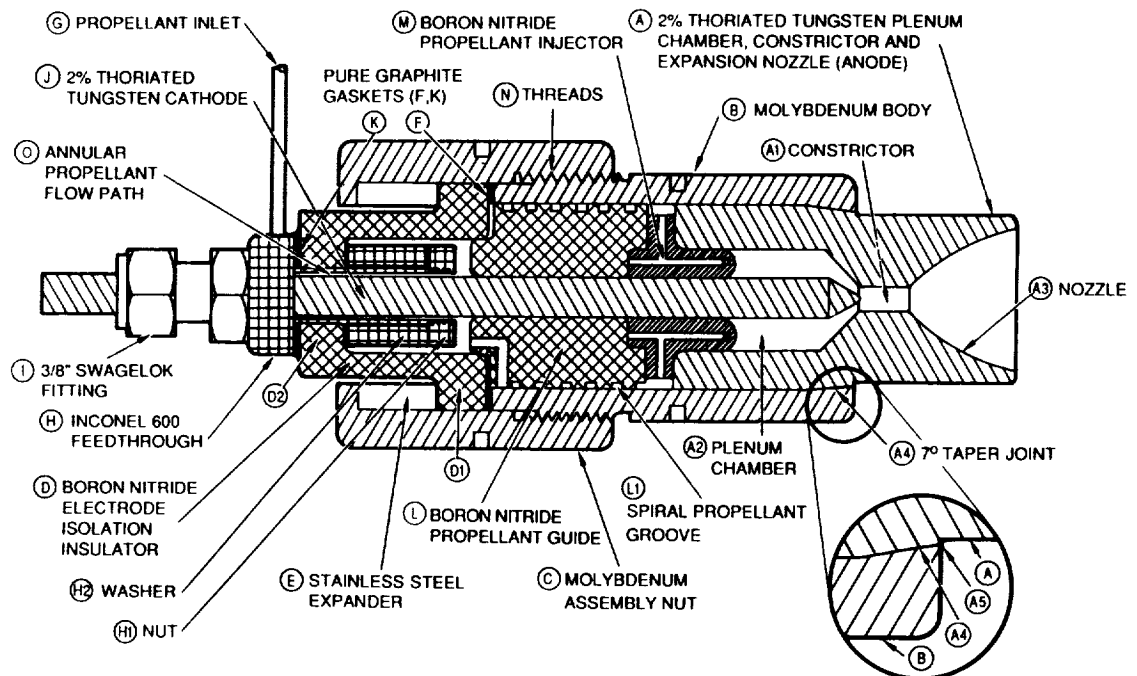


Figure 3-5. Schematic of the D-1E arcjet engine.

3.5.1 Design

The D-1E arcjet design uses a single-piece plenum chamber-constrictor-expansion nozzle (A, Fig. 3-5), made of 2-percent thoriated tungsten, which also forms the discharge anode. The constrictor (A1) is 0.200" (0.50 cm) in diameter and has a length of 0.414" (1.05 cm). These dimensions were originally defined by Avco Corporation in the early 1960s. The plenum chamber (A2) has a diameter of 0.800" (2.03 cm) and a 49.5° half-angle taper at the upstream (constrictor) end. This engine has a contoured nozzle (A3) which is discussed in detail in Section 5.4 (Nozzle Effects); the nozzle has an exit diameter of 1.150" (2.93 cm) and an area ratio of 33. The nozzle block (A) is fitted into a cylindrical molybdenum body (B) which has a matching 7° taper (A4) on its front edge. Lapping and pressing the tungsten (A) and molybdenum (B) parts together at the 7° taper (A4) effects a gas-tight seal between the engine body (B) and the nozzle block (A).

The engine is held together by threading a 2.5 inch (6.35 cm) diameter molybdenum assembly nut (C) onto the threaded end of the molybdenum body (B). This nut holds the boron nitride insulator (D) in place which closes the back of the engine. A lip on the back of the assembly nut (C) presses an expander (E) against the large diameter outer flange (D1) of the boron nitride insulator (D) which, in turn, compresses the pure graphite gasket (F) against the back of the molybdenum body (B) to provide a gas-tight seal. The expander (E) is required because the molybdenum (C) expands more than the boron nitride (D1) at high temperatures and would reduce pressure on the graphite gaskets (F). The stainless-steel expander (E) has a larger coefficient of linear expansion than molybdenum and provides adequate thermal expansion to maintain the gasket pressure. If the gasket material is over- or under-compressed, or if it is not seated properly, cyclic heating will relax pressure on the gaskets allowing them to leak.

The ammonia propellant is fed into the engine through a stainless-steel tube (G) welded onto the side of an Inconel 600 feedthrough (H) at the back of the engine as shown in Fig. 3-5. A standard 3/8 inch stainless-steel swagelock bulkhead fitting (I) is welded to the feedthrough (H) and provides a seal on the cathode (J). The feedthrough (H) is sealed against the small diameter inner lip of the boron nitride insulator (D2) with pure graphite gasket material (K) by tightening an Inconel 600 nut (H1) and thick washer (H2) against the inner lip surface of the insulator (D2). The propellant flows through an annulus 0.025 inch (0.06 cm) wide (O) between the cathode (J) surface and the inside diameter of the feedthrough (H) into a small plenum cavity. The propellant then flows along the hot inner surface of the molybdenum body (B) through a square cross-section spiral propellant groove (L1) machined into the outer surface of a boron nitride propellant guide (L). A small amount of propellant also flows between the propellant guide (L) and the cathode (J). The upstream end of the propellant guide (L) fits into the insulator (D) to preclude a line-of-site discharge path between the propellant guide (L) and the insulator (D) and thus prevent arcs between the electrodes.

The propellant injector (M), made of high-purity (high-temperature) boron nitride, serves as both the propellant injector and an insulator. Propellant is injected into the plenum chamber through four 0.063" (0.16 cm) diameter holes drilled through the boron nitride. The downstream ends of these four holes are at an angle of 60° to the axis of the engine. In this way the propellant is injected tangentially into the plenum chamber at a radius of 0.295" (0.75 cm) and with a downstream inclination of 30°. The distance between the downstream face of the injector and the arc discharge is greater in the D-1E engine than in the Baseline engine (Fig. 3-1). The greater distance reduces the thermal load on the injector face. The upstream end of the injector (M) fits into the propellant guide (L) to preclude a line-of-sight discharge path between the propellant guide (L) and injector (M) and thus prevent arcs between the electrodes.

The 2-percent thoriated tungsten cathode (J) is nominally 0.375" (0.95 cm) in diameter and 7.75" (20 cm) long. The baseline cathode configuration has a 60° included angle tip with a 0.060 (0.15 cm) radius point. The design of the D-1E engine allows for the cathode to be re-spaced or replaced without disassembling the engine.

3.5.2 Materials

The nozzle block (A in Fig. 3-5) and cathode (J) are fabricated from 2-percent thoriated tungsten rod. This material is commercially available and machinable, and has the necessary high-temperature properties. This material is specified as 98.0 ± 0.2 -percent tungsten and 2.0 ± 0.2 -percent ThO_2 . The largest impurity is molybdenum, at up to 300 $\mu\text{g/g}$. The nozzle block is machined from 1.5" (3.81 cm) diameter rod and the cathode from 0.375" (0.95 cm) diameter rod. These are the same materials used on previous engine designs.

The propellant injector (M), propellant guide (L) and electrode isolation block (D) are fabricated from high-purity HBC-grade boron nitride rods. This material is sintered together from boron nitride powder under high pressure and contains no binder material. HBC-grade boron nitride has a flexural strength of approximately 2000 psi at room temperature which rises to 10,000 psi at 1500 °C. It has a coefficient of thermal expansion of less than 0.1 percent over the temperature range 25 to 1800 °C. This material is generally chemically inert in the arcjet environment. However, its long-term chemical compatibility with tungsten and decomposed ammonia is unknown. The propellant injector (M) is made from 1.0" (2.54 cm) diameter rod stock, the propellant guide (L) from 1.5" (3.81 cm) diameter rod stock, and the electrode isolation block (D) from 2.0" (0.064 cm) diameter rod stock.

Pure graphite gasket material (Grafoil) is used in the engine seals. This material is capable of sealing at temperatures up to 3315 °C in an inert atmosphere.¹¹⁴ The gaskets are cut from 0.015 inch (0.038 cm) and 0.025 inch (0.064 cm) thick Grafoil material.

The engine body (B) and nut (C) are fabricated from 2.0" (5.08 cm) diameter and 2.5" (6.35 cm) diameter fully dense molybdenum rod stock. The cathode feedthrough (H) is fabricated from a stock 3/8" swagelok bulkhead fitting (I) welded to an Inconel 600 feedthrough. Inconel 600 is the preferred material for this component because it does not chemically react with ammonia or with its decomposition products (e.g., nitrogen) while stainless steel, for example, does.

3.5.3 Radiative Design

One of the major operational challenges associated with radiation-cooled thermal arcjet engines is the high temperatures at which the thruster components must operate. Thermal analysis done by the AVCO Corporation affords insight into limiting temperatures, temperature gradients and heat flow paths that the arcjet nozzle block must withstand for long periods ⁵³ (Ref. 5). The results of these calculations are shown in Fig. 3-6 for a 30-kW arcjet operating on hydrogen propellant. Note that there is some natural regenerative cooling since about 10 percent of the total engine power is conducted from the hot expansion nozzle back to the cooler propellant plenum chamber, heating the incoming propellant. The maximum nozzle surface temperature appears to occur at the arc attachment area and can be as high as 2500 K for an engine input power of 30 kW_e.

These high temperatures have led to operational problems during engine operation. Historically, the first major problem encountered was electrode and seal failure from overheating. Overheating can induce evaporation of electrode material and result in shorter electrode life. Overheating of other engine parts such as joints, seals and insulators can cause propellant leaks.

The D-1E engine design addressed the high-temperature concerns in several ways which are reviewed here. The 7° taper joint seal (A4, Fig. 3-5) is located midway down the nozzle (A) outer diameter and at the end of the molybdenum body (B) so that the location where the molybdenum body (B) and tungsten nozzle (A) are in contact is closer to the heat-generating source than in the baseline design. This allows the heat to be more effectively distributed between the nozzle block (A) and body (B), resulting in a lower nozzle temperature.

Propellant is introduced into the engine at the cathode feed through (G, H) and flows within an annulus between the cathode (J) and the inside diameter of the feedthrough (H). This allows the propellant to absorb the heat conducted back along the cathode (J) and thus to reduce the temperature of the rear engine seals as compared to the baseline engine. As with the baseline engine, the propellant then flows through a square spiral propellant groove (L1) along the inside diameter of the molybdenum body (B) to remove additional conducted heat (preheating the propellant), which protects the main engine seal (K) and minimizes the heat load on the threads (N).

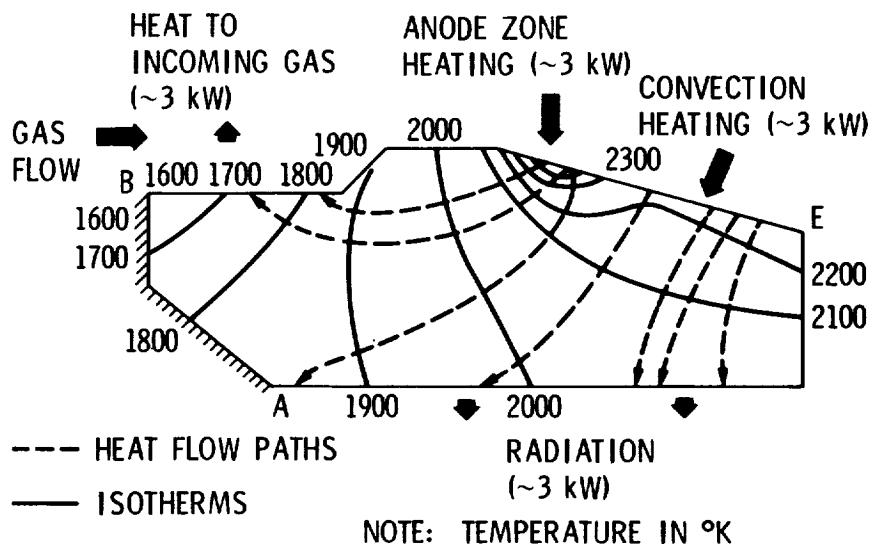


Figure 3-6. Results of heat transfer calculations in the nozzle block of a 30-kW arcjet (Ref. 5).

The D-1E engine design includes a high-temperature high-emissivity coating on the outer nozzle and engine body surfaces to enhance radiative cooling. At arcjet nozzle operating temperatures, the emissivity of bare tungsten is roughly 0.4 as shown in Fig. 3-7.⁹⁵ A coating of ZrB_2 , 0.015" (0.038 cm) thick, is plasma-sprayed onto the outer engine surfaces to increase the emissivity. Experiments described in Chapter 5 (Section 5.3.1) show that ZrB_2 increases the emissivity to between 0.55 and 0.6 providing a 120 °C nozzle temperature reduction. This reduction in nozzle operating temperature should lead to longer anode life, provide wider engine design latitude and ease spacecraft thermal integration issues.

3.5.4 Cathode Tip Shapes

Six tip configurations were tested and are shown in Fig. 3-8. All cathodes have a nominal diameter of 0.95 cm. The baseline cathode is a 60° cone with a 0.15 cm radiused tip. The 45° reduced radius cathode has a tip region diameter of 0.70 cm and terminates in a 45° cone with a 0.05 cm radiused tip. The rationale for testing such a cathode is that if the tip area temperature is higher (by increased ohmic heating and reduced rearward thermal conduction), an increased overall tip temperature should allow for a larger thermionic emission zone, thereby reducing the peak temperature of the cathode. The dimpled cathode is the baseline configuration with a 0.25 cm radius hemisphere inverted into the 60° cone. This was the general appearance of the cathode at the end of the 573-hour endurance test without the whiskers.

The flat-face cathode has a 0.51 cm diameter circular face and a 100° conical section sloping to the 0.95 cm diameter rod. This angle matches the converging section of the plenum chamber. The large tip cathode has a larger diameter tip than the other cathodes (1.27 cm) and has a 60° half angle cone-shaped tip. This design was selected because erosion testing of 1-kW arcjets has shown that the erosion rate dropped for cathodes of increasing diameter. Finally, the modified flat face has a rounded conical section to increase the distance between the cathode and the plenum walls. The nominal cathode mass was approximately 265 g.

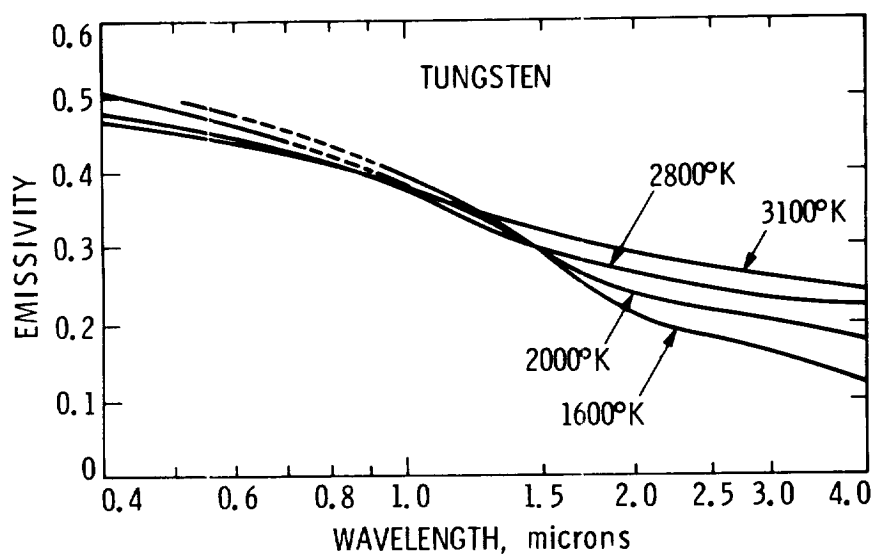


Figure 3-7. Normal emissivity of tungsten (Ref. 95).

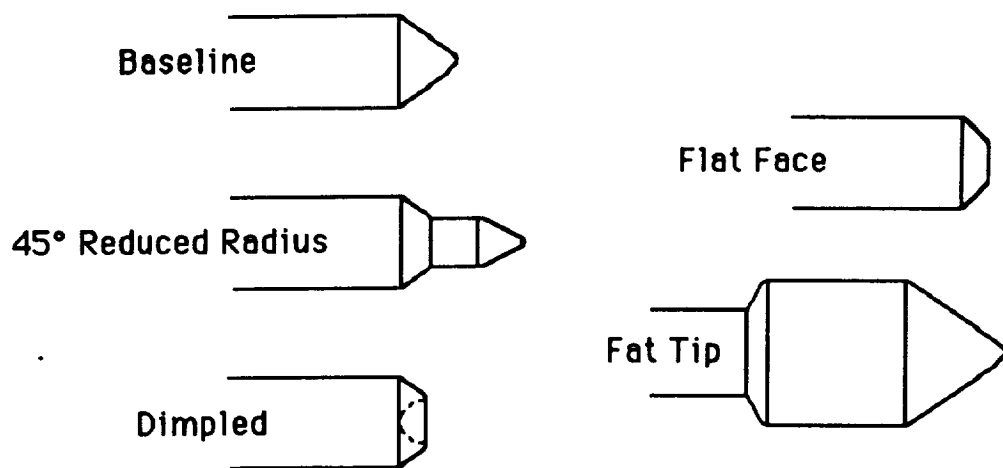


Figure 3-8. Cathode tip shapes.

4.0 MATERIALS ANALYSIS

Two activities are described in this chapter. The first is an analysis of the electrodes and injector of a 30-kW class arcjet which was operated for 573 hours during an Air Force-sponsored program.^{84,85} While the materials analysis was supported solely by the SDIO-sponsored program which is the subject of this report, the results were also reported in Refs. 84 and 85, and are being reviewed here for completeness and because the experimental test program was originally based on these results. The second activity is a materials review directed toward identification of possible alternate materials for the critical engine components. This chapter is drawn primarily from Refs. 79 and 107.

4.1 ANALYSIS OF USED ARCJET COMPONENTS

To be effective, arcjet thrusters must operate reliably for very long periods of time. One thousand to fifteen thousand hours per thruster is considered to be the minimum useful lifetime. At present, the only known life-limiting mechanism is electrode erosion and subsequent whisker growth. This was shown in a long-duration test of the baseline arcjet run on ammonia.^{84,85} The baseline arcjet is described in Section 3.1 above. In this test the arcjet ran for a total accumulated run time of 573 hours. For the first 109 hours the arcjet was operated continuously at a nominal power of 28.6 kW and an ammonia mass flow rate of 0.31 g/s. A facility failure caused a shutdown at that point in time. For the remainder of the test (464 hours) the arcjet was operated at a nominal power of 25.1 kW and a mass flow rate of 0.32 g/s. During the remaining 464 hours of testing the test was interrupted an additional three times because of facility failures. These occurred at 113, 151 and 369 hours into the test. Further details can be found in Refs. 84 and 85.

After the termination of the test at 573 hours, the thruster was disassembled and examined. The cathode, anode/nozzle, and injector had experienced noticeable erosion. These parts were sectioned and analyzed to improve understanding of the erosion processes, and to support the design of an improved arcjet engine.

4.1.1 Cathode

A before and after picture of the cathode tip is shown in Fig. 4-1. An oblique view of the test cathode is shown in Fig. 4-2. Notice that a crater was carved into the cathode tip and a ring of whiskers grew out from the crater rim. The net cathode mass loss over the full 573 hours was 1.95 ± 0.15 g, for an average loss rate of 3.4 mg/hr. The net volume loss was 0.1 cm^3 . Notice, from Fig. 4-1, that the whiskers grew toward the anode and that the minimum electrode gap was 1 mm. It is surmised that at 573 hours into the test, a whisker either touched the anode or got close enough to establish a high-current arc between itself and anode wall. The rush of current through the whisker, approximately 200 A, melted it and surface tension drew the molten tungsten into a ball on the cathode. Such a ball

can be seen in Fig. 4-2 at about 120° clockwise, on the top of the cathode. The DACU detected a terminal voltage of 99.9 V and since the lower tolerance limit was set at 100.0 V, it terminated the test. The control of and design for whisker growth seems to be an important consideration for achieving the desired operation life time. It has been speculated that the growth of cathode whiskers may be influenced by power supply ripple.

ORIGINAL PAGE
BLACK AND WHITE PHOTOGRAPH

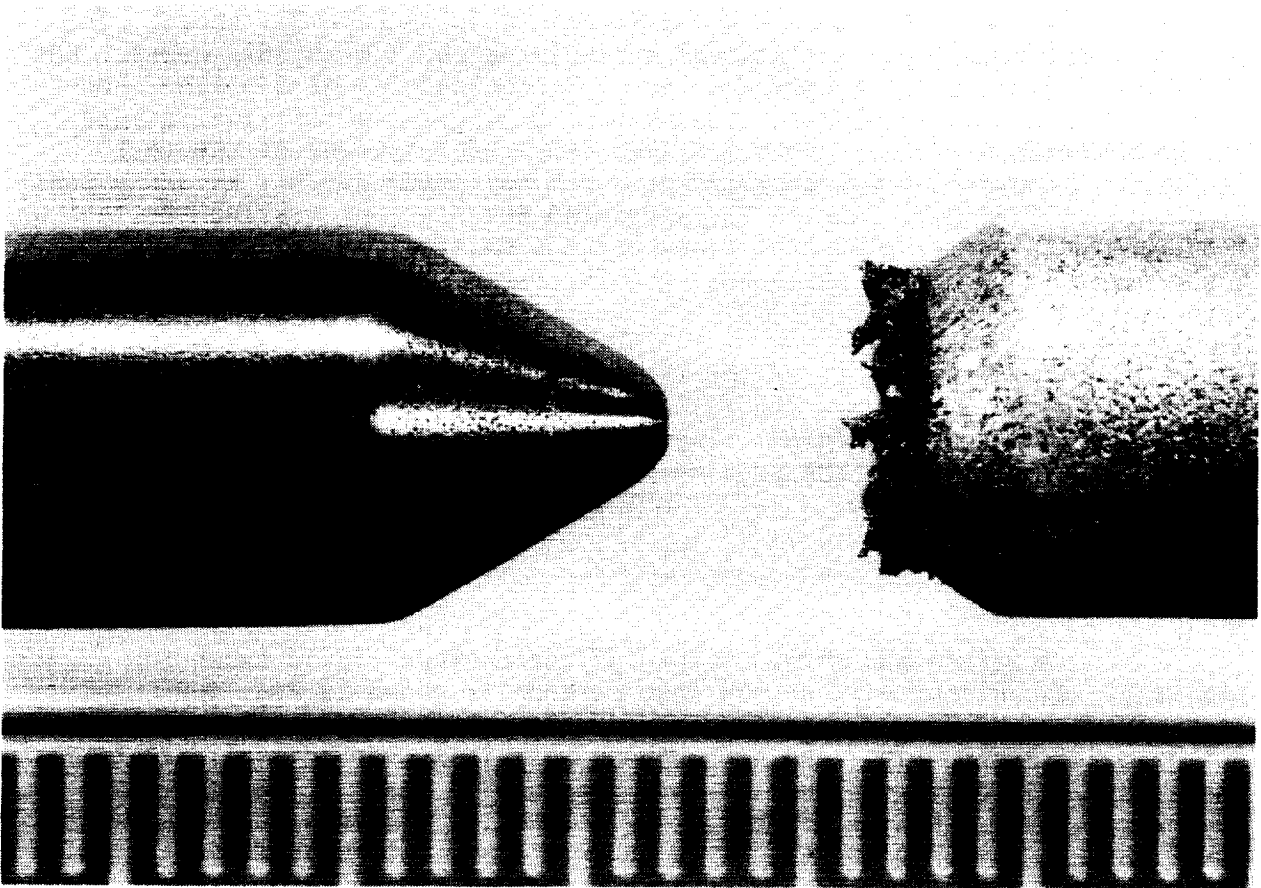


Figure 4-1. Before and after photographs of the cathode tip (573-hour test) (Ref. 79).

ORIGINAL PAGE
BLACK AND WHITE PHOTOGRAPH

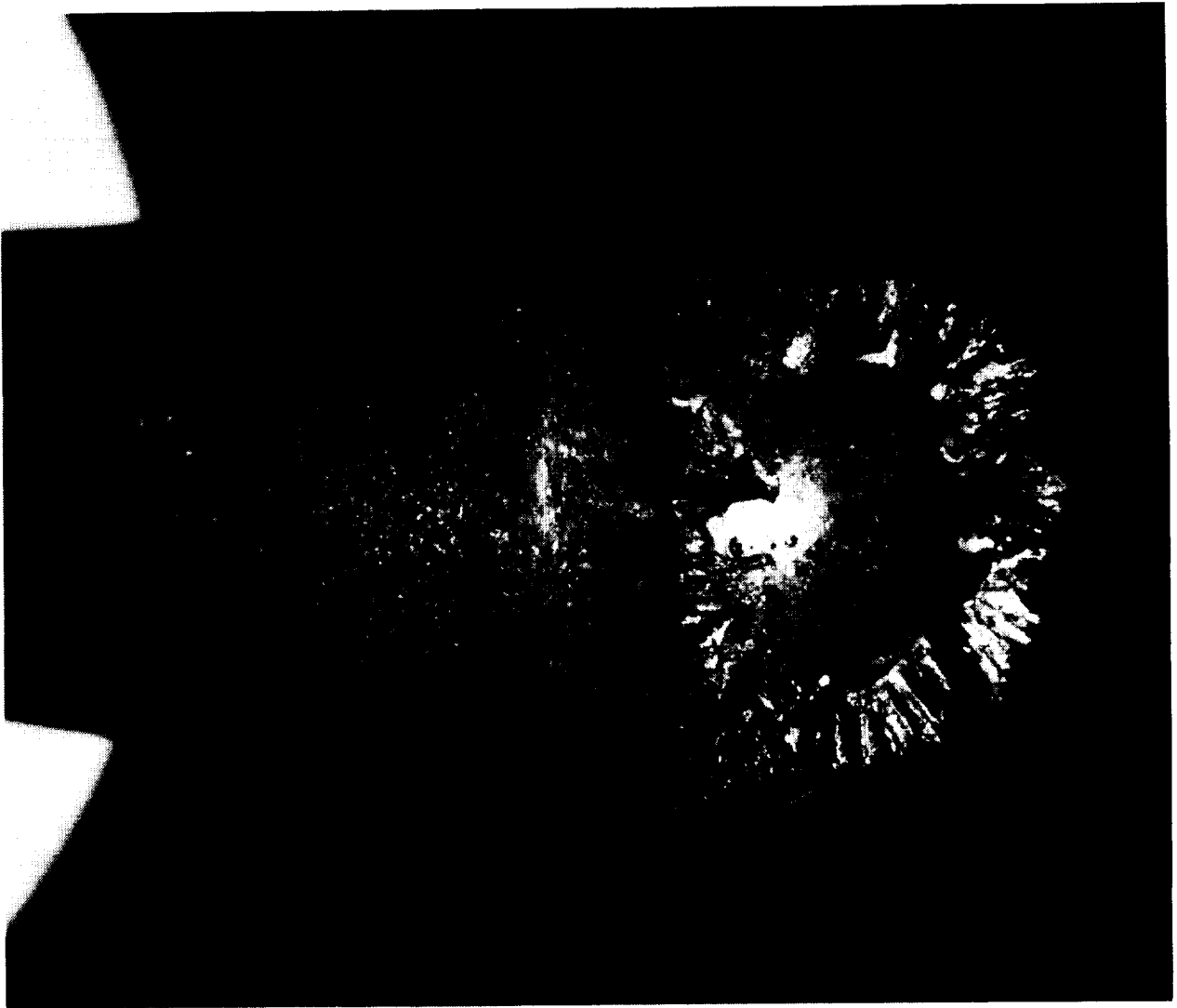


Figure 4-2. Oblique view of cathode tip (375-hour test) (Ref. 79).

The cathode tip was sectioned, polished and etched. A picture of the section is shown in Fig. 4-3. Notice that the crater has an almost perfect hemispherical shape and that the whiskers are growing radially outward. This type of arcjet cathode cratering has been reported in the literature;^{54,113} however, to our knowledge, no one has presented a model or detailed experimental measurements of this type of cratering.

ORIGINAL PAGE
BLACK AND WHITE PHOTOGRAPH



Figure 4-3. Cathode tip cross section (573-hour test) (Ref. 79).

A possible cause of the proposed stagnating gas flow is shown schematically in Fig. 4-4 and based on the following considerations. The result of the interaction between the axial arc current and its own azimuthal magnetic field is an inward-directed radial body force. To balance this body force, a radial pressure gradient is set up such that the gas pressure on centerline is higher than the ambient pressure. This pressure difference, $\Delta P(r)$, is taken from Ref. 101 and is given by:

$$\Delta P(r) = \frac{\mu}{4\pi^2} \left[\frac{i}{r_0} \right]^2 \left[1 - \left[\frac{r}{r_0} \right]^2 \right] \quad (4-1)$$

Here, μ is the permeability, i is the total arc current, r_0 the local arc radius and r the radial spatial variable. The pressure on the arc centerline, relative to ambient, is obtained by setting $r = 0$. The observed arc radius was about 0.75 mm; hence, for a current of 200 A, ΔP was about 18 mm Hg. As is shown in Fig. 4-4, the arc radius must bulge out near the cathode since, assuming thermionic emission, the cathode surface area required to support the arc was much larger (41 mm²) than the 1.8 mm² arc cross-sectional area. Because of this bulging to a radius of approximately 2.5 mm, ΔP near the cathode surface was reduced to about 2 mm Hg, resulting in an axial pressure gradient of about 32 mm Hg/cm (assuming constant ambient pressure). This axial gradient may have driven a flow of hot gas toward the cathode surface, and it then would have convected the tungsten vapors radially out

along the emitting surface, resulting in the deep, symmetric cavity. Additionally, as the arc radius bulges out, an axially directed electromagnetic body force component would have developed, further enhancing the flow of hot gas toward the cathode tip. This additional flow would have turned radially outward along the cathode emitting surface, because of symmetry, and would have added to the convection of tungsten vapor toward the crater rim. These vapors would then be convected out to the rim of the crater where the temperature may be low enough to promote epitaxial growth of whiskers from the tungsten vapor. Alternately, eddy flows caused by swirl in the main propellant flow may lead to a stagnation region on the cathode tip.

Another possible source of tungsten to support whisker growth is a tungsten ion current. However, a careful analysis of the rim area with a scanning electron microscope revealed no micro-arc spots or other evidence of current collection.

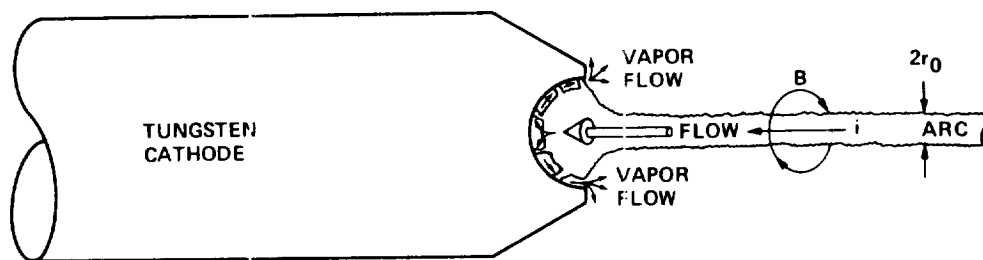


Figure 4-4. Possible cause of cathode tip cratering (Ref. 101).

As is also shown in Fig. 4-4, the arc root is believed to be connected to the cathode surface through a multitude of migrating micro-arcs, since the gas conductivity near the surface is severely limited by the gas temperature which must be in near equilibrium with the surface temperature. The surface temperature can not, on average, be much different from the melting temperature of tungsten (3400 °C). The low conductivity causes current to be carried across this layer by high current density micro-arcs. Fig. 4-5 is an end view of the cathode and shows that most of the cathode surface is covered with pits caused by the micro-arcs. Individual micro-spots can be more clearly seen in Fig. 4-6. The spot diameter appears to be about 10 μm and is surrounded by splashed tungsten, clearly indicating the pressure of molten tungsten. The arc spots could also have been formed during the attempted restart of the engine at 573 hours.

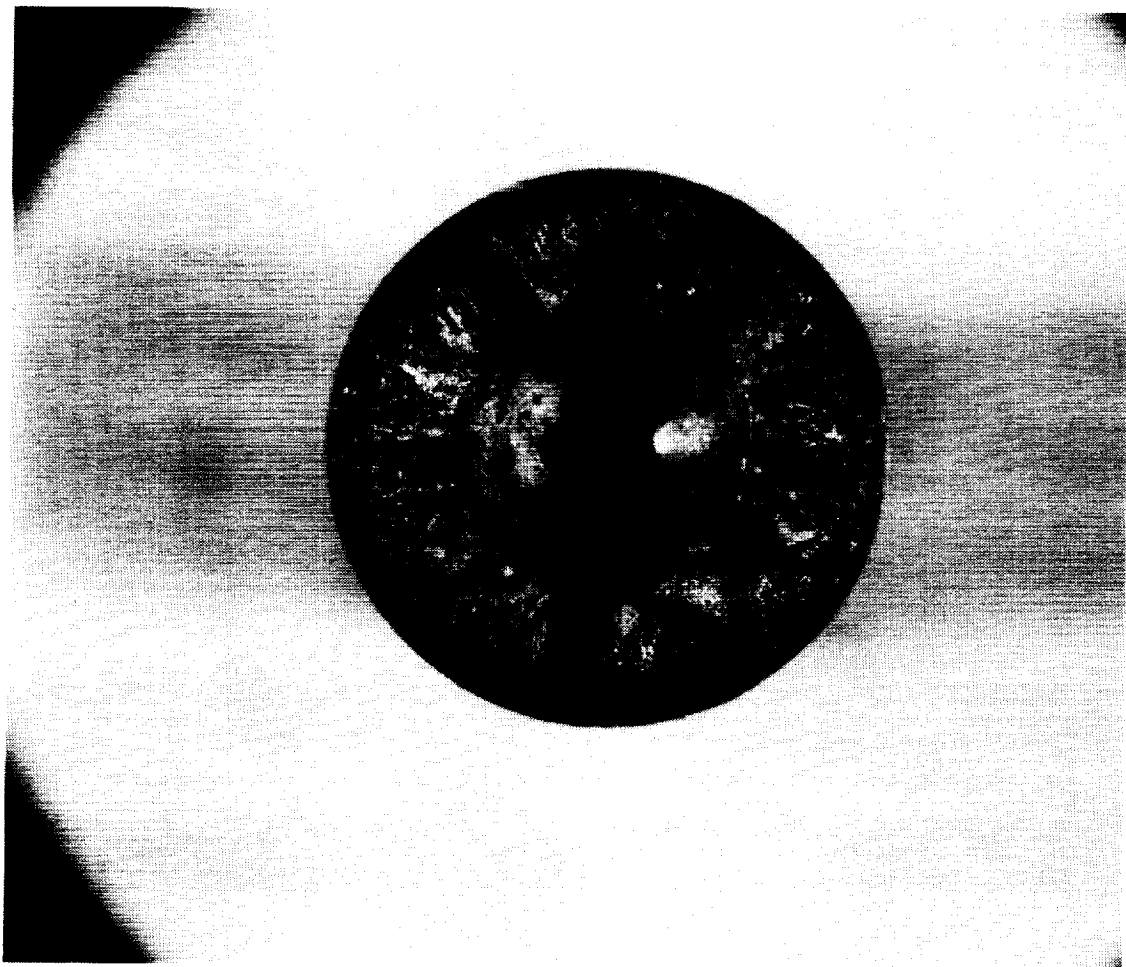


Figure 4-5. End view of cathode tip (573-hour test) (Ref. 79).

ORIGINAL PAGE
BLACK AND WHITE PHOTOGRAPH

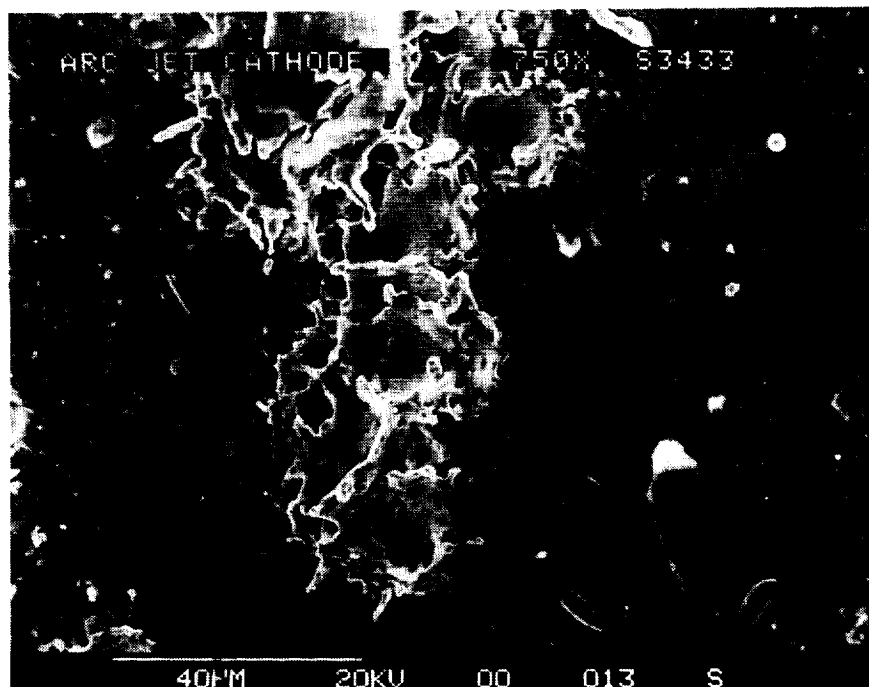


Figure 4-6. Cathode tip microspots (573-hour test, 750 x magnification).

A possible cause of the arc spot motion over the electrode surface is discussed in Ref. 101. Using tungsten property data from Ref. 48, at the melting point the vapor pressure is 17 mtorr, the evaporation rate is 2.28×10^{-4} g/cm²-s and the thermionic emission is 479 A/cm². Ignoring tungsten redeposited as whiskers and taking the total loss as 1.95 g and the total run time as 573 hours, the average vaporization rate is 9.5×10^{-7} g/s. Dividing this by the arc current results in a tungsten loss of 4.3×10^{-3} μ g/coulomb. This result should be compared with the measured loss of 3×10^{-2} μ g/c and the calculated loss of 10^{-2} μ g/c found in Ref. 101. The pressure at the cathode tip was probably higher in the current experiment than it was in Ref. 101 and which may explain the reduced loss. Also, the information in Ref. 48 is based on Langmuir's work, which is presently being reexamined. The values indicate that cathode mass loss is driven by evaporation.

4.1.2 Anode/Nozzle Analysis

After completion of the long duration test and subsequent attempt at a restart the anode-nozzle was sectioned and the less damaged half was ground flat and smooth. A picture of this half is shown in Fig. 4-7. The lower contour of the constrictor was undamaged and clearly shows the erosion pattern caused by the long duration test. As can be seen in Fig. 4-7, the erosion starts at about 1 mm into the constrictor. The constrictor radius

then starts increasing at an ever-increasing rate for the next 6.5 mm, is then constant at 3.0 mm for the next 4.0 mm and then slowly blends into the 19° half-angle cone. The erosion ends about 4 mm into the expansion nozzle. By performing a graphic integration on the data, the amount of tungsten eroded was determined to be 0.71 cm³ or 1.37 g. A careful inspection of the nozzle contour part of this plot indicates that the eroded material may have been deposited on the nozzle wall starting about 11 mm from the exit plane. The thickness of this deposited layer increased linearly and reached about 0.2 mm at the exit plane. The volume and mass of this layer was calculated to be 0.075 cm³ and 1.45 g. Note that these determinations are at best an estimate since they involve very small changes in radius: 0.5 mm for the constrictor and 0.2 mm maximum for the nozzle. This result suggests that most of the material, evaporated from the constrictor wall, flowed downstream in the laminar boundary layer and redeposited on the cooler downstream wall of the expansion nozzle.

ORIGINAL PAGE
BLACK AND WHITE PHOTOGRAPH

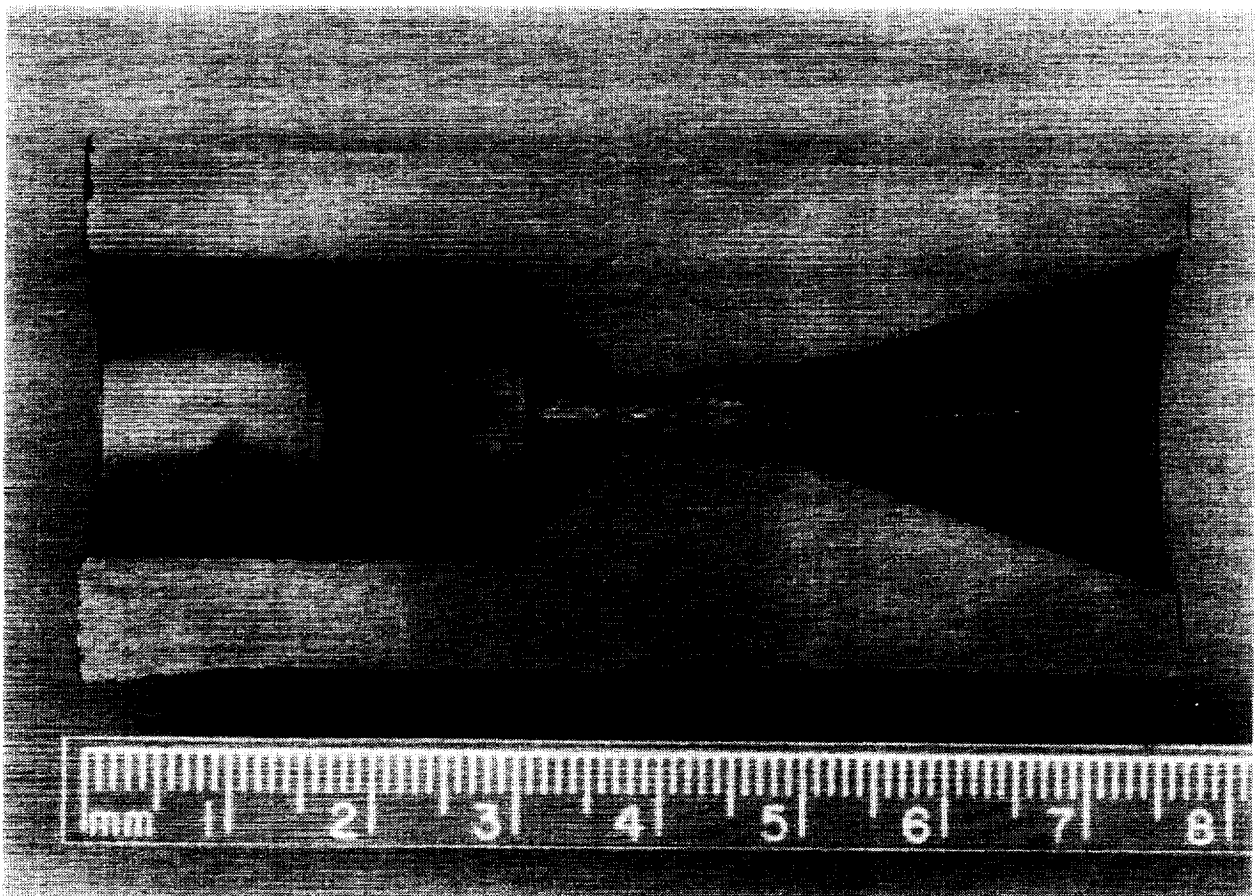


Figure 4-7. Cross-section of the anode (573-hour test) (Ref. 79).

Note also that the plenum chamber walls, though stained, were not affected by the long test duration. The machining marks are still visible on the 50° half angle cone wall.

A quantitative microprobe analysis of the sectioned anode-nozzle was also performed. Ten points were selected along the inner edge of the 50° cone, constrictor and expansion nozzle with a point spacing of approximately 5 mm. A reference point was taken at the very back of the anode nozzle piece. The reference point indicated a thorium content of 1.88 atomic percent with a statistical error of 5.49 percent. Interestingly, about 2 percent molybdenum was also found at this point. Apparently the molybdenum diffused into the tungsten from the engine body during the long duration test. For the rest of the data, the thorium content was 1.2 atomic percent (+0.2, -0.4) and this data had a statistical error of 6.4 percent (+2.8, -1.0). Therefore, a significant amount of thorium was still found in the anode/nozzle surface material. A low concentration of 0.85 atomic percent was found about 5 mm downstream of the end of the constrictor, where the arc is thought to have attached to the nozzle, causing increased heating.

These results suggest that the anode/nozzle suffered no damage that was directly due to the arc during normal operation. However, due to the high operating temperatures, most of the constrictor wall and the sharp corner between constrictor and expansion nozzle evaporated at an approximate rate of 6.6×10^{-7} g/s, or 3.0×10^{-3} μ g/c. Also, using a Scanning Electron Microscope, the walls of the nozzle where the arc was expected to terminate was studied. No unusual effects could be seen except for a greater depletion of thorium from the area.

4.1.3 Injector

The propellant injector was badly eroded during the 573-hour duration test. This was unexpected since the injector used in a previous continuous 168-hour test was unaffected. The eroded injector and a similar but unused injector are shown in Fig. 4-8. The diameter of each of the four injection nozzles has increased from the original 1.6 mm to about 2.4 mm; an area increase of 2.25. It also appears that if the test had continued much longer, the tangential injection would have stopped and the propellant would have been injected axially. Loss of tangential propellant injection, or swirl, could have resulted in arc instability and eventually led to engine damage.

ORIGINAL PAGE
BLACK AND WHITE PHOTOGRAPH

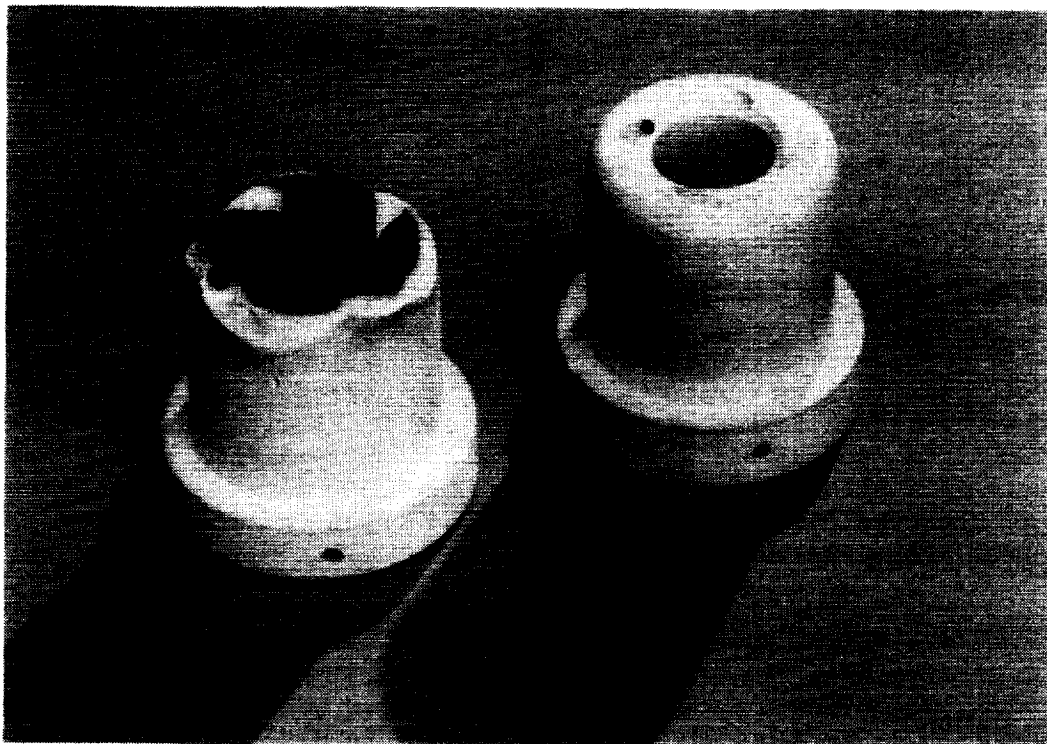


Figure 4-8. Photographs of unused and eroded injectors.

The eroded end of this propellant injector has been analyzed using EDAX with an X-ray beam having a $600\text{ }\mu\text{m}$ spot size, and with a scanning electron microscope. The spots analyzed with the X-ray beam were composed of the black deposits that can be seen in Fig. 4-8 plus the boron nitride just below the deposit. The black deposit was found to be tungsten (7 percent) with a smaller amount of thorium (0.5 percent). Boron and nitrogen were the primary components found. Carbon, oxygen and sodium were also found; these are believed to be deposits from handling. The fact that the content of this sample is predominately boron nitride suggests that the black deposit thickness was less than $10\text{ }\text{\AA}$ since the total X-ray sample depth was $20\text{ }\text{\AA}$ at most. The tungsten and thorium are believed to have been deposited on the insulator material face from gas recirculation in the plenum chamber.

The SEM analysis of the eroded areas revealed nothing unusual about the surface. These surfaces are made up of $10\text{ }\mu\text{m}$ striated particles, arranged randomly, as would be expected of hot-pressed boron nitride. No machine marks were present because the surfaces were eroded.

4.2

MATERIALS EVALUATION

The basic components of present arcjet thrusters are fabricated from materials which were selected on the basis of their performance in similar development work in the 1960s. In the last five years, some research efforts have focused on increasing the lifetime of the low power 1-kW arcjet engine.^{23,61,104} In these efforts significant progress has been made in reducing the erosion of the cathode and anode/nozzle by optimizing the start-up procedures and changing the electrode configurations without changing materials. While this approach has worked for 1-kW arcjets with an arc current of 15 A higher power 30-kW arcjets, with typical arc currents of 260 A offer a more severe environment which requires more attention to materials.

The analyses of used electrode materials described above pointed out that minimizing electrode erosion, and specifically reducing whisker growth, are key to the development of long-lived 30-kW class arcjets. The experimental efforts described in Chapters 5 through 7 were designed in part to reduce erosion and whisker growth through better engine design, electrode configuration changes and reduction of input power ripple. Another approach to reduce erosion and whisker growth is through the use of alternate materials for the critical engine components. Below are descriptions of the present materials and their limitations, identification of the desired material properties, and suggestions for alternate materials.

4.2.1

Electrode Materials

The theories and erosion models for both vacuum and high-pressure arc discharges, including erosion during start-up and continuous steady-state operation, have been reviewed. Although some uncertainties still exist, particularly in the near-cathode plasma region, it has been found that the principal sites for mass loss during arc discharge are at the cathode spots (Ref. 57). There is general agreement that there are three different mass loss fluxes which originate from the cathode: ions (ionized vapor), molten droplets and metal vapor. The extent of each erosion process varies in a complicated way, with the choice of cathode material, cathode size, arc current, arcing time, gas pressure, spot velocity, pattern of spot movement, etc. (see Refs. 24, 40, 41, 100 and 101 for further discussions of this subject). Based on material analysis of the baseline engine cathode described above, evaporation of metal vapor appears to be the predominant cathode mass loss mechanism for the arcjet tests described.

The thoriated tungsten cathode is supposed to maintain high thermionic electron emission (with a work function of 2.7 eV) within the range of operational temperatures. The emission takes place from a monatomic layer of thorium present on the cathode tip. According to Smithells,¹⁰⁶ above 2100 K, the rate of evaporation of thorium is higher than the rate of diffusion-induced replacement. Therefore, thorium should be depleted, leaving a pure tungsten surface with a correspondingly higher typical work function of up to 4.55 eV. Under this circumstance a much higher surface

temperature is needed to maintain the same electron emission current density. At 2100 K, the thermionic emission current density is a maximum of about 5.5 A/cm². This current level is appropriate only for a low current arc discharge.

In a 30-kW arcjet engine, much higher emission current density (over 1000 A/cm²) is needed to sustain a high arc current. This observation is in agreement with the thorium depletion found in the baseline arcjet cathode operated for 573 hours. The surface morphology of the thorium-depleted cathode indicated that a very high surface temperature (close to or slightly above melting point) was needed in order to maintain a high electron emission current density. At these high temperatures, mass loss by evaporation of molten metal is significant. Again, the material mass loss rate of the baseline arcjet cathode, 4.3×10^{-3} g/s, corresponds to an evaporative process.

An optimum cathode material for use in high-current, high-temperature arc discharge conditions should meet the criteria listed below.¹⁰⁷

- 1) Low vapor pressure
- 2) Low evaporation rate
- 3) High melting point
- 4) Low work function at operating conditions
- 5) High ion sputter resistance
- 6) Chemical stability with high-temperature propellant species
- 7) Good thermal shock resistance
- 8) High electrical conductivity
- 9) High thermal conductivity
- 10) High emissivity
- 11) Good high-temperature mechanical properties
- 12) Machinability/formability
- 13) Comparable coefficient of thermal expansion to materials it must contact
- 14) Low cost and ready availability

Several groups of material types which may provide increased cathode and/or anode life are listed below. These selections are based on thermophysical and thermionic property comparisons.^{41,49,102,110,121}

* Pure tungsten:

- Polycrystalline W: Same work function as W/ThO₂ at high temperatures; no depletion/sputtering of Th nor Th contamination of engine components.
- Preferentially oriented W, single crystal and CVD (Chemical Vapor Deposition) W: Same as above; the low work function will reduce the cathode surface temperature.

* Borides of rare-earth metals:

- Lanthanum hexaboride LaB_6 : Very good thermionic emission (work function 2.5 - 2.9 eV for polycrystalline), high sputtering resistance, relatively high melting point and low evaporation rate, high electrical and thermal conductivities. Preferentially-oriented single crystals with work function down to 2.2 eV⁷⁷, but they have low thermal shock resistance and a maximum surface temperature limit which may not be high enough for some applications.
- Zirconium diboride ZrB_2 : Higher melting point, but higher work function than LaB_6 (3.60 eV); high resistance to the action of an electric arc; high emissivity.

* Carbides:

- Tantalum carbide TaC , zirconium carbide ZrC : Very high melting point and low evaporation rate; relatively low work function (3.5 eV for polycrystalline), good sputtering resistance, low electrical resistivity, high emissivity. Use of a single crystal could result in a lower work function, but with low thermal shock resistance, possible dissociation and subsequent loss of carbon by sublimation, and possible reaction with propellant.

* Impregnated tungsten materials:

- Tungsten impregnated with BaAl_2O_4 : High temperature impregnate (melting point 2443 K), low work function (2.1 eV).⁷⁵ May encounter depletion and chemical reactivity at operational temperatures.
- Tungsten matrix impregnated with Emission-Active Phases (EAP) such as LaB_6 , ThC , ZrN , Zn-O : Increased thermionic emission, decreased time of arc initiation; may prevent arc spots from contracting, which causes a clustering of microcraters and enhances cathode erosion. These materials need more study and development work.

Additional information can be found in Ref. 107.

4.2.2 Insulator Materials

The boron nitride propellant injector was badly eroded during the long duration test of the baseline engine, and black deposits were found in the vicinity of the eroded areas. These deposits were identified as primarily tungsten with smaller concentrations of boron, nitrogen and thorium, as well as air/handling contaminants, such as oxygen and probably carbon. Since the tungsten and thorium are believed to have been continuously deposited through evaporation from the tip region and subsequent gas recircularization, the

following phenomenon could explain the possible erosion mechanism of boron nitride. A chemical reaction can occur between boron nitride and tungsten at elevated temperatures.⁷⁸ It is hypothesized that boron diffuses at operational temperatures into the tungsten deposit and forms very brittle and weak tungsten boride compounds. When a high enough boron concentration is attained, a eutectic solid results, which melts at about 2473 K. No evidence of molten material was found on the boron nitride surfaces and the most severe erosion was in the area around the four injection holes. Therefore, it is hypothesized that the erosion was due to mechanical wear of brittle and weak tungsten boride layers caused by shear effects of the flowing propellant.

High-purity boron nitride (BN) was used for the insulator/propellant injector. All of the Group VI-B materials, such as tungsten and molybdenum, react with boron nitride during prolonged exposure at elevated temperatures (about 1273 K) to form very brittle and weak metal boride layers.^{50,78} Since the metal-borides are good conductors of electricity, there is the danger of electrical shorting through surface breakdown of the layer formed on the BN body. Also, BN may be attacked by hydrogen and to a lesser extent by nitrogen (both possible products of dissociated ammonia) at high temperatures during prolonged exposure.⁵⁰ Mass loss related to propellant incompatibility can presumably occur through the formation of volatile boranes.

Insulator materials in severe environments must also maintain many of the same properties as potential electrode materials. The important exceptions are that they must offer good electrical resistance; they should not emit thermionically at operating temperatures; and emissivity and resistance to sputtering are less important qualities than for electrode materials.

Although some materials possess many properties necessary for a superior high-temperature electrical insulator, we must consider the possible chemical reactions which these materials can undergo with propellants, deposited materials and materials in contact with each other during long term arcjet operation. Oxide ceramic insulators, such as alumina (Al_2O_3) and beryllia (BeO) appear to have better chemical compatibility with H_2 and N_2 than boron nitride during prolonged exposure at high temperatures. Also, these materials do not react when in contact with refractory metals at high temperatures under H_2 , N_2 , or vacuum atmospheres. Considering all criteria, BeO could be the best choice since it has a higher melting point, good thermal conductivity and better thermal shock resistance. One possible disadvantage is that beryllium itself is toxic.

Some of the relatively new ceramic matrix composite insulators, such as silicon carbide or alumina reinforced with fibers may be useful for arcjet application. In addition, anisotropic properties of certain insulator ceramics can be used to improve heat transfer, thermal stability and mechanical properties at high temperatures.

5.0 PERFORMANCE TESTING

Engine performance testing was carried out with the engine designs discussed in Chapter 3. In these tests, the following equations were used to calculate various performance parameters.

Engine input power:

$$P = IV \quad (5-1)$$

where I is the engine operating current, and V is the engine operating voltage.

Specific impulse:

$$I_{sp} = F/\dot{m}g_0 \quad (5-2)$$

where F is the measured engine thrust, \dot{m} is the mass flow rate of the ammonia propellant, and g_0 is the acceleration of gravity at the Earth's surface.

Efficiency:

$$\eta_T = F^2/2\dot{m}P \quad (5-3)$$

with the parameters as defined above.

5.1 EXPERIMENTAL PROCEDURES

Preparation for arcjet testing included engine assembly, leak-testing, cathode placement, installation of the engine in the facility, the pretest facility checks, and weighing and photographing of the cathode to be run. The engine was then assembled and leak-checked. The nozzle was blocked with a rubber stopper and the engine pressurized with 5 psia of compressed N_2 . The engine was held under water to detect air bubbles. The cathode to be run was inserted into the engine body and pressed against the inlet to the constrictor. An axial gap was specified, which is the distance the cathode is pulled back from the inlet to the constrictor, was specified. A swagelok fitting on the cathode feedthrough (see Fig. 3-5) was tightened onto the cathode, and the actual gap was remeasured and noted. (The assembly procedure differs slightly for the fat-tip cathode in that the cathode had to be installed during initial engine assembly.) The engine was installed in the vacuum tank and aligned and the tank was then pumped down to about 0.002 torr. The engine was then left to outgas overnight. Before the start of the test the thrust stand was calibrated and the required facility checks are conducted.

Prior to engine operation, ammonia propellant was flowed through the engine for 10 minutes to evacuate any residual liquid in the lines. After flowing the ammonia, the start-up began with a glow discharge on argon. The argon flow-rate was set at approximately 3.5 slpm and the voltage on a start-up power supply was slowly increased until the gas broke down and a plume appeared. This generally occurs at glow discharge conditions of 0.05 to

0.1 A and 160 V and acts to clean the cathode surface. After 30 to 45 minutes of operation on a cleaning glow discharge the current level was increased to about 1 A, and the cathode was allowed to heat for 3 to 5 minutes. At this point the tip of the cathode was observed to be red hot. The argon flow was increased to 10-12 slpm and the start-up supply was increased to its maximum, at about 200 V and around 2A. The main power supply was then turned on at about 100 A and 20 V. The start-up supply was turned off, and the current from the main power supply was increased to about 165 A. At this current level the nozzle turned red hot within four minutes. The propellant flow was then switched to ammonia. Once the engine was operating on ammonia, it could be set at the desired operating point. This start-up method avoided detectable damage to the electrodes; no sparks were observed during the transient. Upon removing the cathode after a start-up, the only noticeable change to the cathode was that the finish was dulled.

During engine operation, the Data Acquisition and Control Unit (DACU) monitors important engine and facility parameters, and can initiate a test shut-down if any one of a set of parameters exceeded operator-defined tolerances. In addition, the parameters were plotted every 24 hours to monitor the cyclic effects such as ambient temperature and power grid usage, and to provide information on trends in engine operation. The DACU was generally set to sample data every two seconds and store sampled data every two minutes. Complete facility checks were performed by the test engineers about four times each day. During these checks, cooling line temperatures and pressures were recorded, as well as the oil levels of the vacuum pumps and main power supply parameters. Also, the nozzle was visually checked and described in the laboratory notebook, and photographs were taken of oscilloscope traces of both the current and voltage.

After operation, the engine was removed and leak-checked. The cathode was removed by sliding it out of the upstream end of the engine. The engine was then disassembled at the main seal. In the case of the fat-tip cathode, however, the engine had to be disassembled at the main seal first so that the cathode could slide out in the downstream direction. The cathodes were immediately photographed and weighed, and if conditions warranted, the nozzle and/or injector were also photographed.

As the engine ran, the arc voltage increased while the arc current dropped slowly. As a result, over periods of tens of hours the engine power increased and had to be manually reset to the nominal operating point of 30 kW. The operator defined tolerances were then updated in the computer.

5.2 CATHODE VARIATION EFFECTS

Tests were conducted to determine what effect cathode tip shape and spacing have on engine performance, and to define design modifications which would minimize cathode erosion without diminishing performance. The thrusters used for the tests discussed in this chapter were described in Chapter 3.

5.2.1 Performance

The performance characteristics of the baseline MOD I engine are compared to the baseline MOD II arcjet in Fig. 5-1. The engines are identical except for cathode design and placement. The engines exhibit identical performance, within experimental error. Note that the mass flow rates in Fig. 6-1 are not corrected for the systematic mass flow measurement error discussed in Section 5.6; this figure should only be used qualitatively. (Data in this report is corrected for this error unless noted otherwise.)

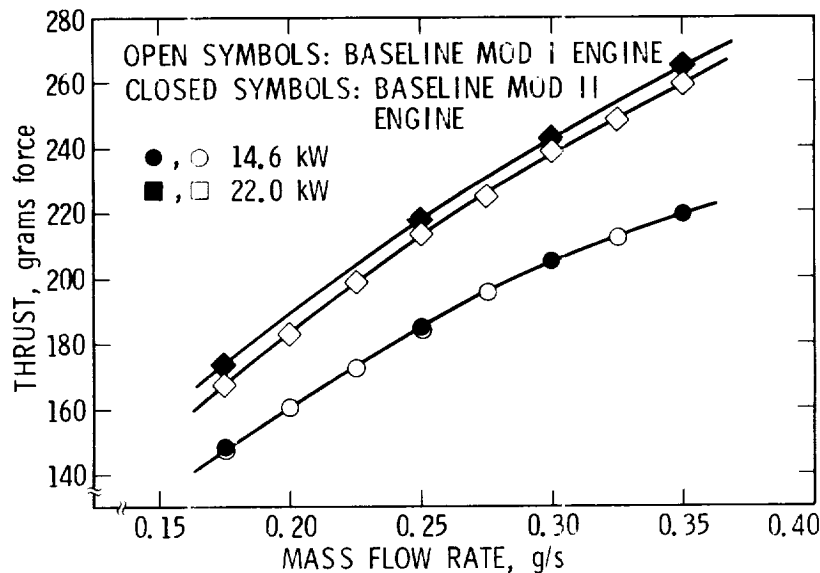


Figure 5-1. Thrust vs. \dot{m} (baseline MOD I and baseline MOD II).
(This data for comparative purposes only; see text.)

5.2.2 Electrical Characteristics

While the performance characteristics between the MOD I and MOD II engines were similar, the V-I characteristics were not. The electrical characteristics of the MOD I engine are compared to those of the MOD II engine, which uses a 45° reduced radius cathode, in Fig. 5-2. To minimize the change in the propellant velocity distribution at the constrictor inlet, the 45°-tipped cathode was placed in the plenum chamber in a position that maintained the size of the annulus between the cathode tip surface and the corner of the constrictor inlet. Thus, the tip of the new cathode (MOD II) is further into the constrictor than is that of the baseline (MOD I). This in turn leads to a shorter arc length and lower engine operating voltage. Note that the mass flow rates in Fig. 5-2, as well as in Fig. 5-3 below, are not corrected for the systematic mass flow measurement error discussed in Section 5.6; these figures should only be used qualitatively.

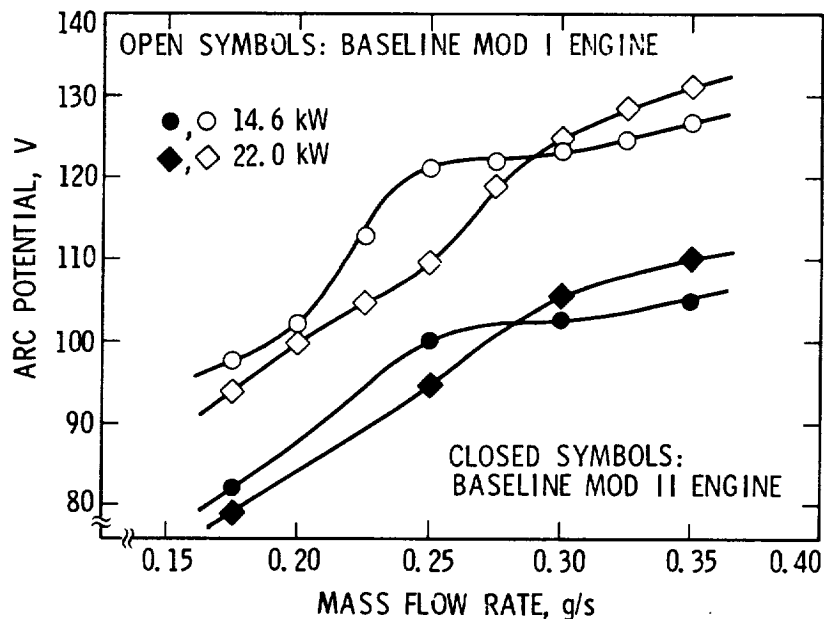


Figure 5-2. Arc potential vs. \dot{m} (baseline MOD I and baseline MOD II).
(This data for comparative purposes only; see text.)

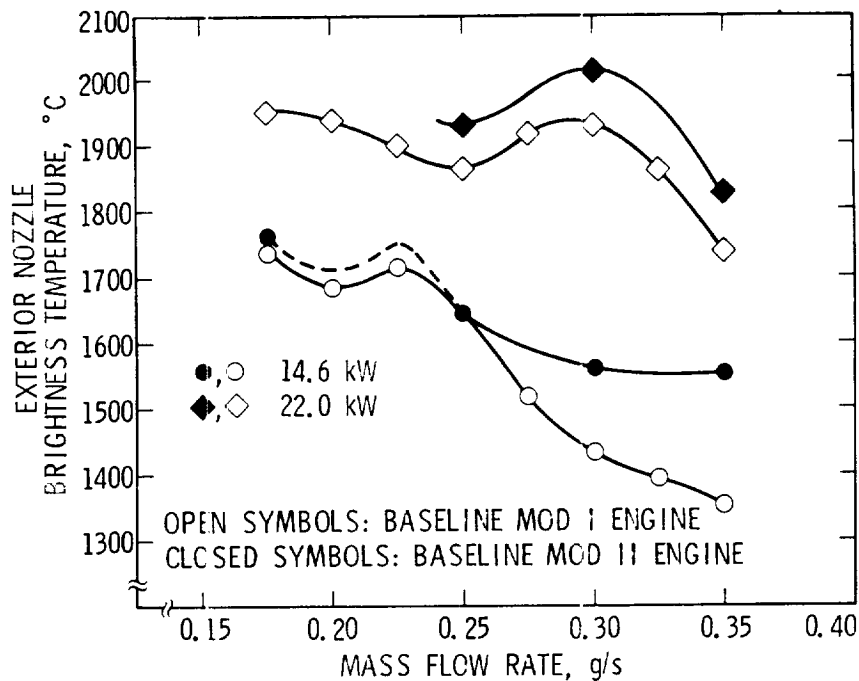


Figure 5-3. Nozzle temperature vs. \dot{m} (baseline MOD I and baseline MOD II).
(This data for comparative purposes only; see text.)

As expected, the MOD II engine exhibited a significantly lower arc potential. The voltage dropped 15 percent over the mass flow range indicated. This led to a corresponding increase in arc current to maintain the same power level and an increase in the overall anode block temperature due to increased ohmic heating (Fig. 5-3).

The electrical characteristics of the D-1E arcjet using four different cathode tip shapes are shown in Figs. 5-4 to 5-7 as functions of arc length and mass flow rate. The effect of mass flow rate on arc potential as a function of arc current for a particular arc length is shown in Fig. 5-8. As can be seen in the figures, the engine voltage increases with the flow rate and arc length. Note that the data in Figs. 5-4 through 5-8 and 5-10 were taken between March 1988 and March 1989; the mass flow rates indicated in the figures have not been corrected. As discussed in Section 5.6, these mass flow rates may, with fair reliability, be corrected by multiplying them by 1.26. The data in these figures (voltage, current, geometric arc length), and the trends reflected, are not affected by the mass flow error.

5.2.2.1 Geometric Arc length. To compare electrical characteristics as a function of arc length, a Geometric Arc Length (GAL) is defined for the placement of each cathode relative to the surrounding engine (see Fig. 5-9). This is the arc length noted in Figs. 5-4 to 5-8. The arc length is determined

by calculating the axial distance from the cathode tip to the plane of the upstream edge of the constrictor. Since the tests done to map the electrical characteristics (prior to the erosion tests) used the same nozzle body, the length of the constrictor was constant. The geometry of the downstream attachment point is unknown, so for the purpose of this analysis the arc is assumed to have the shape shown in Fig. 5-9, attaching at the downstream edge of the constrictor. Variations of the arc attachment to the anode are not included in this preliminary analysis. Note that for the dimpled cathode and flat-face cathodes (see Fig. 3-8), the arc is assumed to begin not on a peak but, instead, in the center of the dimple and at the center of the flat face. Geometric arc length error is ± 0.16 cm.

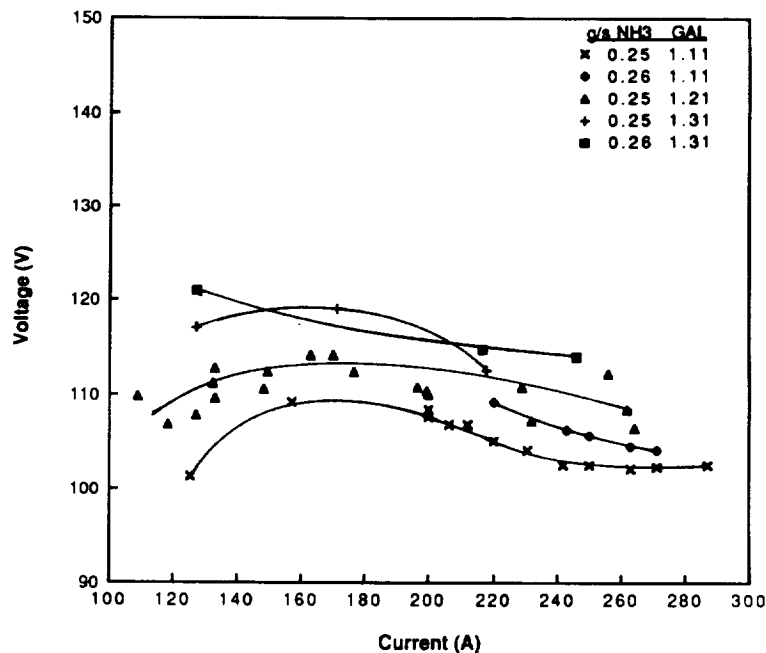
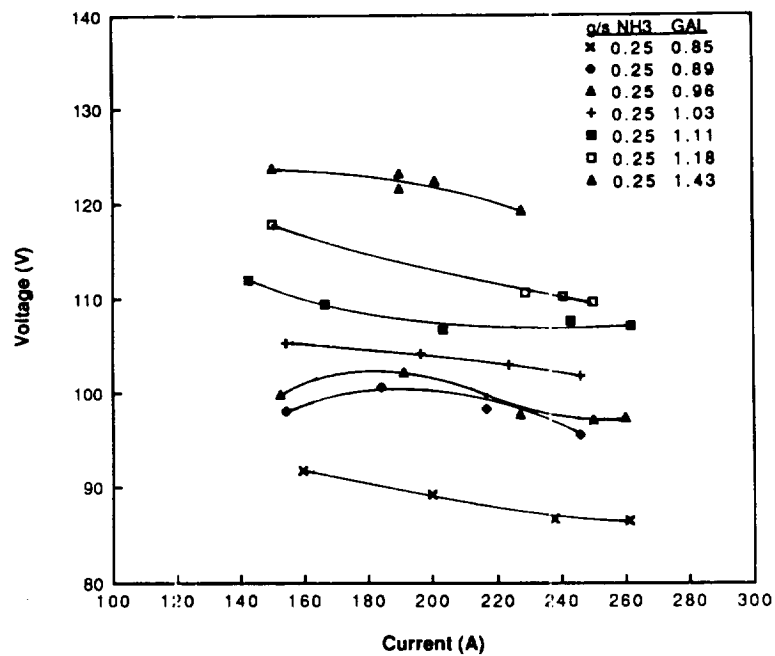
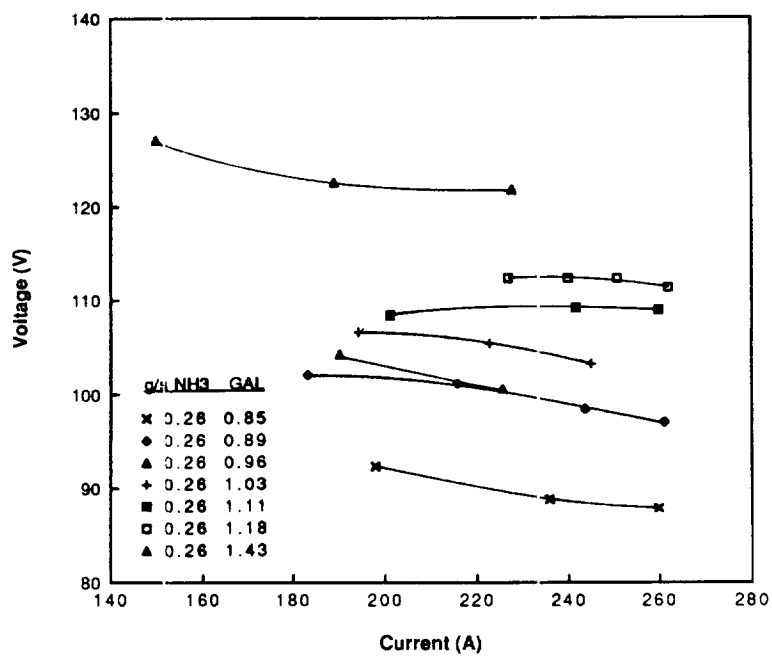


Figure 5-4. D-1E electrical characteristics (baseline cathode).
(The mass flow rates in this figure must be multiplied by a correction factor of 1.26. See Section 5.6.)



a) $\dot{m} = 0.25 \text{ g/s NH}_3$



b) $\dot{m} = 0.30 \text{ g/s NH}_3$

Figure 5-5. D-1E electrical characteristics (45° red. radius cathode).
(The mass flow rates in this figure must be multiplied by a correction factor of 1.26. See Section 5.6.)

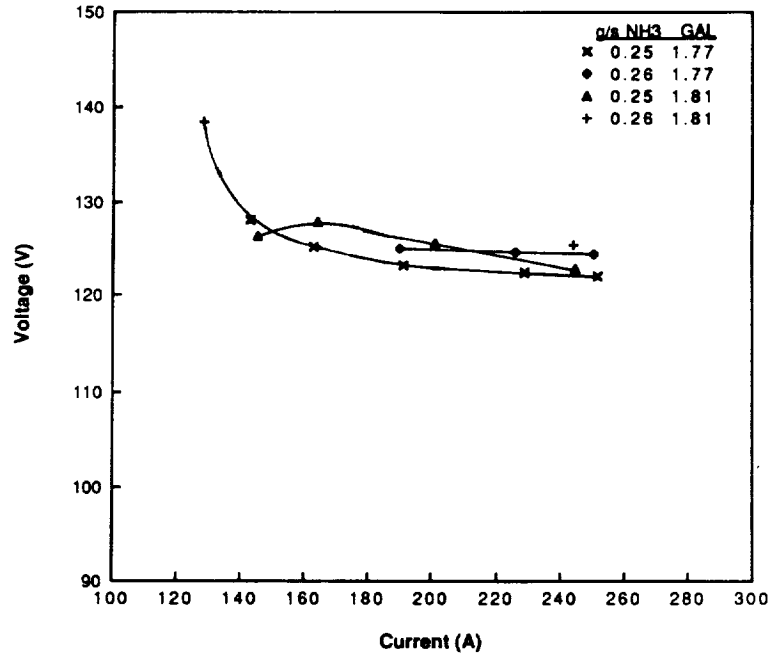


Figure 5-6. D-1E electrical characteristics (dimpled cathode).
(The mass flow rates in this figure must be multiplied by a correction factor of 1.26. See Section 5.6.)

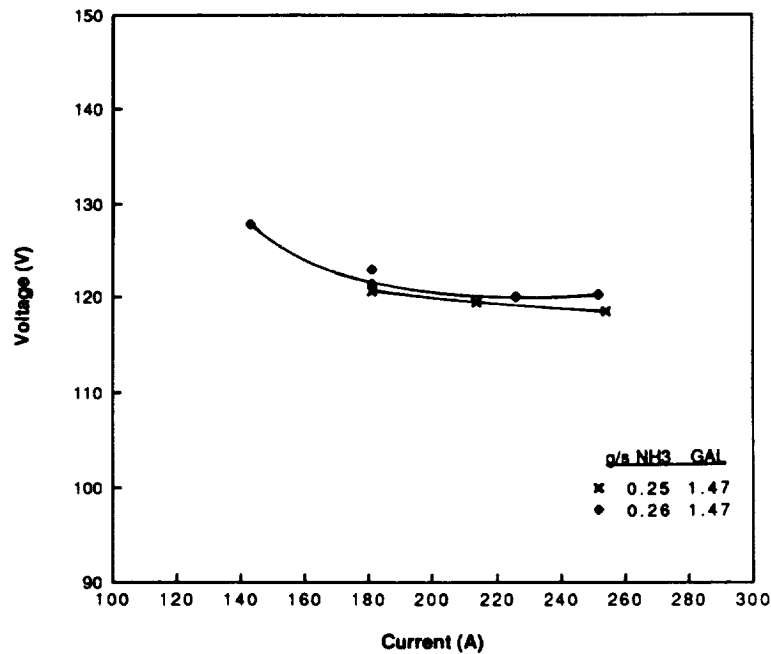


Figure 5-7. D-1E electrical characteristics (flat-face cathode).
(The mass flow rates in this figure must be multiplied by a correction factor of 1.26. See Section 5.6.)

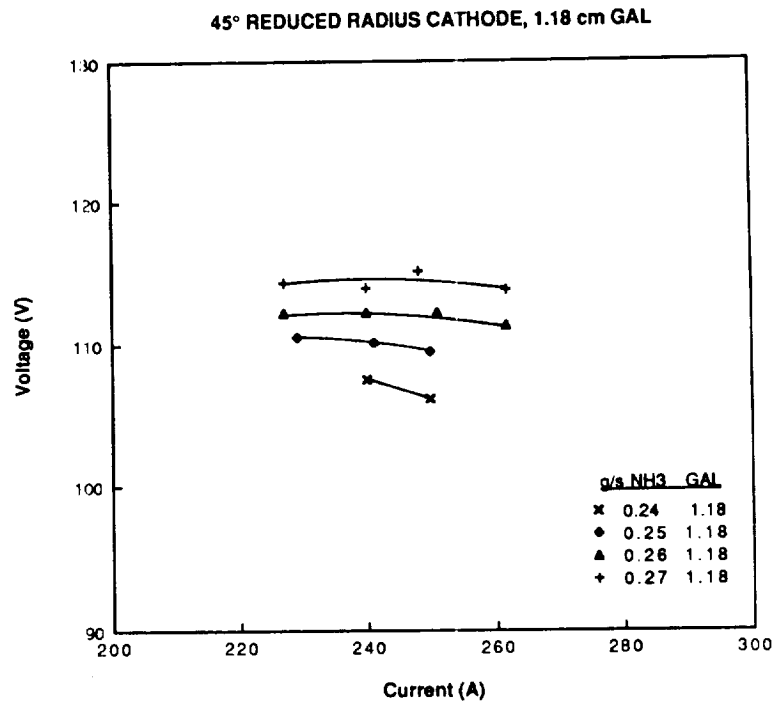


Figure 5-8. Voltage vs. current as a function of \dot{m} at one GAL.
 (The mass flow rates in this figure must be multiplied by a correction factor of 1.26. See Section 5.6.)

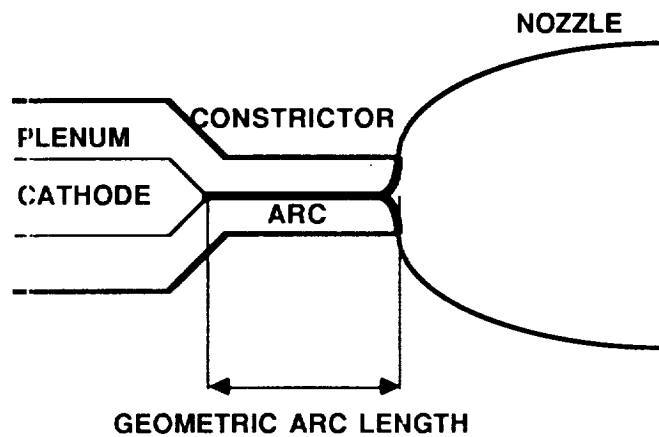


Figure 5-9. Definition of GAL.

For each combination of tip shape, geometric arc length and ammonia flow rate, a plot of power level versus arc current was made. A first-order curve fit gave an equation relating the power to the current. These relations, calculated for the various test cases, were used to construct curves showing arc current as a function of geometric arc length, for specified power levels (Fig. 5-10). As the geometric arc length increases, as it must when the cathode tip erodes, the slope of the current at a constant power level decreases, as if approaching an asymptote. If arc current approaches an asymptote and power is held constant, then voltage must also approach a constant value. This seems to lead to an unphysical situation, since further cathode erosion increases the arc length. It is speculated that these data represent an approach to a maximum sustainable arc length, and that if further erosion occurs once the maximum length is approached, a reconfiguration of the arc geometry may be required. This reconfiguration is likely to take the form of an upstream migration of the anode arc attachment, into the constrictor, which would likely result in destructive erosion. The relation of a geometric approximation of the arc length to the electrical properties of an arcjet is useful both to the design of an arcjet for a specified lifetime, as well as the prediction of the lifetime of a given design.

The geometric arc length was calculated for conditions before and after the 413-hour test (discussed in detail in Chapters 6 and 7) which was run at a mass flow rate of 0.31 g/s. The geometric arc length was calculated to have grown 0.58 cm to a final length of 2.05 cm. The data points from the 413-hour test were consistent with the previous arc length test data.

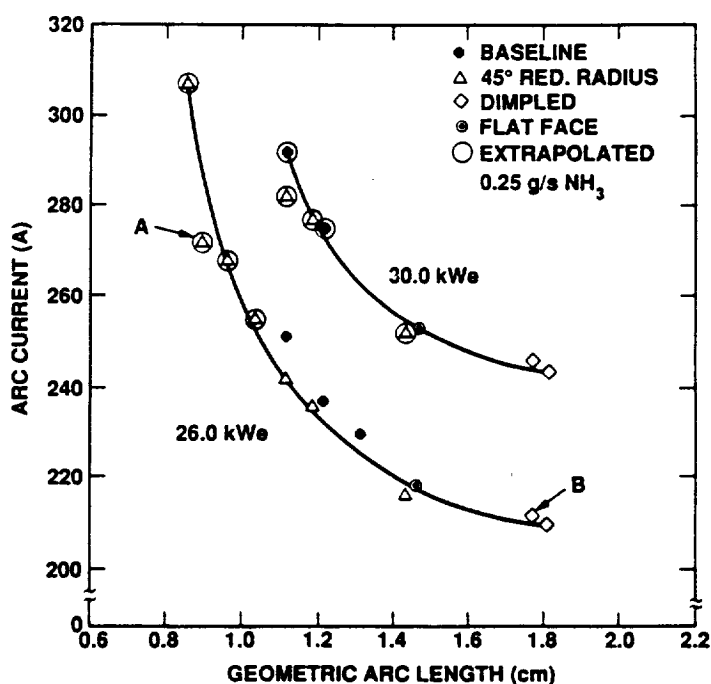


Figure 5-10. Current vs. GAL. (The mass flow rates in this figure must be multiplied by a correction factor of 1.26. See Section 5.6.)

5.3 ENGINE RADIATIVE DESIGN COMPARISON

Results of experiments describing arcjet operation with a high-emissivity nozzle coating and operation of a new engine design, the D-1E, are described and compared to Baseline engine operation in this section.

5.3.1 High-Emissivity Coatings

High-emissivity coatings can be used to increase the radiative ability of a high temperature surface. A series of experiments was carried out to validate the feasibility of using high-emissivity coatings on arcjet engine nozzles. The coating used was ZrB_2 and was applied by plasma spraying. Initial validation experiments were conducted using the Baseline and Baseline MOD III engines and are described below. Long-term compatibility tests were conducted using the D-1E engine and are described in Chapters 6 and 7.

5.3.1.1 Electrical Characteristics. The V-I characteristics are the same for both the baseline and baseline MOD III engines and are shown in Fig. 5-11. Knowledge of the engine V-I characteristics is important when analyzing engine thermal behavior since anode heating is driven in part by current collection through the anode sheath. The solid lines represent constant mass flow, while the dashed lines are for constant power. The mass flow rates in Fig. 5-11 are not corrected for the systematic mass flow measurement error discussed in Section 5.6; this figure should only be used qualitatively.

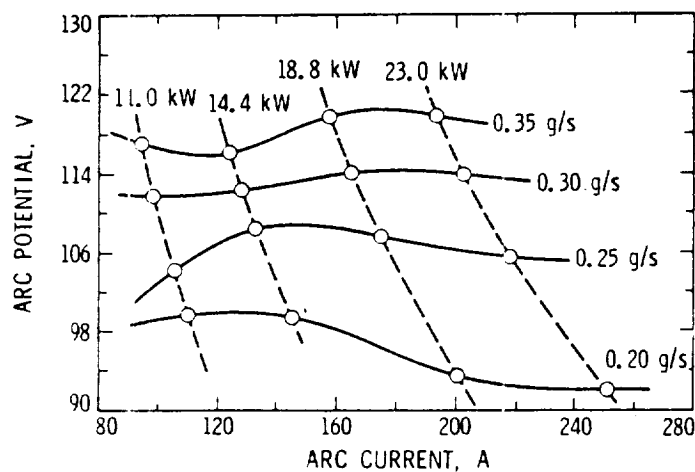


Figure 5-11. Baseline engine voltage-current (V-I) characteristics. (This data for comparative purposes only; see text.)

5.3.1.2 Nozzle Temperature Reduction Tests. The infrared optical pyrometer which monitored the nozzle temperature uses a room temperature silicon detector element, has a spot size of 0.64 cm and operates in the wavelength range of 0.6 to 1.0 micrometers. The emissivity of tungsten (see Fig. 3-7) is relatively insensitive to temperature in this wavelength range.⁹⁵ The pyrometer was located outside of the vacuum tank and viewed the engine through a 1.9 cm thick glass window. Type-K thermocouples were used to monitor the temperatures at the rear of the engine.

Comparisons of the indicated nozzle surface brightness temperature, at a point 1 cm upstream of the nozzle exit plane of the baseline engine, before and after coating with ZrB_2 are shown in Figs. 5-12 and 5-13. Over a range of mass flow rates, the ZrB_2 -coated engine (Baseline MOD III) operated about 120 °C cooler over the power range considered. This result indicates a 35-percent increase in surface emissivity at 1800 °C as obtained from the Stefan-Boltzmann law by assuming a constant radiated power for both engines. A constant radiated power is assumed since the engine is run at the same mass flow rate and power (same voltage-current characteristic) both before and after coating with ZrB_2 ; the only modification made to the engine is the increase in the radiating surface emissivity. As noted earlier, the reported emissivity of tungsten is about 0.4 and that of ZrB_2 ranges from 0.5 to 0.95. The results presented in this publication suggest that the emissivity of ZrB_2 is about 0.55. The mass flow rates in Figs. 5-12 and 5-13 are not corrected for the systematic mass flow measurement error reported in Section 5.6; these figures should only be used qualitatively.

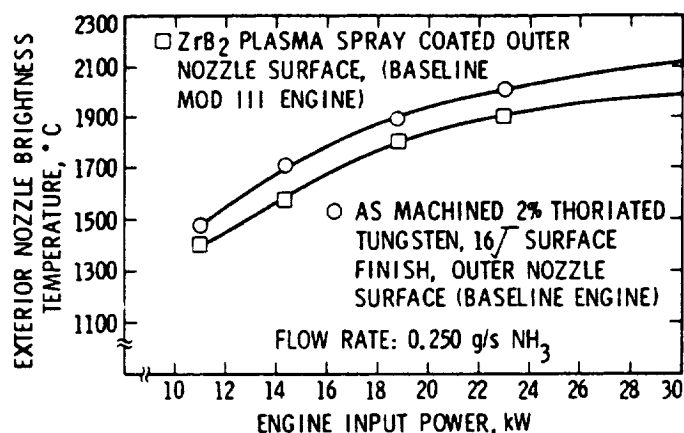


Figure 5-12. Nozzle brightness temperature as a function of power for a mass flow rate of 0.25 g/s, with and without ZrB_2 coating.
(This data for comparative purposes only; see text.)

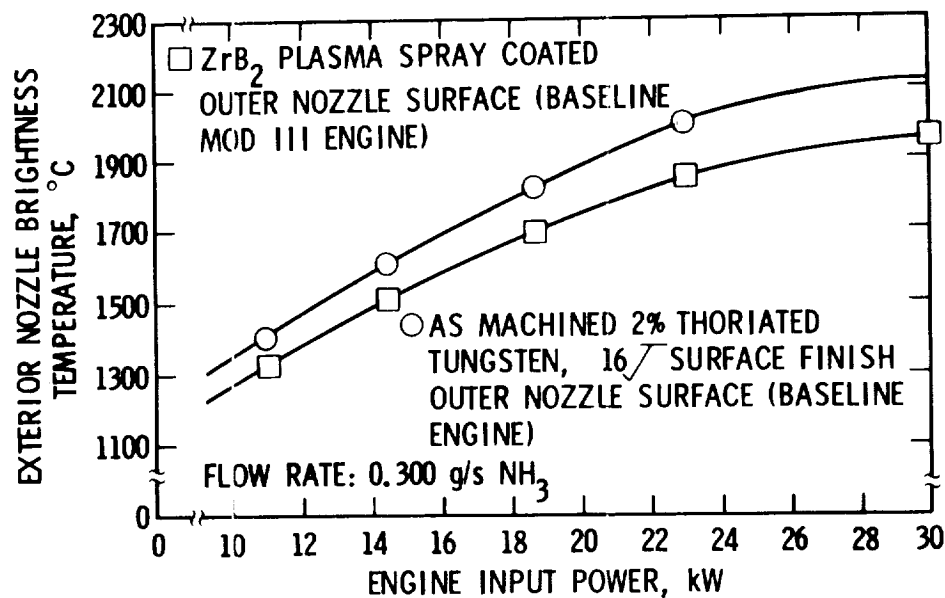


Figure 5-13. Nozzle brightness temperature as a function of power for a mass flow rate of 0.30 g/s with and without the ZrB₂ coating.
(This data for comparative purposes only; see text.)

The engine was run at powers ranging from 10.0 kW to 37.0 kW and mass flow rates of 0.20 g/s to 0.35 g/s to characterize the performance of the coating. Further details on the operating characteristics and performance of the baseline engine design can be found in Refs. 32, 80, 84 and 85. The coated baseline engine was run for more than 30 hours at difference powers and flow rates and subjected to numerous start sequences with no apparent change in the ZrB₂ coatings mechanical properties or high temperature optical properties.

The mat grey room temperature appearance of the ZrB₂ coating took on a yellowish tint following engine operation on both the tungsten nozzle and molybdenum body substrates. It should be noted that this coating has also been applied to the molybdenum anode block of a magnetoplasmadynamic (MPD) thruster being run on argon propellant. The molybdenum MPD thruster anode operates in the same temperature regime as the molybdenum arcjet body. However, in the case of the MPD thruster, no coating color change was evident. Therefore, it is believed that the ZrB₂ coating is undergoing a mild chemical reaction with the ammonia propellant when it is cold flowed prior to a test and/or with the dissociated ammonia products created by arcjet operation. The long term effects of this process must still be determined.

5.3.2 Verification of D-1E Engine Thermal Design

Tests were conducted to examine the temperatures of the D-1E engine at various locations. As above, the bare tungsten nozzle surface temperature at a point 1 cm upstream of the nozzle exit plane was continuously measured with an infrared optical pyrometer. Two type K thermocouples were attached to the engine to monitor the temperature of engine component which could not be measured with the optical pyrometer because they were below its lower sensitivity limit of 1200 °C. As shown in Fig. 5-14, one of these thermocouples was spot-welded to the side of a nut welded to the Inconel 600 feedthrough, 90° from the propellant inlet tube, while the other was clamped onto the side of the molybdenum assembly nut about 1 cm from the upstream edge of the nut.

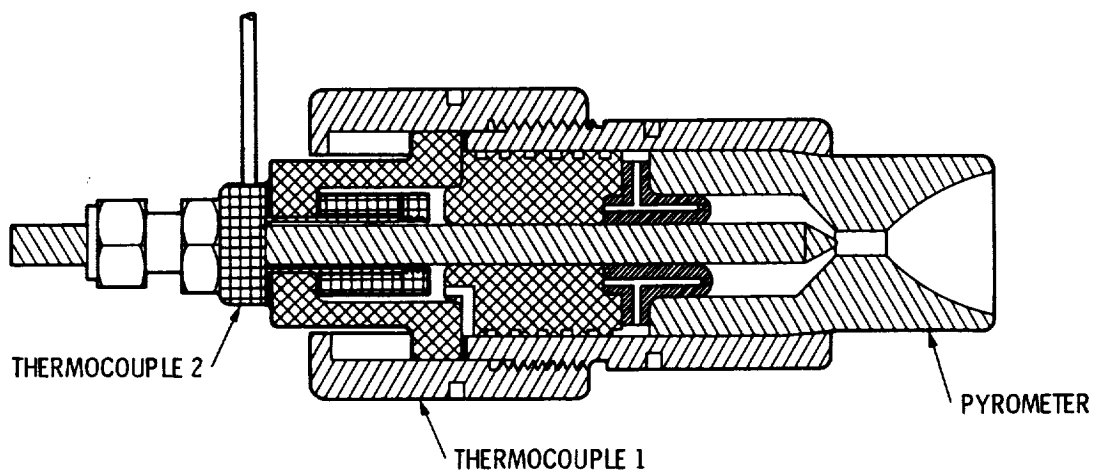


Figure 5-14. Location of thermocouples on the D-1E arcjet.

5.3.2.1 Electrical Characteristics. The D-1E engine voltage-current (V-I) characteristics are shown in Fig. 5-15. Again, the solid lines represent constant mass flow, while the dashed lines represent constant power. This characteristic is similar to that of the baseline engine.

The V-I characteristic shown in Fig. 5-15 should be compared to that of the baseline MOD-I engine (see Refs. 28, 32). The baseline MOD-I engine employs a bell-shaped nozzle which is identical to the nozzle of the D-1E engine. The same constant power and constant mass flow rate characteristics are exhibited for both engine designs; however, for constant power and flow rate, the D-1E engine operates at a voltage 10 percent lower than the baseline MOD I engine. This difference is believed to occur because the D-1E engine expands less than the baseline MOD I engine, resulting in a smaller minimum gap between the cathode cone and constrictor inlet. The arc is shorter, and the operating voltage lower.

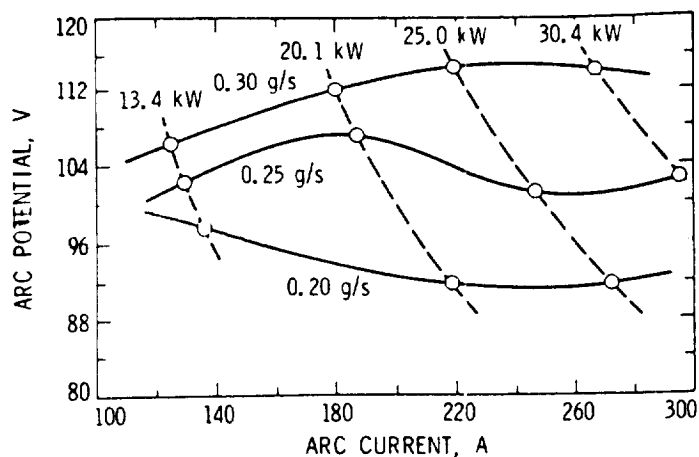


Figure 5-15. D-1E engine voltage-current characteristics.
(The mass flow rates in this figure must be multiplied by a correction factor of 1.26. See Section 5.6.)

5.3.2.2 Thermal Design Results. The D-1E engine was operated over a power range of 13.2 to 30.4 kW_e and mass flow rates of 0.25, 0.31 and 0.38 g/s to characterize its thermal design. The exterior engine temperature at the three locations discussed above is shown in Fig. 5-16 as a function of electrical input power for constant mass flow rate.

As can be seen in Fig. 5-16, the nozzle brightness temperature increases with increasing input power and is, in general, substantially lower for the D-1E engine as compared to the baseline engine. For example, at a corrected mass flow rate of 0.38 g/s and a power of 23 kW_e, the D-1E engine had a nozzle temperature of about 1750 °C while the baseline engine operated with a nozzle temperature of 1970 °C. This results primarily from the location of the 7° taper joint, where the nozzle block and engine body are in intimate contact. This joint is at the front edge of the engine body on the D-1E engine, as opposed to several centimeters back from the front edge as on the baseline engine. As a result, the taper is closer to the nozzle heat source in the D-1E engine and conducts more heat into the engine body effecting a larger nozzle radiating surface.

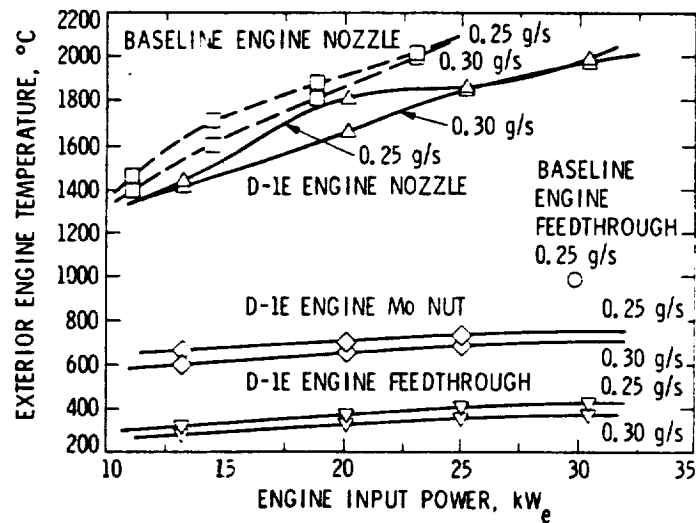


Figure 5-16. D-1E exterior engine temperature as a function of input power for constant mass flow rate.
(The mass flow rates in this figure must be multiplied by a correction factor of 1.26. See Section 5.6.)

In addition, in the baseline engine the nozzle was forced to radiate energy directly to the engine body inner surface for about half its length before reaching the direct conduction path at the 7° taper joint. In the D-1E engine the 7° taper joint is encountered first, producing a more effective radiative design. It should also be noted that the D-1E engine runs with a cooler nozzle block than the baseline MOD-I engine even though the D-1E engine requires more current to run at the same power. Assuming that the anode fall is constant with respect to current, the D-1E engine incurs a higher anode heat load than the baseline MOD-I engine. Even so, the nozzle temperature is lower. Therefore, two features, an improved thermal conduction path and a more effective radiative design, provide a reduced nozzle temperature in the D-1E engine.

At a corrected ammonia mass flow rate of 0.38 g/s and a power of 30 kW_e the baseline engine cathode feedthrough reached a temperature of about 1000 °C while the D-1E engine feedthrough temperature measured only 425 °C (Fig. 5-16). This results from the fact that the cathode is cooled directly by the cool incoming propellant gas in the D-1E engine (Fig. 3-5). There is no active cathode cooling at the back of the baseline engine (Fig. 3-1). This regenerative cathode cooling maintains the feedthrough at a temperature far below the material thermal yield point.

Also shown in Fig. 5-16 are the temperature characteristics for the molybdenum assembly nut and Inconel feedthrough at the back of the engine. These quantities are important since heat at the back of the engine could be conducted into the host spacecraft in a flight system. Both of these parts exhibited relatively small temperature increases with increasing input power and decreasing mass flow rate. For example, the temperature of the assembly nut increased 2.8 percent for a corresponding power increase of 20 percent, or a 20 °C increase in temperature for a 4.9-kW_e power increase. The Inconel feedthrough temperature increased from 348 °C to 396 °C when the mass flow was decreased from 0.38 g/s to 0.31 g/s at an engine power of 25.0 kW_e.

The exterior nozzle temperature is plotted as a function of specific power in Fig. 5-17. The specific power, P_S , is defined as the engine input power, P_E , divided by the mass flow rate, \dot{m} . As can be seen, each pair of curves in Fig. 5-16 are reduced to a single curve in Fig. 5-17. Engine temperature rises as specific power increases. The temperature rise is linear for the components at the back of the engine and is non-linear for the nozzle temperature increase. The D-1E engine nozzle operates at a lower temperature for a given specific power than the baseline engine.

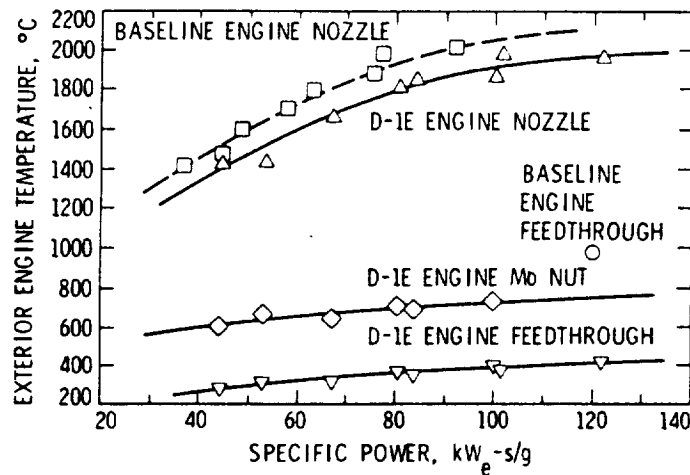


Figure 5-17. D-1E exterior engine temperature as a function of specific power (kW_e-g/s).
(The mass flow rates in this figure must be multiplied by a correction factor of 1.26. See Section 5.6.)

5.4 NOZZLE EFFECTS

This section, which describes nozzle profile design and effects, is based largely on Ref. 11.

5.4.1 Flow Characteristics

Arcjets typically produce a high-temperature, high-velocity, low density gas flow. For temperatures greater than 2000 K and a propellant flow rate on the order of 0.25 g/s, the low values of Reynold's number (using throat diameter as the characteristic length) indicate that viscous effects are important and that the flow in the supersonic nozzle will either be characterized as a thick boundary layer or as fully viscous flow.

In addition, the arcjet produces a radial temperature profile at the nozzle throat which is highly peaked. This peaked profile is such that the centerline temperature can be tens of thousands of degrees Kelvin while the gas near the walls (which makes up the majority of the propellant flow) is only a few thousand degrees.⁵ The very high centerline temperature implies that the central core of gas will be fully ionized. Additional complexities are introduced as a result of arc heat addition in the constrictor region,

by heat transfer to the nozzle walls, by possible boundary layer flow such that flow within the layer is in equilibrium and outside the layer frozen, and by possible rarefied gas effects.

Until recently, arcjet engines have generally utilized conical nozzles due to a lack of adequate analytical tools to define a proper nozzle contour for the arcjet flow conditions, and because of difficulty, machining refractory metals. In 1985 an approximate analytical technique was used to design a preliminary bell-shaped nozzle for use with an arcjet.¹¹ This nozzle was machined in Pocco graphite and tested. While the nozzle eroded significant on its upstream end, the data clearly demonstrated improved performance.

5.4.2 Nozzle Profile Definition

Chemical rockets use contoured, bell-shaped nozzles to maximize thrust efficiency. However, due to the flow properties in arcjets as described above, the techniques used to define the nozzle contours for chemical rockets cannot be directly applied to arcjet engines. Therefore, assumptions and approximations must be made in order to define an initial bell-shaped nozzle configuration.

Given the above defined flow characteristics and constraints cited above, Brophy, et. al.,¹¹ generated an optimum nozzle contour using an approximate boundary-layer displacement thickness addition process. In this process, the desired nozzle wall contour is obtained by adding the boundary-layer displacement thickness, δ^* , to an optimum inviscid expansion nozzle contour (Fig. 5-18). The inviscid nozzle was generated using a computer routine based on the analysis of Rao⁹² with specified values for the nozzle exit area ratio, specific heat ratio, ambient to chamber stagnation pressure ratio, and the geometry upstream of the throat. The boundary layer thicknesses for this investigation were calculated using a computer routine developed to predict laminar boundary-layer flow through a supersonic nozzle.²¹ Figure 5-18 shows the inviscid nozzle generated by the Rao analysis and the inviscid nozzle modified by adding δ^* ("modified Rao").

In using the boundary layer routine discussed above, certain arcjet flow characteristics were neglected: the highly peaked radial temperature profile, the fully ionized central core, and heat addition in the supersonic region. Thus, the resulting bell-shaped nozzle contour is not an optimum contour for an arcjet but instead serves as an initial nozzle configuration. This nozzle contour was machined into a graphite block. Subsequent testing against a baseline nozzle (19° half-angle with an exit to throat area ratio of 22.5) revealed an 8-percent improvement in thrust and in specific impulse for operation at 15 kW_e, 0.31 g/s ammonia.¹¹

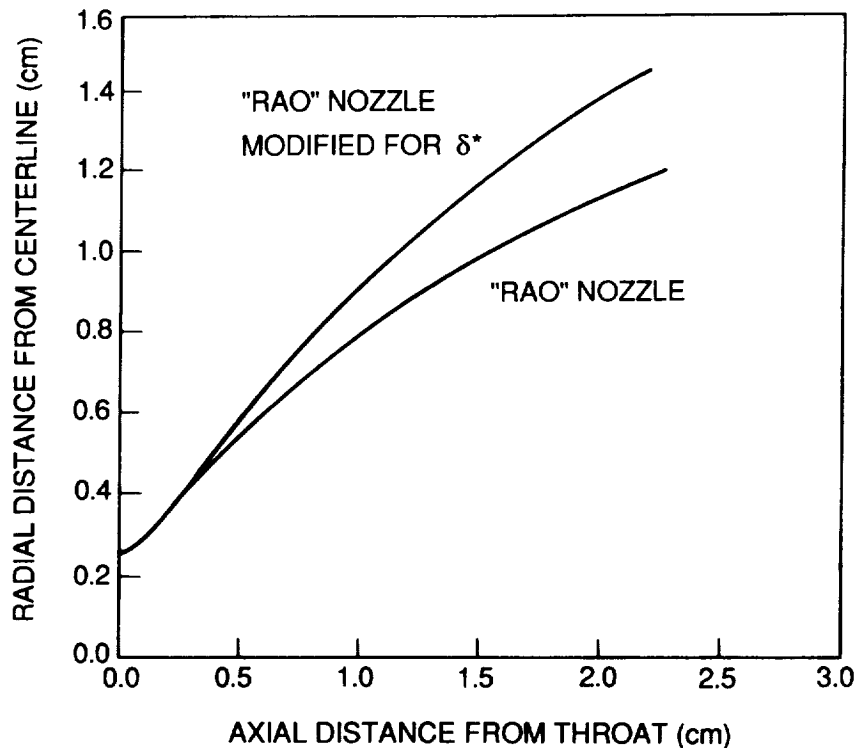


Figure 5-18. Optimum inviscid expansion nozzle contour (Ref. 11).

During the course of this program tests were carried out to verify the performance improvements using nozzles fabricated from thoriated-tungsten. The aim of these tests was to quantify the performance improvements and examine, in detail, the performance envelope of an arcjet using a contoured nozzle. These tests are described in this section and were performed using the Baseline MOD I engine and compared to data from the baseline engine, both of which are described in Section 3.0 above.

5.4.3 Conical/Bell Comparison

A comparison of engine thrust, as a function of engine power and ammonia mass flow rate, is given in Fig. 5-19 for the baseline and baseline MOD I engines. (Figures 5-19 through 5-21, introduced in this section, are uncorrected for the mass flow measurement error described in Section 5.6.).

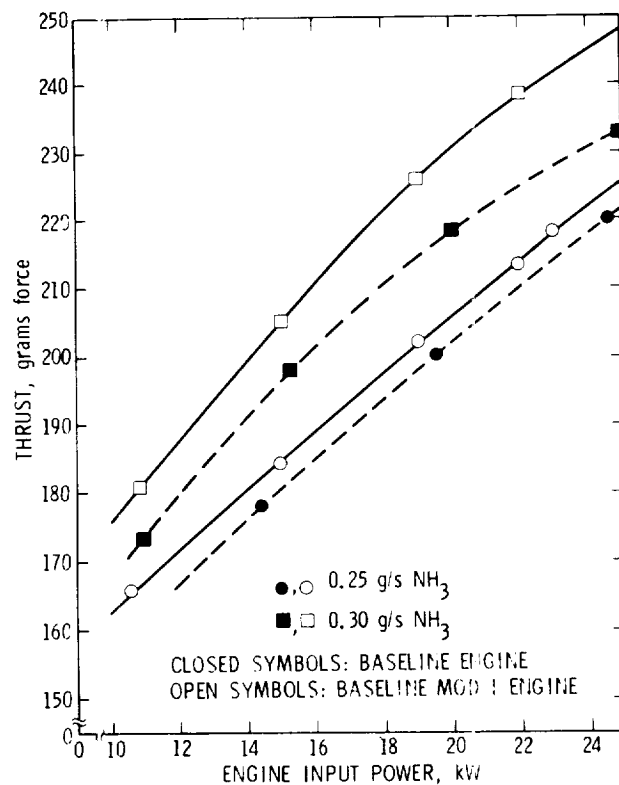


Figure 5-19. Thrust as a function of P, \dot{m} (baseline, baseline MOD I engines).
(This data for comparative purposes only; see text.)

These figures should only be used qualitatively. Note that, since mass flow rate appears in the denominator of the expressions for specific impulse and thrust efficiency, the correct magnitude of these parameters (as shown in Figs. 5-20 and 5-21) can be estimated by dividing the indicated values by 1.26. For an uncorrected ammonia mass flow rate of 0.25 g/s, the bell-shaped, contoured nozzle provided a uniform thrust improvement, as a function of power of 0.05 N. At an uncorrected mass flow rate of 0.30 g/s, the thrust improvement varied from 0.08 N at low power to 0.15 N at 25 kW. These improvements correspond to 2-10 percent improvements in engine thrust as a result of the use of a contoured nozzle.

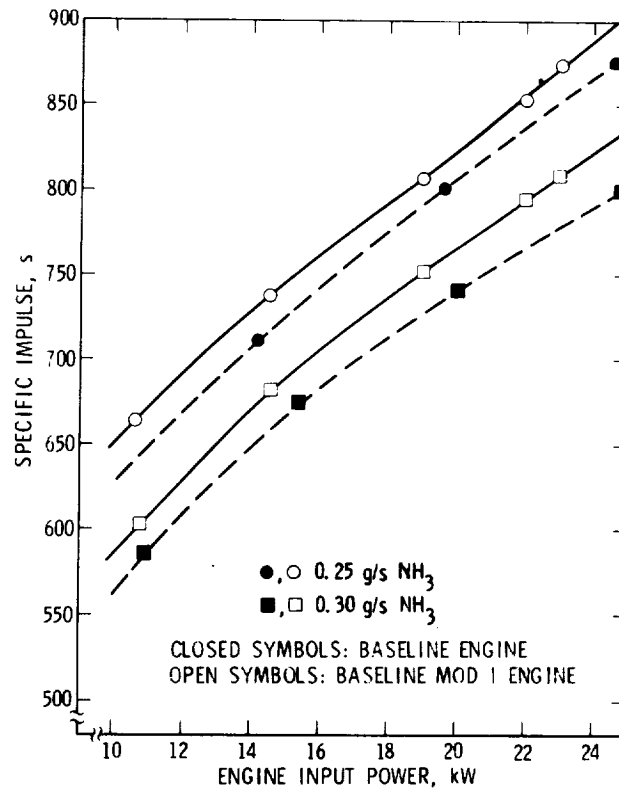


Figure 5-20. I_{sp} as a function of P, \dot{m} (baseline, baseline MOD I engines). (This data for comparative purposes only; see text.)

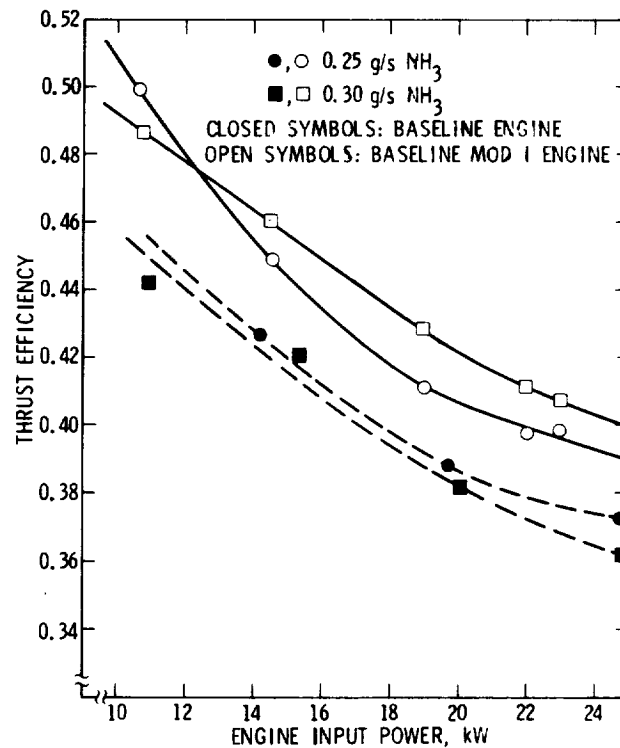


Figure 5-21. Efficiency as a function of P, \dot{m} (baseline, baseline MOD I engines). (This data for comparative purposes only; see text.)

The specific impulse and thrust efficiency are calculated using the measured values of thrust, mass flow rate, and input power according to Eqs. 5-1 to 5-3. Figures 5-20 and 5-21 show these results as functions of power and mass flow rate. Use of a contoured nozzle led to typical improvements in specific impulse of 25 s or 3 percent. Since thrust efficiency depends on the square of the thrust, this parameter shows a more pronounced difference between the two engine performance characterizations. At 0.25 g/s (uncorrected), typical thrust efficiency improvements were on the order of 5 percent. However, when the flow rate was 0.30 g/s (uncorrected), the efficiency improved by 10 percent. It is significant to note that for the conical nozzle the thrust efficiency decreased with increasing mass flow rate, whereas the efficiency crossed over at low engine input powers and improved with increasing mass flow rate for the contoured nozzle. This is because the thrust improvement provided by the contoured nozzle overpowers the increasing mass flow rate due to the efficiency's dependence on the square of the thrust.

5.4.4 Detailed Engine Performance with a Bell Nozzle

This section presents the results of a detailed investigation into the operating characteristics of an ammonia arcjet engine using this preliminary bell-shaped nozzle (the baseline MOD I engine). The tests were conducted in the facility described in Ref. 85. Engine performance characteristics were obtained over a power range of 10.6 to 23.0 kW and an (uncorrected) ammonia mass flow range of 0.18 to 0.35 g/s. Figures 5-22 through 5-27, introduced in this section, are uncorrected for the systematic mass flow measurement error described in Section 5.6. These figures should only be used qualitatively.

Figure 5-22 (MOD I data) shows the engine thrust as a function of engine power and ammonia mass flow rate. The thrust values were calculated from the measured LVDT output and the LVDT calibration. Corrections were applied for variation of LVDT temperature and for variation of the temperature of the flange that supports the thrust stand. These corrections were of order 0.01 N.

The voltage and current were monitored as functions of engine power and mass flow. The voltage measurements were corrected for the voltage drop across the mercury pots and coaxial current feed. This correction was at most 0.75 V. The corrected current and voltage measurements are shown in Figs. 5-23 and 5-24, respectively, as functions of arc power and ammonia mass flow rate.

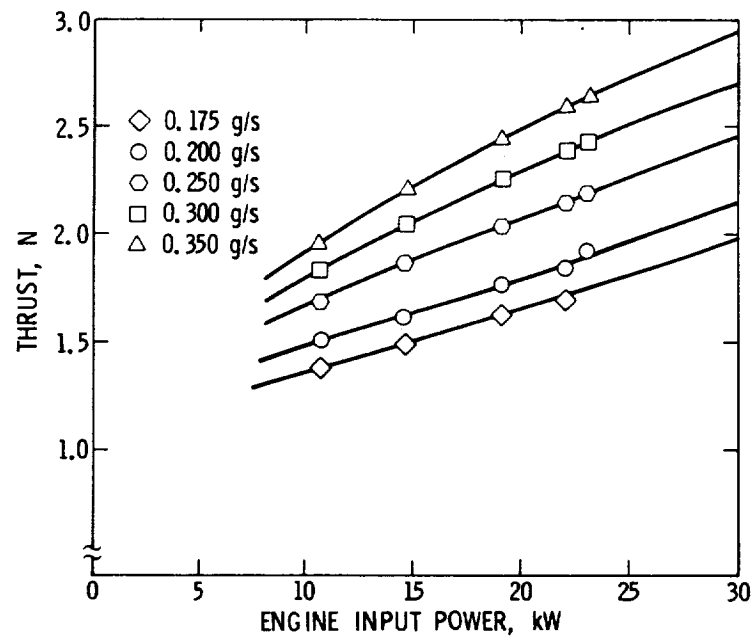


Figure 5-22. Thrust as a function of P , \dot{m} (contoured nozzle).
(This data for comparative purposes only; see text.)

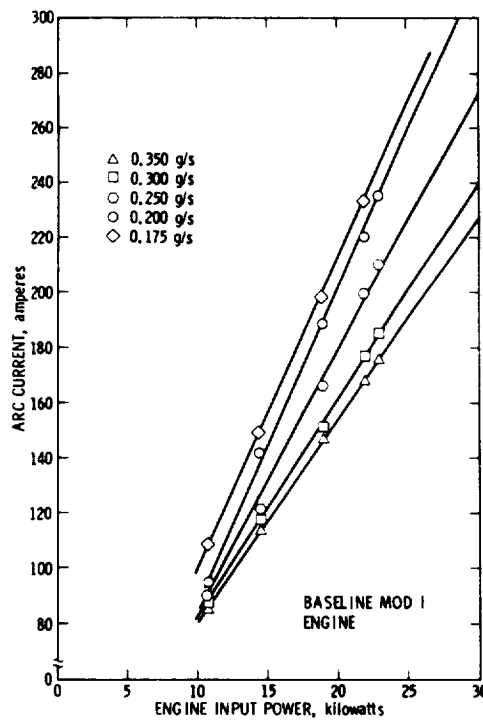


Figure 5-23. Current vs. power (contoured nozzle).
(This data for comparative purposes only; see text.)

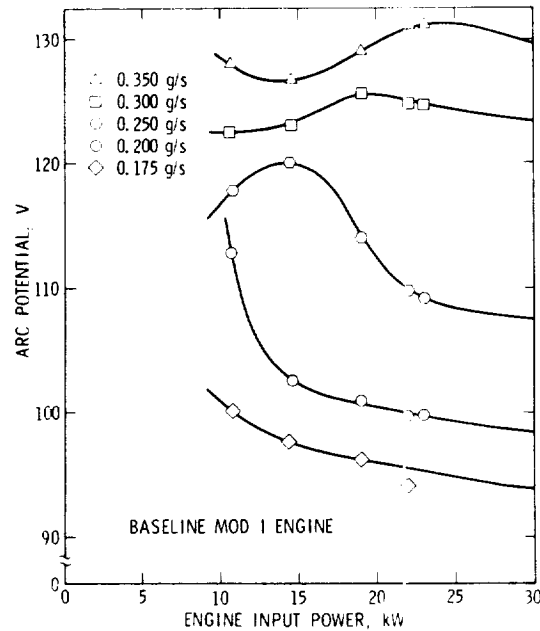


Figure 5-24. Voltage vs. power (contoured nozzle).
(This data for comparative purposes only; see text.)

The engine voltage-current (V-I) characteristics are shown in Fig. 5-25. The solid lines in Fig. 5-25 represent constant mass flow while the dashed lines represent constant power. The engine V-I characteristic exhibits a negative resistance character at constant mass flow rate for high power and low mass flow rates. However, at high mass flow rates and low power, the resistance characteristic appears to be positive. This behavior can also be seen on the voltage characteristic of Fig. 5-24. This behavior can have implications with regard to power conditioning unit design. The lines of constant power have a slope of approximately -0.67 V/A and are generally parallel to each other. Therefore, this engine exhibits a strictly negative resistance characteristic as a function of mass flow at constant power.

The nozzle outer surface temperature, at a point 1 cm from the nozzle exit plane, was continuously measured with an infrared optical pyrometer located outside of the vacuum tank. The corrected temperature measurements are shown as functions of engine input power at constant mass flow rate, and as functions of mass flow rate at constant input power in Figs. 5-26 and 5-27, respectively. The brightness temperature increases with increasing input power, as can be seen in Fig. 5-26.

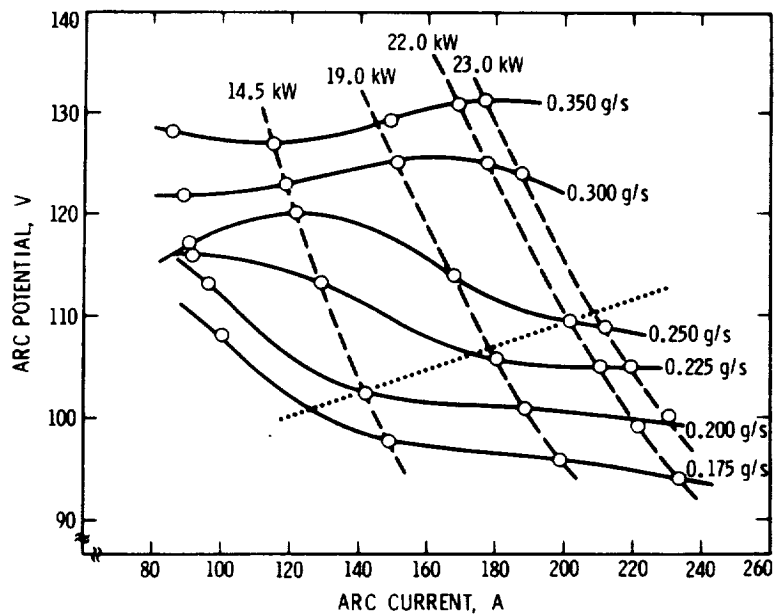


Figure 5-25. V-I characteristic (contoured nozzle).
(This data for comparative purposes only; see text.)

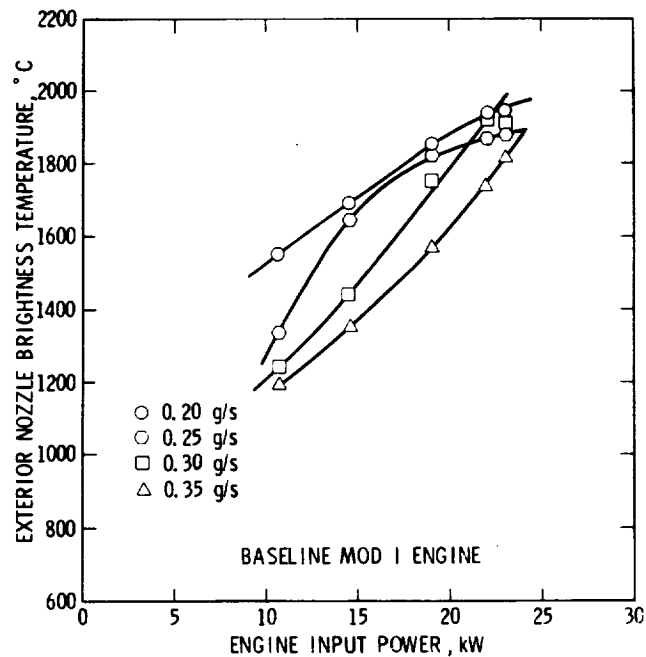


Figure 5-26. Nozzle brightness temperature as a function of P , \dot{m} .
(This data for comparative purposes only; see text.)

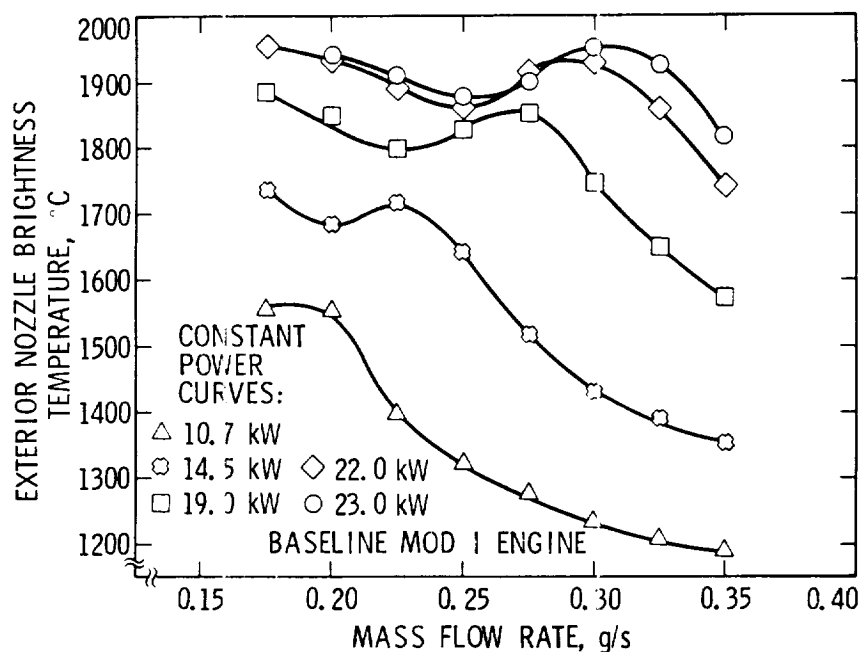


Figure 5-27. Nozzle brightness temperature as a function of \dot{m} .
(This data for comparative purposes only; see text.)

When the brightness temperature is plotted as a function of mass flow rate for constant power, Fig. 5-27, the curves exhibit a local minima. The line along which these local minima lie is given by:

$$T_B = 3400 \left(\frac{s}{g} \right) \dot{m} + 1010 (^\circ\text{C})$$

for the range of the data collected in these experiments where T_B is the measured brightness temperature. The data which lie along this line correspond to the data which lie along the dotted line in Fig. 5-25. The dotted line in Fig. 5-25 runs through a knee in the curves after which the data becomes relatively flat. This line could represent a dividing line between two different arcjet operational "modes."

5.5 D-1E PERFORMANCE

The general V-I characteristics for the D-1E engine were shown in Fig. 5-15. The V-I characteristics around the 30-kW operating point are shown in detail in Figs. 5-4 to 5-8 for several different mass flow rates and cathode tip geometries and spacings. The D-1E operation temperature envelope was shown in Figs. 5-16 and 5-17. As previously noted the V-I characteristics are fairly similar to previous engine designs while the engine operates at much

lower temperatures. Performance data is taken from the 252-hour run using the modified flat-face cathode (#25) and a 100-hour run using the baseline cathode (#22), both of which are discussed in detail in Chapters 6 and 7. The performance is summarized in Table 5-1. (These values are corrected for the mass flow measurement error; see Section 5.6.)

TABLE 5-1. D-1E Performance Data

NH ₃ (g/s)	Average Thrust (N)	Average I _{sp} (s)	Average Efficiency, (%)	Average Power (kWe)
0.31	2.24	738	26.9	30.1
0.34	2.49	747	30.4	30.0

5.6 IDENTIFICATION AND RESOLUTION OF A PERFORMANCE DISCREPANCY

This section describes a joint JPL/Astronautics Laboratory/Rocket Research Company (RRC) effort, performance between June 1989 and September 1989, to determine the causes of discrepancies found between JPL and RRC arcjet test results. The JPL mass flow measurement was found to be in error by 20 percent. These tests took the form of a direct facility-to-facility comparison between JPL and RRC. The facilities provide similar results when the flow controller error is accounted for. JPL data presented in this report, unless otherwise noted, have been corrected for the flow controller error.

5.6.1 Performance Discrepancy Identification

Arcjet technology evaluations were conducted by Rocket Research Company (RRC) during 1986 under Air Force sponsorship.^{18,105} Short-term testing was conducted with several internal engine geometries and propellants at power levels between 5 and 35 kW. The RRC engine designed to run on ammonia, designated RRC-2, was based on the AVCO R-3 internal design, as were the JPL engines. At the same indicated nominal mass flow of 0.25 g/s, the RRC-2 engine operated at lower voltages and had lower indicated performance than did the similar JPL baseline engine. Significant engine and facility design differences were assumed to account for the discrepancies.

Subsequent RRC tests in 1989 were designed to repeat the 1986 JPL/AL test and validate the failure mechanism. Tests with an arcjet very close in design to the JPL D-1E engine led to the discovery of a significant systematic difference in indicated engine performance and operating voltage between JPL and RRC data.¹⁷

Two discrepancies were noted between JPL test results and the checkout tests performed for the RRC/AL endurance test. The values of measured thrust and measured voltage were lower in the RRC tests for the same indicated operating conditions. The "measured" specific impulse (calculated from the measured

thrust and mass flow rates) is shown as a function of power divided by mass flow rate for JPL and RRC test results in Fig. 5-28. The (uncorrected) JPL test data shown in Fig. 5-28 are from the Baseline MOD I engine. The baseline MOD I engine is shown schematically in Fig. 3-2. The RRC data is a compilation of data from the 1986 arcjet technology program, the RRC/AL endurance test effort, and 1 to 2-kW arcjet testing. The engine used in the RRC/AL endurance test program is shown schematically in Fig. 5-29. Of particular interest is the apparent nature of the discrepancy in Fig. 5-28; that is, the apparent shift between the curves with no trend toward divergence or convergence. The curves appear to be displaced vertically about 110 s in specific impulse. In addition, the V-I curves corresponding to the 0.25 g/s mass flow are displaced approximately 10 V between the JPL and RRC data over the engine current range tested.

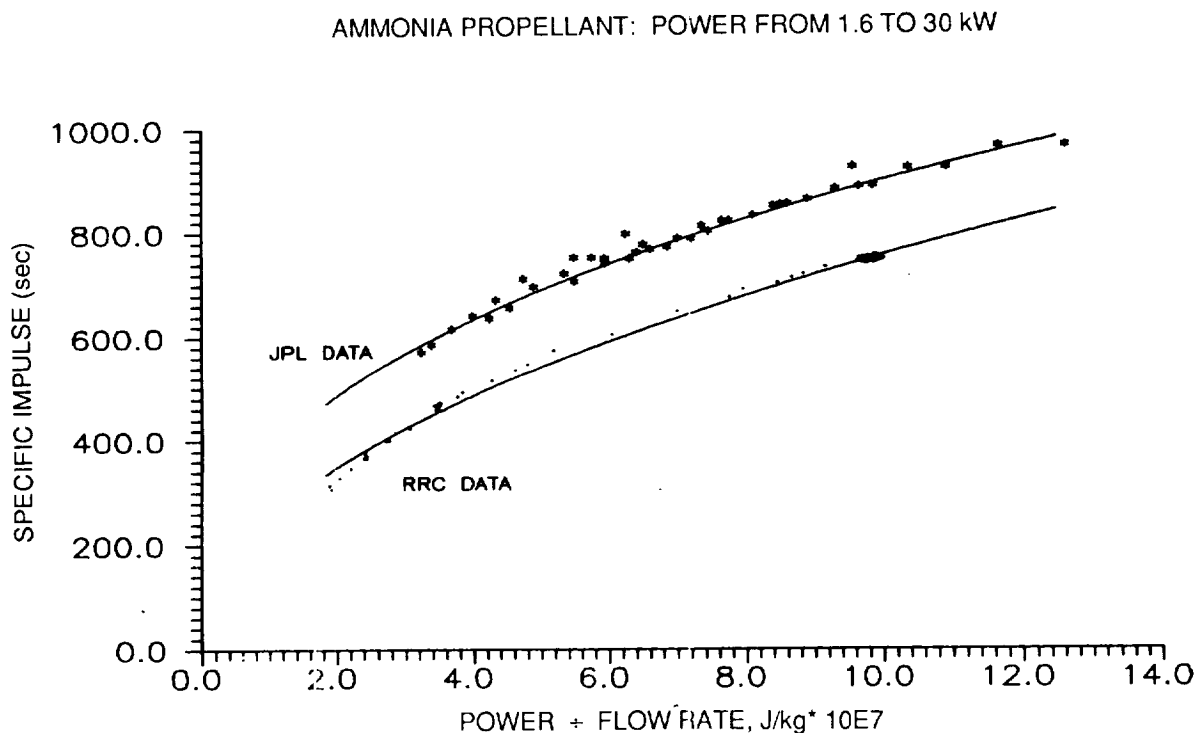


Figure 5-28. I_{sp} vs. P/\dot{m} (JPL and RRC test results).
(JPL data are uncorrected for the mass flow calibration error.)

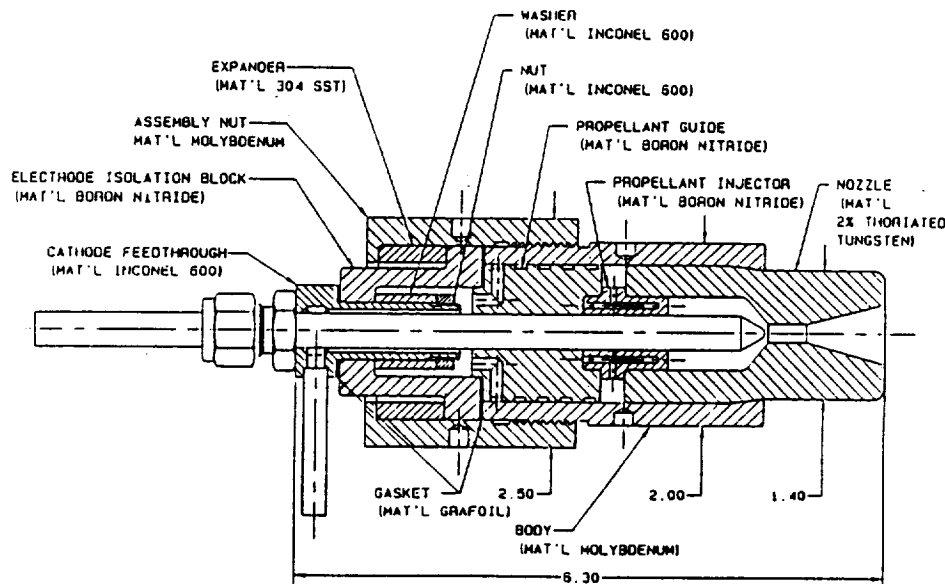


Figure 5-29. Schematic of RRC engine.

5.6.2 Experiments to Resolve the Discrepancy

The cause of these performance parameter discrepancies were not immediately apparent. The following possible sources were considered.

- The engine: JPL used a bell nozzle on the baseline engine design while RRC used a conical nozzle on the D-1E design;
- The flow controller: JPL used a Sierra Instruments thermal-type mass flow controller while RRC used a Micromotion coriolis-type mass flow meter with a motorized regulator for control;
- The diffuser: JPL used a gas-dynamic diffuser to collect the exhaust plume, and RRC did not;
- The thrust stand: JPL used a cantilevered beam, and RRC used a null balance, hinged arm.

An experimental program was laid out to determine the cause of the discrepancies based on these possible options. Tests were conducted to determine if the performance and voltage discrepancies were related or independent of each other. This program included running an RRC/AL endurance test engine at JPL and running a D-1E engine (shown schematically in Fig. 3-5) and JPL flow controller at RRC. Vacuum-effects testing was also conducted at RRC to determine if increased background pressure could affect the engine electrical characteristics and examine the effect of the diffuser on arcjet operation.

An RRC/AL endurance test engine was run at JPL in late June 1989. The engine's specific impulse was slightly below the JPL characteristic for the Baseline MOD I engine. This 15 to 20 s difference in specific impulse is consistent with previous data comparing conical nozzle performance with bell-shaped nozzle performance. The V-I characteristic for the RRC/AL endurance test engine running at JPL is also closer in magnitude to the baseline MOD I characteristic than when the same engine was run at RRC. These results indicated that while the nozzle shape might explain a small portion of the differences noted, facility variations were more important. This test did verify that the differences seen were real since identical engines had been run at both facilities.

In order to explain the voltage differences seen between the JPL and RRC tests, an experiment was conducted at RRC to see if the exit conditions at the nozzle could have an effect on the arc voltage. It was suggested that the diffuser used at JPL might create a shock near its inlet, causing the arcjet to exhaust into a higher pressure region than that being measured in the far field, resulting in a higher arcjet chamber pressure and therefore a longer, higher-voltage arc.¹⁵ The vacuum chamber pressure was varied from 0.060 Torr to in excess of 10 Torr. The nominal background pressure at 0.25 g/s of ammonia is 0.120 Torr at 25 kW in the RRC facility. Lower pressures were obtained by using a second set of pumps while higher pressures were obtained by bleeding gaseous nitrogen into the vacuum chamber. No effect was seen on indicated engine thrust until the background pressure was over 0.450 Torr. Engine operating voltage remained constant independent of the vacuum chamber pressure as shown in Fig. 5-30.

Calibration checks were conducted to determine the accuracy of the flow controllers used at RRC and JPL. These tests were conducted by placing a bottle of ammonia on a precision scale and monitoring the bottle mass loss over time as compared to the flow meter set point. An initial test at RRC demonstrated that the Micromotion flow meter was indicating within 3 percent of the actual flow, in agreement with previous tests. In a subsequent test using a tighter "dead band" on the motorized regulator, the Micromotion was found to be accurate to better than 1 percent. Similar initial tests of the Sierra Instruments MFC indicated it was reading low by approximately 15 percent.

The D-1E engine and Sierra MFC were installed in the RRC facility in the middle of August. The Sierra MFC was plumbed in series with the motorized regulator and Micromotion flow meter as shown in Fig. 5-31. Test procedures required each ammonia flow setting to stabilize for 20 minutes before data was recorded. Measurements were recorded for both increasing and decreasing mass flow values to observe any hysteresis effects. Both the Sierra MFC and motorized regulator were used to control the flow at different times. The results of the head-to-head comparison are shown in Fig. 5-32. If the flow meters gave the same indicated flow rate, the data would lie along the dashed line. However, the Sierra MFC indicated a flow rate approximately 20 percent below that of the Micromotion flow meter.

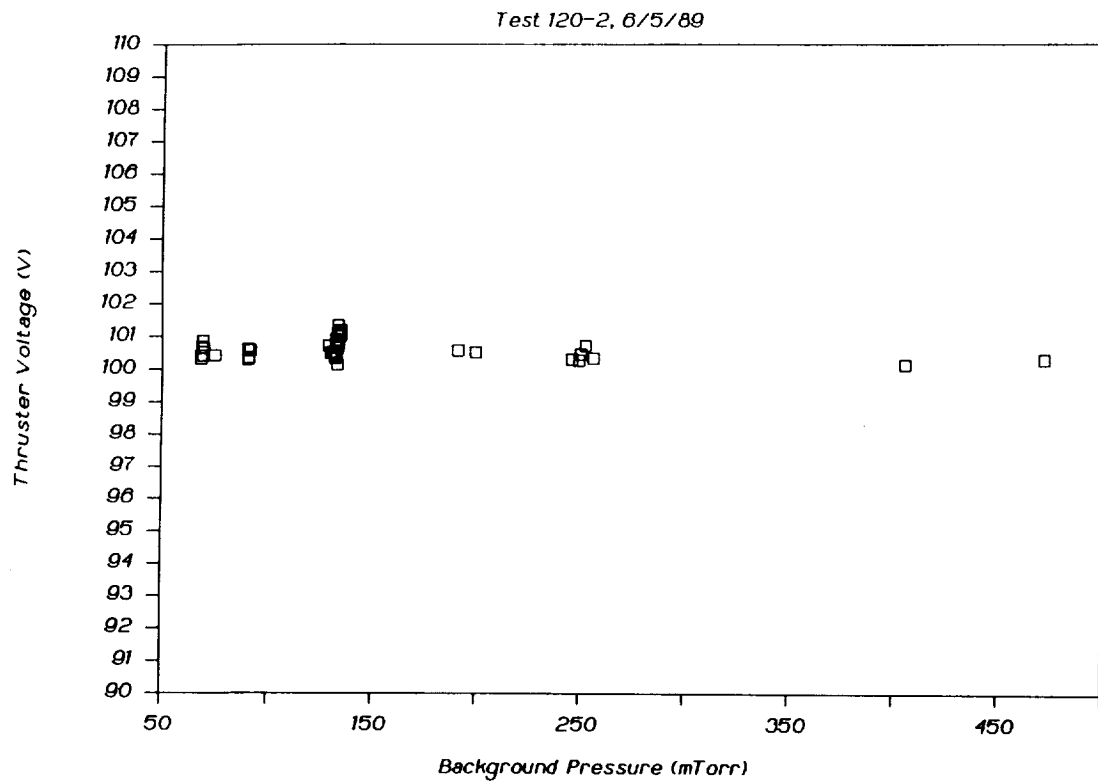


Figure 5-30. Thruster voltage vs. vacuum chamber pressure.

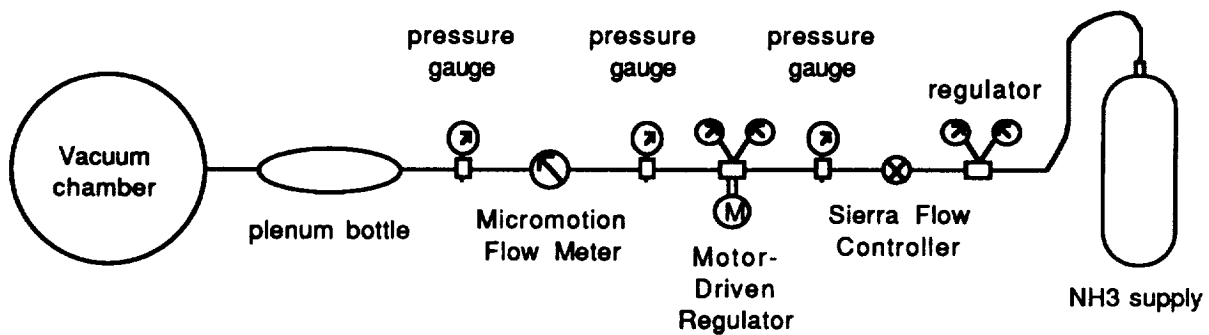


Figure 5-31. Mass flow controller test plumbing at RRC.

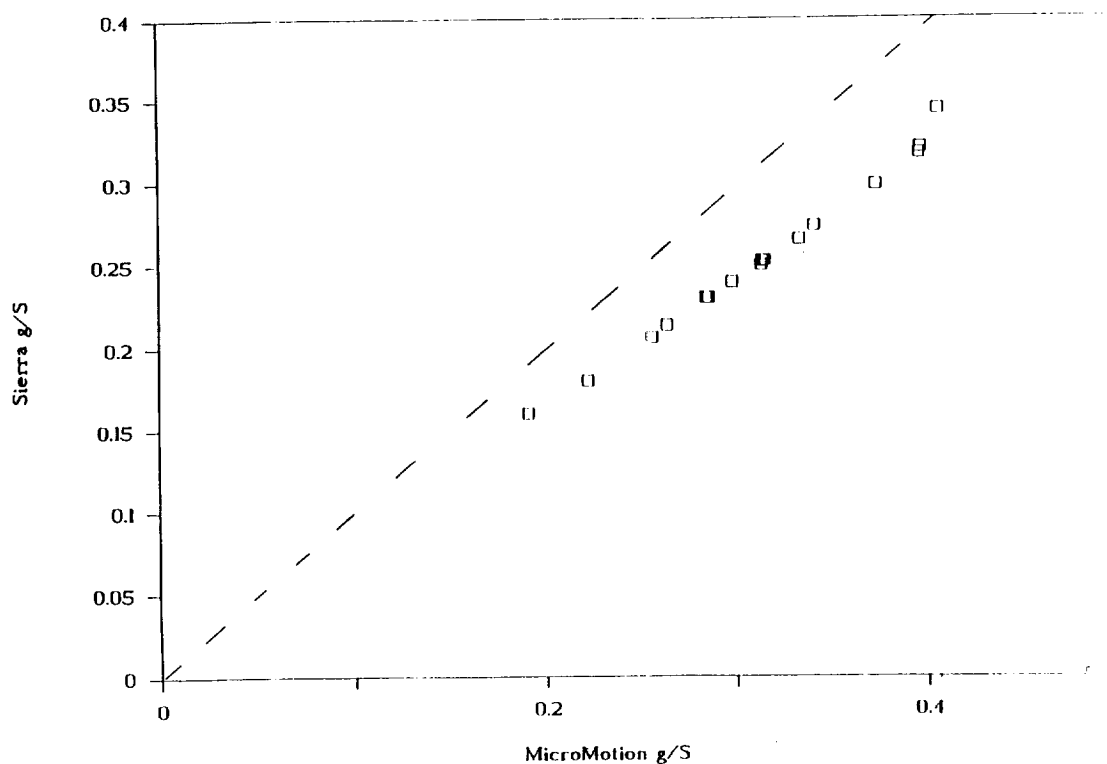


Figure 5-32. Results of mass flow controller comparison.

Detailed calibration checks of the Sierra MFC were undertaken over the next three weeks at JPL. These tests were done by, again, monitoring the mass loss from a bottle of ammonia over time. A vendor calibration check was also included. The results of the first three of these tests are shown in Fig. 5-33. The first three tests were conducted before the vendor calibration check and the last three tests after the vendor calibration check. Tests 1 through 4 were conducted using a propellant feed system setup as shown in Fig. 5-34. A 22.9 m length of tubing was coiled up in a water bath at 20 °C to ensure that the gas temperature would remain a known constant value for the duration of the tests. The gas was then routed past an external thermocouple into the Sierra MFC. As seen in Fig. 5-33, the MFC was indicating a flow rate 20 percent lower than the actual averaged mass flow from the bottle. Tests 5 and 6 were conducted using the plumbing system shown in Fig. 5-35. This represents the standard facility ammonia-propellant plumbing system at JPL which was used in all previous engine testing (no water bath), except that the ammonia storage bottle was in the laboratory building for better climate control. The 22.9 m length of tubing was used to connect the ammonia supply in the building to the original facility plumbing outside. Test 6 used the same setup as Test 5 except a small heater-wrapped plenum was placed in the propellant line 80 cm upstream of the Sierra MFC. The Test 6 data was corrected for the MFC temperature effects as supplied by the vendor.⁸ Both Tests 5 and 6 agreed with the earlier tests; the MFC used by JPL indicated a flow 20 percent less than the actual flow. It should be noted that the Sierra MFC was found by the vendor to be in calibration to better than 1 percent after Test 3, indicating conclusively that the calibration process is inaccurate.

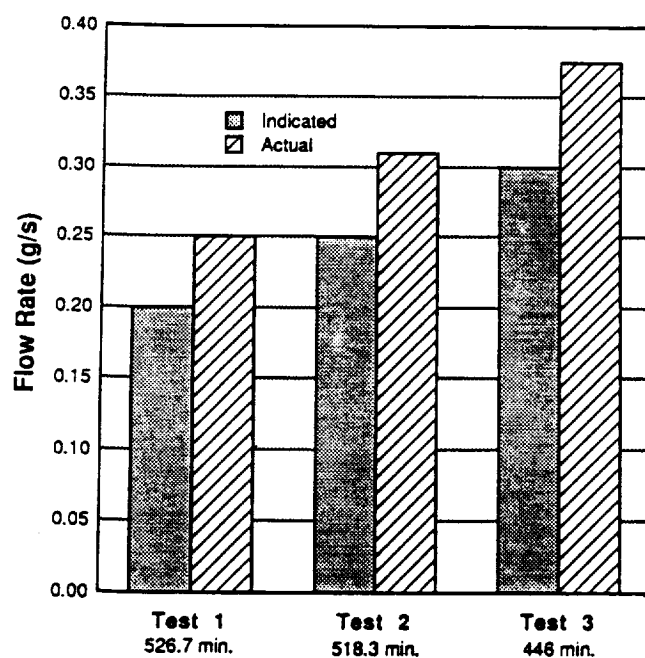


Figure 5-33. Results of further calibration check (Tests 1-3).

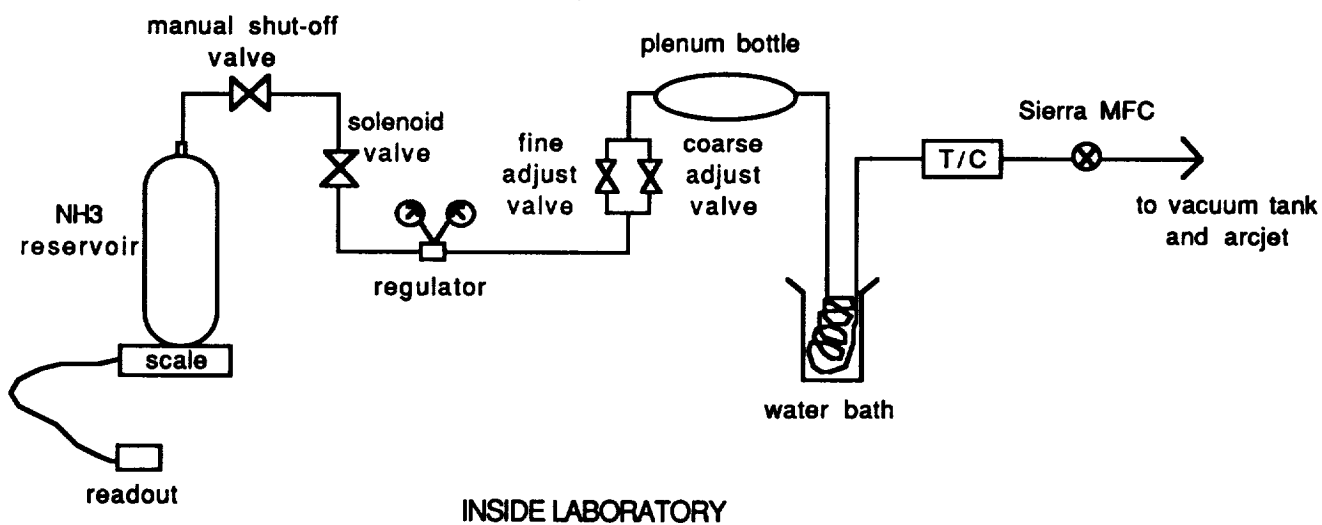


Figure 5-34. Propellant feed setup (Tests 1-4).

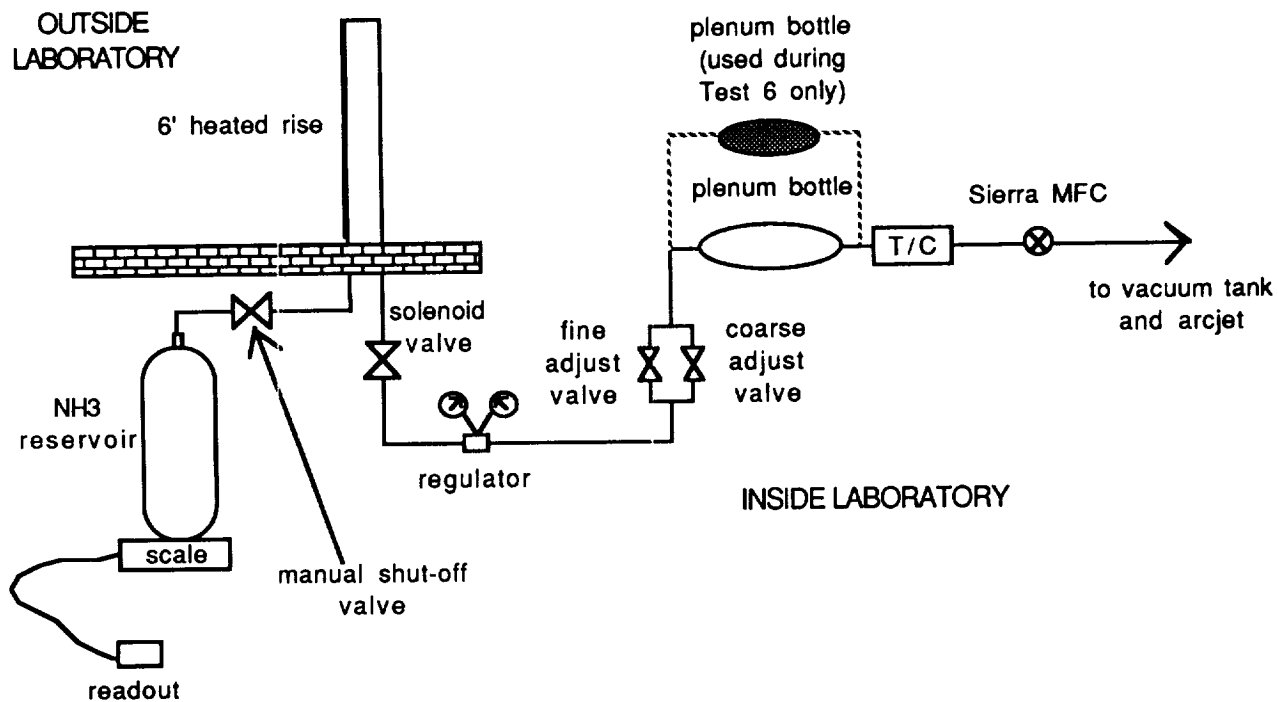


Figure 5-35. Propellant feed setup (Tests 5 and 6).

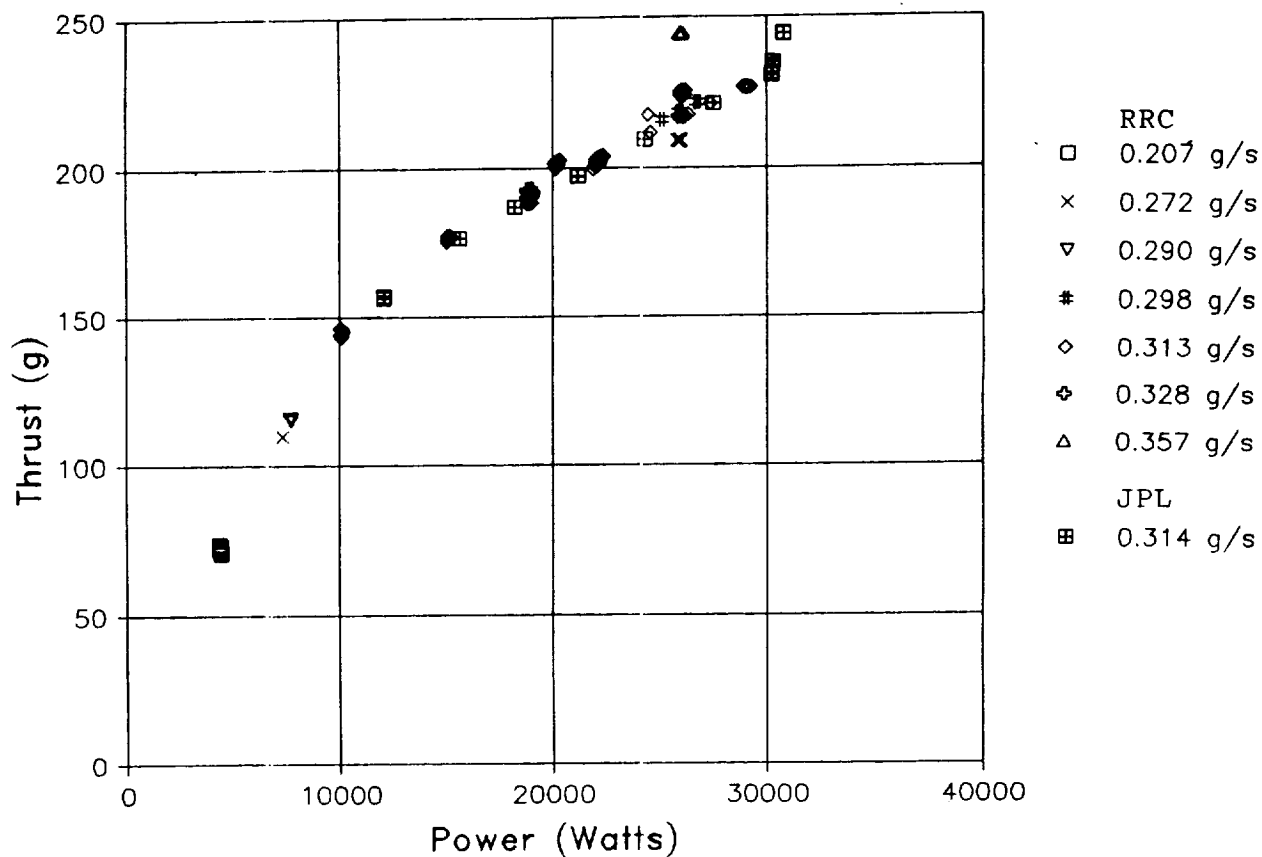


Figure 5-36. Indicated thrust comparison with corrected flow.

5.6.3 Discussion

A 20-percent error in the Sierra MFC calibration appears to explain the observed discrepancies in voltage and performance. The indicated thrust at both JPL and RRC is in agreement to within 2 percent when the difference in the flow meters is accounted for, as seen in Fig. 5-36. The "measured" specific impulse (calculated from the measured thrust and corrected mass flow rates) is shown as a function of power divided by corrected mass flow rate for D-1E engine operation at JPL and RRC (and compared to the Baseline MOD I engine) in Fig. 5-37. A correction factor of 1.26 was applied to the mass flow data used in determining performance at JPL. When the correction is applied, the higher actual mass flow for the same value of thrust results in a drop in the specific impulse and efficiency. The nominal operating point being used at JPL for 30-kW duration testing is shown in Table 5-2 with both the corrected and uncorrected performance values. The tests discussed in Ref. 27 were run at these conditions. The performance test data comparisons between JPL and RRC, coupled with the vacuum effects testing, indicate that the diffuser used at JPL has no major effect on arcjet electrical or performance characteristics.

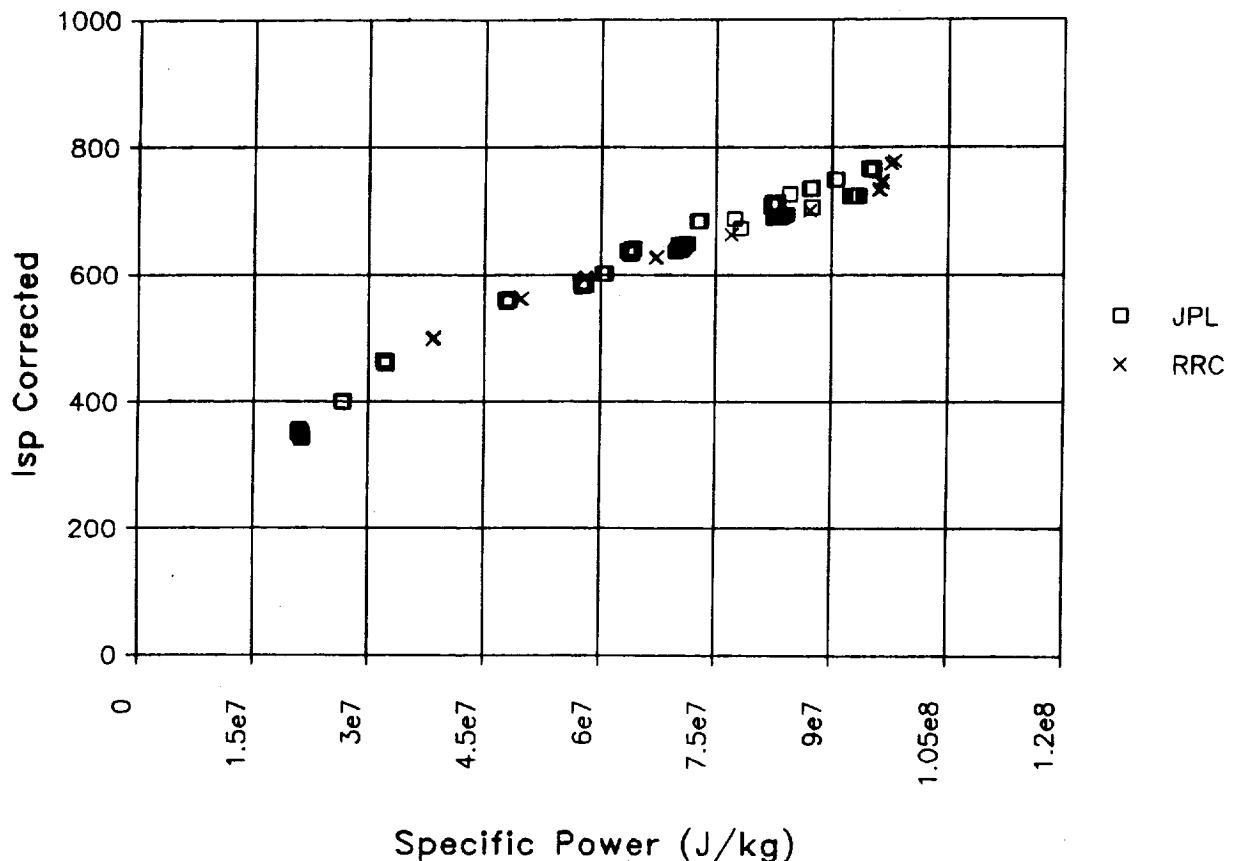


Figure 5-37. I_{sp} vs. P/\dot{m} comparison with corrected flow.

Table 5-2. 30-kW Duration Test Performance at JPL

Parameter	Uncorrected	Corrected
Power, kW	30.3	30.3
Mass Flow Rate, g/s	0.26	0.33
Thrust, N	2.42	2.42
Specific Impulse, s	950	754
Efficiency	0.37	0.29

5.6.3.1 Sierra Instruments Mass Flow Controller (MFC) Operation. The Sierra MFC (used at JPL) uses a thermal-type mass flow meter (MFM).^{76,103,111} This meter is shown schematically in Fig. 5-38. The gas enters the flow body and divides into two paths, one through the sensor tube (m_1), the other through the bypass (m_2). The flow m_1 is generated by a small pressure drop, P_1 - P_2 , through the bypass and is typically 30 percent of the total flow. Two balanced resistance temperature detector (RTD) coils around the tube direct a constant amount of heat into the gas stream. During operation the gas mass flow carries heat from the upstream coil to the downstream coil. The resulting temperature difference between the two coils results in a resistance difference between the two coils. The coils are two of the legs in a bridge circuit which produces an output voltage directly proportional to the resistance difference and hence the temperature difference. The gas in the tube is assumed to be ideal and to have constant properties (i.e., temperature and pressure independent). Over a specified design range, the resistance difference has been shown to be linear function of the mass flow rate to within 0.5 percent. Parameters such as the heat input to the gas by the coils, heat conduction losses through the sensor tube, non-linearity effects in the flow split and the gas property variations would have to be included in a detailed model of flow controller operation. However, proper calibration can account for these factors without requiring a detailed understanding. The Sierra MFC includes a built-in electromagnetic servo control valve and electronics to form a compact MFC.

5.6.3.2 Micromotion Mass Flow Meter (MFM) Operation. The Micromotion MFM (used at RRC) is a coriolis-type MFM. A schematic of this type of device is shown in Fig. 5-39. All of the mass flow goes through the sensor tube in these devices. A thin-walled, U-shaped flow tube inside the sensor housing is vibrated at its natural frequency by a magnetic device located at the apex of the bend in the tube. The vibration is small in amplitude with an oscillation frequency of, nominally, 80 Hz. As the gas flows through the tube, it takes on the vertical motion of the tube. When the tube is moving upward during half of its cycle, the gas flowing into the tube resists being forced upward by "pushing down" on the tube (Newton's 3rd Law). Having been forced upward, the gas flowing out of the meter resists having its vertical motion decreased by "pushing up" on the tube. This action causes the tube to twist. When the tube is moving downward during the second half of its vibration cycle, the tube twists in the opposite direction. The amount of twist is directly proportional to the mass flow rate of the gas moving through

the tube. Magnetic sensors and electronics are used to convert the tube velocities into mass flow rates. A separate motor-driven regulator is placed upstream of the Micromotion MFM at RRC. The output signal from the Micromotion MFM is used to drive the regulator and maintain a constant flow rate. A dead band is used so that the regulator is only driven if the flow rate goes beyond certain tolerance limits.⁷⁶

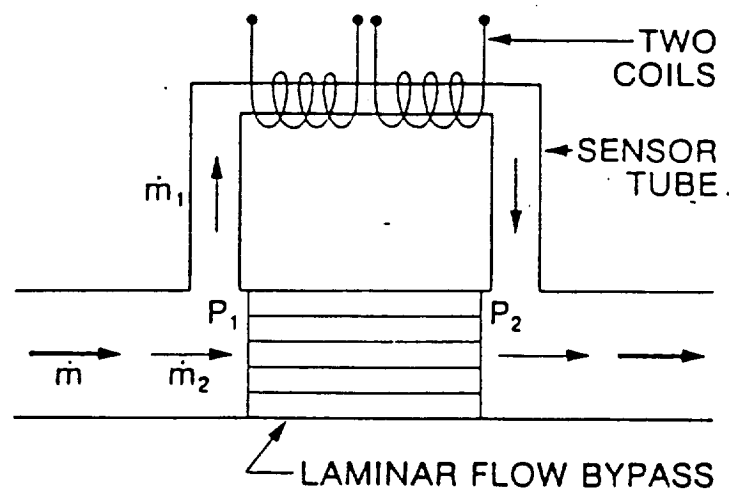


Figure 5-38. Schematic of Sierra MFC.

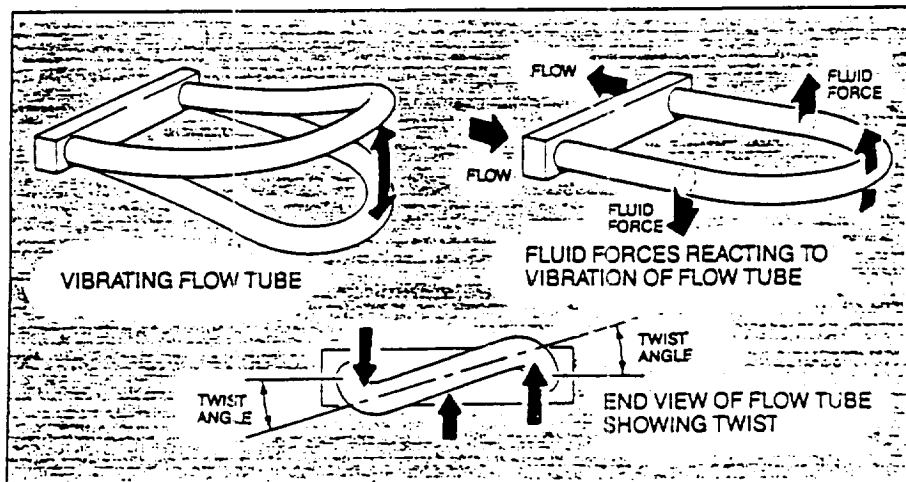


Figure 5-39. Schematic of Micromotion MFM.

5.6.3.3 Sources of MFC Error. After determining that the MFC was the cause of the discrepancies, it was found that the calibration technique used in industry for thermal-type MFCs is inaccurate if the gas is near its saturation pressure and departs from ideal gas properties. Calibration is accomplished by flowing a quantity of gas at a constant rate through the device and measuring the time it takes to fill a known volume with gas (a volumetric calibration procedure). By knowing the gas properties (temperature and pressure), the volumetric mass flow can be calculated. Calibrations are generally done at engineering standard conditions, 70 °F and 1 atm of pressure.⁸ Production MFCs can be calibrated using either primary standards or transfer standards. Primary standards employ the U.S. National Bureau of Standards primary measurements of time and distance and are generally only used for non-hazardous gases. Most MFCs, including those used for ammonia, are calibrated using transfer standards which employ a mass flow meter calibrated with primary standards on a non-hazardous reference gas. The flow rate for the reference gas is then "transferred" to the gas of interest through the use of a so-called K-factor ratio.

The K-factor ratio is a ratio of properties for the gas of interest to the same properties for the reference gas. The K-factor ratio used by Sierra Instruments is given by:

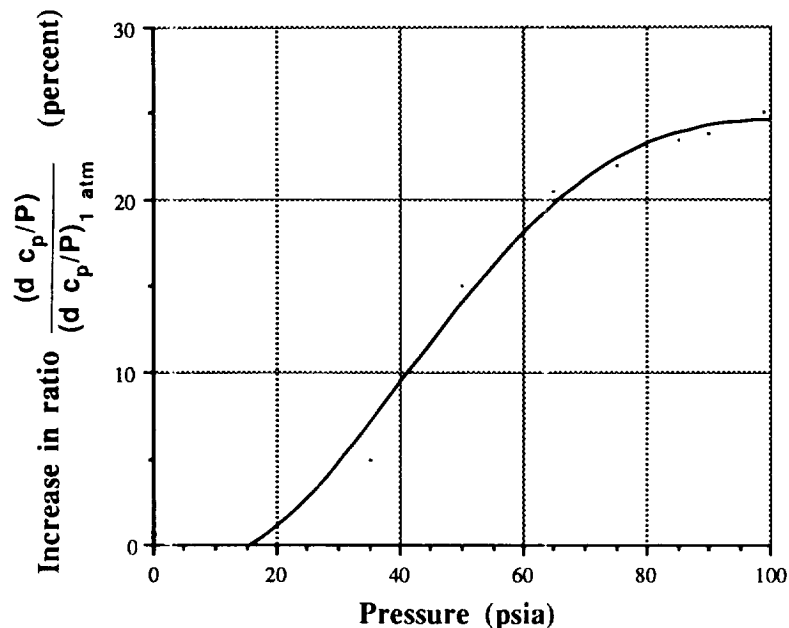
$$K_1/K_2 = (N_1/d_1C_{p1})/(N_2/d_2C_{p2}) \quad (5-4)$$

where subscript 1 denotes the gas of interest and subscript 2 denotes the reference gas.¹⁰³ In this equation, N is an experimentally-determined correction factor which accommodates molecular structural effects, d is the gas density at the standard condition, and C_p is the specific heat at constant pressure, also for the standard condition. The reference gas used by Sierra Instruments for ammonia is now nitrous oxide, N_2O (a MFC industry standard), and the corresponding K-factor ratio is 1.028.¹⁰³ This calibration technique is repeatable and consistent as long as the same reference gas is used, a requirement of the microelectronics industry who defined the MFC standards. The Sierra MFC claims an accuracy of ± 1 percent of full scale (including linearity) over input gas temperature and pressure ranges of 15-25 °C and 10-60 psia, respectively.¹⁰³

However, real gas effects (namely, an increase in the specific heat and in the ratio of density to pressure with increasing pressure) can have a significant impact on the actual flow conditions. A comparison of the dC_p/P ratio (where P is pressure) for ammonia at various pressures to that at 1 atm (14.7 psia), both at constant temperature, is shown in Fig. 5-40. This approximate curve applies to the ammonia temperature range of 60 to 100 °F. As pressure increases within the tolerance limits for the MFC, this ratio increases by 25 percent due to real gas effects. With an inlet pressure of 45 psia, as is typically used at JPL, the increase in K-factor is between 10 and 15 percent. It appears that the MFC error is traceable to an error in the K-factor for the N_2O -to- NH_3 transfer caused by real gas effects. More precise understanding of the calibration error would require a detailed model of flow controller operation.

5.6.4 Corrections for Published Data

The data in Refs. 11, 20, 25-38, 58, 79-85, 99 and 107 were generated at JPL and require correction. References 25, 26, 29, 31, 33, 36, 37 and 99 are mission design and analysis papers which cite arcjet performance from testing done at JPL. The analysis is valid, but the cited performance can no longer be considered accurate and is now optimistic in most cases. The high specific impulse cases (those greater than 950 s) can be considered an upper bound on possible mission performance. Reference 31 includes the bounding case of an 800 s, 30-percent efficient arcjet, close to the corrected performance given in Table 5-2.



(This approximate curve applies to ammonia temperatures between 60 and 100 °F)

Figure 5-40. Variation of the product of density and specific heat for ammonia at various pressures.

In order to identify where reliable data corrections are possible, the calibration history of the Sierra MFC is given in Table 5-3. All calibrations done since March 1989 used nitrous oxide as the reference gas. Therefore all data reported since that date can be corrected by increasing the mass flow rate by the factor 1.26, determined from the experiments discussed earlier in Section 5.6. The specific impulse and thrust efficiency were calculated in all the references using Eqs. 5-2 and 5-3, respectively. Published values of these quantities should be divided by 1.26, since mass flow rate appears in the denominator of the equations used to calculate them. The error on the corrected mass flow is ± 3 percent. This correction is valid for the data reported in Ref. 27 corresponding to Cathodes 20, 22 and 24.

Table 5-3. Sierra MFC Calibration History

Date	Vendor	Reference Gas	Actual Gas	Notes
6/85	Sierra	Air	NH ₃	New, In specs
1/86	Sierra	N ₂	NH ₃	In specs
1987	-	-	-	Facility moved
3/88	D Munns	*	NH ₃	In specs
3/89	Sierra	N ₂ O	NH ₃	7% low, rebuilt, Then in specs
8/89	Sierra	N ₂ O	NH ₃	In specs

* Vendor records incomplete

A calibration was performed in March 1988 with an unknown reference gas; a calibration check, in March 1989, showed that the meter was reading 7 percent low compared to Sierra specifications. It is unknown if the meter was reading 7 percent below Sierra specifications the whole year or drifted there late in the test cycle. The test data taken during this year-long period were consistent in terms of indicated performance with the data taken after March 1989. Therefore, all the data taken between March 1988 and March 1989 should be correctable by applying the same correction factor (1.26) to the mass flow values, but the error is much larger: -3 percent and +10 percent. This mass flow correction factor applies to data in Refs. 20, 27, 38, 99 (Cathodes 4, 13, 14, 15, and 17), 26, 36 and 58. Data from the period March 1988 through March 1989 appear uncorrected in this report, with notation indicating parameters which should be corrected, and the appropriate factor. In these cases, confidence in the correction is supported by comparing with data taken since March 1989.

Absolute correction factors and uncertainties for data taken before March 1988 are difficult to determine. As can be seen in Table 5-3, different reference gases were used. In addition, the tests were conducted in another facility with a different propellant plumbing system which no longer exists. These considerations affect the data in Refs. 11, 25, 28-37 and 79-85. For example, the baseline MOD I data shown in Figs. 5-1 and 5-3 is from Ref. 30. The 1.26 mass flow correction factor does bring this data to within the thrust stand uncertainties of later tests. However, a firm correction factor and uncertainty can not be explicitly stated for all the data taken before March 1988. In this report, affected data taken before March 1988 are noted as being useful for comparative purposes only. Table 5-4 summarizes the correction of data affected by the mass flow calibration error.

Table 5-4. Summary of Data Correction Procedure

DATE TAKEN:	03/89 - 09/89	03/88 - 03/89	Prior To 03/89
Correction Factor:			
Mass Flow Rate	Multiply by 1.26	Multiply by 1.26	---
specific impulse	Divide by 1.26	Divide by 1.26	---
thrust efficiency	Divide by 1.26	Divide by 1.26	---
Mass Flow Rate Error	±3 Percent	-3, +10 Percent	---
Notation in This Report	Shown in Corrected Form	Shown Un- corrected, With Correction Factor Noted	Shown Un- corrected, Noted For Comparative Use Only

The AVCO ammonia arcjet data from the 1960s must be reevaluated in light of the MFC problem, particularly since it is in agreement with the uncorrected JPL data. Details of the ammonia propellant plumbing system used by AVCO are unavailable. It is believed that variable area/float flow meters were used. The gradation markings on such a flow meter could be inaccurate if a transfer gas standard was used to define them. The hydrogen arcjet data reported by AVCO is still believed to be valid since transfer gas standards appear to be accurate for hydrogen.

5.7 DIRECT START TESTING

For space applications, arcjets will need to be started directly on the propellant. The laboratory two-fluid technique, glow discharge to arc discharge on argon, then transitioning to ammonia, would greatly complicate the propellant feed system and reduce reliability.

Two start techniques have been demonstrated for starting 1-kW arcjets.^{23,47,61,62,104} The first uses a high voltage spike through the propellant gas at the proper flow rate while the second uses a momentary interruption of the propellant flow to generate a breakdown in the gas at a lower voltage. Using either of these techniques, 1-kW arcjets start at effectively full power in a few seconds. The high-voltage spike technique has been selected for flight development due to pulsed gas valve reliability and ease of start circuit development.

Both techniques are more difficult to implement in 30-kW class arcjets since the electrodes are much larger and do not heat quickly enough to enable the engine to start at full power. A laboratory high-voltage spike technique has been implemented by RRC for higher power arcjets.¹⁷ The engine is started at low power and reduced gas flow. Both parameters are increased to maintain electrode heating and operating stability up into the engine operating range.

A different laboratory direct-start technique was attempted at JPL. The general technique includes establishing a glow discharge on ammonia using a start supply with high-voltage capability, transitioning to an arc discharge at several kilowatts and finally activating the run supply and turning the start supply off. Due to start power supply overheating, the entire technique was not demonstrated in one attempt; each step was, however, demonstrated separately.

During the first series of tests the start supply was used to establish a discharge directly on ammonia. The flow rate was 0.30 g/s. The start supply voltage was turned up until electrical breakdown occurred. Breakdown occurred between 825 and 950 V. The start supply power was then slowly turned up until 1.5 to 2.0 kW were being supplied to the engine, typically 2 to 4 A at 500 to 700 V. During the time at 1.5 to 2.0 kW, the plume would rotate and change in intensity. A flat-faced cathode was used (see Fig. 3-8). The total allowed time at 2 kW was limited to two minutes.

The run power supply would activate only after the engine voltage was below about 400 V. In order to get the engine voltage to drop, the cathode was found to require a longer heating time. Start attempts were then conducted with the engine starting on argon and allowed to heat up. The transition to ammonia was made while still on the start supply. After a minute of operation on the start supply with the argon off, the run supply was turned on. Through experimentation it was found that the run supply would take over operation of the engine only when the engine voltage was below 200 V and the run supply was delivering over 80 A of current. During the transition, the engine voltage would oscillate between 180 and 600 V. Further validation of this technique is needed to fully understand the electrical behavior of 30-kW class arcjets at several kilowatts of power. The RRC technique avoids low output power from the run supply by initially dumping excess power into resistors, which are switched out to increase power to the engine. An understanding of 30-kW class arcjet operation at low powers is needed to develop a space-qualifiable start technique for high power arcjets. Both demonstrated laboratory techniques would require massive start-up circuits.

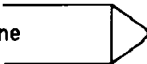
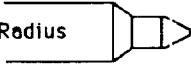

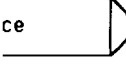

6.0

ENDURANCE TESTING

A series of endurance tests was conducted, using the D-1E arcjet engine, to evaluate the effects of cathode tip shape, spacing and power source ripple on engine operation and cathode erosion. The D-1E arcjet is described in Chapter 3. The experimental procedures for these tests were the same as noted in Section 5.1. The general results of these tests are summarized in Table 6-1. The five 100-hour tests, the 413-hour test and the 252-hour test were voluntarily terminated. The 53-hour test was shut down by the Data Acquisition and Control System (DACS) due to an area power failure, while the 21-hour test was terminated by the DACS due to cold weather-induced propellant flow system depressurization. The 252-hour test was shut down voluntarily after visual indications were seen that anode damage had occurred. Averaged cathode material mass loss rates ranged from 1.4 mg/hr to 6.2 mg/hr during these tests.

Detailed results from these tests are presented below. An event time line is given for tests longer than 100 hours. Results are reported for voltage, current, power, impedance, nozzle brightness temperature, and thrust. Data are provided for specific impulse and efficiency when the thrust was deemed accurate. The general behavior of the engine voltage-current operating point is also given. The results are grouped into three sections: (1) power unfiltered; (2) power filtered; and (3) long-term (power filtered) tests greater than 100 hours in length.

Table 6-1. Summary of Endurance Tests

	TEST DURATION (hrs)	INPUT CURRENT RIPPLE	GEOMETRIC ARC LENGTH* (cm)	WHISKER GROWTH?	EROSION RATE (mg/hr)	ARC CURRENT (A)
Baseline 	# 13 53	3%	1.11	yes	1.5	265-291
	# 14 100	3%	1.11	yes	4.0	289-303
	# 22 100	0.2%	1.11	yes	3.1	264-289
45° Reduced Radius 	# 4 100	3%	1.43	?	2.1	238-252
Dimpled 	# 15 21	0.2%	1.81	yes	6.2	243-247
Flat Face 	# 20 28	0.2%	1.47	no	1.4	234-252
	# 20 413	0.2%	1.47	yes	5.2	215-251
	# 17 100	0.2%	1.47	no	2.0	246-257
	# 25 252	0.2%	1.44	yes	4.1	229-208
Fat Tip 	# 24 100	3%	1.14	yes	3.3	244-277

* AT START OF TEST

6.1

TESTS WITH UNFILTERED POWER

Four endurance runs were conducted using unfiltered input power to the arcjet with a current ripple of 3 percent. These tests used Cathodes 4, 13, 14, and 24. Cathodes 4, 14, and 24 were operated for 100 hours, at a nominal power level of 30 kW and a mass flow of 0.32 g/s of ammonia, and voluntarily shut off. This mass flow rate is correct for Cathode 24, which was tested after March 1989. For the other three cathodes, tested between March 1988 and March 1989, the corrected mass flow rate is the same; the error is somewhat larger. The nominal mass flow rate for these three cases was 0.25 g/s. (See Section 5.6.) Cathode 13 was operated at the same conditions for 53 hours before the test was terminated by the DACS. The startup, run and shutdown procedures were described in Section 5.1, "Experimental Procedures." The results from these four tests are shown in Figs. 6-1 through 6-6. The performance was calculated using Eqs. 5-1 through 5-3.

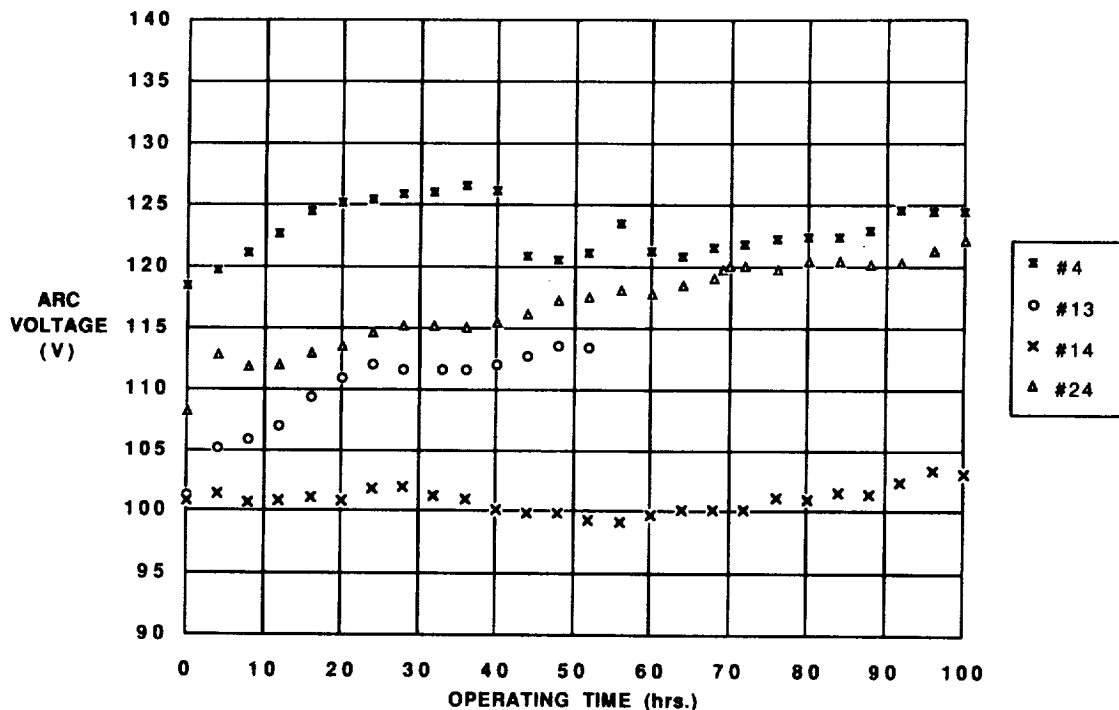


Figure 6-1. Voltage vs. time (unfiltered power tests).

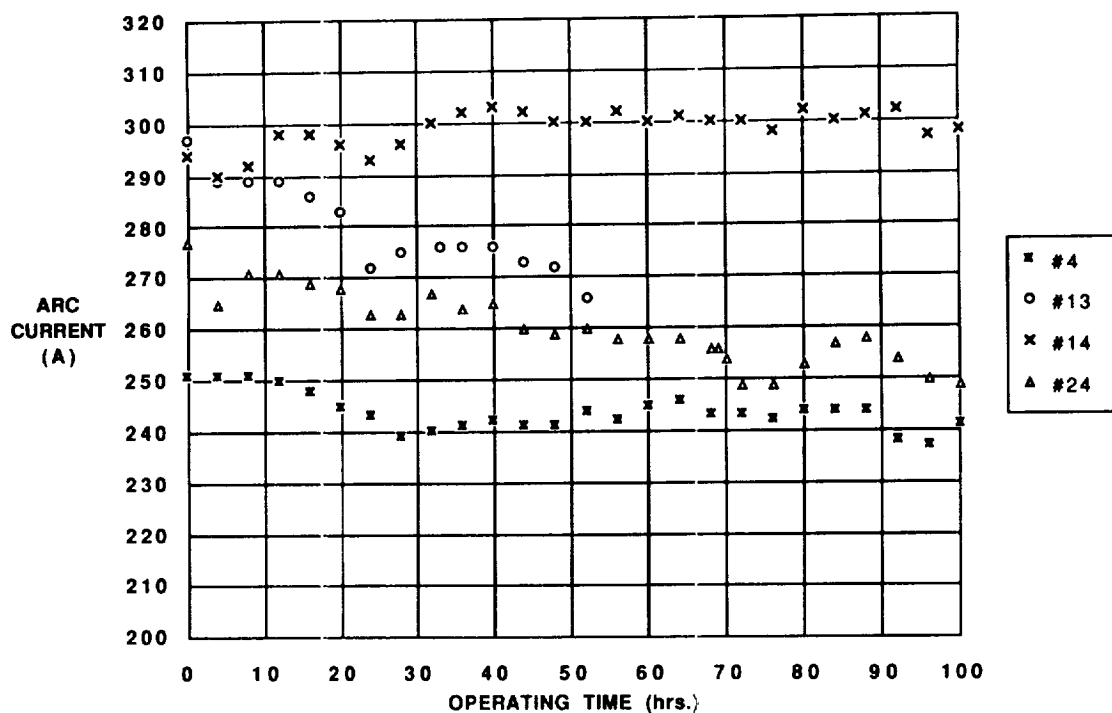


Figure 6-2. Current vs. time (unfiltered power tests).

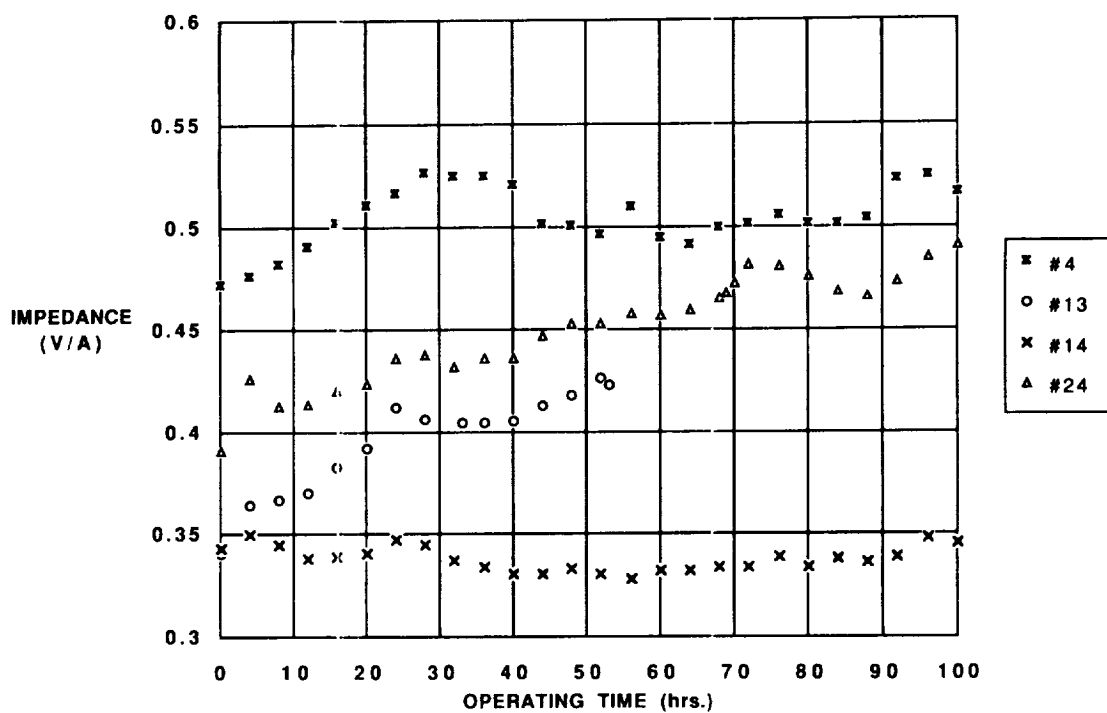


Figure 6-3. Impedance vs. time (unfiltered power tests).

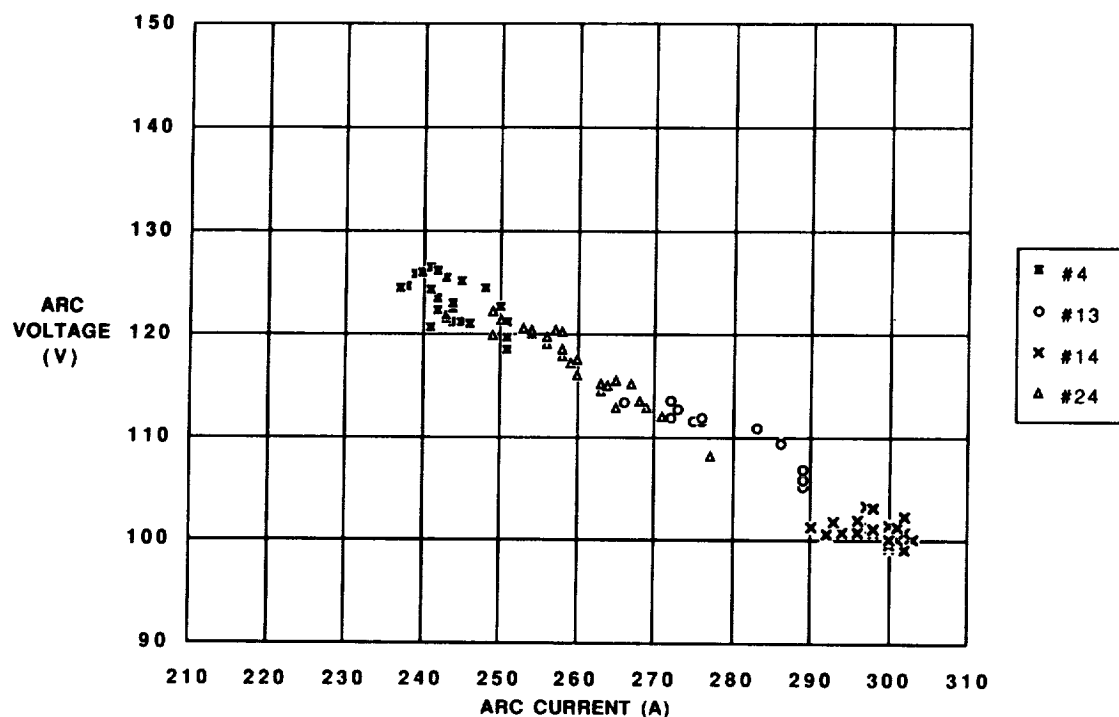


Figure 6-4. V-I characteristic (unfiltered power tests).

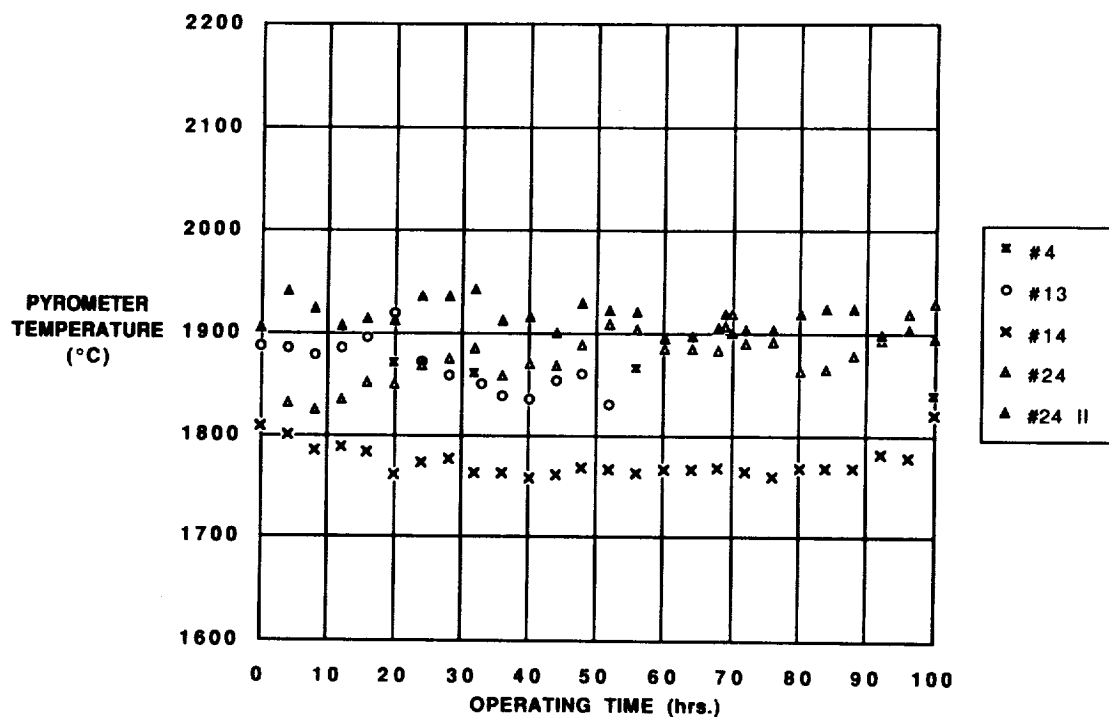


Figure 6-5. Nozzle brightness temperature vs. time (unfiltered power tests).

6.1.1 Test Events

A test using baseline Cathode 13 was performed first. The engine operating point was reached 17 minutes after the main power supply was activated. As the test progressed the power crept up; 20.8 hours into the test the power was reduced from 31.5 kW to 30.3 kW to better maintain the operating point. The power was turned down again to 30.3 kW from 31.1 kW, 50 hours after reaching the operating point. The test was terminated at 53.3 hours into the test by an area power failure.

Cathode 14, also a baseline model, was tested next. The engine reached its operating point 15.1 minutes after the main power supply was activated. The power was turned up to 29.8 kW from 29.4 kW, approximately 9 hours into the test. The initial observation of an asymmetry at the nozzle inlet occurred 21 hours into the test; 46.5 hours into the test the plume was seen to be asymmetric, being more sharply defined in the lower half of the nozzle. The engine was shut off after 100.3 hours of operation.

A reduced radius cathode, Number 4, was run next. After 15 minutes of operation at full power, the engine was shut off due to an ammonia leak from the flow controller solenoid valve. The engine was restarted after replacing the solenoid valve O-rings to repair the leak. The engine reached its operating point approximately 15 minutes after activating the main power supply. The power again dropped at the beginning of the test. The power was brought back up to 29.8 kW from 29.3 kW, 1.6 hours after reaching the operating point. The power was reduced to 30.1 kW from 30.8 kW, 26.5 hours after the test was restarted. An asymmetry at the nozzle inlet was also observed. The test was terminated after 100 hours at the operating point.

The final test using unfiltered input power was done using Cathode 24, which had an enlarged tip. This test also used a nozzle machined from pure tungsten. The first start attempt terminated when evidence of an engine leak was discovered. The engine was removed and the cracked rear insulation was replaced. The engine was reinstalled in the vacuum tank and restarted. The power was reduced from 30.5 kW to 30.15 kW after 35 hours of operation. After another 19 hours of operation, the power was reduced from 30.5 kW to 30.46 kW. The power was reduced a third time from 30.5 kW to 30.1 kW after 71 hours of operation. The engine was turned off after 100.3 hours of operation.

6.1.2 Performance

The engine voltage, current, and impedance are shown in Figs. 6-1 through 6-3 as a function of accumulated test time for each test. During the course of these tests data was being sampled every 2 seconds and stored every 2 minutes. The data presented in Figs. 6-1, 6-2 and 6-3 represent a data point every 4 hours. The power varied around the nominal 30 kW operating point from 29.3 kW to 31.7 kW during these tests. In all four tests the voltage demonstrated a generally increasing trend. Each data point has been corrected for the power lead voltage drops discussed in Chapter 2 of this report. The general voltage-current characteristic operating point is shown

in Fig. 6-4. The time scale is not explicit due to data scatter. The brightness temperature of the nozzle at a wavelength of $1\text{ }\mu\text{m}$ is shown in Fig. 6-5. This was measured at a point 1 cm behind the nozzle exit on the outer surface.

Thrust data for these tests are not shown. Data for Cathodes 4 and 24 are inaccurate. Data for Cathode 4 were affected by thrust stand misalignment while the data for Cathode 24 was invalidated by the hardening of the oil barrier on the mercury in the mercury pots. The thrust data for Cathodes 13 and 14 are questionable due to a thrust stand mounting flange substitution. The original stainless-steel flange was replaced with an Invar flange to further minimize heating effects. The Invar flange turned out to deform more than the stainless-steel flange and was switched back to stainless for further tests.

6.2 TESTS WITH FILTERED POWER

Three endurance runs limited to a maximum of 100 hours were made using filtered input power to the arcjet with a current ripple of 0.2 percent, 15 times smaller than the unfiltered case. These tests used Cathodes 15, 17 and 22. Cathodes 17 and 22 were operated for 100 hours, at a nominal power level of 30 kW and a mass flow of 0.31 g/s of ammonia, and voluntarily shut off. This mass flow rate is correct for Cathode 22, which was tested after March 1989. For Cathodes 15 and 17, which were tested between March 1988 and March 1989, corrected mass flow rate is the same; the error is somewhat larger. The nominal mass flow rate for these two cases was 0.25 g/s. (See Section 5.6.) Cathode 15 was operated at the same conditions for 21 hours before the test was stopped by the DACS. The results for these three tests are shown in Figs. 6-6 through 6-11.

6.2.1 Test Events

Cathode 15 was designed with a dimple on the downstream face. The engine was on at full power 8 minutes after activating the main power supply. After 3 minutes a large arc occurred at the back of the engine and the test was shut down. The rear insulator was cracked at the cathode attachment face resulting in a propellant leak. The increased gas density supported an arc between the calibrator attachment and heat shield. The crack was believed to have occurred during assembly. The engine was rebuilt and the test restarted. The engine was at the operating point 11 minutes after the main supply was activated. The DACS shut down the test after 21 hours of operation. This shutdown is believed to have been caused by a propellant line depressurization resulting from lack of ammonia vapor due to cold temperatures. The test was terminated at this point.

Cathode 17 was a flat-face cathode and was run next. After the initial engine start, the mass flow was increased 10 percent to smooth out voltage and current oscillations and was then returned to the nominal 0.31 g/s value several minutes later. Approximately 20 hours into the test the power was increased by 0.1 kW to 30.0 kW. About 31 hours into the test the power was reduced from 30.4 kW to 30.1 kW. The test was terminated at 100 hours.

Cathode 22 had a baseline tip shape. Approximately 4 hours after the start of the test an asymmetry was noted in the nozzle. Approximately 20 hours into the test the mass flow was increased by 20 percent for several minutes to try to "blow" the arc out of the constrictor. No change occurred. The power was increased by 0.5 kW to 30.1 kW. One and a half hours later, 45-1/2 hours into the test, the power was reduced 0.2 kW to 30.0 kW. The power was turned down again 50 hours into the test by 0.3 kW; 67.7 hours into the test power was again decreased from 30.7 to 30.1 kW. The power was reduced from 30.5 kW to 29.9 kW 88 hours into the test.

6.2.2 Performance

The engine voltage, current, and impedance are shown in Figs. 6-6 through 6-8, respectively, as a function of accumulated test time for each test. Again, a data point is shown every 4 hours and the voltage shows a generally increasing trend. The power lead voltage drop correction has been applied. The general behavior of the engine V-I operating point is shown in Fig. 6-9. The nozzle brightness temperature at a point 1 cm behind the nozzle exit plane is shown in Fig. 6-10 for each test.

The engine thrust is shown in Fig. 6-11. The data are shown at 4-hour intervals. The data have been corrected for LVDT temperature, zero shift and mass flow. However, the data for Cathodes 15 and 17 were inaccurate due to a thrust stand alignment problem. Data for Cathode 22 are accurate.

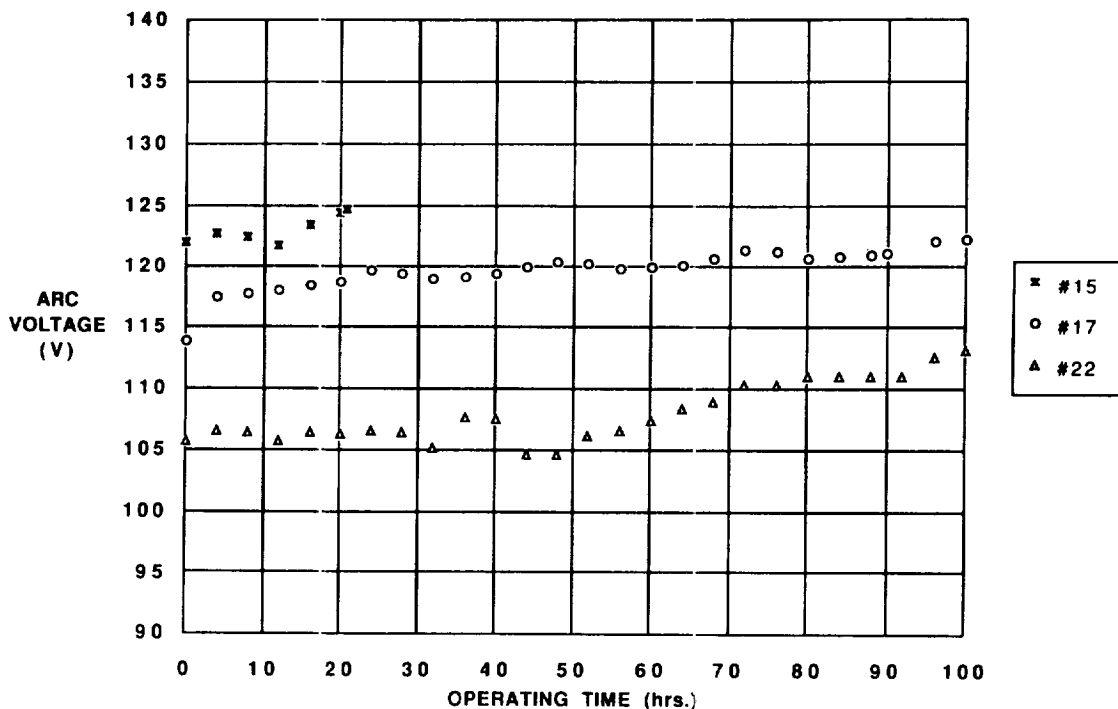


Figure 6-6. Voltage vs. time (filtered power tests).

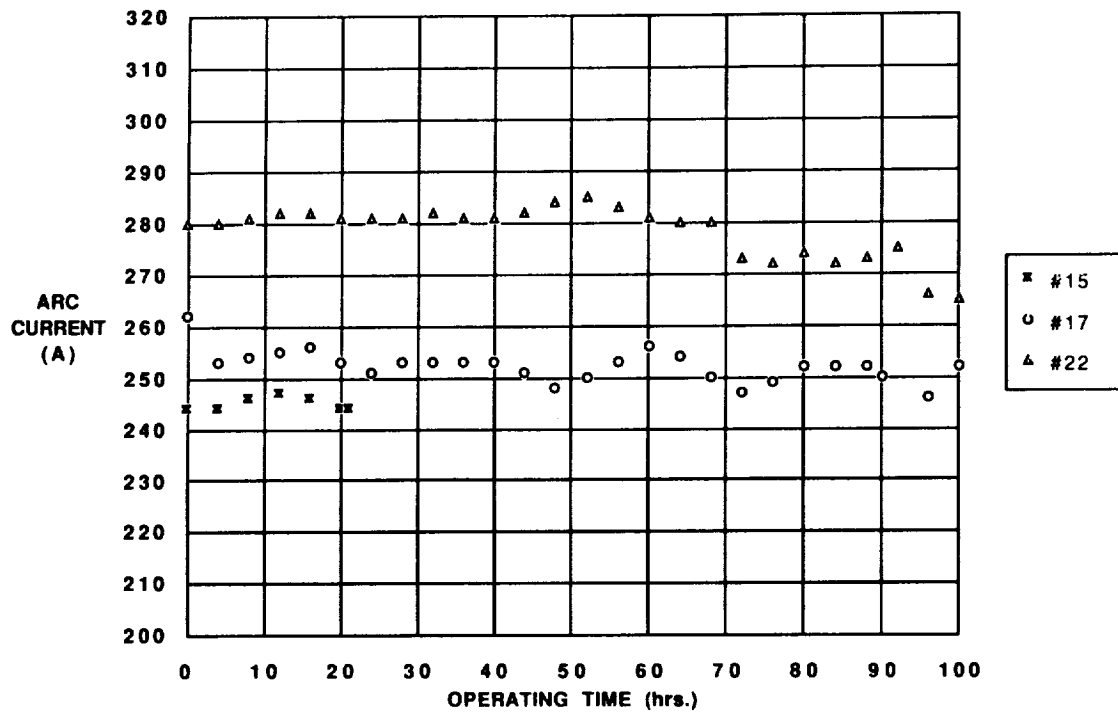


Figure 6-7. Current vs. time (filtered power tests).

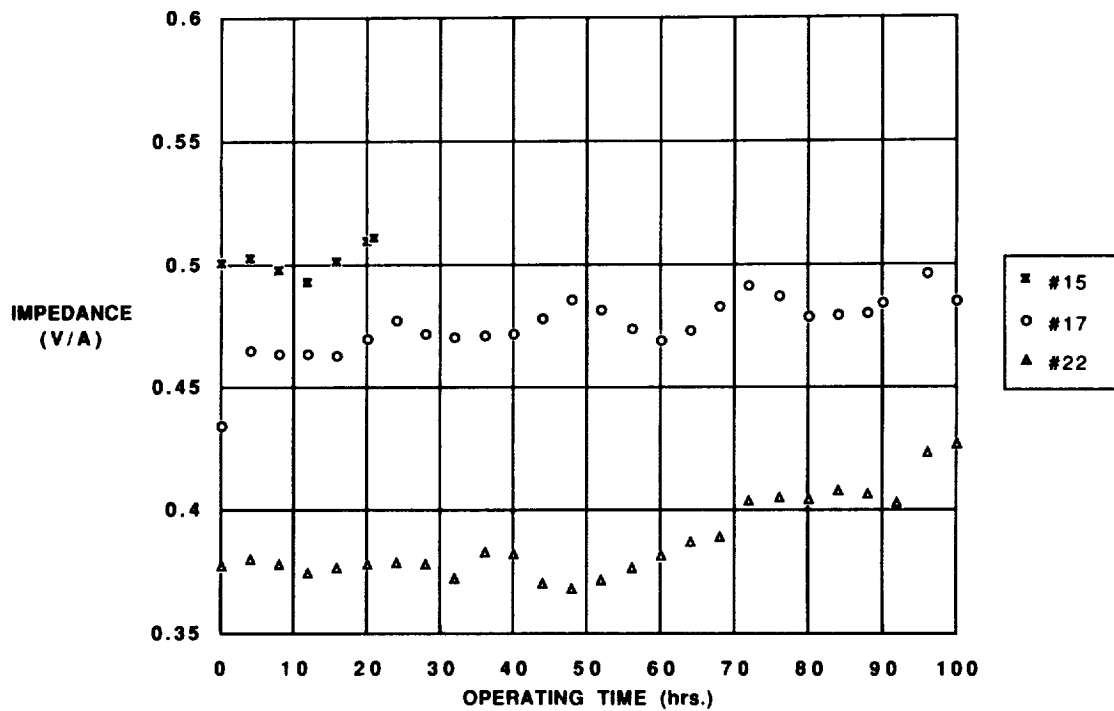


Figure 6-8. Impedance vs. time (filtered power tests).

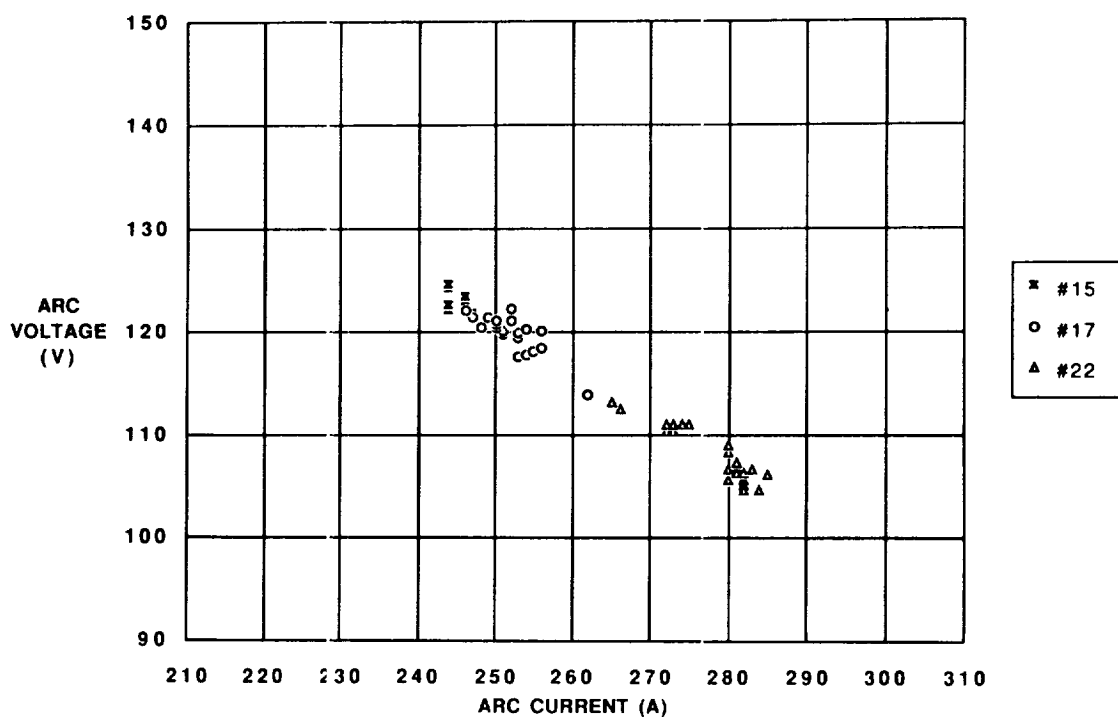


Figure 6-9. V-I characteristic (filtered power tests).

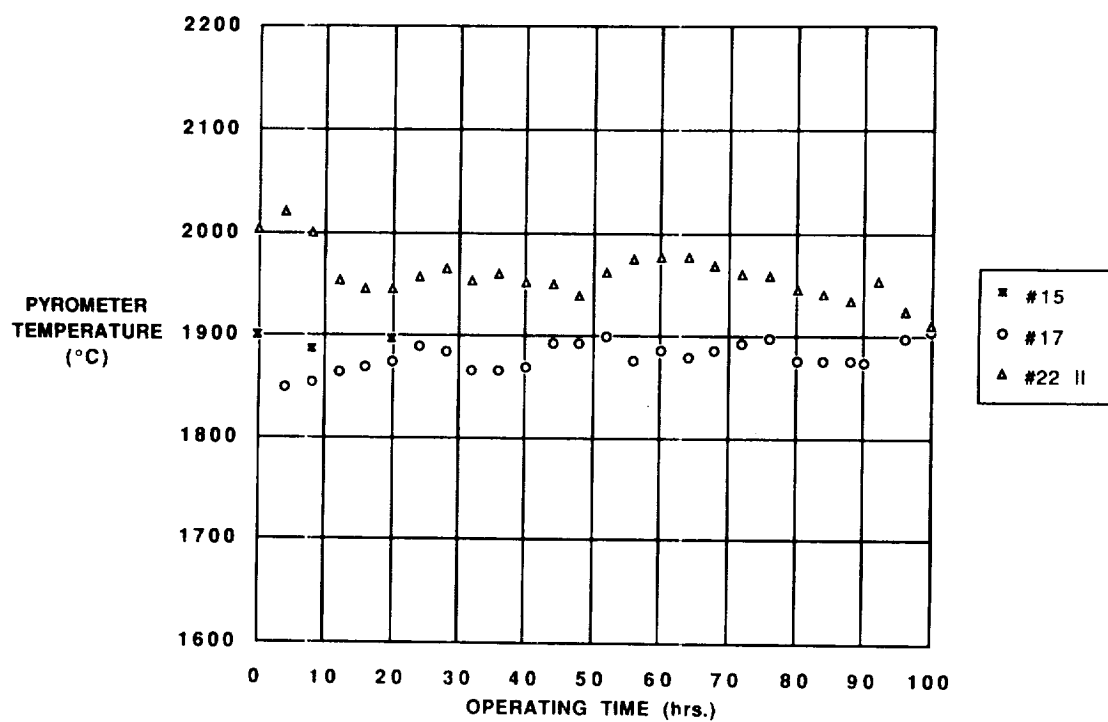


Figure 6-10. Nozzle brightness temperature (filtered power tests).

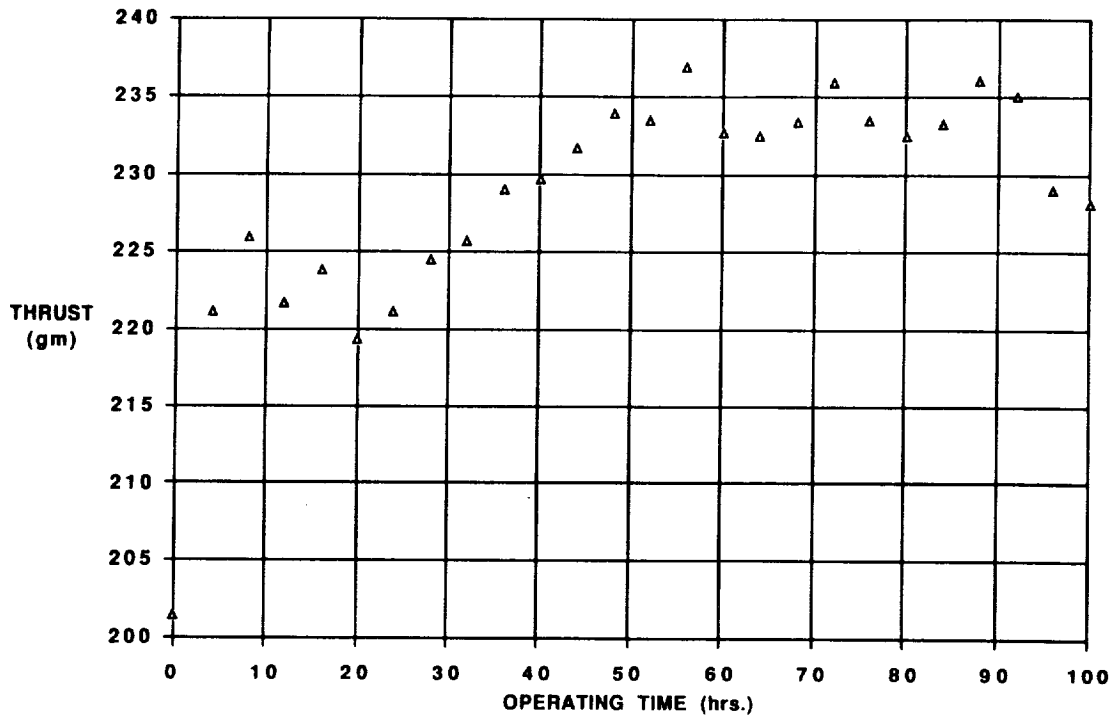


Figure 6-11. Thrust vs. time (filtered power tests).
(Cathode 22 data only.)

6.3 LONG-TERM TESTS (WITH FILTERED POWER)

Two long-endurance runs were conducted using the D-1E engine design. In both cases the input power to the engine was filtered to limit current ripple to 0.2 percent. Cathodes 20 and 25, both flat faced, were used for these tests (see Table 6-1). Cathode 25 also had rounded shoulders to blend smoothly into the cylindrical portion of the cathode. Cathode 20 was operated at a nominal power of 30 kW and a mass flow of 0.31 g/s of ammonia, for an accumulated time of 413 hours. Cathode 25 was operated at a nominal power of 30 kW and an ammonia mass flow of 0.34 g/s for 252 hours.

6.3.1 Test Events

The events that occurred during each test are summarized in Fig. 6-15. Event 1 is the initial engine start in both cases.

6.3.1.1 413-Hour Test. The engine, with Cathode 20 installed, was turned on and powered up to 24.7 kW when it became obvious that the engine had a propellant leak. The engine was turned off, allowed to cool and then removed from the vacuum facility and disassembled. It was found that the main gaskets were over-compressed, causing the insulator to crack across the bearing surface. A new insulator was made and the engine was reassembled with new gaskets. The engine was restarted (Event 2) two days later. All facility and engine parameters were nominal.

After 27 hours and 56 minutes of operating time at nominally 30 kW, the engine was voluntarily shut down (Event 3). In the 1-1/2 hours before the shutdown, the propellant flow had decayed from 0.31 g/s to 0.28 g/s. It was found that the valve seats in the ammonia flow controller were replaced with the wrong material by the vendor when it was overhauled and calibrated prior to the start of the test. The flow controller was repaired and the test restarted 6 days later (Event 4). The engine was at 30 kW for 19 minutes and was shut off again due to an apparent propellant leak. The gaskets were again found to be over-compressed which caused a crack in the insulator. The insulator was remade and the engine reassembled. Care was taken to make sure the bearing areas on both sides of the insulator were identical. The test was restarted 7 days later (Event 5). All facility and engine parameters were nominal.

After another 51 hours and 25 minutes of operating time at the 30-kW operating point the engine was again voluntarily shut down (Event 6). This was done because one of the four V-belts on the last stage of the vacuum pumping system began to fray. Before the start of the test all of the belts on the pumps were inspected and found to be in good condition. The engine was without power for a total of 18 minutes while the belts were changed. The pumps were reactivated and the test was immediately restarted. The engine was back at the nominal operating point within 40 minutes from the time the shutdown began.

Following the belt change, the engine operated for 333 hours and 25 minutes without interruption (the longest recorded uninterrupted operated time for an ammonia propellant arcjet at 30 kW). At Events 7, 8 and 9 (see Fig. 6-12) the power was adjusted down to maintain the average operating condition close to the nominal 30-kW point. At Event 7 the engine was powered down from 30.8 kW to 30.15 kW. At Event 8 the power was reduced from 31.5 kW to 30.1 kW. At Event 9 the power was reduced from 30.43 kW to 30.07 kW.

During the test the voltage exhibited a generally linear increase with time, while the thrust was decaying linearly with time. It was decided that after reaching 400 hours of operating time, the engine would be shut down to investigate the causes of these two trends (Event 10). It was believed that the thrust decay was due to evaporation of the mercury in the pots, reducing the buoyant force on the coaxial current feeds. A reduction in the buoyant force would allow the engine to sag forward on the thrust stand and would be manifested as a reduction in the indicated thrust. After the engine was shut down and allowed to cool, the vacuum facility was opened up and the engine removed. The mercury levels in the pots were found to have dropped to about half the original levels, thus explaining the steady drop in thrust.

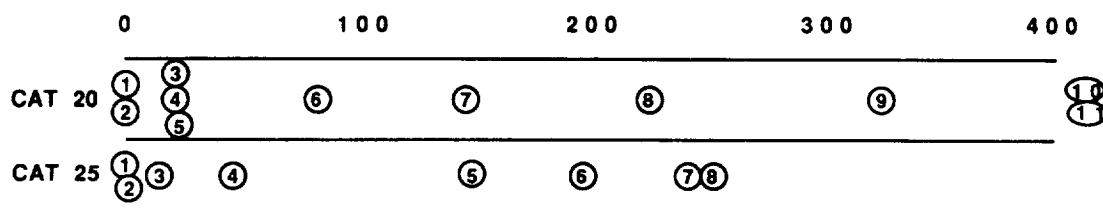


Figure 6-12. Long-term test timeline.

The arc voltage increase is believed to be due to the formation of a crater in the cathode tip. In order to check the depth of the crater, a 0.50 cm diameter pointed depth gauge was dropped into the constrictor. The centerline of the cathode was found to have receded 0.58 cm. A depression of this depth increased the geometric arc length by about 40 percent. Such an arc length increase should explain the voltage increase. However, in the 1986 endurance test (Refs. 82, 84 and 85) (baseline cathode, conical nozzle) the centerline of the cathode recessed about 0.74 cm over 573 hours of operation and the voltage increased only a total of about 11 V.

At this point, the decision was made to continue the test without disassembling the engine because the last shut down was voluntary and was not induced by an engine failure. The mercury pots were refilled and the engine was reinstalled in the vacuum facility. Event 11 in Fig. 6-13 marks the restarts of the engine. The engine was restarted 8 times and operated on ammonia but "extinguished" in each case: during these starts, the arc voltage would steadily increase to above 170 V, at which point the engine would extinguish. Engine operation would also extinguish whenever the arc current dropped below 168 A. It was determined that the propellant flow controller was allowing excessive flow rates, causing the plenum pressure to be a factor of 3 higher than normal. Subsequent testing showed that the flow controller was malfunctioning and causing the excessive flow rates. The excessive flow rates may have "pulled" the arc off the cathode tip by "pushing" the nozzle attachment point downstream toward the nozzle outlet. This could increase the arc length beyond what the propellant gas could support and extinguish the arc.

6.3.1.2 252-Hour Test. The times at which the major events occurred during the test are shown on Fig. 6-12. Event 1 is the initial start of the test: the engine operating point was set at 249 A and 120 V (about 29.8 kW) about 20 minutes after activating the run supply. The mass flow was increased to 0.34 g/s from 0.31 g/s in an effort to increase the engine operating margin 15 minutes later at event 2. At Event 3 (14 hours, 29 minutes after start) the power was adjusted up 0.5 kW to 29.9 kW. At Event 4 (48 hours, 36 minutes after start) the power was adjusted down 0.25 kW to 30.1 kW. At Event 5 (146 hours, 44 minutes after start) the power was adjusted down 0.8 kW to 30.3 kW.

Event 6 occurred approximately 194 hours into the test; the voltage ripple (oscilloscope) showed a change in character from one 10 V spike per trigger to multiple 20-30 V spikes and other noise. Event 7 began at 247 hours, 30 minutes of operating time: the current rose from 214 A to 223 A in a 3-minute period, voltage dropped 12.6 V and power dropped from 30.6 kW to 29.0 kW. The nozzle brightness temperature also dropped about 130 °C. The downstream view of the engine showed that the constrictor changed shape over an 8-hour, 25-minute period due to erosion. A black line extended from the constrictor to the outer edge of the nozzle which looked like a crack (but was later determined to be a tungsten track extending from the constrictor and not a crack). The power continued to drop from that point (probably due to facility effects; i.e., local power grid usage). Engine operation was voluntarily terminated after 252 hours and 20 minutes of continuous operation to examine the nozzle (Event 8).

6.3.2 Performance

The engine voltage, current, and impedance are shown in Figs. 6-13 through 6-15, respectively, as a function of accumulated test time for both the 413- and 252-hour tests. A data point is shown every 4 hours. Except for the end of the 252-hour test, the voltage for each test shows a generally increasing trend. The behavior of the engine V-I operating point is shown in Fig. 6-16 for each test. The nozzle brightness temperature is shown in Fig. 6-17.

The engine thrust for the 252-hour test is shown in Fig. 6-18 as a function of accumulated test time. The data are shown at 4-hour intervals and were subjected to the same corrections as the data above. Data for the Cathode 25 test are accurate. Mercury evaporation caused the thrust data for Cathode 20 to be unreliable.

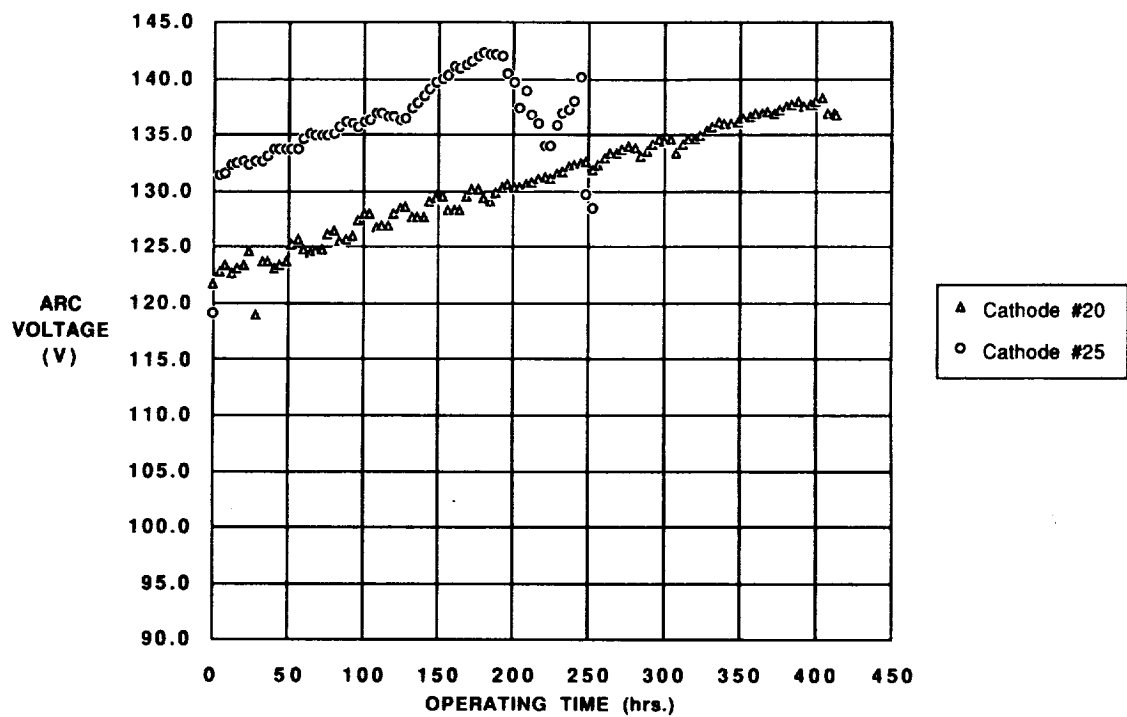


Figure 6-13. Voltage vs. time (long-term tests).

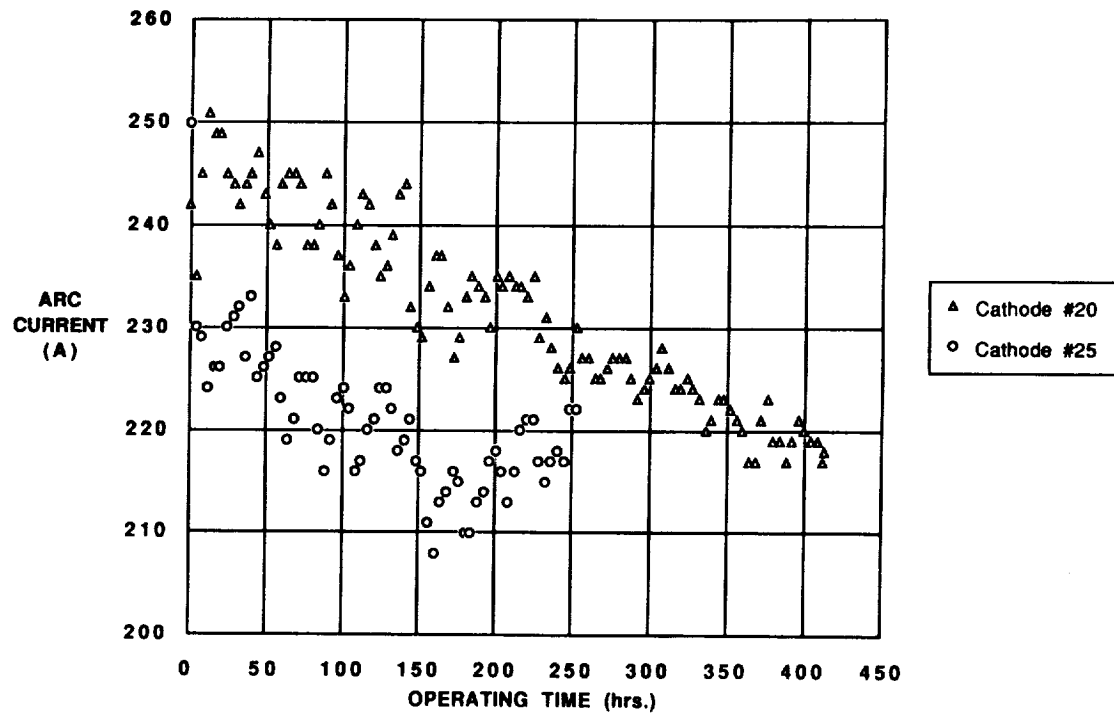


Figure 6-14. Current vs. time (long-term test).

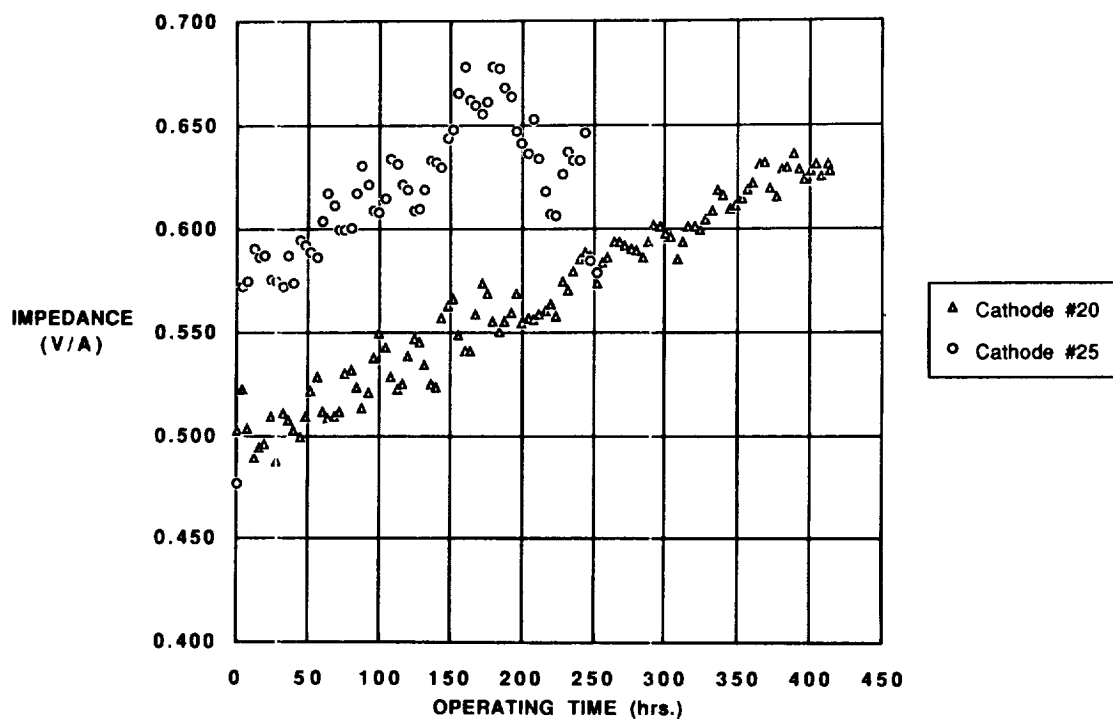


Figure 6-15. Impedance vs. time (long-term tests).

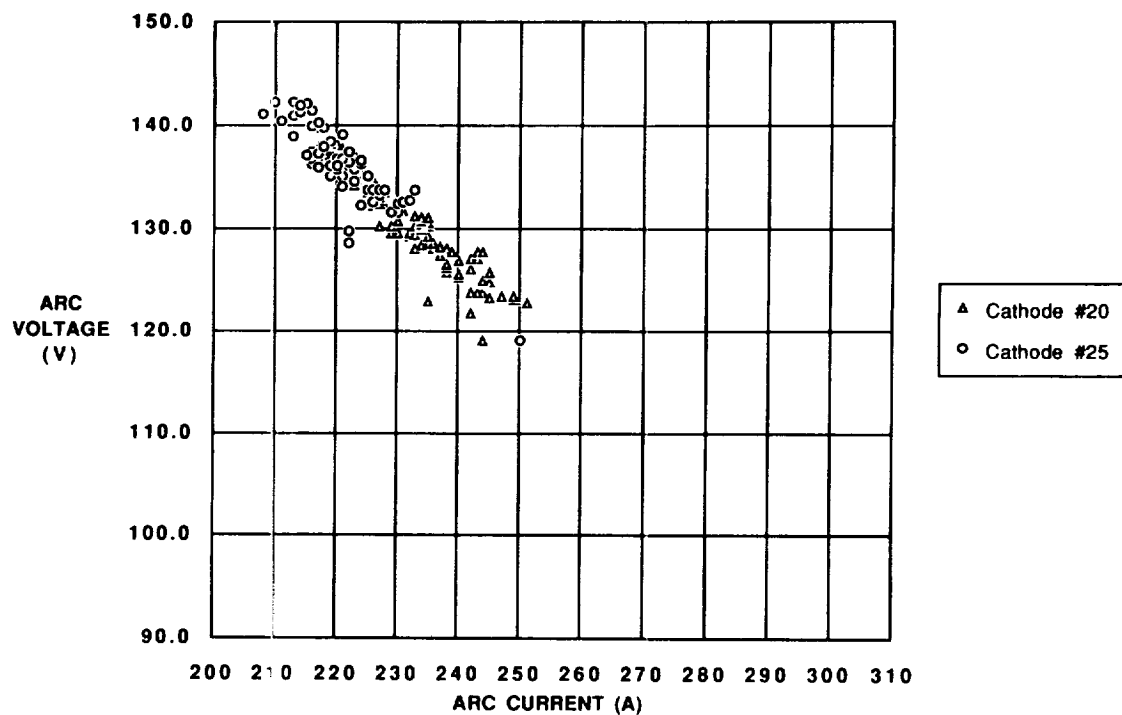


Figure 6-16. V-I characteristic (long-term tests).

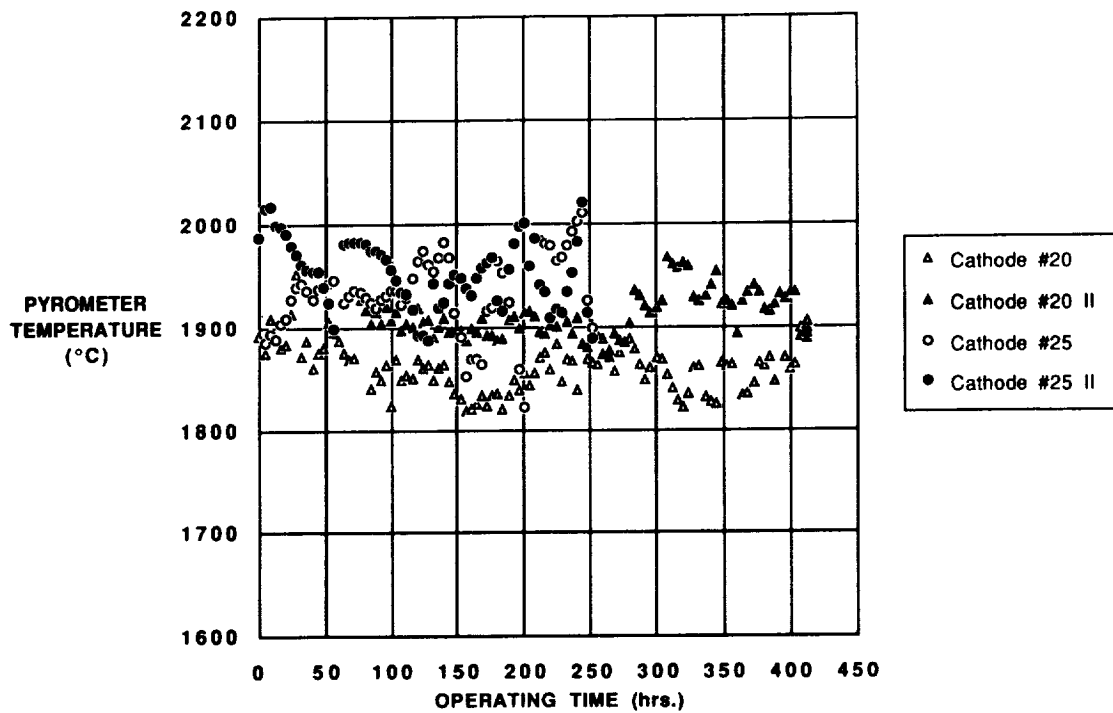


Figure 6-17. Nozzle brightness temperature (long-term tests).

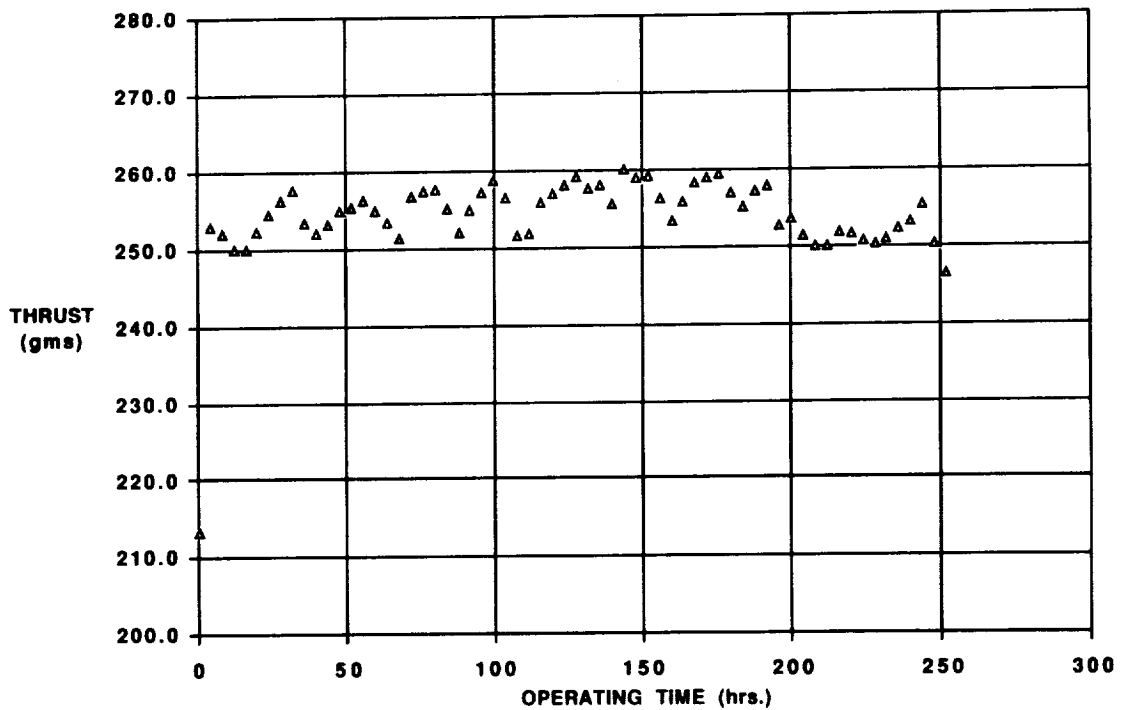


Figure 6-18. Thrust vs. time (long-term test).
(Cathode 25 data only.)

7.0

DISCUSSION OF ENDURANCE TEST RESULTS

The preliminary results from a series of 30-kW arcjet endurance runs were summarized in Fig. 7-1. Five 100-hour tests, a 413-hour test, a 252-hour test, and several shorter tests were conducted. Cathode material mass loss rates ranged from 1.4 mg/hr to 6.2 mg/hr. Figure 7-1 shows the variation of voltage. There was a general upward trend in the voltage (reduction in current) during each of the tests. A 24-hour variation resulted from day/night variations in temperature and local area power grid loads.

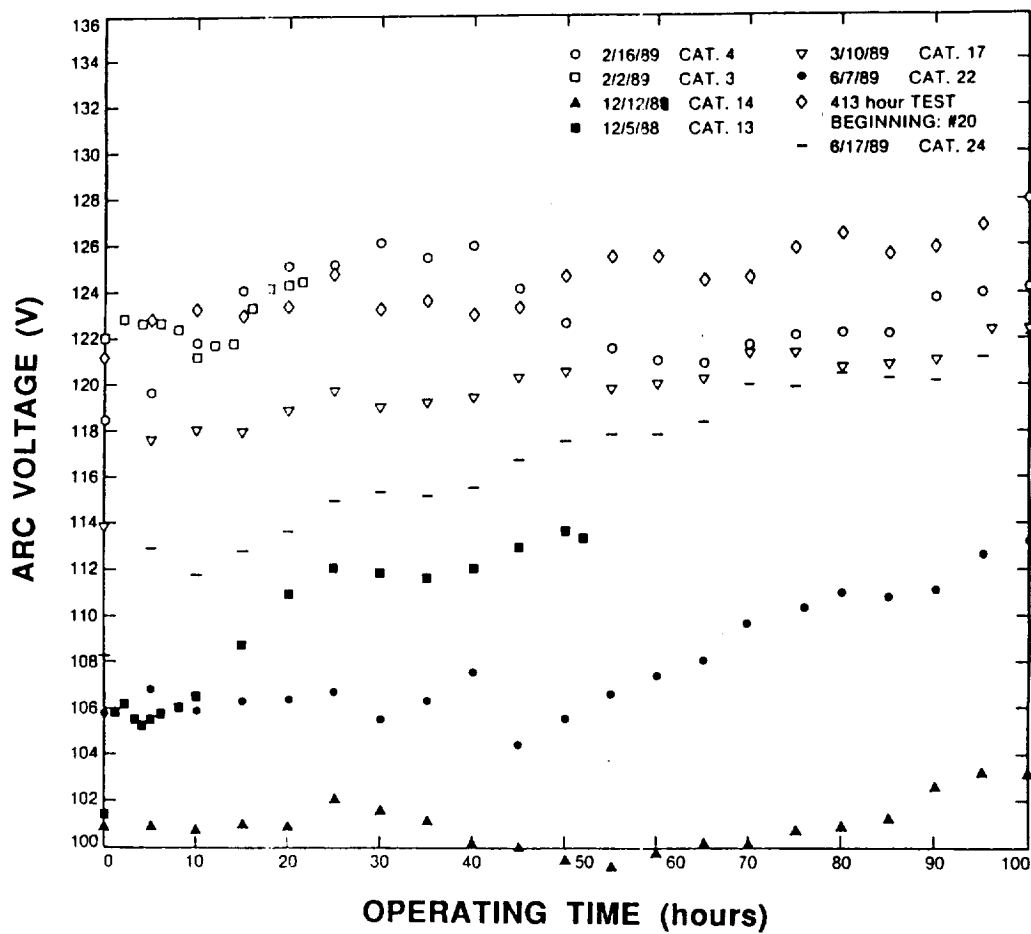


Figure 7-1. Arc voltage variations over 100 hours.

7.1

EFFECT OF ELECTRICAL FILTERING

There has been speculation that the ripple on the power input to the arcjet can influence whisker growth on the cathode tip. A series of 100-hour endurance tests at nominal power levels of 30 kW, with and without a capacitance-inductance filter (L-C filter), was conducted to examine this issue. A description of the filter and its location in the test facility are given in Section 2-4. The results from this series of tests are described below.

As can be seen from Table 6-1, whiskers were evident in almost every case, filtered or unfiltered. The column "whisker growth" in Table 6-1 refers to macroscopic whiskers which can be seen without magnification. Scanning electron micrographs will be made of each cathode tip to look for microscopic whiskers similar to those found on the tip of the cathode used in the endurance test of the baseline engine.^{5,6,7}

The tips of cathodes 22 and 24 are shown in Fig. 7-2 after 100 hours of operation at 30 kW. The average erosion rates for Cathodes 22 and 24 were 3.1 mg/hr and 3.3 mg/hr, respectively, and agree within the uncertainties for the mass loss measurements. Both cathodes started with a 60° included angle cone that ended in a 0.15 cm radiused tip. Cathode 22 was run using the L-C filter, while Cathode 24 was operated without filtering. As a result, Cathode 24 saw a current ripple which was about 15 times higher in magnitude than Cathode 22, as can be seen in Fig. 7-3. In both cases the whiskers were approximately the same size and density. This implies that within the bounds of the test facilities, reducing the current ripple by a factor of 15 does not eliminate whisker growth for the baseline cathode shape.

No macroscopic whiskers were evident on Cathodes 17 and 20 (both flat face) after 100 hours and 28 hours of operation, respectively. A view of the tip of Cathode 17 is shown in Fig. 7-4 after 100 hours of operation at 30 kW using filtered input power. This cathode geometry also exhibited the lowest mass loss rate of those tested over 100 hours of operation.

The tip of Cathode 4 (reduced radius) is shown in Fig. 7-5 after 100 hours of operation on unfiltered input power. There are no macroscopic whiskers evident on the cathode tip like those shown in Fig. 7-2. However, there is some structure on the edge of the eroded region that could be "roots" of whiskers. It is interesting to note that the eroded region has a slightly dished appearance and is not an inverted hemisphere as it is with the other tip geometries.

A cathode that had a dimple premachined into the tip, Cathode 15, was also run. This cathode exhibited the highest mass loss rate, 6.2 mg/hr, of those tested. In addition, the rim of the crater exhibited well-defined thick whisker structures after only 21 hours of operation at 30 kW using filtered input power (Fig. 7-6). This suggests that whisker growth is driven by the formation of a cathode tip crater.

ORIGINAL PAGE
BLACK AND WHITE PHOTOGRAPH

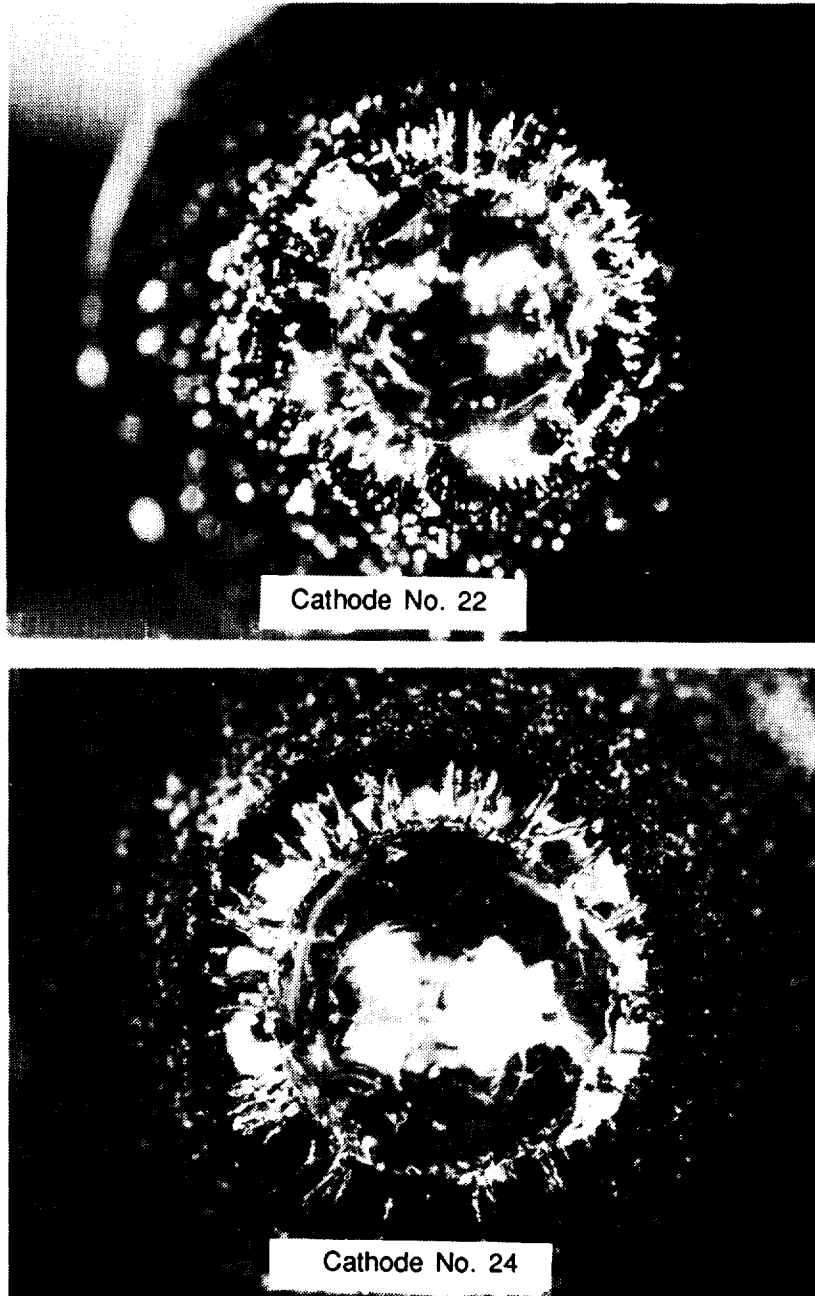
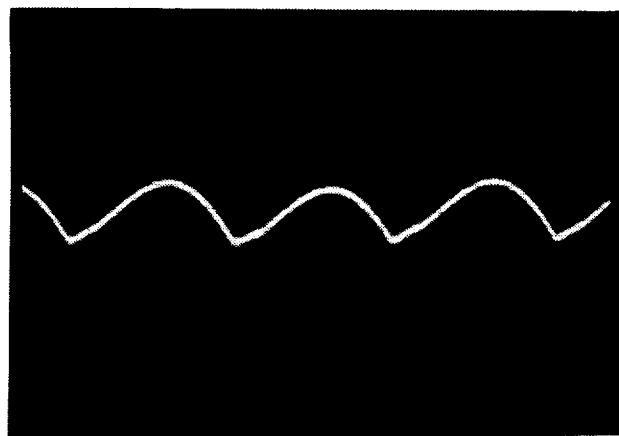
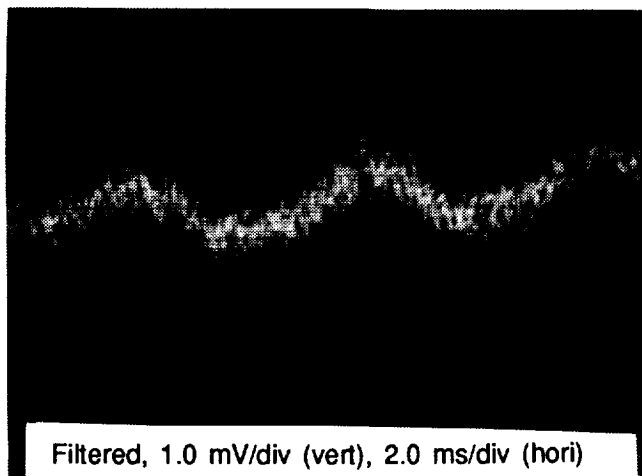


Figure 7-2. Tips of Cathodes 22 and 24 after 100 hours of operation.

ORIGINAL PAGE
BLACK AND WHITE PHOTOGRAPH



Unfiltered, 20.0 mV/div (vert), 2.0 ms/div (hori)



Filtered, 1.0 mV/div (vert), 2.0 ms/div (hori)

Figure 7-3. Filtered and unfiltered current ripple.

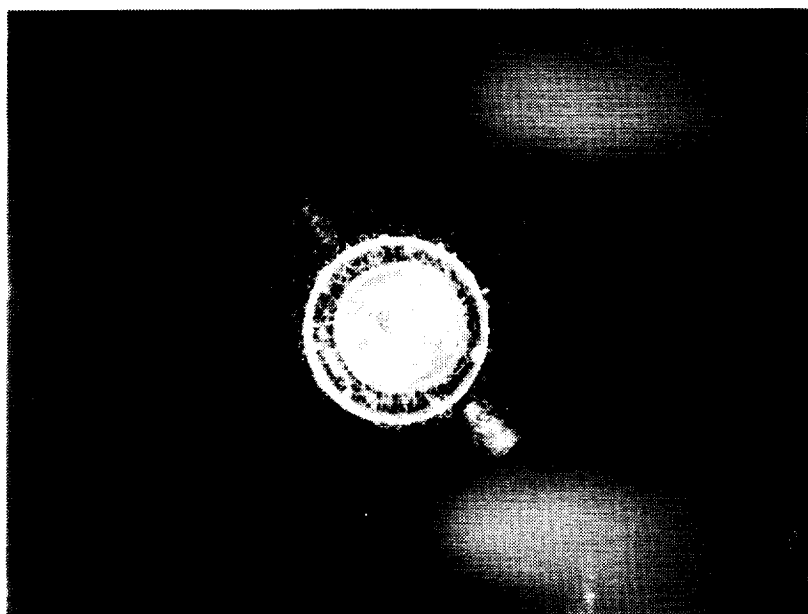


Figure 7-4. Tip of flat-face Cathode 17 after 100 hours of operation.

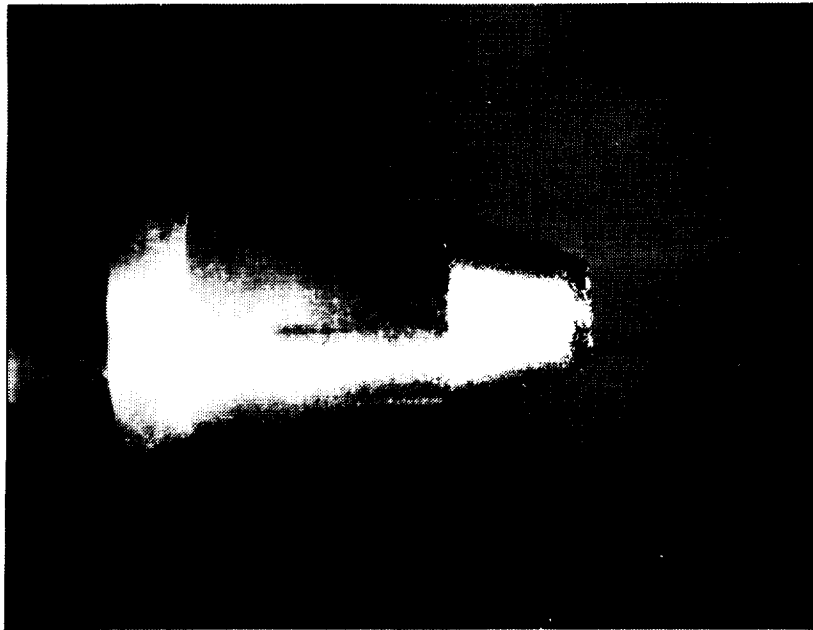


Figure 7-5. Tip of Cathode 4 after 100 hours of operation.

ORIGINAL PAGE
BLACK AND WHITE PHOTOGRAPH

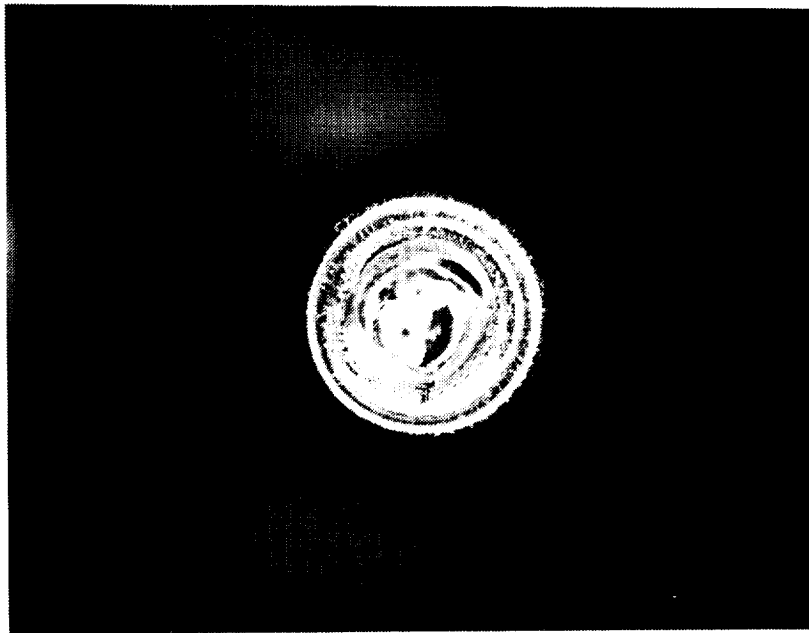


Figure 7-6. Tip of Cathode 15 after 21 hours of operation.

7.2

413-HOUR ENDURANCE TEST

Based on the results of the first series of 100-hour tests (Cathodes 4, 13, 14, 15 and 17) the flat-face cathode geometry was selected for use in a longer duration electrode erosion characterization test. This test was run for 413 hours and 13 minutes at the nominal 30-kW operating point before it was voluntarily terminated. The results of this test were summarized in Figs. 6-13 through 6-18. During the test, data were recorded every two minutes.

7.2.1

Electrical Characteristics

The engine arc voltage was shown in Fig. 6-13 as a function of time over the entire 413-hour test. These figures show that the engine voltage was increasing in a generally linear fashion with time. The voltage was 121.5 V at the start of the test, 136.8 V at the end of the test and reached a maximum value of 138.1 V about 15 hours before the test was terminated. The voltage change over 413 hours was 16.6 V using the maximum value as the upper limit, or about 4.1 V for 100 hours.

Since the arc voltage was increasing in time during the test, the engine operating point on a voltage-current (V-I) curve must also have changed. Figure 6-16 shows how the engine V-I operating point changed in time. While the time scale is not explicitly marked due to the scatter in the data (see Power section below) the points generally fall along a straight line with a slope of -0.5 V/A .

The engine operating power is shown over the 413-hour test duration in Fig. 7-7. During the course of the test the power varied from 29.4 kW to 31.4 kW, with an average value of approximately 30.3 kW. The large variation in operating power can be attributed to the effects of day/night temperature cycles on the power supply and day/night local area power grid load cycles. The highest power operation always occurred at night, usually between 11 P.M. and 6 A.M., when both power demands and the air temperatures are lowest. The lowest power operating points occurred in the early to mid-afternoon. The power fluctuations resulted primarily from variations in arc current of up to 12 A from day to night, with much smaller voltage variations.

The difference in voltage behavior between this 413-hour test and the previous 573-hour test may be related to the nozzle shape. The bell-shaped nozzle used in the D-1E engine opens rapidly at the constrictor outlet while the conical nozzle diverges much more slowly. This implies that the fluid flow properties in the conical nozzle change more slowly than with the bell-shaped nozzle. Since the arc attachment region in the nozzle is governed, in part, by local gas density, the conical nozzle may provide a broader low-density region for arc attachment to occur. As the cathode tip recedes, the arc attachment in the nozzle could also move upstream in the nozzle toward the constrictor outlet, minimizing the total voltage change. In the bell nozzle the rapid divergence could lock the attachment region in place.

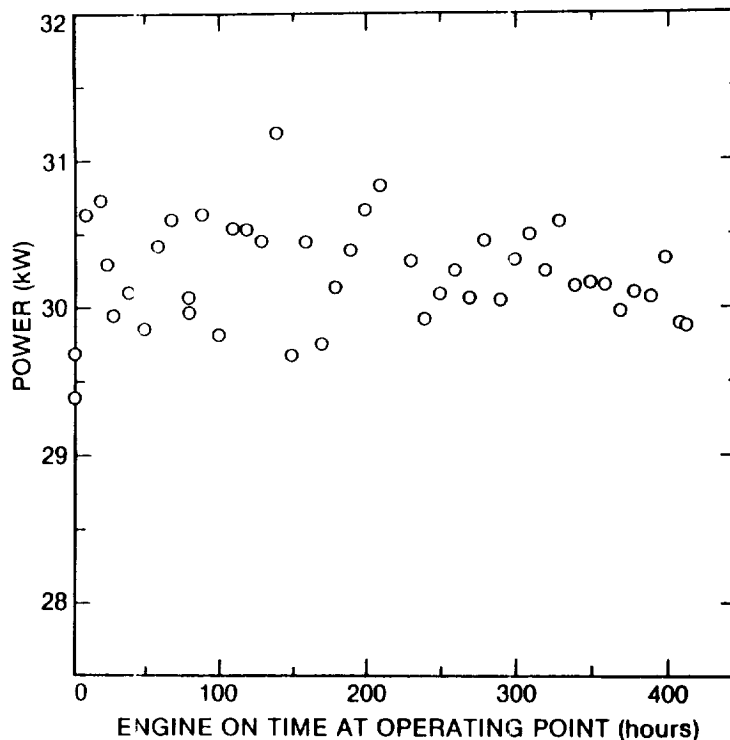


Figure 7-7. Operating power as a function of time (413-hour test).

7.2.2 Performance

As noted in Section 6.3.2, the engine thrust as a function of time for this test is not shown due to inaccuracy introduced by the evaporation of mercury from the feed pots.

7.2.3 Component Conditions

A photograph of the D-1E engine is shown in Fig. 7-8 after 413 hours and 5 minutes of operation at 30 kW. The engine is shown with the thrust stand mounting bracket and coaxial current feeds attached. This is the configuration in which the engine was removed from the thrust stand after 413 hours and 5 minutes of operation at 30 kW and was reattached after the mercury pots were refilled. As can be seen in Fig. 7-8, the ZrB_2 high-emissivity coating had partially evaporated on the top of the nozzle along the front edge. This material loss is due to a facility view factor problem. The top of the nozzle is in close proximity (2 - 3 cm) to a windage shield on the bottom of the thrust stand. The space between the nozzle surface and other facility components is at least 30 cm on the other sides of the nozzle. As a result, heat radiated up by the nozzle is reflected directly back down onto the top of the nozzle greatly increasing the heat load on the top of the nozzle. The increased heat load may cause the coating to evaporate. The thickness of the coating on the rest of the nozzle remained unchanged.

7.2.3.1 Cathode. The cathode used for the endurance test (Number 20) is shown in Fig. 7-9 after 413 hours of operation at 30 kW including 8 restart attempts. The restart attempts destroyed any fine whisker structure that may have been present; from the irregular surface structure it is surmised that whiskers were present during engine operation. This means that reducing the current ripple to about 0.2 percent does not eliminate whisker growth on flat-face cathodes over long-term operation. The cathode lost 2.16 g of tungsten over 413 hours of operation, corresponding to an average mass loss rate of 5.2 mg/hr. (The 1986, 25-kW duration test cathode had a mass loss rate of 3.5 mg/hr over 573 hours.)

The arcjet facility in which these tests were conducted provides a view of the operating engine axially up the nozzle so that the cathode tip, constrictor and interior nozzle surface can be seen. A window located on the back wall of the chamber and another window on the elbow of the diffuser enable this view. During the first 75 hours of the test there was a very bright (white) spot about 1.5 mm in diameter on the center of the cathode tip (constrictor diameter is 5.0 mm). The region around this spot was uniform in color and brightness. Over the next 75 hours this spot grew to about 2.3 mm in diameter. The bright spot on the cathode tip remained this size for about the next 150 hours. However, the dark region around the spot was no longer uniform in color; it was marked with small bright areas and several very dark regions which appeared as dark spokes. These bright and dark areas appeared to vary slowly with time over tens of hours. Over the last 100 hours of the test the bright spot grew in diameter and the region around the cathode spot got smaller. During the last few tens-of-hours of the test, the area around the spot became uniform in color and brightness again.

The structure around the bright spot may have been associated with the formation of whiskers. These "whiskers" did not become evident until after about 150 hours of engine operation. This is consistent with the fact that no macroscopic whiskers were found on Cathode 17 after 100 hours of operation. It also appears that the crater was starting to grow in diameter after approximately 75 hours. The crater could increase in diameter if the arc attachment moved from the center of the tip depression up to the rim and then back down to the bottom again. If the cathode arc attachment moved from the center of the tip depression to the rim, the arc length would decrease and lead to a sudden drop in voltage. In examining Fig. 6-13, it can be seen that at 250 hours, 305 hours and 405 hours, for instance, the voltage dropped suddenly. After the test was terminated, the cathode tip crater was found to be slightly larger in diameter than the constrictor. The diameter of the crater on Cathode 17 was about 2.0 mm. These data imply that the width of the crater grows as the crater gets deeper. It appears that the structure around the cathode spot was lost from view because the crater grew larger in diameter than the constrictor.

ORIGINAL PAGE
BLACK AND WHITE PHOTOGRAPH

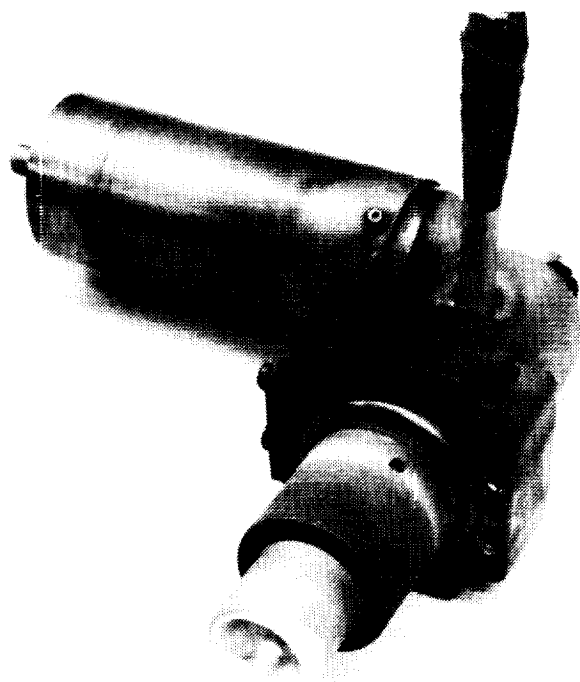


Figure 7-8. D-1E arcjet after 413 hours at 30 kW.



Figure 7-9. Cathode after 413 hours of operation and 8 restart attempts.

7.2.3.2 Nozzle. As can be seen in Fig. 7-10, the nozzle is in excellent shape after 413 hours of operation. There is no apparent erosion of the downstream end of the constrictor as was the case in the 1986 endurance test, (Refs. 82, 84 and 85) even though the engine operated at a power level which was about 20 percent higher. There does appear to be some deposited material on the downstream end of the nozzle, which is believed to be tungsten from the cathode tip. Other than the coating loss on the top of the nozzle (a facility-related viewing problem), there are no signs of overheating or unusual wear on the nozzle or constrictor. The D-1E engine thermal design appears to provide more margin for high power operation than previous engine designs and demonstrates that improved design can eliminate the nozzle wear problem.

7.2.3.3 Injector. The injector is shown in Fig. 7-11 after 413 hours of operation at 30 kW. The injector is in very good condition. The propellant injection ports are still the original size, and the top surface of the injector has not changed shape as was the case in the 1986 endurance test,^{82,84,85} even though the operating power was 20 percent higher. The top surface has a black deposit which was found in previous tests to be primarily tungsten.^{82,84,85} The D-1E injector is subjected to a smaller heat load since it is about 1 cm further back in the plenum chamber (further from the arc) than in the 1986 duration test. Improved design appears to have eliminated the injector wear problem.

ORIGINAL PAGE
BLACK AND WHITE PHOTOGRAPH

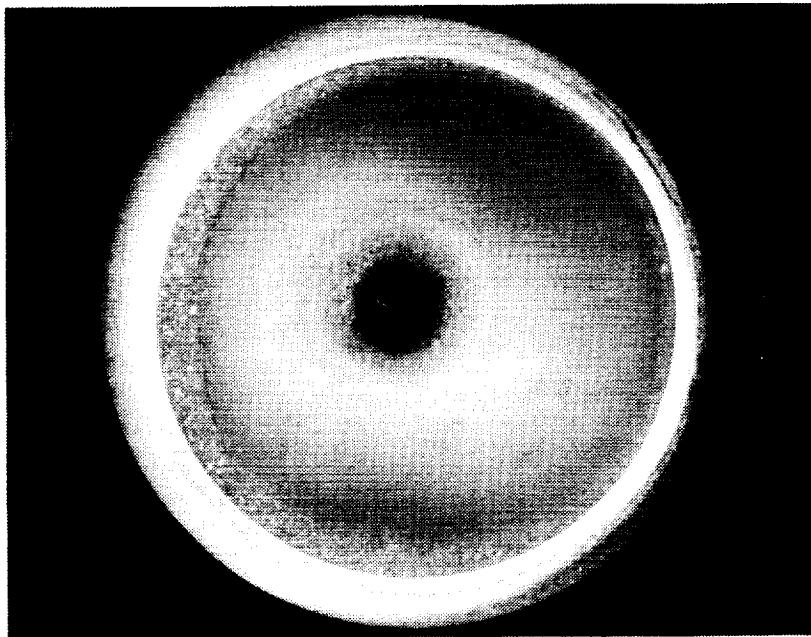


Figure 7-10. Nozzle after 413 hours of operation at 30 kW.

ORIGINAL PAGE
BLACK AND WHITE PHOTOGRAPH

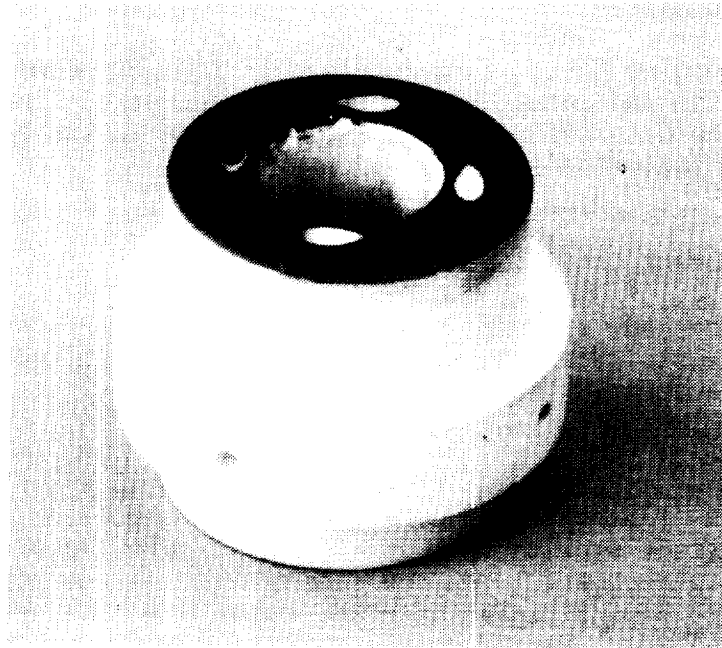


Figure 7-11. Injector after 413 hours of operation at 30 kW.

7.3 252-HOUR ENDURANCE TEST

A modified flat-face cathode was designed for the second long-duration electrode erosion characterization test. The 50° angle of the sides of the tip of the flat-face cathode used in the 413-hour run parallel the downstream taper of the plenum chamber wall. It was decided that this angle was not steep enough since the whiskers that grew from the erosion of the front face must have nearly bridged the distance between the cathode tip and the plenum chamber wall. To avoid this possible problem during the second test, the angled section was rounded to blend smoothly into the body of the cathode, in order to increase the distance between the sides of the cathode tip and the plenum chamber wall. It was also decided to increase the mass flow rate from 0.31 g/s to 0.34 g/s to further increase the engine operating temperature margin. The cooling lines to the Hg pots were flushed prior to the test; during the test the temperature of the cooling lines was 6 °C cooler than during the 413-hour test.

7.3.1 Electrical Characteristics

The engine arc voltage is shown in Fig. 6-13 as a function of time over the entire 252-hour test. The engine voltage increased linearly to about 142 V at 195 hours. The voltage then decreased during the next 29 hours to 134 V. The voltage increased again over the next 23 hours to 143 V. The last two data points shown are after Event 5, when the voltage suddenly dropped to 130 V.

7.3.2 Performance

The engine thrust as a function of time is shown in Fig. 6-18. As can be seen, the indicated thrust generally decreased linearly with time. The scatter in the data can generally be attributed to the current fluctuations, as indicated in Fig. 7-12.

7.3.3 Component Conditions

The cathode and nozzle showed significant erosion and asymmetric wear during this test. The wear is believed to have resulted from excessive arc length reattachment. The injector showed no wear.

7.3.3.1 Cathode. Cathode 25 is shown in Fig. 7-13 after 252 hours of operation at 30 kW (one start). Over the operating period, the cathode lost 1.03 g for an average erosion rate of 4.1 mg/hr. The tip of the cathode shows asymmetric attachment. On the side of the cathode tip opposite where the arc appears to have attached near the end of the test are large protruding whiskers.

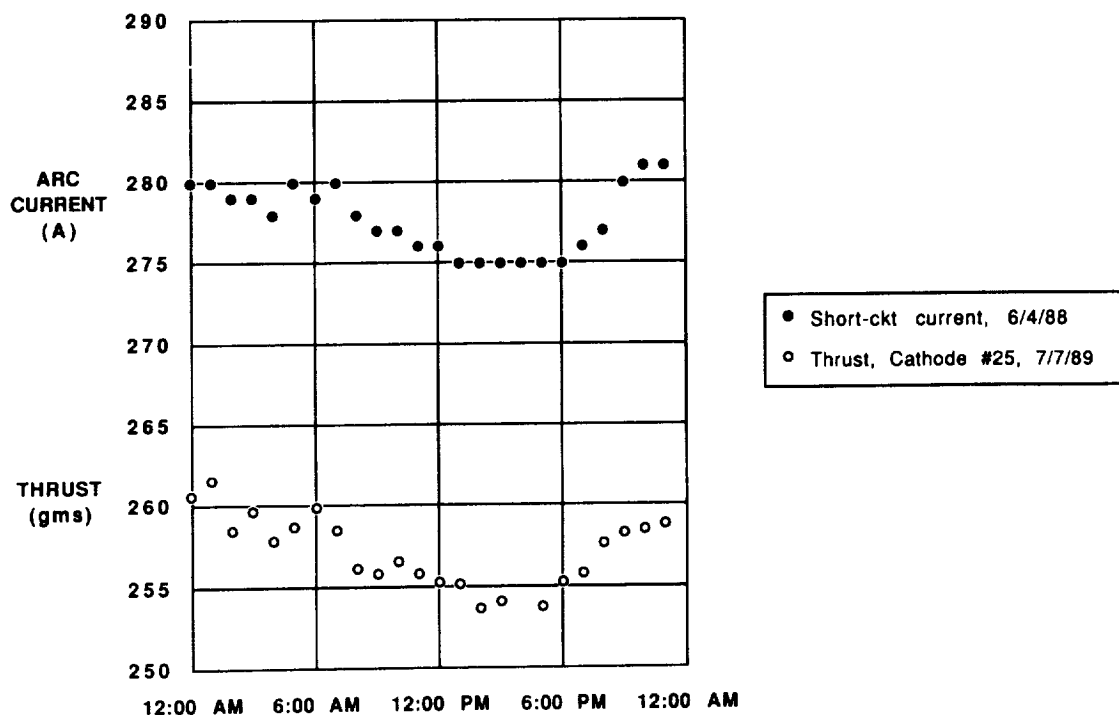


Figure 7-12. Thrust-current correlation over 24 hours.

ORIGINAL PAGE
BLACK AND WHITE PHOTOGRAPH

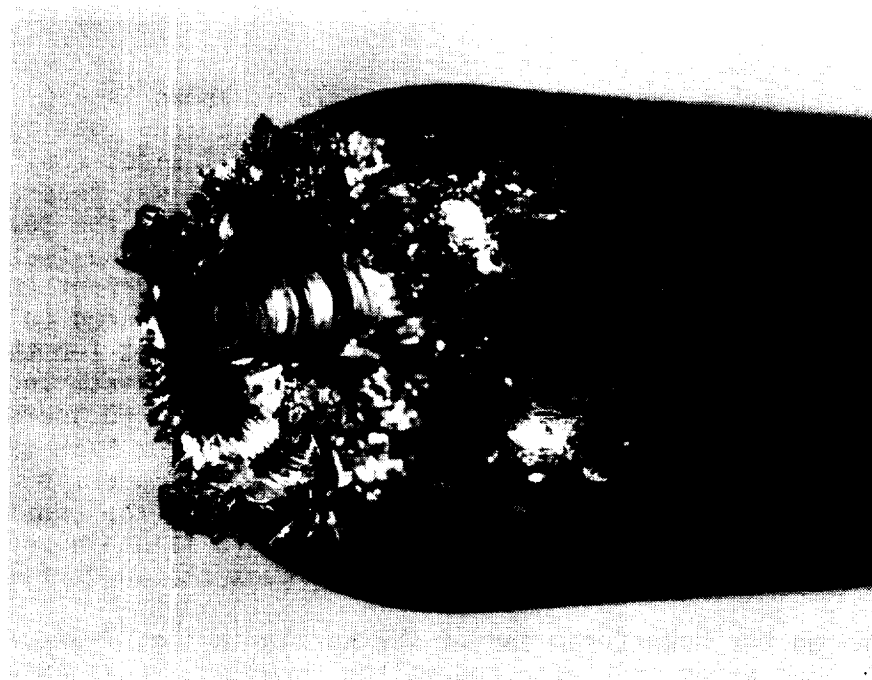
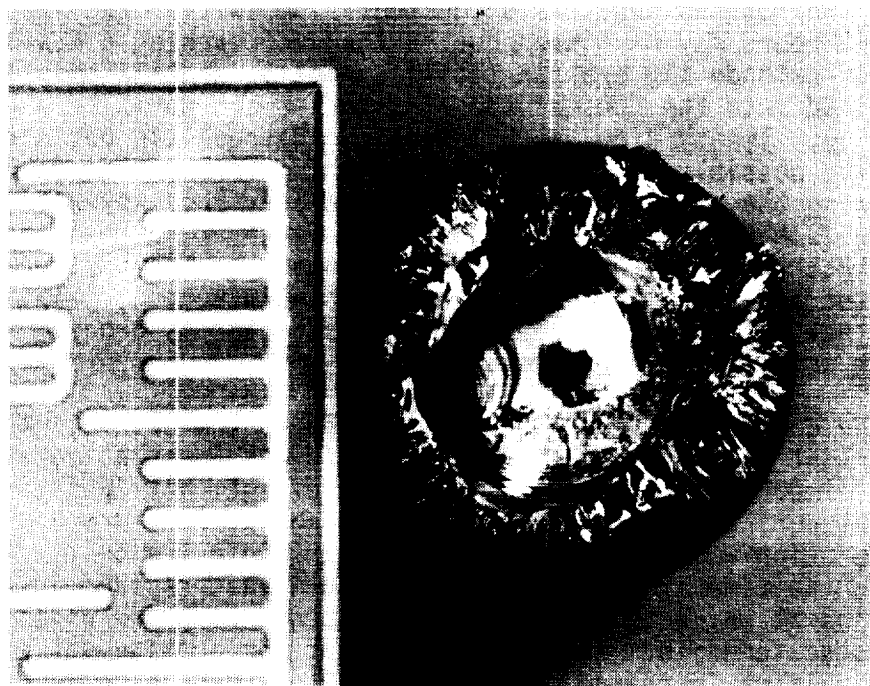


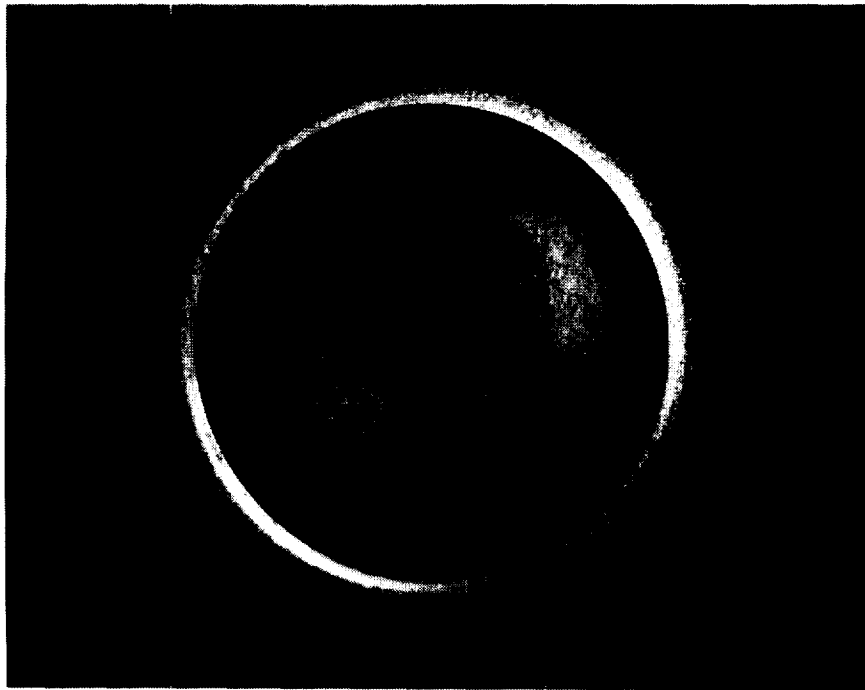
Figure 7-13. Cathode 25 after 252 hours.

A scenario relating the asymmetric tip erosion to the behavior of the voltage over the last 60 hours is suggested. The initial decline in the voltage at 195 hours may have been due to the arc reaching a maximum length, as a result of cathode tip erosion (still symmetric at this point) causing the arc to be pulled into the constrictor. A shorter arc would have caused the voltage to drop. Twenty-nine hours later, the cathode tip began to erode asymmetrically, possibly due to the arc attaching to one side in the constrictor and allowing the arc length to again increase. This asymmetric erosion continued for 23 hours until the arc moved so far over to the side of the cathode tip that the anode attachment point jumped to the upstream edge of the constrictor opposite the tip attachment point (Event 5). This is supported by the fact that the upstream edge of the constrictor is eroded, which did not occur for any of the other tests.

From the downstream view (looking axially up the nozzle), the structure around the bright spot at the center of the tip was first noted at 146 hours of operating time. This is consistent with the fact that "whiskers" did not become evident during the 413-hour test until about 150 hours had passed. Constrictor erosion was first noted at 225 hours into the test. This would correspond to the time after which the arc would have receded into the constrictor and at which the cathode tip had begun to erode asymmetrically in the suggested scenario. Whether the constrictor erosion got worse during the time the voltage increased is unknown. After Event 5, however, constrictor erosion increased markedly. In addition, a black crack-like line appeared, extending from the constrictor to the outer edge of the nozzle. Upon examining the engine after the test it was discovered that the line was a molten tungsten track on the surface of the nozzle and not a crack.

7.3.3.2 Nozzle. A photograph of the nozzle is shown in Fig. 7-14, after 252 hours and 20 minutes of operation at 30 kW. The ZrB_2 coating was almost completely worn off the exterior of the nozzle on all sides (not just the top). The nozzle brightness temperature for this test was generally on the order of 40 °C - 75 °C higher at the operating point than the temperatures measured during all the other tests. This may be due to the fact that the higher mass flow rate for this test dictated different current and voltage levels to achieve 30 kW; the impedance is -0.55 V/A (compared to -0.5 V/A for the 413-hour test). This higher impedance may account for the higher nozzle temperature. In addition, at 146 hours into the test, increased loss of the high-emissivity coating was noted. Over the last 50 hours, the brightness temperature was on the order of 100 °C greater than seen in previous tests, and measured as high as 2000 °C even though the mass flow rate was higher. This may be a symptom of arc attachment within the constrictor. A shorter arc means that the current must be higher to maintain the operating power which in turn increases anode heating through the anode fall.

Looking up the downstream end of the nozzle in Fig. 7-14a, the constrictor shows asymmetric wear and molten tungsten tracks extending from the constrictor edge into the nozzle, including the long streak reaching to the edge of the nozzle. From the upstream side the constrictor is eroded (see Fig. 7-14b). It appears that bits of tungsten from the cathode solidified on the plenum wall around the constrictor.



ORIGINAL PAGE

BLACK AND WHITE PHOTOGRAPH

a) Downstream.



b) Upstream.

Figure 7-14. Engine nozzle after 252-hour test.

The ZrB_2 coating on the exterior of the nozzle is almost completely worn away. As surmised above, this is probably due to the higher operating temperature of the engine over the duration of the run. The generally higher operating temperature may have resulted from the higher impedance at which the engine operated and/or could have been caused by engine operation in a different "mode".

7.3.3.3 Injector. The injector, as with the 413-hour test, was in very good condition. The propellant injection ports were still the original size and the top surface of the injector had not changed shape. Again, the top surface was covered by a black deposit.

7.4 CATHODE EROSION

Combining the results of the endurance tests enables several important points to be made. First, as arc current increases it appears that the cathode tip erosion rate also increases. This can be seen by examining the erosion rates for the five cathode configurations tested for 100 hours (Table 6-1). When the erosion rates are placed in order from lowest (2.0 mg/hr) to highest (4.0 mg/hr), there is a general correspondence with increasing arc current values as shown in Fig. 7-15. Cathodes 4 and 17 both were run at nominal arc currents of 245 to 250 A and exhibit the same basic erosion rate. Cathodes 22 and 24 were run at a nominal arc current of 265 to 270 A and also have the same basic erosion rate. Cathode 14 operated at, nominally, 295 A and has the highest erosion rate. For Cathodes 14 and 22 (both the baseline geometry), the cathode with the higher operating current (Number 14) had the highest erosion rate. The slope of the line in Fig. 7-15 is 0.011 g/C. Therefore, even though the operating conditions and/or cathode configurations were different for these five 100-hour tests, there does appear to be a correlation between higher operating currents and increased tip erosion. A 50 A increase in emitted current has resulted in a doubling of the erosion rate over 100 hours of engine operation.

More significantly, it appears that the cathode mass loss rate increases with time. This can be seen by examining the erosion rate data for flat-face cathodes as shown in Fig. 7-16. Cathodes used for day-long check out runs (5 to 8 hours) show no detectable mass loss. Flat-face Cathode 20 exhibited an average mass loss rate of 1.4 mg/hr after 28 hours of operation while the cathode used in the 100-hour test, Cathode 17, exhibited an average mass loss rate of 2.0 mg/hr. Cathode 25 had an average mass loss of 4.1 mg/hr after 252 hours of operation. After a total of 413 hours of operation Cathode 20 had an average mass loss rate of 5.2 mg/hr. While asymmetric erosion on Cathode 25 and restart attempts on Cathode 20 probably increased their average erosion rates, an increasing erosion rate trend is present. An increasing mass loss in time is contradictory to previous thought.^{3,53,84,85}

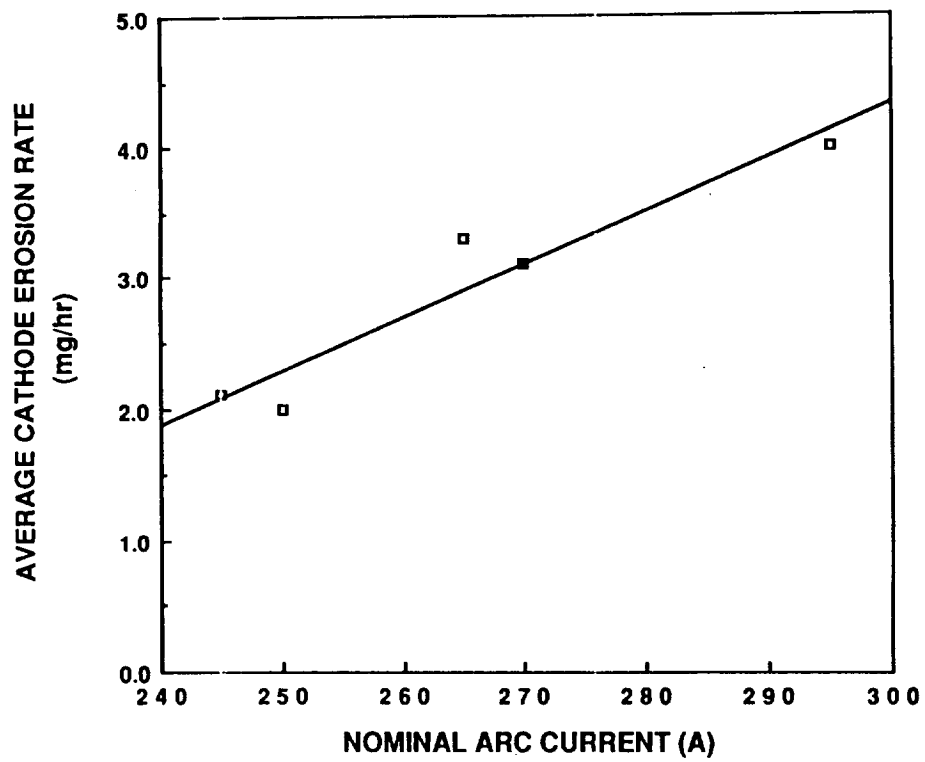


Figure 7-15. Effect of arc current on cathode erosion.

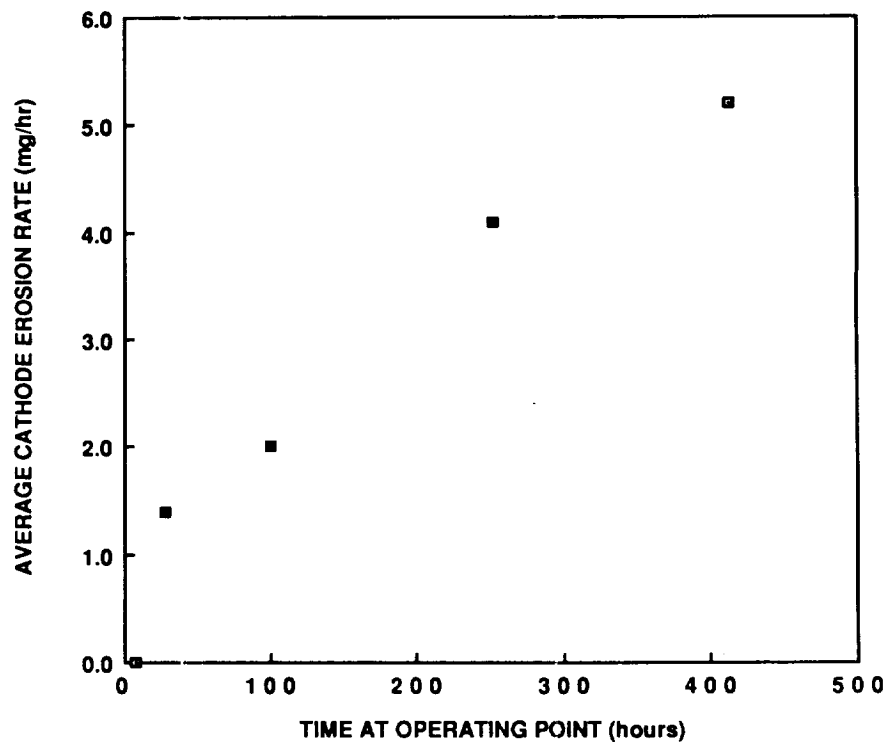


Figure 7-16. Increase of flat-face cathode erosion rate with time.

Increasing mass loss in time could be explained gas-dynamically by gas recirculating in the cathode tip crater. As gas flows past the cathode tip over a growing tip crater, the size of the eddies generated at the sharp corner could grow. If these eddies act to increase gas circulation in the crater, then tungsten vapor can be swept out of the crater at higher rates, increasing the mass loss with time.

Preliminary analysis has shown that the cathode tip surface temperature has a strong dependence on the material work function. This is in agreement with the experimental evidence which indicates that the cathode tip erosion rate is increasing with time. As the cathode is run, the surface thorium layer becomes depleted, requiring a higher tip operating temperature to support the thermionic current emission. As the tip temperature increases, the thorium is depleted at a higher rate causing a further rise in the tip temperature. This process appears to continue until the base tungsten material reaches its melting point, at which time a crater starts to form. Within the first 5 to 8 hours of operation the cathode appears to support the discharge from a low work function surface since no tip melting or mass loss occurs. For longer test durations, melting and mass loss are evident and seem to increase with time (Fig. 7-16). The preliminary analysis (see Section 8.0) has further shown that for a material work function of approximately 3.6 eV, the cathode tip will be near the melting point of tungsten and can support the discharge while still maintaining a reasonable tip heating rate. This suggests that molten tungsten has a significantly lower work function than solid tungsten although still much higher than that of thoriated tungsten. The actual work function for molten tungsten is probably different from that suggested by the simple model. Therefore, increased work function-induced melting, coupled with possible gas dynamic effects, could accelerate the cathode tip erosion rate with time.

8.0

MODELING

The objective of the arcjet heat transfer and sheath modeling effort was to quantify the cathode tip heating phenomena. The modeling effort was composed of two separate analyses that were combined to achieve an overall solution. The first is a 3 species model of the plasma sheath region; and the second is a one-dimensional heat transfer model of the cathode. The plasma sheath model generates an estimate of the heat load to the cathode surface.

8.1

PLASMA SHEATH MODEL

The interaction between a plasma and a material surface is characterized by the formation of a charge separation layer commonly referred to as a plasma sheath. The characteristic length scale for the sheath thickness is the Debye length, L_D , as shown in Fig. 8-1. There are various currents (ion and electron) and heat fluxes (ionic, electronic, convective, radiative and evaporative) which act between the sheath region and cathode surface. In addition, the cathode tip is likely to exhibit two phases, liquid and solid, which have different heat conduction and electrical characteristics. Only the solid phase is considered here; convective and evaporative heat fluxes are not included.

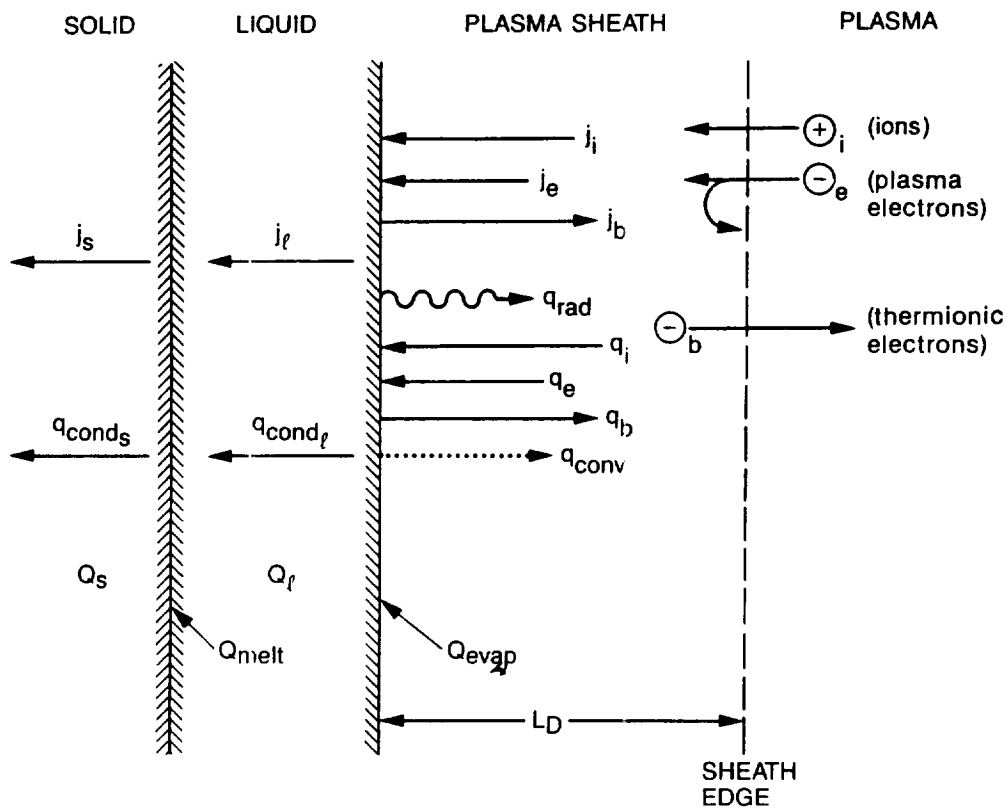


Figure 8-1. Schematic of cathode tip/plasma sheath interactions.

The plasma sheath model calculates the plasma properties normal to the cathode surface, the surface heat transfer, and the current density. Three species of particles are considered: (1) singly-charged, monoenergetic, positive ions; (2) Maxwellian plasma electrons (electrons originating in the plasma beyond the sheath edge); and (3) monoenergetic thermionic electrons (electrons emitted from the cathode surface). The particle energy and current density conservation equations are combined with the Poisson charge equation to form the overall sheath model. The Debye shielding length is significantly smaller than the mean free paths of the particles. Therefore, the sheath may be considered as collisionless and the total energy (kinetic plus potential) of each species of particle is constant.

Thermionic electron emission is significant at the cathode tip because of the high material temperatures. The thermionic emission current (j_b) is calculated using the Richardson equation and includes the reduction of the material work function (χ_{material}) because of the surrounding electric field (E_c) (commonly known as the Schottky effect). The change in the material work function because of the Schottky effect is given by:

$$\chi_{\text{eff}} = \chi_{\text{material}} - \sqrt{\frac{eE_c}{4\pi\epsilon_0}} \quad (8-1)$$

where e is the electron charge, ϵ_0 is electrical permittivity of free space, and χ_{eff} is the effective material work function. The Richardson equation describing the thermionic current density is given by:

$$j_b = A_R T_c^2 \exp\left(\frac{-\chi_{\text{eff}}}{k_b T_c}\right) \quad (8-2)$$

where the value of the electric field at the cathode surface, E_c , is calculated from the sheath model (see Eq. 8-14).^{45,87} T_c is the cathode surface temperature, A_R is the Richardson Coefficient, and k_b is the Boltzmann constant.

Electrons produced by thermionic emission are accelerated away from the cathode surface. The thermionic electrons are assumed to be monoenergetic with a total energy, $U_{b,c}$ that is composed of the particle kinetic and potential energies, as seen in the following energy balance equation:

$$\frac{1}{2} m_b v_b^2 - e(V_c - V) = 2 k_b T_c = U_{b,c} = \text{constant} \quad (8-3)$$

where m_b is the electron mass, v_b is the electron velocity, V_c is the cathode voltage, and V is the voltage at the position of interest.

The flux of all particles within the sheath is continuous, since no ionization or recombination occurs. The thermionic current density equation is:

$$j_b = e n_b v_b = \text{constant} \quad (8-4)$$

where n_b is the thermionic electron number density.

Considering Eqs. 8-3 and 8-4, the thermionic electron number density, n_b , is given by the following:

$$n_b = \frac{j_b}{e} \left(\frac{m_b}{2} \right)^{1/2} (e(V_c - V) + U_{b,c})^{-1/2} \quad (8-5)$$

The ions are also assumed to be monoenergetic. The energy balance equation for the ions is:

$$\frac{1}{2} m_i v_i^2 - eV = eV_o = \text{constant} \quad (8-6)$$

where m_i is the ion mass, v_i is the ion velocity, $n_{i,0}$ and $v_{i,0}$ are the reference values for the ion number density and velocity at the sheath edge, and V_o is the equivalent voltage for the ion total initial energy.

The ion current density given by:

$$j_i = e n_i v_i = e n_{i,0} v_{i,0} = \text{constant} \quad (8-7)$$

Considering Eqs. 8-6 and 8-7, the ion number density, n_i , is given by the following:

$$n_i = \frac{j_i}{e} \left(\frac{m_i}{2e} \right)^{1/2} (V_o + V)^{-1/2} = n_{i,0} \left(1 + \frac{V}{V_o} \right)^{-1/2} \quad (8-8)$$

The plasma electrons (electrons originating in the body of plasma located beyond the sheath edge) are assumed to have a Maxwellian energy distribution. The plasma electron number density, n_e , is given by:

$$n_e = n_{e,0} \exp \left(\frac{-eV}{k_b T_e} \right) \quad (8-9)$$

where T_e is the electron temperature, and $n_{e,0}$ is the electron number density at the sheath edge.

Only electrons with energies greater than the sheath retarding potential will reach the cathode surface. These electrons provide the plasma electron current density, which can be expressed as:

$$j_e = -\frac{e n_{e,0}}{4} \left(\frac{8 k_b T_e}{\pi m_e} \right)^{1/2} \exp \left(\frac{-e V_c}{k_b T_e} \right) \quad (8-10)$$

The Poisson charge equation is used to describe the electric field and the electric potential distributions. The Poisson charge equation is:

$$\frac{-d^2V}{dy^2} = \frac{dE}{dy} = \frac{\rho^c}{\epsilon_0} = \frac{e}{\epsilon_0} (n_i - n_e - n_b) \quad (8-11)$$

where ρ^c is the electrical charge density. Using a set of normalizing variables, Eq. 8-11 is transformed into Eq. 8-12.

$$-\frac{d^2\eta}{d\zeta^2} = \frac{d\gamma}{d\zeta} = \bar{\rho}^c = v_i \left(1 + \frac{\eta}{\eta_0} \right)^{-1/2} - J_b (\eta_c - \eta + \bar{U}_{b,c})^{-1/2} - \exp(-\eta) \quad (8-12)$$

where the normalizing variables are:

$$\begin{aligned} \zeta &= \frac{y}{L_D} & \gamma &= \frac{E e L_D}{k T_e} & L_D &= \left(\frac{\epsilon_0 k_b T_e}{n_{e,0} e^2} \right)^{1/2} \\ \eta &= \frac{eV}{k T_e} & \bar{U}_{b,c} &= \frac{2 T_c}{T_e} & J_b &= \frac{j_b}{e n_{e,0}} \left(\frac{m_e}{2 k_b T_e} \right)^{1/2} \end{aligned}$$

Equation 8-12 is integrated once to determine the electric field distribution using Eqs. 8-5, 8-8, and 8-9 for the particle number densities with boundary conditions of $\eta = 0$ (reference zero voltage) and $E = 0$ (negligible electric field in the quasi-neutral plasma) at the sheath edge. Using $\frac{d\eta}{d\zeta}$ as an integration factor yields:

$$\begin{aligned} \gamma &= \frac{-d\eta}{d\zeta} \\ &= \left[4 v_i \eta_0 \left(\left(1 + \frac{\eta}{\eta_0} \right)^{1/2} - 1 \right) + 4 J_b \left((\eta_c - \eta + \bar{U}_{b,c})^{1/2} - (\eta_c + \bar{U}_{b,c})^{1/2} \right) + 2 \exp(-\eta) - 2 \right]^{1/2} \end{aligned} \quad (8-13)$$

Equation 8-13 can then be numerically integrated to determine the sheath voltage distribution. Then the plasma particle number density distributions and the electric field distribution can be determined from Eqs. 8-5, 8-8, 8-9, and 8-13.^{45,87} For this investigation only the value of the electric field at the cathode surface is needed and is given by:

$$\gamma_c = \frac{E_c L_D}{k_b T_e} = \left\{ 4 v_i \eta_0 \left[\left(1 + \frac{\eta_c}{\eta_0} \right)^{1/2} - 1 \right] - 4 J_b \left[(\eta_c + \bar{U}_{b,c})^{1/2} - \bar{U}_{b,c}^{1/2} \right] + 2 \exp(-\eta_c) - 2 \right\}^{1/2} \quad (8-14)$$

Since the plasma is assumed to be quasi-neutral at the sheath edge, the ion number density at the sheath edge can be obtained using Eqs. 8-5, 8-8, 8-11, and the normalizing variables to yield:

$$v_i = \frac{n_{i,0}}{n_{e,0}} = 1 + j_b (\eta_c + \bar{U}_{b,c})^{-1/2} \quad (8-15)$$

The initial ion energy is determined using the Bohm minimum ion energy sheath criteria. This is done by setting $\frac{d\rho^c}{d\eta} = 0$ at the sheath edge where $\eta = 0$ (Refs. 9, 87) and yields the following expression for the initial ion energy, η_0 :

$$\eta_0 = \frac{U_{i,0}}{k_b T_e} = \frac{v_i}{2 - j_b (\eta_c + \bar{U}_{b,c})^{-3/2}} \quad (8-16)$$

In general, the heat load to the cathode is a result of the energy deposited by the ion and plasma electron impacts and recombination, minus the energy carried off by thermionic emission, thermal radiation, heat conduction into the cathode, and the evaporation and melting of the cathode material. For this investigation only ion and plasma electron impacts, thermionic electron emission and thermal radiation effects are considered. Therefore, the energy balance at the cathode surface can be expressed as:

$$q_{tot} = j_i (V_c + \varepsilon_i - \chi_{eff}) + j_e \left(\chi_{eff} + \frac{2k_b T_e}{e} \right) - j_b \left(\chi_{eff} + \frac{2k_b T_c}{e} \right) - \epsilon_T \sigma (T_c^4 - T_a^4) \quad (8-17)$$

where ϵ_T is the thermal emissivity, σ is the Stefan-Boltzmann constant, and T_a is the anode temperature.

The net current density is given by:

$$j_{tot} = j_i - j_e + j_b \quad (8-18)$$

The sheath region property characteristics, current density and heat load to the cathode surface are determined as functions of the model variables. The model variables include the following: (1) gas properties including the ion mass and the ionization energy; (2) the plasma properties at the sheath edge including the electron number density and the electron temperature; (3) the cathode material properties including the material work function, the Richardson coefficient, and the thermal emissivity; and (4) the cathode temperature. A minimum value for the cathode heat load exists as a function of the sheath fall voltage.⁵¹ For large sheath voltages, the heat load is dominated by ion bombardment; while for voltage drops approaching the floating

potential, the plasma electron bombardment becomes significant. Only for large thermionic current values does the thermionic electron heat removal mechanism become significant.

8.2 HEAT TRANSFER MODEL

The cathode heat transfer model consists of a one-dimensional (in the axial direction) variable geometry (radius may vary with axial location) model, and is shown in Fig. 8-2. The model includes radial heat loads that may vary with position and internal heat generation, as seen in Eq. 8-19.

$$\frac{d}{dx} \left(k_T A_c \frac{dT}{dx} \right) + q_r \frac{dA_s}{dx} + Q \frac{dVol}{dx} = 0 \quad (8-19)$$

where A_c is the cathode cross-sectional area, A_s is the cathode radial surface area, k_T is the thermal conductivity, q_r is the radial heat load, Q is the heat generation rate, and Vol is the element volume.

Temperature-dependent thermal and electrical conductivities must be used due to the large temperature gradients within the cathode (700 K at the base and 3600 K at the tip). The use of such temperature-dependant coefficients introduces nonlinearities into the analysis. The boundary conditions include: (1) the base temperature; (2) the tip heat flux; and (3) the radial heat fluxes along the cathode. In the present case the cathode is assumed to be heated only at the tip and subject to radial cooling along the initial 3.56 cm equal to the input tip heat load.

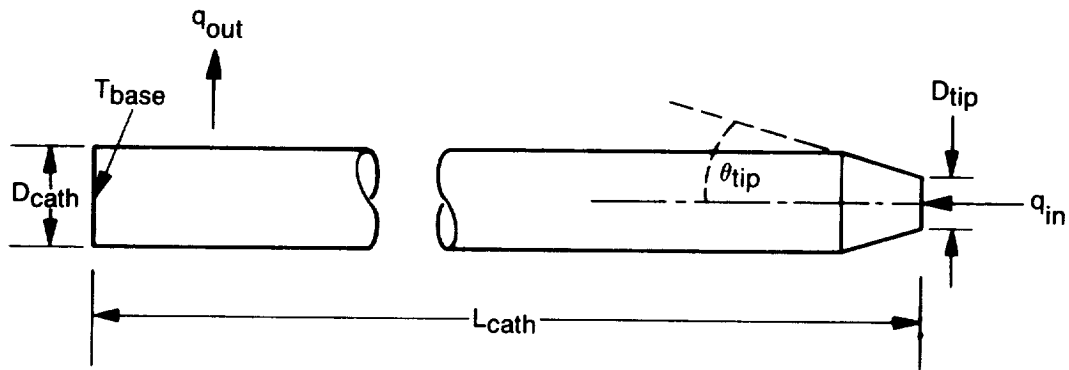


Figure 8-2. Cathode heat transfer model.

8.3 COMBINED MODEL

The two models described above are combined by matching the boundary conditions (the heat flux and the current density) at the cathode surface. A surface heat load and temperature are specified that agree reasonably well with the experimental data. Similarly, the inputs for the sheath model are selected and the surface heat load and current density are calculated. Since an estimate of the average current density is known (from tip attachment area and the input current), the heat load from the sheath calculation may be matched to experimental estimates, as illustrated in Eq. 8-20.

$$q_{\text{eff}} = \frac{j_{\text{ave}}}{j_{\text{tot}}} q_{\text{tot}} \quad (8-20)$$

For example, if the current density calculated from the sheath model is 10 times the average value, then only 10 percent of the attachment area is actually carrying the current (spot mode). The heat load calculated from the sheath model is adjusted by the effective area (10 percent of the attachment area) to determine the actual heat load to the cathode surface. In this manner, the heat load and current density calculated from the sheath model may be compared with the heat load and current input to the cathode surface. A solution exists for the specified boundary conditions and assumptions when the values of these parameters are the same from each model.

8.4 PRELIMINARY RESULTS

The results of a test case with the selected model parameters are shown in Table 8-1.

For the cathode geometry assumed, a tip heat load range of about 140 to 160 W provides a reasonable temperature distribution within the cathode (a base temperature of 700 K and a tip temperature near the melting point of tungsten, 3660 K). This value for heat load to the cathode was then used as the "target value" for the sheath model calculations. For a sheath potential of 7.4 V and a cathode work function of 3.6 eV, the sheath model predicts a surface heat load of 162 W for a 3 mm diameter attachment point. The value of the material work function is assumed to be between the values for thoriated tungsten (2.63 eV) and pure tungsten (4.5 eV) due to the thermal depletion of the thorium from the near-surface layer. The melting point of thorium (2000 K) is significantly lower than the value for tungsten (3660 K). The thorium diffuses through the tungsten crystal structure towards the surface. The actual amount of thorium present at the surface depends on the relative rates of the thorium diffusion and evaporation. For temperatures above 2100 K, the rate of evaporation of thorium is higher than the rate of diffusion-induced replacement.¹⁰⁶ It has been suggested that the material work function may be lower for molten tungsten than for the solid phase. The determination of the tungsten work function in the presence of thorium depletion or melting requires further work.

Table 8-1. Model Parameters and Assumptions

Parameter	Value
Sheath Model	
Electron number density:	$5.0 \times 10^{22} \text{ m}^{-3}$
Electron temperature:	15,000 K
Richardson Coefficient:	$600,000 \text{ A/m}^2/\text{T}^2$
Material work function:	2.6 to 4.5 eV
Cathode surface temperature:	3600 K
Thermal emissivity:	0.4
Ion mass:	$7.06 \times 10^{-27} \text{ kg}$
Ionization energy:	14 eV
Heat Transfer Model	
Cathode length:	12 cm
Cathode diameter:	0.95 cm
Tip half angle:	30°
Tip heat load:	100 to 300 W
Base temperature:	700 K

9.0

DIAGNOSTICS

Arcjet engines are being studied as an option for use in Earth orbital applications. Engine performance testing^{1,18,20,27,28,30,32,34,38,64,80,82,84,85,105,107,118} and duration testing^{27,80,82,84,85} have pointed to certain design improvements which will help make the engine more suitable for primary propulsion functions. To further understand the engine performance characteristics, a physical understanding of engine operation is required. Diagnostic techniques can be applied to the exhaust plume to help gain a better understanding of engine operation by examining neutral and charged particle densities, temperatures, and velocity distributions. Information about the flow field can be used to evaluate the inefficiency due to flow non-uniformity. In addition, the frozen-flow loss, i.e., the energy loss due to dissociation, excitation and ionization of the propellant gas, also requires evaluation. Such information can then be used to form models of engine operation and plume flow patterns. Techniques to make these measurements were reviewed at the Arcjet Plume Diagnostics Workshop in 1986.³⁵

Three diagnostic techniques were demonstrated during the course of this program. First, a summary of the previously known arcjet plume properties is given. The results from emission spectroscopy of the arcjet plume are then described, followed by discussion of the results from a co-funded program on laser-induced fluorescence. This program was performed primarily by a professor and graduate student from the University of Southern California, with support from a Caltech President's Fund Grant; the research was performed in the facility supported by the SDIO. Finally, feasibility tests of epithermal neutron analysis are described. These tests were done in conjunction with Rolls Royce, plc, of Bristol, England.

9.1

KNOWN EXHAUST PLUME PROPERTIES

Several experimental studies of the arcjet exhaust plume have been conducted and have concentrated on the region in the vicinity of the nozzle exit. These studies have utilized several different diagnostic techniques including impact pressure probes, mass flux probes, Langmuir probes, spectroscopic techniques and high speed photography. The primary objectives of these studies were to gain insight into the behavior of the constricted arc and determine the power loss mechanisms involved in the arcjet operation.

The bulk of the thermal energy is added to the propellant in a thin cylinder along the center line of an arcjet engine. As a result, the radial enthalpy and velocity distributions are highly peaked at the nozzle exit. These distributions are one cause of nozzle inefficiency. Frozen flow losses are another major loss mechanism and represent energy used to dissociate and ionize the propellant gas.

9.1.1

Particle Effluxes

Arcjet mass effluxes have been examined in the region immediately downstream of the nozzle exit. The nozzle boundary layer has generally been

the outer boundary of the measurements since the subsonic flow would result in large measurement errors for the supersonic probes. The gas velocity profiles have been found to exhibit sharp maxima on the thruster center line^{4,94,115} with typical values of about 14 km/s and 16 km/s reported. However, the mass flux and density profiles exhibit local minima about the thrust centerline.^{94,115} This indicates that the central regions of the flow carry only a small portion of the total mass flux even though a large portion of the kinetic power is found there.

Conflicting results concerning the impact pressure profiles exist. Sharply-peaked profiles,⁹⁴ flat profiles,¹¹⁵ and profiles exhibiting a slight local minima⁴ about the thruster centerline have been noted. Peaked impact pressure profiles should probably be expected in light of the other data unless the centerline particle density is substantially lower than off axis locations. The static gas temperature varies with position along the centerline of the exhaust plume and has been found to range between 100 °K (0.009 eV) and 1500 °K (0.13 eV).^{4,88}

Electron densities have been measured in argon and hydrogen arcjet plumes using both spectroscopic techniques and Langmuir probes. Values of 10^{15} to 10^{20} m⁻³ have been reported.^{66,115,122} The electron density generally increases with increasing input power. Electron temperatures of 0.63 eV to 0.66 eV have been seen in a 3-kW, argon arcjet plume,⁶⁶ 0.47 eV in a 30.7-kW hydrogen arcjet plume¹¹⁵ and 0.5 eV in a simulated fully decomposed hydrazine plume.¹²² The electron density in the arcjet plume decays along the centerline with an inverse square dependence while the degree of ionization is approximately constant as a function of axial distance from the arcjet nozzle.⁶⁸ Gas dynamic expansion dominates electron/ion recombination processes as the source of reduced centerline electron density in the region beyond two nozzle exit diameters downstream of the nozzle exhaust plane.⁶⁸

Electrode erosion is expected to contribute a small quantity of non-propellant particles to the arcjet exhaust plume. The area of greatest erosion in well-designed thrusters was found to be the cathode tip.^{3,53,54,82,84,85} During a thirty-day life test of a 30-kW hydrogen arcjet, the ratio of the electrode mass (m_e) loss with respect to the total exhausted propellant mass (m_p) was 1.3×10^{-5} .⁵⁴ During another recent long-duration test of a 30-kW ammonia arcjet a cathode tip mass loss of 1.95 g of tungsten was reported, corresponding to an m_e/m_p ratio of 1.1×10^{-5} .^{84,85}

9.1.2 Field Effluxes

Photographic and spectroscopic studies have been conducted to examine the degree of ionization and the excited state population density in the plume of an arcjet. This information can be used to estimate the frozen flow losses. Studies with a one-kilowatt hydrogen arcjet showed that plume radiation is responsible for a 5 to 10 percent energy loss,^{39,88} with the radiating volume and plume density increasing with increasing input power. Most of the radiated energy appeared to lie in the near-UV and IR regions, with only a relatively small amount in the visible region. Radiation fields which have a greater spatial extent should be expected during the operation

of high power arcjets in space. Analysis of the radiation emitted during ground tests is difficult since impurity gases in the vacuum facility can mask the non-impurity radiation.^{66,88}

The energy in arcjet plumes is thought to be distributed in a non-equilibrium manner characterized by a non-Maxwell-Boltzmann population of excited state densities with electron temperatures much greater than the static gas temperature.^{66,88} There is no pronounced evidence of collisional or radiative coupling between the excited states.⁶⁶

9.2 EMISSION SPECTROSCOPY

This section presents results from an effort to develop a technique to measure velocity and temperature distributions using emission spectroscopy. This non-intrusive technique enables the measurement of radial, azimuthal and axial velocity distributions along with the temperature distribution of the species whose emissions are being monitored. Results of a radial velocity survey in an arcjet engine plume are presented. The technique to determine velocities involves a measurement of the Doppler shift of an optically thin line resulting from recombination and relaxation processes in the high Mach number stream. The temperature of the atoms can also be calculated from the same measurement using the Doppler broadened line widths. The shifts and line widths have been measured with a scanning Fabry-Perot spectrometer. The experiments were done using the baseline engine design, described in Section 3.1. Data was taken at an engine power of 20 kW and an ammonia mass flow rate of 0.375 g/s.

9.2.1 Optical Setup

The optical instrumentation is shown in Fig. 9-1. The arcjet was located on the centerline of the 1.2 m diameter vacuum tank; the facility is described in Chapter 2. All optical elements were located outside of and immediately adjacent to the vacuum tank. Light from the arcjet plume was collected by an 80 mm diameter, 1000 mm focal length lens after first being deflected by a steerable mirror. By pitching and yawing this mirror, with the aid of differential micrometers, the collection point in the plume could be moved both radially and axially. Also, by moving the mirror-lens-iris combination along an optical rail, as shown in Fig. 9-1, the angle between the optical axis at the plume and the plume centerline could be varied. This flexibility was necessary in order to probe for the various velocity components in the plume.

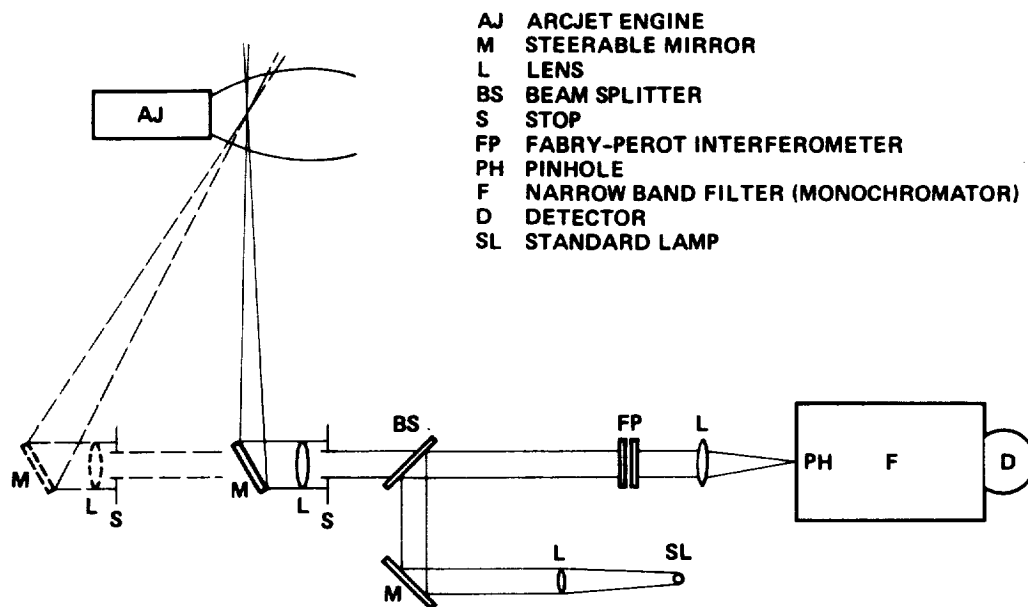


Figure 9-1. Fabry-Perot spectroscopic system.

An iris diaphragm was located at the collecting lens. This aperture stop was used to adjust the intensity reaching the detector. The collected light from the plume then passed through a 50% beam splitter and a scanning Fabry-Perot Interferometer. This interferometer had a clear aperture of 32 mm and could be operated anywhere between 4500 and 6500 Å with a free spectral range, variable in seven steps, between 0.1 and 21 Å. With a minimum Finesse of 25, the range of bandpasses available was 0.004 to 0.845 Å. The light emerging from the interferometer was collected by a 40-mm diameter by 160-mm focal length lens and focused into a 0.3-mm diameter pin hole. The pin hole was used as the entrance slit of a 20 cm focal length scanning monochromator with a spectral range of 300 to 850 nm and a minimum band pass of 0.4 nm. The monochromator was used as a narrow band tunable filter to prevent light from all but a few transmission notches from reaching the detector. The optical detector was a side-on photo multiplier tube with good response in the range 1850 to 9300 Å. It had a current amplification of 10^7 , a maximum sensitivity of 4.2×10^5 Å/W and a rise time of 2.2 ns.

In order to measure the Doppler shift, light collected from the arcjet plume had to be compared with light from the same atomic or ionic transition originating from a known stationary source. A low-pressure, glow-discharge hydrogen lamp was used as a source. Radiation from this source was collected by a 1.3-cm wide by 5-cm long cylindrical lens and mixed with that from the arcjet plume with the aid of a second steerable mirror and the 50% beam splitter, as is shown in Fig. 9-1.

9.2.2 Representative Results

Figure 9-2 is an oscilloscope trace of the detector output when light from only the standard lamp was allowed through the system. That is, light from the plume was blocked. For all the results of this report the atomic hydrogen transition at 6563 \AA (Balmer) was used. In Ref. 67, this line was shown to be optically thin in arcjet plumes. Superimposed on the detector output is a representation of the ramp voltage applied to the three piezoelectric elements that push one mirror of the interferometer toward the other during the wavelength scan. The two transmission peaks indicate that two complete orders are displayed; since the interferometer had a 2-mm spacing, the wavelength scale from peak-to-peak, or free-spectral-range, was 1.077 \AA . The distance between peaks across the oscilloscope face can be arbitrarily changed by changing the time rate of change of the voltage driving the piezoelectric elements. The line's full width at half of its maximum intensity, or FWHM, is 0.39 \AA . This large width complicates the data reduction procedure since the expected shifts are 0.1 \AA or less.

Next, the light from the standard lamp was blocked while that from the plume was allowed to pass to the detector. The results are shown in Fig. 9-3. The large oscillations of the detector output at 180 Hz were caused by the ripple from the full-wave rectified power supply driving the arcjet engine. The relative magnitude of these oscillations decreased as engine power was increased. Again notice the large line width of the radiation from the arcjet plume, somewhat larger than that from the standard lamp. In this case the FWHM was 0.56 \AA . The actual line width was somewhat less than this because in the data of Fig. 10-3, the orders are overlapping. That is, the right-side wing of the left peak is overlapping the left-side wing of the right peak. The presence of the ripple and large line width again complicates data reduction.

The oscilloscope was always triggered from the voltage ramp and hence the trigger point was stable and independent of the light source that was being viewed. This stability is confirmed in both Figs. 9-2 and 9-3 since each picture represents 2.5 overlapping traces. For each data point, two pictures, similar to Figs. 9-2 and 9-3, were taken in rapid succession. The line width across some convenient horizontal reticle line was then measured and divided in half to define the line center and the distance from this line center to the central vertical reticle line. This distance was then subtracted from the corresponding distance for the second picture. In this way each pair of pictures yielded two data points and in each case these two points were identical to three decimal places in terms of wavelengths (units of \AA). The distance between each line center and the central vertical reticle line was converted to \AA by using the fact that the total distance between line centers in each picture was one FSR of 1.077 \AA . The difference in line center position between pairs of pictures, in \AA , was then the Doppler shift due to the component of the plume velocity vector along the optical axis.

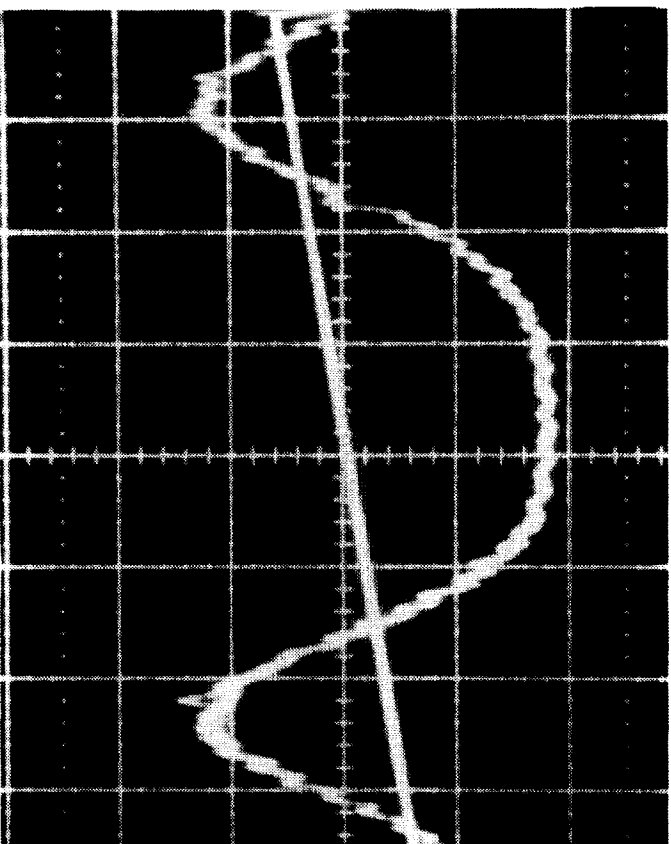


Figure 9-2. Scan of standard lamp output at 6563 Å.

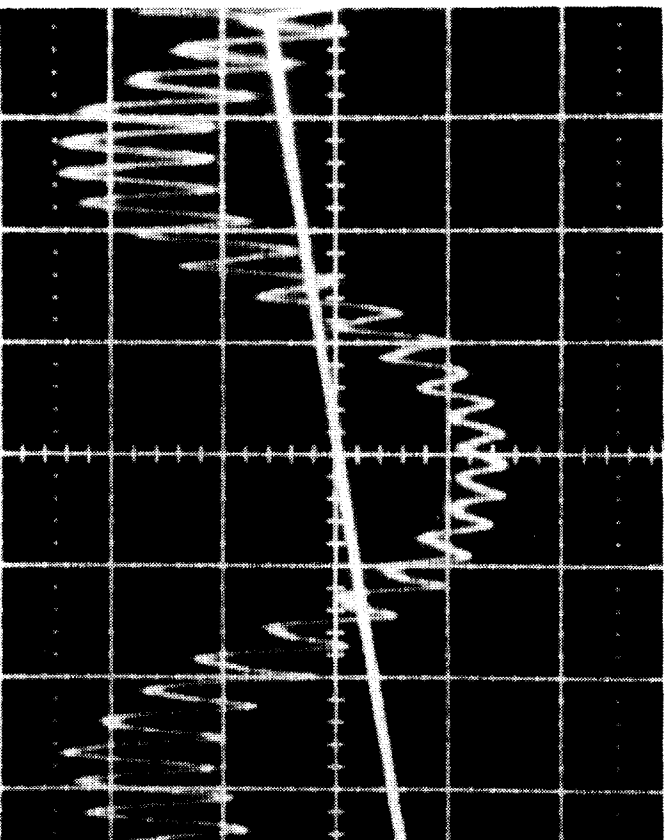


Figure 9-3. Scan of arcjet plume output at 6563 Å.

Two sets of data were obtained. The first was obtained by viewing the plume with the optical axis perpendicular to the plume centerline and the second set was obtained by viewing the plume with the optical axis inclined to the plume centerline by an angle of 78.4° (see Fig. 9-1). The spatial resolution at the plume was about 2 mm. For each of these data sets the mirror was pitched in order to obtain data from various radial positions in the plume. Both of these radial scans were done within 5 mm of the arcjet exit plane.

The maximum light intensity for each radial data point for the perpendicular data set is shown in Fig. 9-4. The intensity was normalized with the maximum centerline intensity and the radius, r , was normalized with the radius of the nozzle exit, $R_0 = 1.21$ cm. Since too few data points were taken on both sides of the maximum to clearly define the profile, each measured data point (shown as a circle) was replotted at the same radial position on the opposite side of the centerline. These repeated data points are indicated by squares. The intensity is down to 10 percent of maximum at the nozzle exit radius.

The data taken at an angle of 78.4° was normalized in the same way and is shown in Fig. 9-5. For this data set, enough data points were obtained to clearly define the radial profile. The normalized intensity profiles of Figs. 9-4 and 9-5 are nearly identical.

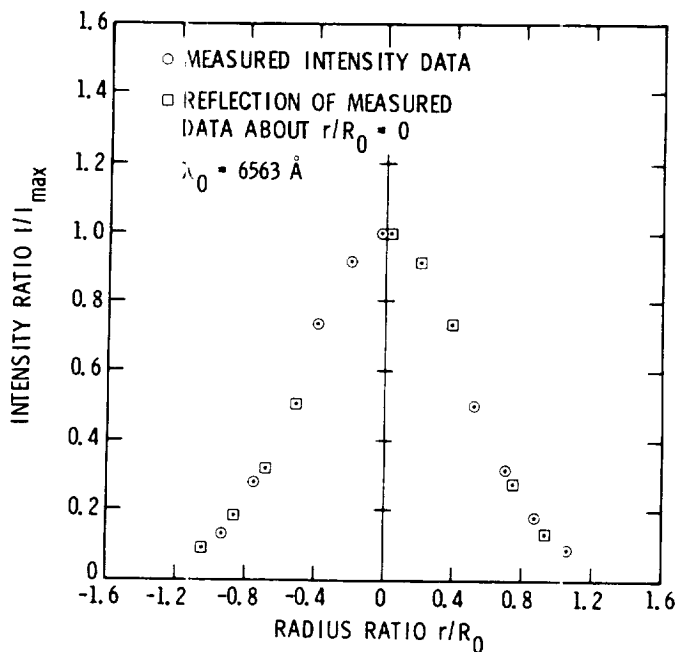


Figure 9-4. Intensity distribution measured perpendicular to axis.

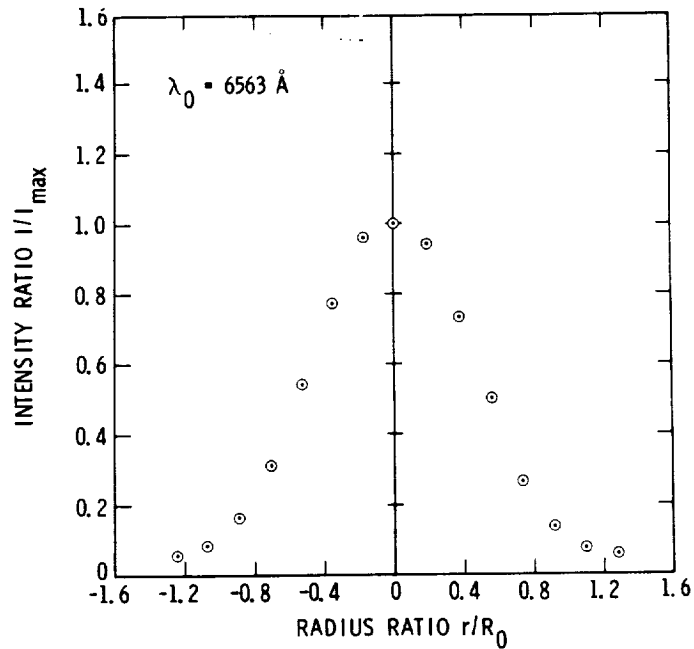


Figure 9-5. Intensity distribution measured at an angle of 78.4°.

The Doppler shift for each data point of the perpendicular data set was used to calculate the velocity vector component parallel to the optical axis. Since the optical axis was perpendicular to the plume axis, the axial velocity could not affect the measured shift. For this data set, any measured Doppler shift could only be due to radial and azimuthal velocity components. Also, when looking at the center of the plume, only a radial velocity component could be detected.

The velocity component parallel to the optical axis was calculated from the following expression (Ref. 3):

$$v = c\Delta\lambda/\lambda_0 \quad (9-1)$$

where c is the speed of light, λ_0 is the unshifted line center wavelength and $\Delta\lambda$ is the measured Doppler shift. These results are shown in Fig. 9-6. Very little shift was detected at the center of the plume, indicating little or no radial velocity component. Therefore, the data shown in Fig. 9-6 was labeled as azimuthal velocity v_ϕ , vs. normalized radius. Although there was much scatter, it does seem that the plume was rotating as a solid body. Assuming this to be true, the two data sets were then used to calculate the axial velocity distribution in the following way. At each radial point, the resultant velocity vector had an unknown magnitude v_R , and an unknown

inclination to the plume vertical center plan, α . The two measured velocity components, v_ϕ perpendicular to the plume axis and v_b inclined 11.6° to the perpendicular, were related to v_R and α by the two simultaneous equations:

$$v_\phi = v_R \sin \alpha \quad (9-2)$$

$$v_b = v_R \sin (\alpha - 11.6^\circ) \quad (9-3)$$

These two equations were used to calculate α and v_R . The axial velocity was then determined from

$$v_z = v_R \cos \alpha \quad (9-4)$$

For these calculations the azimuthal velocity was assumed given by the straight line drawn through the data points as shown in Fig. 9-6, or

$$v_\phi = s r^2 \quad (9-5)$$

where s is the slope of the line. The results of these calculations are given in Fig. 9-7 as axial velocity vs. normalized radius.

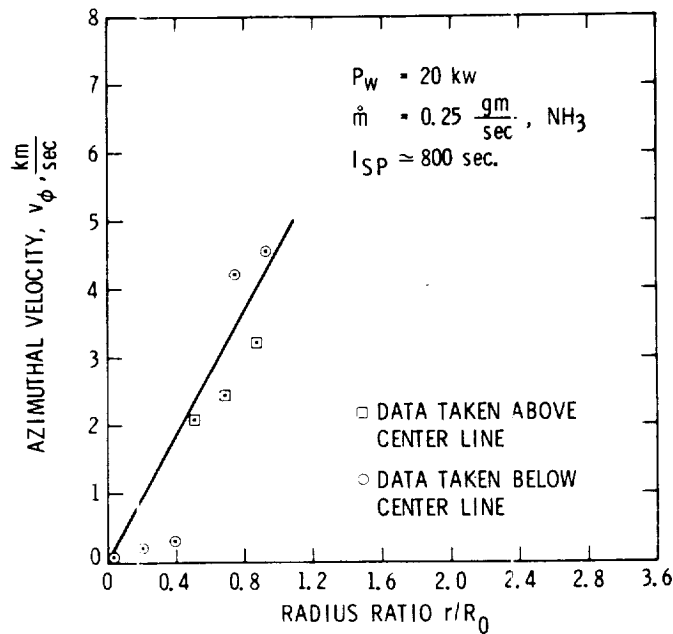


Figure 9-6. Azimuthal velocity distribution.
(The mass flow rate shown in this figure should be multiplied by 1.26. See Section 5.6.)

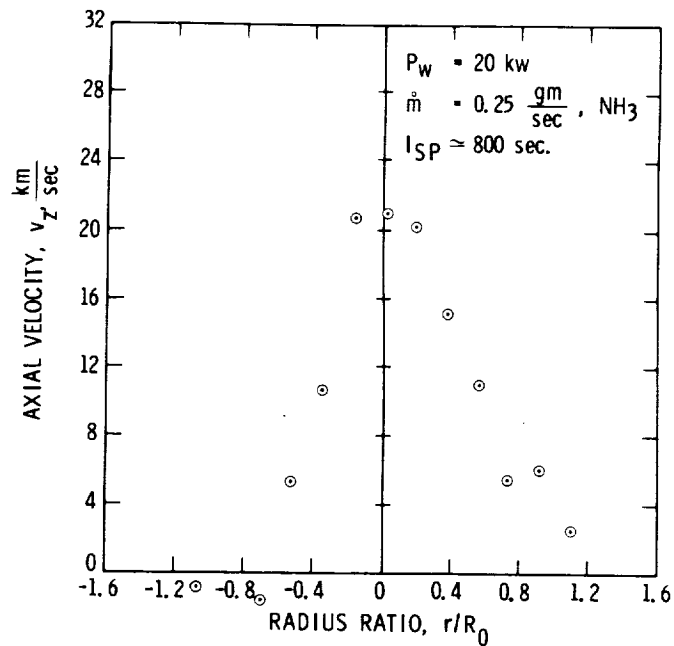


Figure 9-7. Axial velocity distribution.
 (The mass flow rate shown in this figure should be multiplied by 1.26. See Section 5.6.)

9.3 LASER-INDUCED FLUORESCENCE

The velocity profiles presented in Section 9.2 are averaged over the collection volume of emitted light to the detection optics. An inversion process must be used to deconvolve the data to get point velocities. This is particularly difficult for the axial velocity profile data due to the elliptical cross section of the plume when light is collected at an angle. This section describes a series of test results from the use of Laser-Induced Fluorescence (LIF) to examine the velocities of an arcjet plume. This technique avoids the need for an inversion process by monitoring light fluoresced from a small discharge volume into which is focused a laser beam. The laser beam focus defines the spatial resolution. LIF promises greater detail in the analysis of plume flow fields. This work was done in collaboration with the University of Southern California, Aerospace Engineering Department.

The work described in this section validated the feasibility of using LIF to measure arcjet plume velocity profiles. Each molecular species in the plume has a different velocity; this work focused on the velocity of atomic hydrogen. The velocity was obtained by measuring the Doppler shift of the broadened atomic hydrogen Balmer α line in absorption; this provided the bulk velocity of H in the direction of the pump laser beam. The shape of the absorption line is, in general, due to a combination of thermal (Doppler) and electronic (Stark) effects; in cases where one or the other is

clearly dominant, the line width can provide a measure of either translational temperature or electron density. The density is thought to be sufficiently low so that atomic transition lines are not significantly broadened by collisions. The plume is believed to be field-free, so that there is no DC Stark shift. The transitions are affected, then, only by Doppler shift and by Doppler and Stark broadening. The transition lines are dominated by Stark broadening. Measurement of an absorption line profile (of the line shape and position relative to the unshifted line) can be used to provide a measure of electron density as well as H velocity. The variation of LIF signal with laser pulse energy, i.e., the pump saturation curve, is determined by electron temperature as well as density, since the upper state of the pump transition is depopulated primarily by electron collisional quenching. The experiments were conducted using the D-1E arcjet described in Chapter 3. The engine was operated at powers of 12 to 14 kW at a mass flow rate of 0.31 g/s of ammonia.

9.3.1 LIF Technique

The center frequency of a transition will be shifted by an amount proportional to the velocity of the atom in the direction of the detector, in emission, or in the direction of the light source, in absorption. The velocity is related to the peak shift as shown in Eq. 9-1, repeated here for convenience:

$$v = c\Delta\lambda/\lambda_0 \quad (9-1)$$

where $\Delta\lambda$ is the shift of the profile peak with respect to its position when $v = 0$, λ is the pump wavelength, and c is the speed of light. Thus a peak shift of 0.1 Å corresponds to a flow velocity of 4.6 km/sec for Balmer α pumping. The flow is toward the laser source, so the shift is in the direction of increasing wavelength. Arcjet plume velocities are of the order of 20 km/sec, corresponding to a transition lineshift of order 0.4 Å.

In order to make use of this, the lineshape of the Balmer α transition ($\lambda = 6563$ Å) was measured using LIF at various points in the plume. This involved scanning the frequency of a narrowband pulsed-dye laser while the fluorescence from a small volume along the beam was collected and recorded. (See Fig. 9-8.) In the figure, the volume of collected fluorescence shown is much larger than the actual volume; the smaller the collection volume, the better the spatial resolution. Since the plume conditions remain generally constant on a time scale of hours, the requirements on the speed of such a scan are not stringent. Frequency selectivity was provided solely by the pump laser tuning, not by discrimination in detection, so that the variation of measured LIF signal with wavelength represented the absorption line profile in the direction of the laser beam. This work involves weak (unsaturated) pumping, so that the measured line shape is identical to that in emission. The present work employed the Balmer α line to maximize the experimental sensitivity, shown by Eq. 9-1 to be proportional to the wavelength.

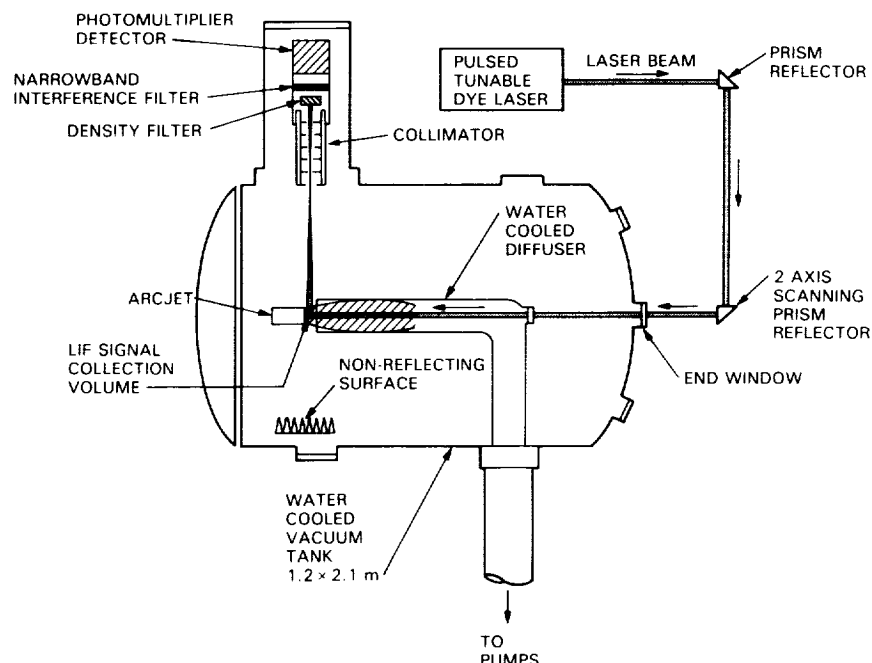


Figure 9-8. LIF experimental setup.

For a given radial position of the laser beam, the dye laser was scanned in frequency over the Balmer α absorption line. The resulting signal was averaged over 100 samples to suppress noise due to laser fluctuation. The signal consisted of a constant offset due to the background plume emission and to directly scattered laser light, as well as the wavelength-dependent LIF signal. Since the pump and signal transitions are the same, differentiation between LIF and scattered laser photons is impossible. The resulting intensity-vs.-wavelength profile, with the offset subtracted, is the absorption line shape if the laser pumping is sufficiently weak. This condition was checked by repeating a scan with larger laser power to verify that the profile was unchanged.

The position of the profile peak was obtained by fitting the data points with polynomials. The flow velocity corresponding to a peak position was given by Eq. 9-2. Note that the experiment provides no absolute reference of wavelength, so that zero velocity must be inferred by the peak position at the edge of the plume.

The flow velocity is obtained at a variety of radial positions by moving the laser beam horizontally as described. This was done with a precision of 0.5 mm. Thus the velocity-vs.-radius data points are characterized by a random horizontal error of 0.5 mm. In addition, the resulting profile must be considered to be convolved with an instrument function of full width equal to 3 mm due to the laser beam size.

9.3.2 Results and Discussion

The raw data and results of a scan with the engine operating at 14 kW are shown in Figs. 9-9 and 9-10, respectively. The velocity profile is sharply peaked at the nozzle exit as expected from early data. The vertical error bars in the velocity profile data are estimates of the accuracy of the horizontal peak positions of the corresponding wavelength scans as determined by polynomial fitting. A peak velocity on the plume centerline of approximately 15 km/s was found. The horizontal error bars correspond to the radial position uncertainty as discussed earlier. Additional data can be found in publication 27 listed in Section 12.0.

The widths of the raw LIF intensity profiles (Fig. 9-9) exhibit Stark broadening. The electron density at the nozzle exit was originally thought to be sufficiently low so that the Stark width of the profiles would be negligible. However, this is clearly far from true. Indeed, the profiles appear broad enough to suggest electron densities of the order of 10^{15} cm^{-3} . It should be noted, however, that there is a large discrepancy among the experimental results giving the expected Stark width as a function of Balmer α linewidth,^{14,44,90} so that the electron density is not precisely known. It is in any case clear that the line shape at the nozzle exit is dominated by electron density rather than neutral temperature, though this may not be true further downstream in the plume. This issue does not affect the quality of the flow velocity measurements, since the peak shift depends only on flow velocity.

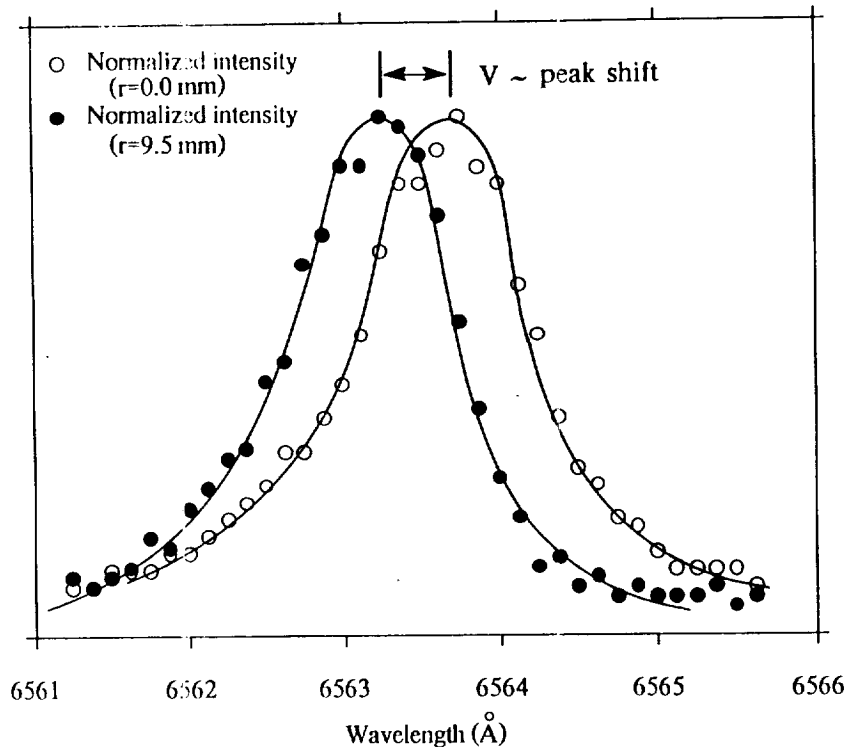


Figure 9-9. LIF signal intensity vs. wavelength.

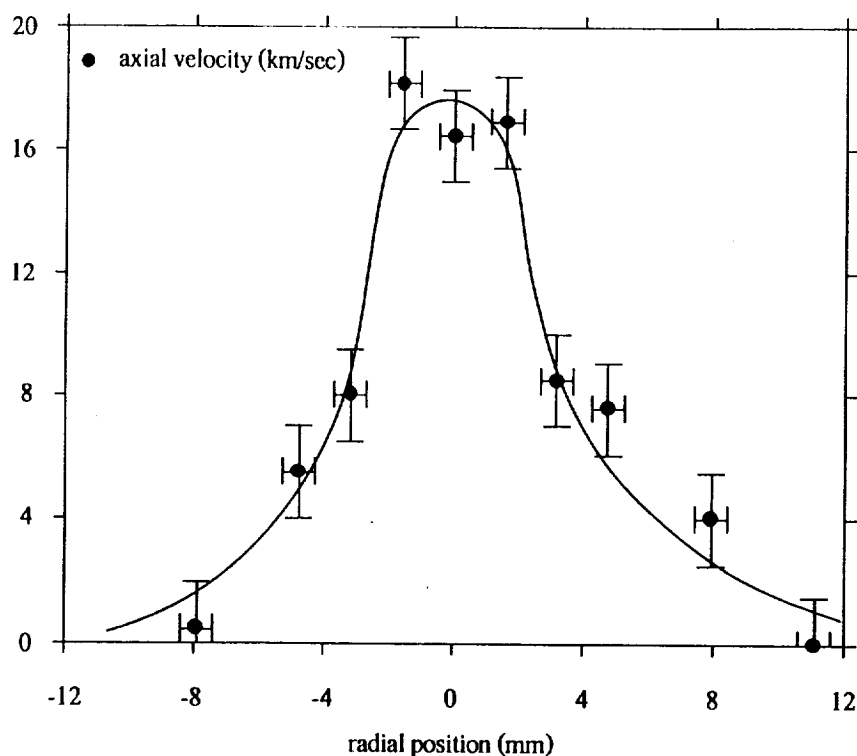


Figure 9-10. Axial velocity vs. radial position.

9.4 NEUTRON ANALYSIS

Techniques to measure arcjet plume characteristics have been discussed in the preceding sections. This section will describe a group of non-intrusive diagnostic techniques which can be used to make real-time measurements of internal engine temperature,^{42,108} monitor electrode erosion patterns,¹⁰⁸ determine electrode material bulk stress/strain levels¹⁰⁸ and possibly examine the distribution of hydrogenous propellants within the engine flow field.^{A,C} The techniques are based on the use of low-energy neutrons and their interaction with solid and gaseous materials. Feasibility experiments were conducted by the University of Bristol and Rolls Royce, plc, both of Bristol, England, in collaboration with JPL. These results are described below after a discussion of the techniques.

9.4.1 Neutron Techniques

The neutron can enter and pass generally unhindered through materials. Its energy and direction will, however, be modified by conditions in the material. The material properties may then be deduced from the neutron exit characteristics. Neutrons are classified with respect to their kinetic energy levels: 'Cold' or subthermal neutrons (of the order 0.004 eV); 'Thermal' neutrons (of the order 0.025 eV); 'Epithermal' neutrons (of the order 0.5 eV to 20 eV). Possible measurements using cold and thermal neutrons are first described briefly. The feasibility experiments and results are then described.

9.4.1.1 Cold or Subthermal Neutrons. The unique property of 'cold' neutrons is that, below the so-called "Bragg edge" of 0.004 - 0.005 eV, coherent neutron scattering from a crystalline lattice structure cannot take place. Coherent scattering is a result of the interference of scattered neutron waves from the neighboring nuclei in lattice planes of known separation, and gives rise to the phenomenon of diffraction. The cross section drops sharply at the energy corresponding to the Bragg diffraction limit. This effect occurs in nearly all crystalline materials including different steels and molybdenum. Tungsten is one of the metals which has a negligible coherent scattering cross-section. (The incoherent scattering cross-section remains unchanged across the Bragg edge). However, hydrogen and hydrogenous materials such as ammonia and hydrazine arcjet propellant share a high incoherent scattering cross-section for cold neutrons. The electrodes are, therefore, relatively less opaque than the propellant to cold neutrons.

For 'cold' neutrons, the principal application would appear to be a radiographic characterization of the hydrogenous propellant location in two dimensions and its real time behavior. This technique has been demonstrated to work for liquid phase flows,^{108,109} but needs further verification for the vapor phase.

9.4.1.2 'Thermal' Neutrons. The edges of the central cathode and the internal contours of the convergent plenum, constrictor and divergent nozzle of the arcjet could be defined by thermal neutron (0.025 eV) radiography since tungsten is sufficiently transparent to thermal neutrons. There is an inherent geometrical limit to the sharpness of the image, which depends on the radiographic geometry, i.e., the distances of source to object, object to imaging system, source size and collimation ratio. However, resolutions on the scale of 5 microns have been achieved. In the proposed experimental arrangement for the arcjet tests at the RAL, a geometric resolution of 250 microns is expected.

Another important set of applications lies in the determination of the lattice strain in crystalline materials.¹⁰⁸ This is achieved by measuring the lattice spacing and comparing it with the spacing in non-stressed conditions. The lattice spacing parameters are measured using neutron diffraction techniques. Neutrons of a specific energy are scattered by the lattice planes through an angle which is precisely defined by the Bragg scattering law and related to the lattice spacing. Typical diffraction measurements would be carried out with a diffraction angle in the range of 90° to 135°. Residual or applied stress may then be deduced by, for example, taking measurements of the material in the unstressed condition and then in the stressed condition. Temperature induced stresses may be determined by this technique.

9.4.1.3 Epithermal Neutrons. In the epithermal neutron (0.5 eV to 20 eV) region, neutrons with energies within certain very narrow bands are strongly absorbed by certain materials. An example of this is shown in Fig. 9-11, where the transmission of neutrons through a tungsten foil is displayed. Many resonances are apparent for the different times of flight of the neutrons, i.e., different energies. The stronger resonances are

generally the most important for this work. The energy and degree of absorption at each resonance is unique and characteristic of the specific material and its temperature.

Materials which may be used for, or with, high temperature arcjet components and have strong non-overlapping epithermal neutron resonances are given in Table 9-1.

Table 9-1. Epithermal Neutron Resonances for Some Arcjet-Compatible Materials

Element	Melting Point (°C)		Resonance Energies (eV)
	<u>Metal</u>	<u>Oxide</u>	
Platinum (Pt)	1772		11.90 19.60
Thulium (Tm)	1545		3.91
Tungsten (W)	3410		4.16
Tantalum (Ta)	2996		4.28
Hafnium (Hf)	2227		1.10 2.38
Hafnium Oxide		2758	
Rhenium (Re)	3180		2.16
Rhodium (Rh)	1966		1.26

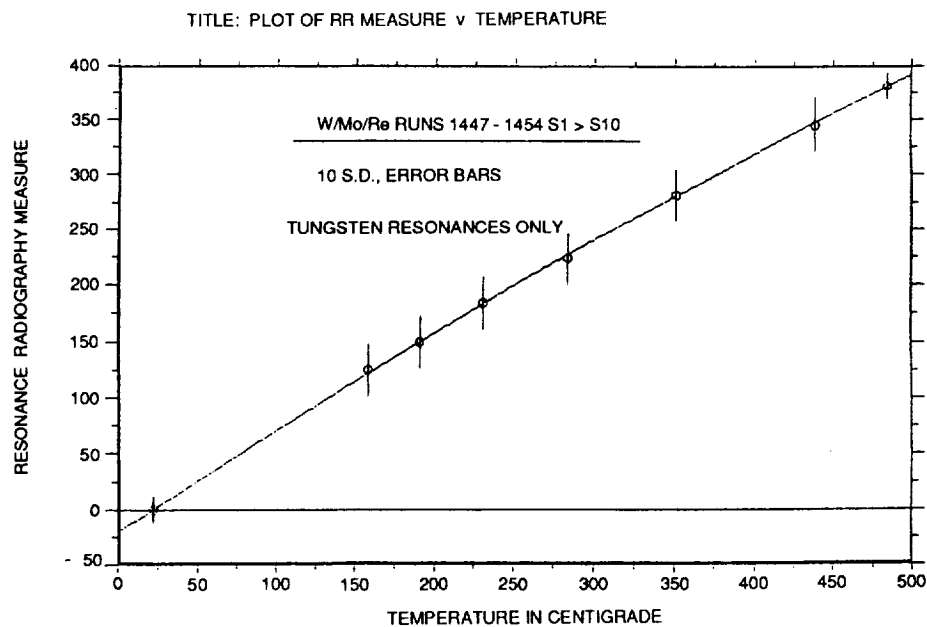


Figure 9-11. Calibration results for tungsten resonance.

The shape of the absorption trough around each resonance is a function of the temperature of the material. As the temperature increases the absorption troughs broaden. For strong narrow resonances such as are present in tungsten and rhenium, the effect of this spread is easier to determine. A detailed analysis of the shape of these absorption bands thus provides a very accurate means of measuring the temperature of the individual materials.

The spectral signatures of many arcjet materials could be simultaneously obtained if care was taken not to overlap the resonances. Thus, for example, materials naturally present would provide bulk temperatures. Surface temperatures could be obtained by plating, plasma deposition or sputtering of a material on the surface of interest, and local temperatures by interrogating small local implantations of tens of microns size in the desired location. Coatings of rhodium, platinum or iridium could provide surface temperatures. Local implants could be provided in the thruster body or anode wall to examine temperature gradients and possibly help identify the arc attachment pattern.

9.4.2 Facilities and Instrumentation

The neutron source used for this work was the large fixed ISIS Spallation Neutron Source facility at the Rutherford Appleton Laboratories (RAL) of the UK Science and Engineering Research Council. It is a pulsed source which produces neutrons from the bombardment of a uranium target by intense 0.4 μ sec duration pulses of high energy protons from a synchrotron accelerator. The high energy neutrons are slowed down within approximately 1 μ sec by a moderating assembly to the appropriate range of energies. A beam of neutrons is allowed to exit from the moderator along an evacuated flight tube to reach the test object and detector system. The neutrons are detected after traversing the flight path and the test object. The time of flight of the neutrons (and therefore their energy) is determined accurately (to better than 1 in 10^3) with respect to the initial sharp proton pulse. A schematic arrangement of source, beam line and detector system is shown in Fig. 9-12.

9.4.3 Feasibility Experiments

Experimental work has been carried out using the ISIS neutron source at RAL on representative arcjet materials to validate epithermal neutron analysis for arcjet applications. A joint experimental program was set up between Rolls-Royce and JPL to determine the feasibility of measuring temperatures on the cathode through the thickness of the tungsten anode and the molybdenum casing. It was assumed that rhenium could either be implanted into or distributed in the cathode material; this was selected as the target material.

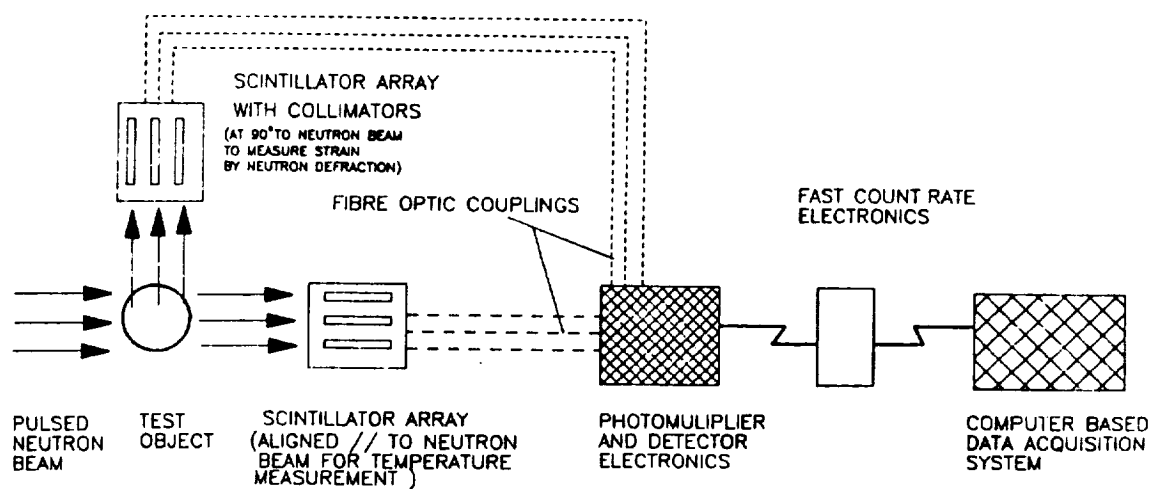


Figure 9-12. Schematic diagram of beam line and detector system.

The material specimens, thoriated (2.0%) tungsten and pure molybdenum, were prepared with dimensions of 3 x 3 x 1 cm. A 100 μm thick rhenium foil was sandwiched between a molybdenum and thoriated tungsten specimen simulating the 30-kW arcjet material thicknesses. The assembly was mounted in an instrumented oven for exposure to the ISIS neutron beam. An array of ten detectors, each with its individual photomultiplier, was positioned at a distance of 12 m from the neutron source.

Each detector measured the time-of-flight distribution of the neutrons transmitted through the full three-layer specimen. At the start of the series of neutron exposures, the specimen was taken to 484 °C and held there until thermal equilibrium was attained. An exposure of 40 minutes was then made. The power to the oven was turned off and the specimen cooled without interference. Successive exposures of 10 minutes duration were taken until the series was terminated. A final 40-minute run was taken at room temperature, which was used as the baseline for temperature measurements.

Temperatures were determined for each of the elements from precision measurements of the width of each of the resonances. Any resonance that is free from overlap of neighboring resonances gives a temperature measurement from the isotope (element) responsible for the resonance. The data from each resonance are combined to give a temperature measurement for the element which is compared to the actual temperature determined from the oven instrumentation.

Figure 9-13, top panel, shows the transmitted neutron counts versus time-of-flight (i.e., energy) for the lowest energy resonances. On this plot there are three very strong resonances: the low-energy resonance at around 600 μsec due to rhenium, and the other two due to tungsten. The lower panel shows the ratio of neutron transmission for the two sample temperatures: 22 °C and 484 °C. The relative height of each peak on either side of the resonance energy gives the measure of temperature.

In summary, using 10 minute runs, one could establish that the temperature of the tungsten element was established to better than ± 2.5 °C. Similar results were obtained for rhenium, while an accuracy of ± 6 °C was found for molybdenum due to sparse data.

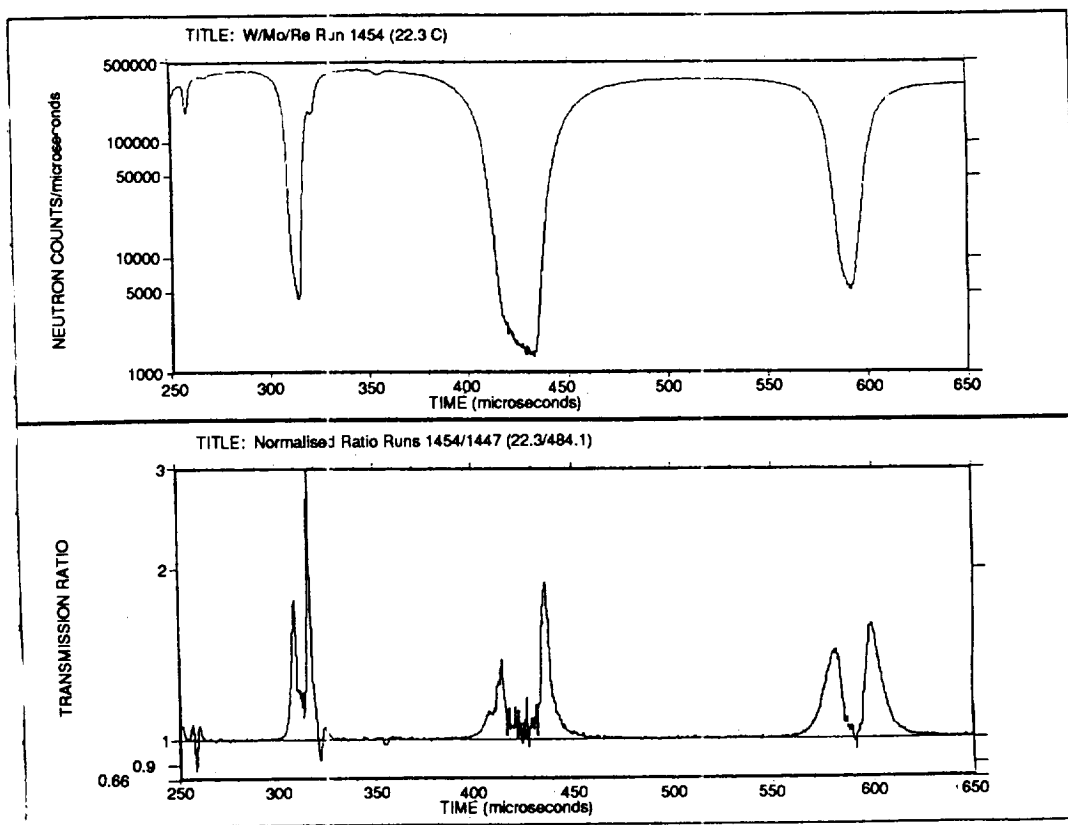


Figure 9-13. Measured neutron transmission vs. time of flight in Mo-Re-W material sandwich.

Electric propulsion, powered by nuclear or solar power, can contribute to several important SDI missions. Electric propulsion can be used for platform orbit raising from low-earth orbit using a Space Reactor Power System (SRPS). This option provides increased payload margins compared to advanced chemical propulsion.^{31,56,117} Electric propulsion and SRPS power can also be used for continuous defensive maneuvering to make platform and satellite tracking a full-time job for an adversary. Housekeeping SRPS power coupled with electric propulsion can be used for platform stationkeeping, thus prolonging spacecraft orbital lifetime. Scheduled platform maintenance and resupply functions can best be accomplished using a high specific impulse, reusable, solar electric vehicle. Solar-powered electric propulsion would allow a ferry vehicle to come to very low orbits (250-300 km) without adverse political or safety consequences associated with nuclear power, enabling a single vehicle to perform the complete resupply function. Finally, when a platform or satellite has reached the end of its useful life, the electric propulsion system can be used to boost the platform to a disposal orbit using the SRPS decay power. The development of suitable space power sources is key to enabling these capabilities.

The SP-100 SRPS is presently being developed by the Power Office of the Key Technologies (KT) Directorate of the SDIO. The SP-100 power system is the nuclear option in the SDIO baseload power development program and is based on a 2.6 MW_t, fast-spectrum, liquid-metal-cooled reactor coupled with an out-of-core thermoelectric conversion system. An SP-100 Flight Experiment has been conceived as a first demonstration of space-based operation of the SP-100 SRPS, with a primary goal being the demonstration of the seven-year, full-power life of the SP-100 power system. Arcjet electric propulsion is baselined as the active load for the SP-100 Flight Experiment and will be used to demonstrate Nuclear Electric Propulsion (NEP) orbit transfer and maneuvering capabilities. Demonstration of NEP is the second objective of the mission.

This section describes some general mission capabilities of advanced arcjet technology using 30-kW and 100-kW and SRPS power levels. Baseline descriptions of 100-kW_e and 30-kW_e SP-100 Flight Experiment spacecraft and mission possibilities are presented, along with a discussion of subsystems technology readiness. Deployment of a constellation of space platforms is considered in terms of launch vehicle, platform mass and launch rate. Finally, the use of electric propulsion for defensive maneuvering (to complicate hostile tracking during times of threat) is considered. All of the orbital analysis described is based on well-known orbital mechanics for low-thrust, electric propulsion transfers. More detailed information concerning the analyses described in this chapter can be found in Refs. 25, 26, 29, 31, 33, 36, 37 and 116.

10.1 ARCJET MISSION CAPABILITIES

Mission capabilities are discussed for arcjet NEP with a 100-kW nuclear power system. The capabilities are described in terms of payload delivered and trip time as functions of orbital altitude and inclination. Launches are assumed from Kennedy Space Center with the STS.

10.1.1 Arcjet Propulsion System Parameters

The arcjet system technology level assumed for this study is presented in Table 10-1. The baseline system parameters in Table 10-1 represent present performance levels.

Table 10-1. Assumed Arcjet Performance Characteristics

Parameter	Value
Propellant	NH ₃
Input Power Per Thruster (kW)	25
Thruster Efficiency	0.30
PPU Efficiency	0.95
Specific Impulse (s)	800
System Specific Mass Per Engine (kg/kW)	5.0
Thrust Per Engine (N)	1.9

Constraints and Assumptions

Due to safety concerns, the SRPS cannot be operated until the spacecraft has reached a 825-km (450-nmi) orbit. Therefore, a chemical stage will be used to boost the spacecraft to this orbit from shuttle orbit, which is assumed to be 519 km (280 nmi) for this study, before SRPS operation is begun. It is also assumed that a single, dedicated shuttle launch is used. The maximum STS lifting capacity 29000 kg from KSC is assumed. The chemical stage will not perform any part of required plane changes. A chemical system ($I_{sp} = 310$ s) which could be used to make this orbital altitude change, corresponding to a delta-V of 304 m/s, weighs 2720 kg. The total tankage and feed system mass, $M_{f/s}$, is obtained for a given propellant load, M_p , using

$$M_{f/s} = 118.07 + 0.17 M_p + M_p^{2/3} \quad (10-1)$$

This equation includes a 10 percent contingency on all components. This system is to provide a constant mass flow of 0.28 g/s of ammonia to each arcjet thruster for up to a six-month mission duration.

In addition, it is assumed that the shuttle carries 4100 kg of equipment to support the SRPS and payload. The spacecraft bus, which includes the primary command, control and communications equipment, is assumed to have a mass of 1000 kg. The mass assumed for the diagnostics equipment is 500 kg. The mass summary of the known spacecraft components is given in Table 10-2.

Table 10-2. Assumed Mass Summary for the 100-kW_e Arcjet Spacecraft

Subsystem	Mass (kg)
SRPS	3000
Spacecraft Bus	1000
SRPS/Thruster System Diagnostics	500
Arcjet Module	500
Propellant Feed System	*
Miscellaneous	500

* Depends upon propellant load, see above.

Results

NEP transfers are assumed to start at 825 km (450 nmi) and extend through a range of altitudes out to 35743 km (19300 nmi). Orbital inclination changes are also considered to define the complete payload delivery envelope. In some cases, NEP could drive the spacecraft beyond 35743 km, the maximum altitude considered in this analysis. "Payload" is to be as the mass margin at a specific orbital altitude and inclination, assuming a fully-loaded shuttle at launch.

Orbital analysis shows that a 100-kW_e NEP system consisting of baseline 25-kW ammonia arcjets and a 100-kW_e SRPS can raise itself to all altitudes and make changes in orbital inclination of up to 30 degrees with significant payload margins, as can be seen in Fig. 10-1. The transfer times for these maneuvers are shown in Fig. 10-2, and range from a few days to 5.5 months.

10.2 SP-100 FLIGHT EXPERIMENT DEFINITION

The SP-100 Flight Experiment, a flight demonstration of a 100-kW_e class SRPS, has been proposed as an adjunct to the SP-100 program using an electric propulsion module as an active load.¹²³ The primary objective of this proposed flight test is the demonstration of space-based nuclear power system operation. The secondary objective of the SP-100 Flight Experiment is to demonstrate nuclear electric propulsion for orbit raising and maneuvering. As yet undefined tertiary experiments are also possible.

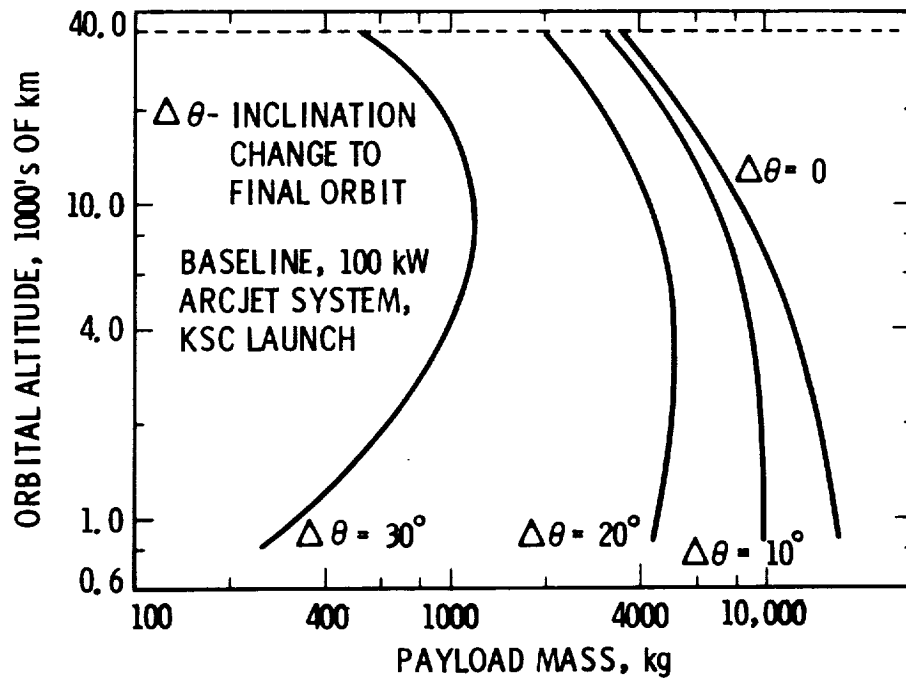


Figure 10-1. Arcjet SRPS payload capability as a function of orbital altitude and inclination.

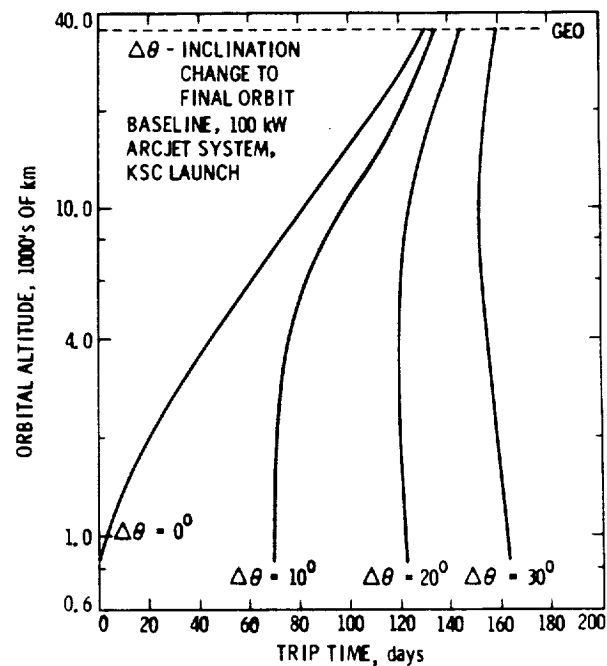


Figure 10-2. Arcjet SRPS trip time as a function of orbital altitude and inclination.

The Flight Experiment test goal is to operate the SP-100 SRPS for its seven-year, full-power life. An active power system load is required for up to six months to verify power system compatibility with a payload and to satisfy potential users of this compatibility.^{120,123} No alternative to electric propulsion has been identified for the active load which meets the Flight Experiment constraints as presently defined.¹²³ The constraints include a low developmental risk and cost, wide performance throttleability, and scalability to future SDI power levels well beyond the 100-kW_e range being considered for the flight demonstration. This mission will provide a unique opportunity to examine the control scenarios required for NEP orbit transfer, to examine the maneuvering of an orbiting spacecraft to enhance operations and survivability, and to examine a representative transfer similar to that required for the SDI. Arcjet electric propulsion has been selected as the baseline electric propulsion system for the SP-100 Flight Experiment.¹²³

This section summarizes top-level studies where baseline spacecraft concepts and mission options were developed for 100-kW and 30-kW SP-100 Flight Experiment options. Detailed descriptions of proposed arcjet/gimbal assemblies, power conditioning unit (PCU) subsystem, propellant feed and storage subsystem, thermal control needs, diagnostics package, and telemetry requirements can be found in the task publications. Projected propulsion system performance was described for two different arcjet technology levels. The spacecraft are assumed to be placed into orbit using a Titan IV Expendable Launch Vehicle (ELV) from KSC. Atlas 2AS and Titan III ELVs are also considered for the 30-kW spacecraft. Specific mission performance is reported for the 100-kW spacecraft for spacecraft deployment demonstrations to SDI platform orbits, a spacecraft on-orbit storage demonstration mission, and an orbit raising round trip. The 30-kW spacecraft is characterized in terms of payload delivered and trip time as functions of spacecraft delta-V.

10.2.1 System Definition

A block diagram of the conceptual arcjet SP-100 Flight Experiment vehicle is shown in Fig. 10-3. It includes all of the primary system components for converting SRPS power into thrust. The power system consists of the SP-100 SRPS which provides both 28-V and 200-V (primary) outputs. The spacecraft bus contains the navigation and the command, data handling and telecommunications subsystems which receive and process ground commands and control overall system operation. The arcjet PCU subsystem starts and runs the arcjets. The propellant system runs parallel to the power train and includes the tankage, valves, lines, etc., required to provide a constant propellant flow rate to each operating engine. The diagnostic package provides the ability to monitor the reactor radiation-induced environment, to measure the particulate and field emissions from the arcjet thrusters in the vicinity of the electric propulsion module and to examine the spacecraft/space environment interactions. Thermal control allows for the rejection of waste heat from the arcjet and PCUs while the structural members connect the subsystems. The expendable chemical boost stage raises the spacecraft to a safe reactor orbit. Any tertiary experiments would also have to be interfaced to the spacecraft bus.

The SP-100 SRPS consists of the Power Generation Module (PGM) and the User Interface Module (UIM). The PGM consists of the reactor, shield, auxiliary cooling loop, thermoelectric electromagnetic (TEM) pumps, power converters, multiplexers and the heat rejection radiator. The UIM is composed of the separation boom, shunt dissipator and the user interface equipment module.

10.2.1.1 100-kWe Spacecraft Concept. A proposed 100-kW_e spacecraft configuration for the SP-100 Flight Experiment is shown in Fig. 10-4. This system is comprised of a 100-kW_e SP-100 SRPS, spacecraft bus, an arcjet propulsion module, and an SRPS radiation/arcjet plume diagnostics package. This spacecraft concept utilizes an end thrust design, through the spacecraft centerline, so that the deployment boom is in compression during thrusting.

The arcjet propulsion module is comprised of: three sets of 4 engines with each set of engines on a single-gimballed platform, a PCU system, the propellant feed system, thermal control, a radiation/thruster efflux diagnostics package and associated structure. During arcjet system operation, one engine from each platform operates to provide thrust. After 1500 hours of operation, an unused engine replaced the operating engine. Three engines are used to accumulate a total operating time of 4500 hours. At that time the arcjet mission has been completed. A fourth set of three engines is provided as backup. There are two dedicated PCUs per gimballed platform with one serving as a spare. Separate propellant feed lines provide ammonia to each platform. Three thrusters can be operated at maximum power using 93 kW_e of input power, accounting for the 98 percent efficiency of the PCU system.

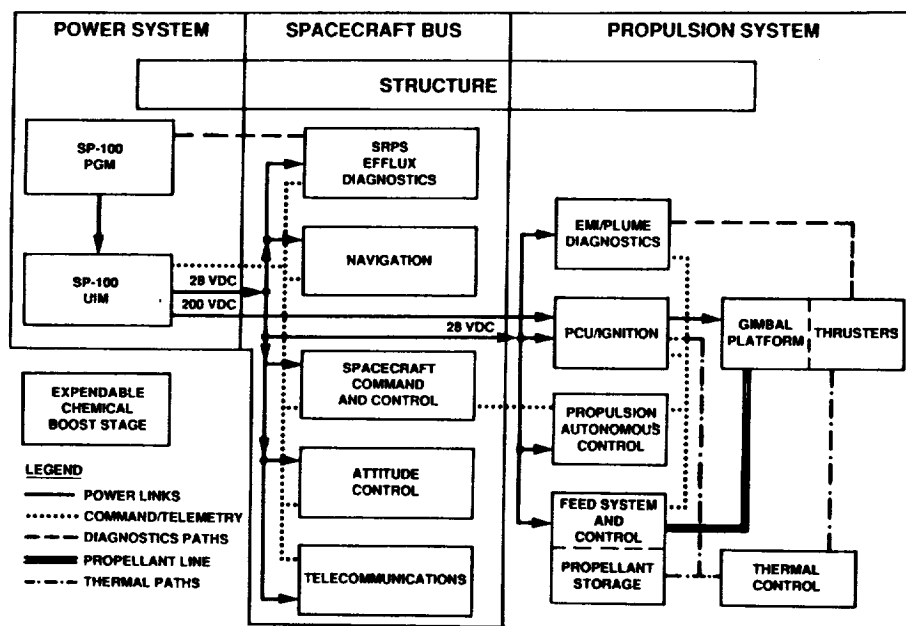


Figure 10-3. Arcjet NEP system block diagram.

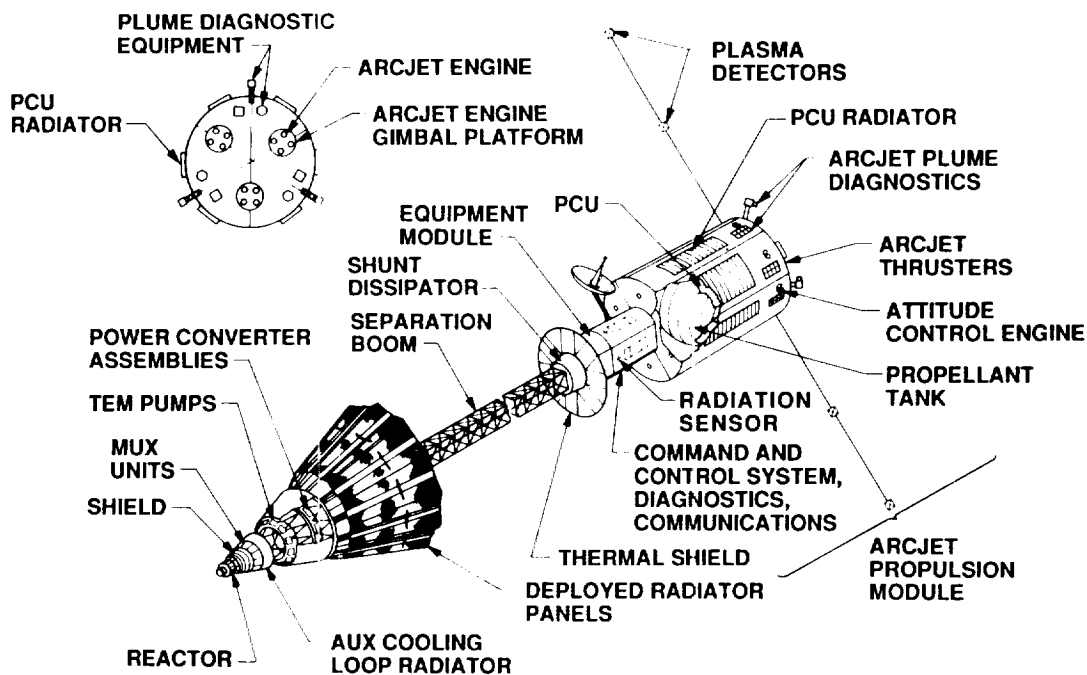


Figure 10-4. Proposed spacecraft configuration for the SP-100 Flight Experiment (100-kW spacecraft).

The thruster module is enclosed within a 4.4-m outside diameter, 6-m long cylinder with the propellant tank located on the end nearest the SRPS. The three sets of arcjet engines and gimbals are located on the end of the cylinder opposite the SRPS. The PCU subsystem is located within the cylindrical enclosure between the propellant tank and engine modules. The six PCU low-temperature radiators are located on the outer surface of the cylindrical enclosure. The combined thrust of this system is 7.6 N when three engines are operating at full power. The command, data handling and telecommunications functions are part of the spacecraft bus.

A mass summary of the spacecraft components is provided in Table 10-3. The mass goal for the 100-kW_e SP-100 SRPS is given as 3000 kg. The propulsion system is assumed to have a mass of 575 kg excluding propellant, tankage and the feed system. The spacecraft bus, which includes the primary command, control and communications equipment, is assumed to have a mass of 1250 kg. The mass assumed for the diagnostics equipment is 300 kg. An additional 550 kg has been set aside as a contingency (approximately 10 percent of the total spacecraft mass excluding the propellant and propellant feed system).

The arcjet propulsion subsystem is comprised of three identical component strings, each individually fed from the SP-100 SRPS and central propellant storage tank. A schematic/block diagram of one of these component strings is shown in Fig. 10-5. The component string is made up of an arcjet engine/gimbal platform (4 engines), a power distribution system including two PCUs, a propellant feed system, and thermal control hardware. More detailed information is given in Ref. 26.

Table 10-3. Projected Mass Summary for the 100-kW_e SRPS SOA Arcjet Flight Experiment Spacecraft

Subsystem	Mass (kg)
SRPS	3000
Spacecraft Bus	1250
Thruster System Diagnostics	300
Arcjet Module	300
Propellant Feed System	*
Contingency	550

* Depends upon propellant load (see Propellant Feed Subsystem section) and launch vehicle mass limit.

10.2.1.2 30-kW Baseline Spacecraft. One of the flight demonstration options being considered includes operation of a 30-kW_e power system for six months to one year in space with a 30-kW_e arcjet system. This option is aimed at minimizing the flight experiment cost while meeting the flight demonstration goals.¹²⁰ A single string 30-kW_e arcjet propulsion system is being developed for the SDIO, consisting of an arcjet, PPU and propellant subsystem.³¹

A proposed 30-kW spacecraft configuration for the SP-100 Flight Experiment is shown in Fig. 10-6. This system is comprised of a 30-kW_e SP-100 type reactor, spacecraft bus, an arcjet propulsion module, and a reactor/arcjet plume diagnostics package. This spacecraft concept utilized an end thrust design, through the spacecraft centerline, so that the deployment boom is in compression during thrusting. A mass summary of the spacecraft components is provided in Table 10-4. More detailed information is given in Ref. 116.

The thruster module is enclosed within a cylindrical volume with a maximum diameter of 3.5 m, which ends in a conic section where the engines are located (see Fig. 10-6). The set of arcjet engines is located on the end of the cylinder opposite the reactor system. The PPU system is located in the cylindrical enclosure between the propellant tank and engine modules with its radiators facing out to space on the outer surface of the enclosure.

10.2.2 Mission Analysis

10.2.2.1 100-kW Spacecraft. The following analysis is based on the well-known orbital mechanics equations for electric propulsion transfers⁵⁶ and on the propellant feed subsystem characterization given above. A launch from KSC using the Titan IV ELV is assessed for three proposed Flight Experiment scenarios. It is assumed that up to three arcjets can operate simultaneously on a spacecraft.

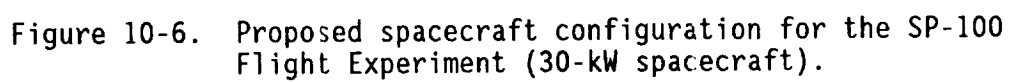
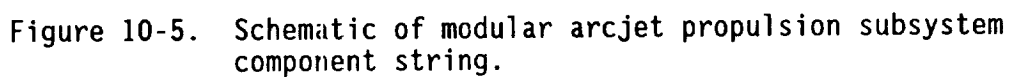


Table 10-4. Projected Mass Summary for the 30-kWe SRPS SOA
Arcjet Flight Experiment Spacecraft

Subsystem	Mass
SP-100 Reactor System Specific Mass (at 30 kW _e)	73 kg/kW _e
Arcjet + PPU Specific Mass	2 kg/kW _e
4 Arcjets + 4 PPUs per Spacecraft	8 kg/kW _e
Spacecraft Bus Mass	800 kg
Diagnostics Package Mass	300 kg

The arcjet system technology level used for this mission analysis is presented in Table 10-5. A baseline engine/PCU required 27.9 kW_e of input power when accounting for the 90 percent efficiency of the PCU. Therefore, a system of three engines requires 83.7 kW_e.

As before, due to safety concerns, the SRPS should not be operated until the spacecraft has reached a 925-km (500 nmi) SRO. An expendable chemical upper stage will boost the NEP flight demonstration spacecraft to SRO from Titan IV separation orbit. It is further assumed that the upper launch mass limit for the Titan IV ELV is 17,700 kg,⁵⁹ that 3300 kg of ASE-type equipment is needed and a dedicated Titan IV ELV is required. The orbit and launch vehicle assumptions are summarized in Table 10-6.

Three missions which could be used to demonstrate SRPS operation are examined. The first two missions involve power system deployment to possible SDI platform orbits of 3000 and 10000 km. An advantage of these orbits is that they contain a minimum of man-made orbital debris, reducing the chance of a collision.⁶⁹ The final mission examines an orbit-raising, round-trip from SRO to some higher orbit with return to SRO.

A 3000-km circular orbit, with a final inclination between 55° and 85°, has been identified as a potential SDI platform orbit.⁷⁰ As a result, this orbital altitude was chosen for this study so that the mission would address the control scenarios required for a low-altitude, high-inclination change, low-thrust mission.⁷⁴ The orbital analysis is done such that the entire available propellant load is consumed to reach the highest inclination possible. In this analysis, the vehicle would achieve a 48.5° inclination, 3000 km orbit in 66 days.

A 10000-km circular orbit was chosen as the target altitude for an arcjet NEP spacecraft throttling demonstration and is compared to a non-throttled case. Again, the analysis is done such that the entire available propellant load is consumed to reach the greatest orbital inclination possible. The results are summarized in Table 10-7. A 10000-km, 5° final orbit could be achieved in 65 days.

Table 10-5. Assumed Arcjet Performance Characteristics (100-kW Study)¹¹

Parameter Technology Level	Baseline
Propellant	NH ₃
Input Power per Thruster (kW _e)	25.1
Thruster Efficiency	0.39
Specific Impulse (s)	867
Thrust per Engine (N)	2.3
Thruster Lifetime* (hours)	5730
PPU Efficiency	0.90
System Specific Mass per Engine** (kg/kW _e)	2.0

* 573-hour lifetime measured.
**Excludes SRPS, spacecraft bus propellant, tankage and feed system.

Table 10-6. Launch Vehicle and Orbit Assumptions⁵⁹

Parameter	<u>Launch Vehicle</u> Titan IV
Payload (kg)	17000
ASE Mass (kg)	3300
Altitude (km)	300 x 925
Inclination	28.5

When the arcjet system is throttled (see Table 10-7), the flight experiment spacecraft is raised from a 925-km, 28.5° orbit to a 10000-km, 28.5° orbit. From this orbit, the vehicle is moved to a 10000-km, 5° orbit with one arcjet operating at full power. The next leg is accomplished using two SOA arcjets operating at full power and results in a final orbit of 10000 km, at 33.5°. The final leg is completed with three arcjets operating at full power until all the available propellant is consumed. This results in a final orbit of 10000 km at 38.5°. This throttling method is not trajectory-optimized so the final orbit has a lower inclination than the unthrottled case. Throttling of the engines provides a demonstration of the SRPS load-following capability in splitting power between the user and power system shunt and demonstrates the flexibility of both the arcjet NEP system and the SP-100 SRPS.

Table 10-7. Summary of Arcjet Throttling Orbital Analysis, SRO to a 10000-km Final Orbit (100-kW Study)

Arcjet Operating Technology Arcjets		Power (kW _e)	Initial Orbit Alt., Incl. (km, deg)	Final Orbit Alt., Incl. (km, deg)	Trip Time (days)	Total ΔV (m/s)	
Un-throttled	Baseline	3	83.7	925, 28.5	10000, 46.5	65	3843
Throttled	Baseline	3	83.7	925, 28.5	10000, 28.5	45	3809
		1	27.9	10000, 28.5	10000, 31.5	19	
		2	55.8	10000, 31.5	10000, 33.5	6	
		3	83.7	10000, 33.5	10000, 38.5	9	

The final mission considered is a round-trip mission from SRO to some High Earth Orbit (HEO) and back to SRO to simulate an Orbit Transfer Vehicle (OTV) mission. This mission provides an opportunity to examine the control scenarios required for a round-trip type OTV mission.⁷⁴ No plane changes are considered. A spacecraft would reach a HEO of 6300 km in 39 days and return to SRO in 22 days.

10.2.2.2 30-kW Spacecraft. Flight mission performance was examined for three launch vehicles; the Titan 4, Titan 3, and Atlas 2AS, launched from the Kennedy Space Center. Mission scenarios were defined in terms of payload mass delivered as a function of delta-V up to a maximum trip time of 6 months. Payload mass was defined as the excess mass when the SP-100 reactor system, arcjet propulsion system, spacecraft structure, bus, telemetry, and diagnostics are deducted from the spacecraft mass in a 900-km circular orbit. The payload mass can be used to accommodate more ammonia or can be used for auxiliary experiments.

The spacecraft assumed for the analysis have a propulsion module consisting of 4 arcjets and 4 PPUs. Since each arcjet/PPU is assumed capable of 1500 hours operation, the total operational capability is 250 days, 60 days more than the assumed 6-month maximum trip time.

For the Atlas 2AS scenario, 6560 kg are deployed into a 900-km circular orbit. An arcjet system launched from an Atlas 2AS has sufficient fuel to operate for 4 months; this corresponds to a 5000 m/s delta-V transfer with no payload. If the arcjet propellant system were scaled down for 2 months' operation, the arcjet stage could transfer 1400 kg of payload to a 2200 m/s delta-V. This corresponds to, for example, a transfer to a 10,000-km altitude, with no plane change. Of course, larger payloads can be carried to smaller delta-Vs, if desired.

10.3 CONSTELLATION DEPLOYMENT

This section outlines considerations for deployment (orbit raising) of a constellation of spacecraft, covering a range of payload masses into high-inclination orbits.³³ A constellation of space platforms is defined as a group of spacecraft, space platforms or satellites which work together to accomplish a particular mission. It is assumed that 100 kW of electric power is on board the platform and that launches are from Vandenberg Air Force Base, California using either Titan IV or Advanced Launch System (ALS) launch vehicles. Ammonia arcjet and xenon ion electric propulsion systems were compared to advanced chemical propulsion in each case. Constellation deployment is characterized in terms of the number of launch vehicles required and the total deployment time. These depend on spacecraft mass, launch vehicle, upper-stage propulsion system, and the time between launches. The total constellation deployment time is also described as a function of the number of launches and the time between launches. More information is available in Ref. 33.

10.3.1 Constraints and Assumptions

The upper-stage propulsion system parameters assumed for this study are summarized in Table 10-8. A chemical propulsion system with Centaur G'-type performance is assumed for the chemical upper-stage propulsion system. This system is based on liquid hydrogen/liquid oxygen engine technology providing a specific impulse of 450 s. The analysis assumes a dry mass-to-fueled mass ratio of 0.15 for the chemical system. The ammonia arcjet system performance is assumed to have a specific impulse of 967 s and an efficiency of 37 percent at 30 kW_e. This performance level is considered advanced arcjet technology. The analysis is conducted assuming an arcjet propulsion system specific mass of 2.0 kg/kW_e, an ammonia tankage fraction of 0.20, and an arcjet lifetime of 1500 hours. A minimum system of three 30-kW_e arcjets is required to process the power and perform the orbit raising function. If the orbit transfer requires more than 1500 hours of burn time, then another set of arcjets must be included on the upper stage. The xenon ion propulsion system performance is derived from recent tests of a 25-cm diameter engine operated at 4.5 kW_e at the Hughes Research Laboratory.^{6,7} This engine exhibited a specific impulse of 3890 s and an efficiency of 76 percent. A propulsion system specific mass of 10.0 kg/kW_e, a xenon tankage fraction of 0.15, and an ion engine lifetime of 4500 hours are assumed. A minimum system of 22, 4.5-kW_e ion engines is required to process the power and perform the orbit raising function.

The SP-100 SRPS power system has a nominal electrical output of 100 kW_e at 200 V_{dc}. The target specific mass is 30 kg/kW_e.⁴³

Table 10-8. Propulsion System Parameters (Constellation Deployment Study)

Parameter	Value		
Propulsion System	Chemical	Arcjet	Ion
Propellant	LH ₂ /LO ₂	NH ₃	Xe
Thruster Input Power (kW)	-	30	4.5
Specific Impulse(s)	450	967	3890
Electric Efficiency	-	0.37	0.76
Thruster Lifetime (hours)	-	1500	4500
Propulsion Sys Specific Mass (kg/kW)	-	2.0	10.0
Dry Mass/Wet Mass	0.15	-	-
Tankage Fraction	-	0.20	0.15

Constellation deployment is considered using two launch vehicles; the Titan IV and the ALS. Only launches from Vandenberg Air Force Base are considered. The Titan IV can deliver a 15,500-kg payload to a 185-km, 70° inclination orbit which will be referred to as Low Earth Orbit (LEO) in this section.⁶⁰ It is assumed that the ALS can deliver a 40,900 kg payload to LEO. Furthermore, it is assumed that the upper-stage propulsion system deploys the SDI constellation from LEO to a polar orbit (90° inclination) at an altitude of 2000 km. The SDI platforms are assumed to have 100 kW_e of electric power on board which can be used by the electric propulsion upper stages during transfer. The platform mass, number of days between launches, and the number of platforms in the constellation are taken as variables in the analysis.

10.3.2 Platform Mass Considerations

Deployment of a constellation of spacecraft using electric propulsion upper stages results in a large reduction in the number of required launch vehicles, as seen in Fig. 10-7. Figure 10-7 shows how the total number of launch vehicles required to deploy a constellation of 50 space platforms varies as the platform payload mass is increased from 5,000 kg to 15,000 kg. The reduction in the number of launch vehicles results primarily from a reduction in the propellant mass required in LEO when using electric propulsion to deploy the constellation. For example, deployment of a constellation of 50 10,000-kg platforms using the Titan IV requires 76 launches with a chemical upper stage. The number of launches is reduced to 54 with an ammonia arcjet upper stage and 40 with a xenon ion upper stage because of their higher specific impulses. The same general trends occur when the larger ALS launch vehicle is considered.

A larger payload mass can be placed in orbit using electric upper stages, when compared to chemical upper stages, if a dedicated (single) launch vehicle is used to deploy each platform. Use of a dedicated launch vehicle alleviates the need for the on-orbit assembly required if multiple launches were to be used. Figure 10-7 shows the maximum platform payload mass per Titan IV launch is 6,570 kg using a chemical upper stage; if an arcjet upper stage is used then the maximum payload is 9,200 kg; and if an ion upper stage is used then the maximum payload is 12,750 kg. In the case of an ALS launch, two platforms with payloads of 8,670 kg each can be placed in orbit using chemical upper stages, while two platforms with masses of 12,000 kg using arcjet upper stages and two platforms with masses of 17,000 kg using ion upper stages can be deployed. In addition, electric propulsion upper stages should provide the spacecraft designer more flexibility. The initial mass of the platform should be less sensitive to payload mass changes since the use of electric propulsion provides a larger mass margin than chemical upper stages. Hence, the same launch vehicle can be used for a wider range of payload designs.

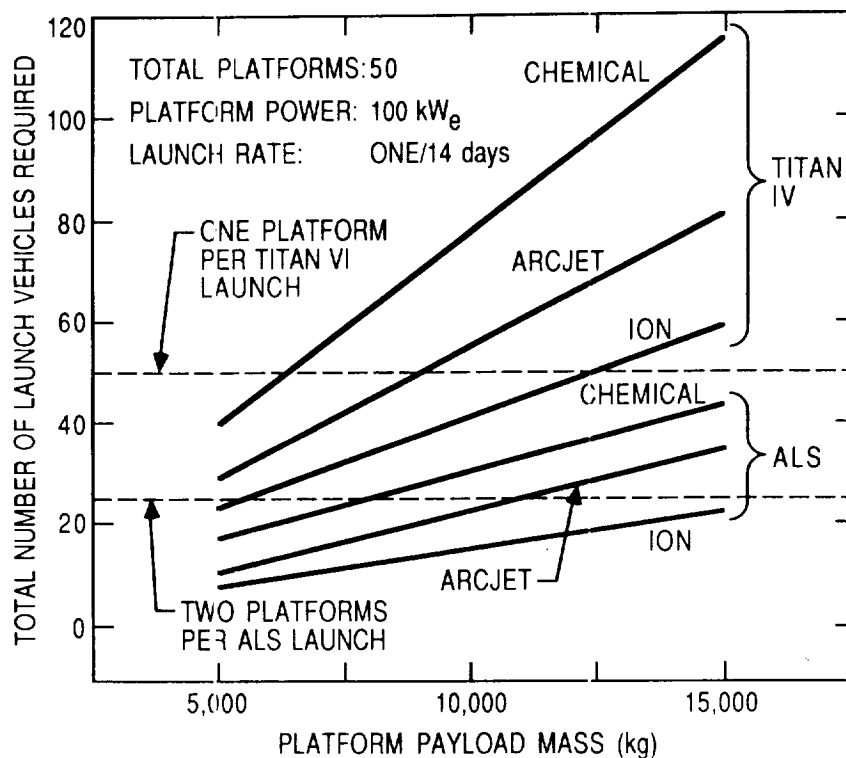


Figure 10-7. Effect of platform payload mass on the number of launch vehicles needed for constellation deployment.

The total deployment time for a constellation of spacecraft can be much lower using electric propulsion upper stages, even though a single electric propulsion transfer takes longer than a chemical transfer. This is illustrated in Fig. 10-8 where the deployment time for a 50-platform constellation is plotted as a function of the platform payload mass assuming one launch every two weeks. The platform payload mass was varied from 5,000 kg to 15,000 kg. The results are also presented as a function of launch vehicle and upper stage technology. For a 10,000 kg payload launched by Titan IV, a chemical upper-stage deployment requires 2.9 years, while an arcjet system requires 2.3 years, and an ion system requires 2.8 years. For the cases considered above, the maximum individual transfer time occurs for the 15,000 kg payload and is 116 days for the arcjet and 187 days for the ion upper stage. The electric systems can deploy the constellation faster than the chemical system because they require fewer launches.

The time required for on-orbit assembly activities is not included in the deployment time shown in Fig. 10-8. Such assembly would be required when multiple launches are used to deploy a space platform. This would probably be a larger penalty when chemical upper stages are used due to the reduced platform payloads available. It is also important to consider that when multiple launches are used, some portion of the on-orbit assembly activities will probably deal with fueling the platforms. The fuels used by electric systems generally do not pose the contamination and explosion hazards associated with chemical propellants.

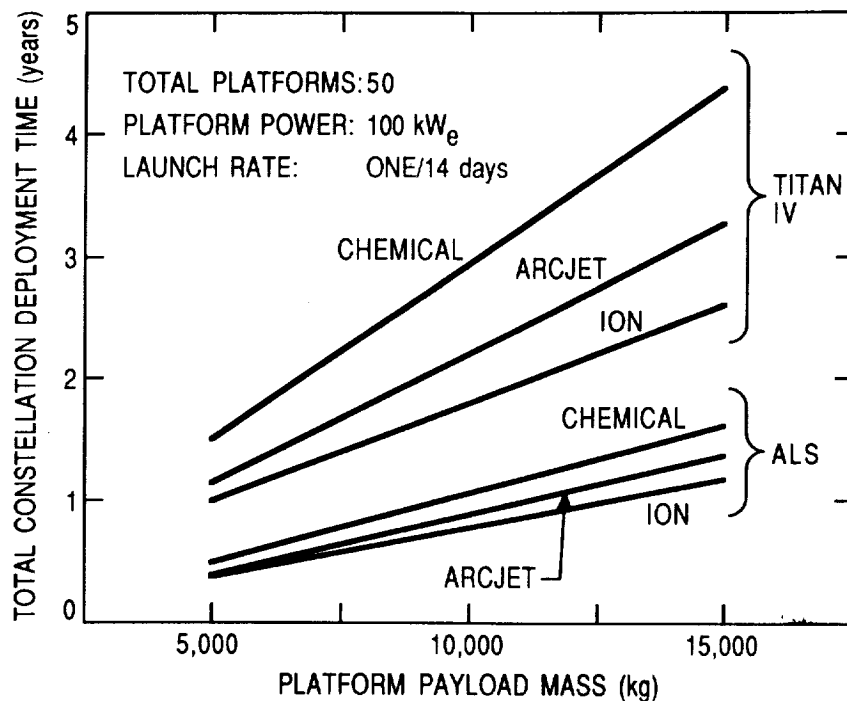


Figure 10-8. Effect of platform payload mass on the total constellation deployment time.

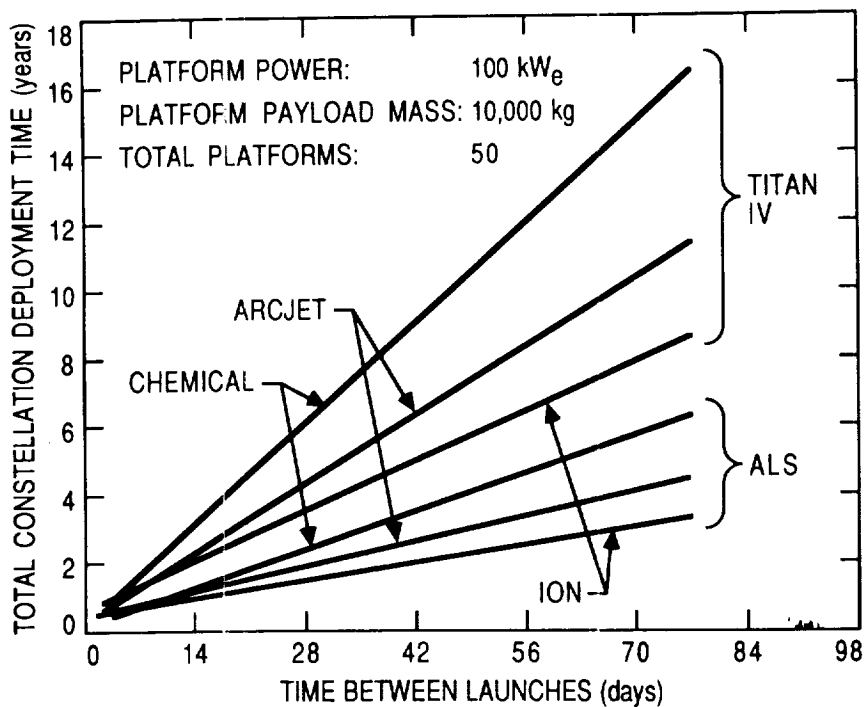


Figure 10-9. Total constellation deployment time as a function of the time between launches.

10.3.3 Effect of Launch Rate

Total constellation deployment time is also driven by the launch rate. This is shown in Fig. 10-9 where the deployment time for a constellation of 50 10,000-kg platforms is presented as a function of the time between launches. The time between Titan IV or ALS launches is varied from one week up to 10 weeks. The total constellation deployment time is lower for the electric propulsion upper stages. The time savings increases as the time between launches increases when using electric propulsion upper stages. This same general trend is also exhibited when an ALS launch vehicle is used. Again, this is a reflection of the fact that fewer launches are required when using electric propulsion upper stages.

10.3.4 Effect of Constellation Size

Deployment of large constellations is driven, primarily by the number of platforms and, hence, the number of launches; not by the upper stage transfer time. This can be seen in Fig. 10-10 where the total constellation deployment time is presented as a function of the total number of platforms in the constellation. A launch rate of once every two weeks and a payload mass of 10,000 kg are assumed. The electric propulsion upper stages provide a reduced deployment time, compared to the chemical system, when more than 10 platforms are deployed by Titan IV launch. Ten platforms, a small constellation size, can be deployed by each upper stage in 7.2 months

(the cross-over point) if the launch rate is once every two weeks. The cross-over point at which electric propulsion enables faster constellation deployment depends on individual upper-stage transfer times and the launch rate. As the time between launches becomes longer, the cross-over point at which electric propulsion becomes deployment-time competitive occurs for a smaller constellation size. As the individual upper-stage transfer time increases, the point at which electric propulsion becomes deployment-time competitive occurs for a larger constellation size.

If the more capable ALS launch vehicle is used, the deployment time tradeoff between the upper-stage systems changes, as shown in Fig. 10-10. The cross-over point is 23 platforms for the arcjet system and 28 platforms for the ion system when compared to chemical propulsion. If more than 33 platforms are involved, the ion system enables faster deployment times than the arcjet system. This cross-over point is driven by the higher dry mass of the ion system and its longer transfer times. It should be noted that even though the chemical system can deploy small constellation slightly faster than electric systems, more launches are required to get the chemical upper stages into LEO, adding to the costs of deployment.

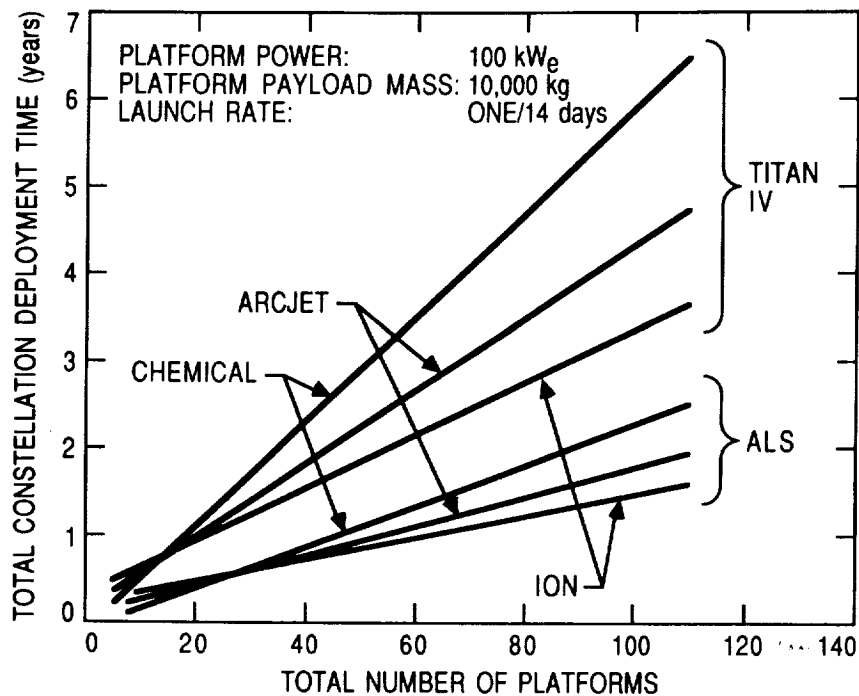


Figure 10-10. Effect of platform number on constellation deployment time.

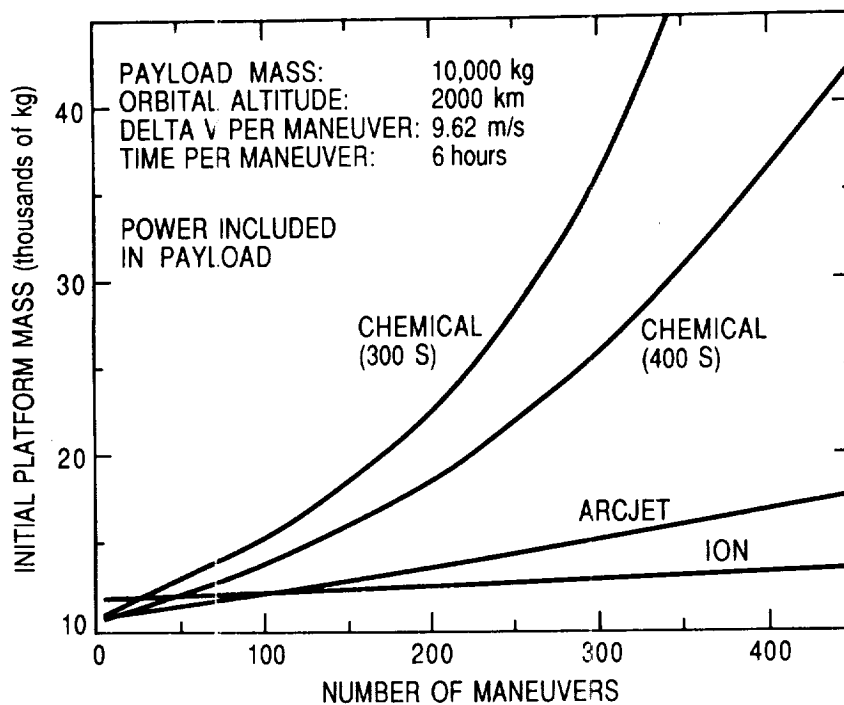


Figure 10-11. Initial platform mass as a function of the number of maneuvers. Power included in payload.

10.4 DEFENSIVE MANEUVERING

There are two types of defensive maneuvers; the fast maneuver to dodge an incoming threat,¹¹⁹ and the continuous, low-thrust maneuver which produces non-Keplerian orbits.⁹⁷ The purpose of the latter type of maneuvering, which is addressed in this publication, is to complicate hostile tracking in order to prevent an attack. This is accomplished by disrupting correlation of the tracking measurements, which then forces a need to do a reinitialization of the target. This process can take from hours to days to accomplish.

This section outlines considerations for continual spacecraft defensive maneuvering. The defensive maneuvering analysis assumes that the power needed for the electric propulsion system is alternately included in the payload or in the propulsion system mass. Xenon ion and advanced ammonia arcjet electric propulsion systems are compared with baseline and advanced chemical maneuvering technologies. Defensive maneuvering is described in terms of the initial platform mass, the number of evasive maneuvers and the delta-V per unit time required for the maneuver. More information is presented in Ref. 33.

10.4.1 Constraints and Assumptions

Two chemical maneuvering propulsion systems are assumed: a baseline system with a specific impulse of 300 s, and an advanced system with a specific impulse of 400 s. These systems effectively bound the present (N_2O_4/MMH

with a specific impulse of 325 s) and near-term (use of fluorinated or chlorinated oxidizer to get a specific impulse of 370 s) maneuvering technologies. The analysis assumes a dry mass-to-fueled mass ratio of 0.15 for the chemical systems.

The electric maneuvering system performance assumed is shown in Table 10-9. The ammonia arcjet system performance is assumed to have a specific impulse of 967 s and an efficiency of 37 percent at 30 kW_e. This performance level is considered advanced arcjet technology. The analysis is conducted assuming an arcjet propulsion system specific mass of 2.0 kg/kW_e, an ammonia tankage fraction of 0.20, and an arcjet lifetime of 1500 hours.

The xenon ion propulsion system performance is derived from recent tests of a 25-cm diameter engine operated at 4.5 kW_e at the Hughes Research Laboratory.^{6,7} This engine exhibited a specific impulse of 2890 s and an efficiency of 76 percent. A propulsion system specific mass of 10.0 kg/kW_e, a xenon tankage fraction of 0.15, and an ion engine lifetime of 4500 hours are assumed. A minimum system of 22 4.5-kW_e ion engines is required to process the power and perform the orbit raising function.

Table 10-9. Propulsion System Parameters (Defensive Maneuvering Study)

Parameter	Value	
	Arcjet	Ion
Propulsion System		
Propellant	NH ₃	Xe
Thruster Input Power (kW)	30	4.5
Specific Impulse(s)	967	3890
Electrical Efficiency	0.37	0.76
Thruster Lifetime (hours)	1500	4500
Propulsion System Specific		
Mass (kg/kW)	2.0	10.0
Tankage Fraction	0.20	0.15

Effective continuous maneuvering has been found to be possible depending on the assumptions made about an adversary's detection capabilities; Rudolph⁹⁷ assumed a detection field-of-view of 2°. For a satellite in geosynchronous orbit, this translated into a requirement that the satellite moves a minimum of 190 km in six hours, corresponding to a delta-V of 3.64 m/s. It was also determined that the propulsion system required a specific impulse between 1000 and 1500 s in order to keep the power requirements below 100 kW_e when maneuvering a 20,000 kg payload.

Continuous maneuvering of a platform with a 10,000-kg payload in a 2000-km polar orbit is considered in this publication. Rudolph's⁹⁷ assumption in that the platform must move out of a 2° field of view in six hours is applied

in this publication. This maneuver requires three complete orbits and has a delta-V of 9.62 m/s. Two cases are considered: (1) the power required for electric propulsion maneuvering is included in the 10,000 kg payload mass, and (2) the electric propulsion system must carry its own power source.

10.4.2 Power Included in Payload

Electric propulsion evasive maneuvering systems can greatly reduce the initial mass of a platform when the payload includes the necessary power. Figure 10-11 presents the initial platform mass as a function of the number of maneuvers. An arcjet upper stage results in a lower initial platform mass, when compared to the chemical maneuvering systems, regardless of the number of evasive maneuvers. The higher dry mass of the ion upper stage results in a higher initial platform mass compared to both the chemical systems and the arcjet system for up to 50 maneuvers. For more than 50 maneuvers the ion upper stage will result in a lower initial platform mass compared to the chemical systems, and for more than 110 maneuvers the ion system results in a lower initial platform mass than the arcjet upper stage. For example, if 200 maneuvers are required during the platform lifetime, use of the baseline chemical maneuvering system will require an initial platform mass of 20,700 kg, including a 10,000-kg payload. Use of an advanced chemical system results in a 18,200-kg initial mass, use of an arcjet system results in a 13,100-kg initial mass, and use of an ion system results in a 12,100-kg initial platform mass.

The electric power requirements for evasive maneuvering are fixed by the maneuver time and the electric engine thrust-to-power ratio. The initial platform power required to enable electric propulsion system maneuvering is given as a function of the number of maneuvers in Fig. 10-12 for a maneuver time of six hours. The platform mass decreases as maneuvers are completed. Consequently, Fig. 10-12 gives the power required for the first maneuver of a series. Since the ion engine has a lower thrust-to-power ratio (about half that of the arcjet) it requires approximately twice the power to complete a maneuver. For example, if 200 maneuvers are needed, then the arcjet system will need 75 kW_e while the ion system will need 134 kW_e to complete the first maneuver. This means that the arcjet system allows a larger non-power platform payload. Finally, it should be noted that if 100 kW_e is the maximum power available, then only the arcjet system is capable of making the required defensive maneuver, providing a capability for up to 425 maneuvers as shown in Fig. 10-12.

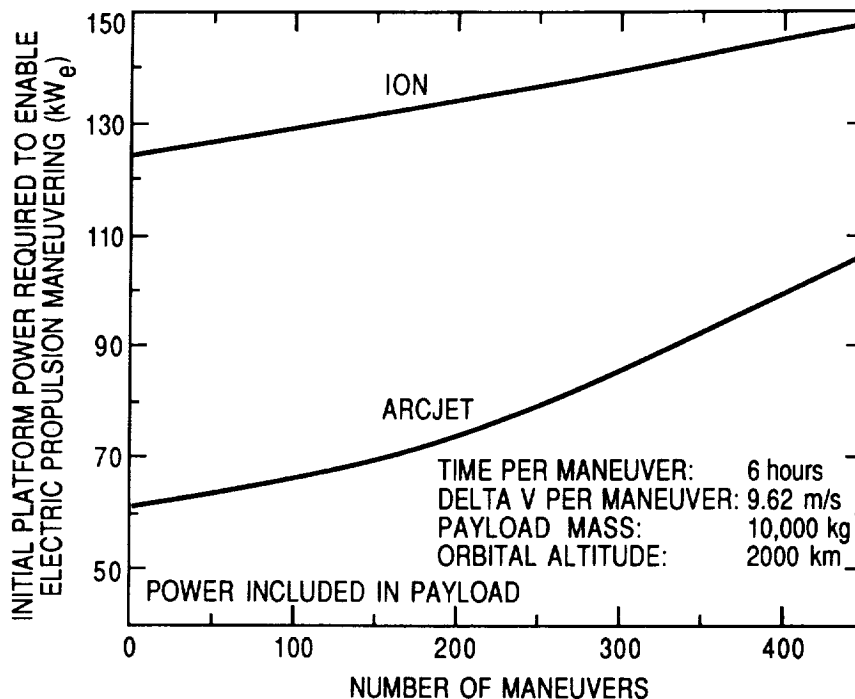


Figure 10-12. Initial payload power required to enable electric propulsion maneuvering as a function of the number of maneuvers.

10.4.3 Power as Part of the Electric Propulsion System

Figure 10-13 presents the initial platform mass as a function of the number of maneuvers for the case where the electric propulsion system carries its own power source. The curves assume that the power source specific mass is 30 kg/kW_e - the goal of the SP-100 SRPS development program. In this case, the electric propulsion systems will be more massive and, as a result, more maneuvers will be required before the electric systems become mass competitive with the chemical systems. For example, more than 90 maneuvers are required before the arcjet system provides a mass benefit compared to the baseline chemical system and more than 144 maneuvers before a payoff is demonstrated with respect to the advanced chemical system. Over 170 maneuvers are required before the ion system shows a benefit with respect to the baseline chemical system, and more than 240 maneuvers to show a mass benefit with respect to the advanced chemical system. If the SP-100 power source has a specific mass of 40 kg/kW_e, the number of maneuvers required to make the electric propulsion systems mass-competitive increases another 20 to 30 percent.

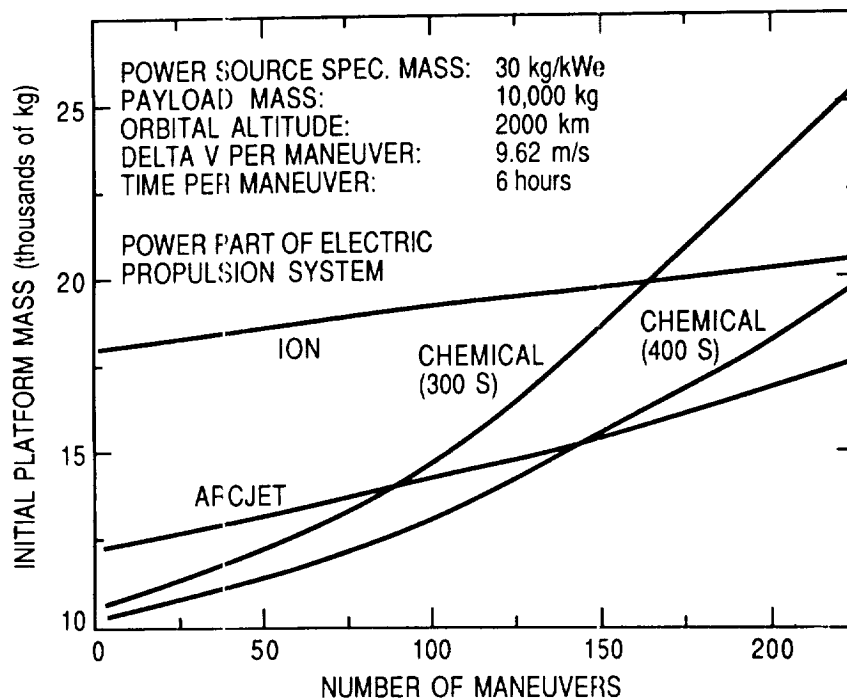


Figure 10-13. Initial platform mass as a function of the number of maneuvers. Power part of electric propulsion system.

The 50-percent increase in initial platform mass required by the ion system compared to the arcjet system is primarily a result of the increased power requirements of the ion system. The electric propulsion system initial power requirements are presented in Fig. 10-14 as a function of the number of maneuvers. Again, this is the electric power required to complete the first maneuver of a series. The arcjet system requires an initial power of 71 kW_e to complete 10 maneuvers while the ion system requires 203 kW_e for 10 maneuvers. A 100-kW_e SRPS will enable the arcjet system to complete 228 maneuvers, while an ion system will not be capable of conducting any 9.62 m/s maneuvers in 6 hours.

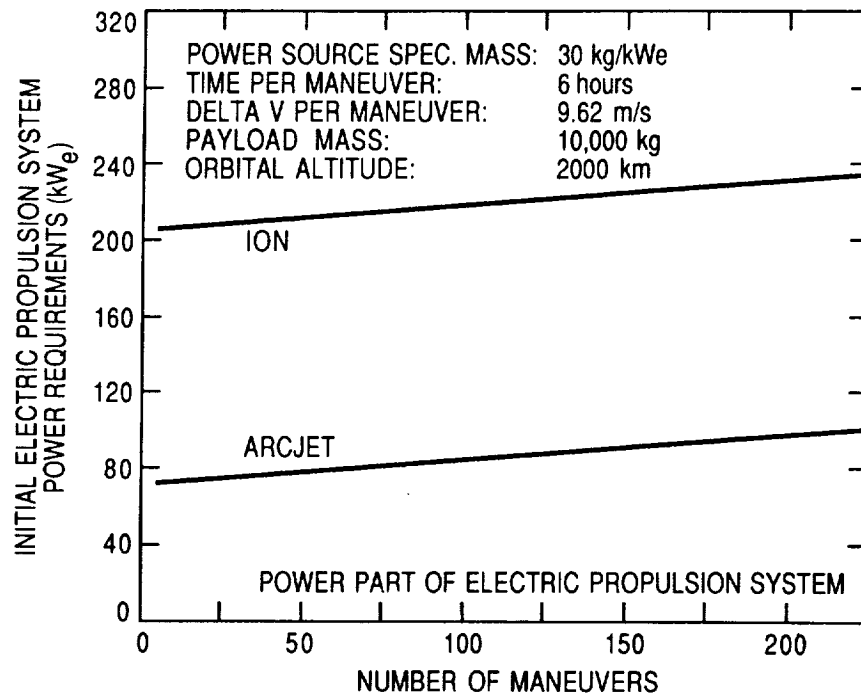


Figure 10-14. Initial electric propulsion system power required for maneuvering as a function of the number of maneuvers.

11.0 CONCLUSIONS AND RECOMMENDATIONS

The purpose of this work was the validation of 30-kW ammonia arcjet technology for use on the SP-100 Flight Experiment. During the course of this program endurance tests of 413 hours, 252 hours, and 100 hours duration were conducted, along with numerous shorter tests, at a nominal power level of 30 kW. Many important technical results obtained during this program have led to an improved understanding of arcjet operation. While 30-kW ammonia arcjet technology may be considered ready for development for a flight demonstration, widespread implementation of arcjets at this power level will require improvement over what is now known to be their performance. Further development may lead to a 30-kW ammonia arcjet with the desired performance (e.g., specific impulse at least above 800 s, thrust efficiency above 35 percent). Alternately, it may be necessary to employ hydrazine or hydrogen as the propellant to achieve the desired performance. The central issue of thruster lifetime was also addressed by this program. While certain of the duration tests were encouraging steps toward a (minimum) operational lifetime of 1500 hours, the data suggest an increase of the cathode tip erosion rate with time. Important technical issues remain to be resolved concerning performance and lifetime. The technical database, diagnostic methods and analyses performed under this program serve as a foundation for the further development of 30-kW class arcjets.

11.1 PROGRAM HIGHLIGHTS

The program was broken down into eight major technical tasks: (1) facility preparation and maintenance; (2) arcjet engine design; (3) materials analysis and evaluation; (4) arcjet performance testing; (5) arcjet endurance testing; (6) modeling; (7) diagnostics development and application; and (8) missions and systems analysis. The major results and conclusions of these tasks are summarized below.

11.1.1 Facilities and Instrumentation

The facility, including the vacuum subsystem, data acquisition and control subsystem, and power subsystem performed well. The cooling water problems evident during the 1986 573-hour tests were completely eliminated by active water treatment and by monitoring the cooling water flow.

Thrust measurements were inaccurate in several cases due to the coaxial current feed interface with the mercury pots. (Data from these tests are not cited in this report.) The mercury level in the pots was found to evaporate over time, particularly during long tests (e.g., Cathode 20). Several low vapor pressure oils were used to prevent this phenomena. Pure silicon oil was found to evaporate over a run of approximately 100 hours (a 1-cm-thick layer). Silicon-based diffusion pump oil reacted with the ammonia and its dissociation products and formed a gasket-like rubber on top of the mercury (Cathode 24 test). This also happened during the 1986 tests but was

thought at the time to be caused by the pressure of water vapor. Fomblin 18-8A diffusion pump oil was found to work very well; there have been no problems with the mercury level after switching to oil.

The most significant problems with the facility were related to the propellant flow subsystem. The location of the propellant storage tank allowed temperature-induced depressurization in cold weather. This problem terminated the test early (Cathode 15). Heat lamps and a rain cover were used to minimize this problem.

The propellant flow controller calibration was found to be inaccurate, causing the actual flow to be 25 percent higher than the indicated flow. The standard transfer gas calibration technique, in which a convenient test gas is used for the calibration and a theoretically-derived factor is used to translate the calibration to the gas of interest, can lead to an incorrect calibration if the gas of interest is at a thermodynamic condition for which real gas effects are important. To ensure proper calibration, flow controllers should be calibrated using the gas of interest. While the absolute value of the flow was wrong, the flow controllers did produce repeatable results, allowing correction of much of the performance data. For some earlier performance data, significant facility changes have prevented confident correction; however, these data may be used to identify qualitative trends.

11.1.2 Engine Design

Arcjet design improvements have enabled lower engine operating temperature. Design improvements include the use of high emissivity coatings to enhance radiative heat rejection. A ZrB_2 high-temperature coating was used to increase the surface emissivity of the nozzle and body radiating surfaces. The ZrB_2 -coated engine operated at a temperature nearly 120 °C cooler than the uncoated baseline engine over the power range considered, indicating a 30-percent increase in the surface emissivity. This coating material maintained its high temperature radiative properties over hundreds of hours of engine operation at different power levels and flow rates, including numerous start sequences. Reduced nozzle temperature should result in longer nozzle lifetime, and should increase the operating power margin for the engine.

The new engine designed for this program, the D-1E shown in Fig. 11-1, has fewer active seals and parts than previous designs. The D-1E engine assembly procedure is simpler and allows easier alignment than that of the baseline engine since there are no bolts. In addition, the new engine design will make future parametric testing simpler because the complexity of parts changeout is reduced.

The D-1E engine operates at lower overall component temperatures than previous designs. The nozzle of this engine operated at a temperature of 1950 °C at 30 kW_e while the baseline thruster nozzle reached 2000 °C at 23 kW_e. This resulted from an improved thermal conduction path leading to a larger effective radiator surface and a more efficient radiator surface design. In addition, the cathode feedthrough of the new engine was more than 400 °C cooler (350 °C versus 800 °C) than that of the baseline engine due to improved regenerative cathode cooling. Use of the ZrB₂ coating enables even lower temperature operation at a given operating point.

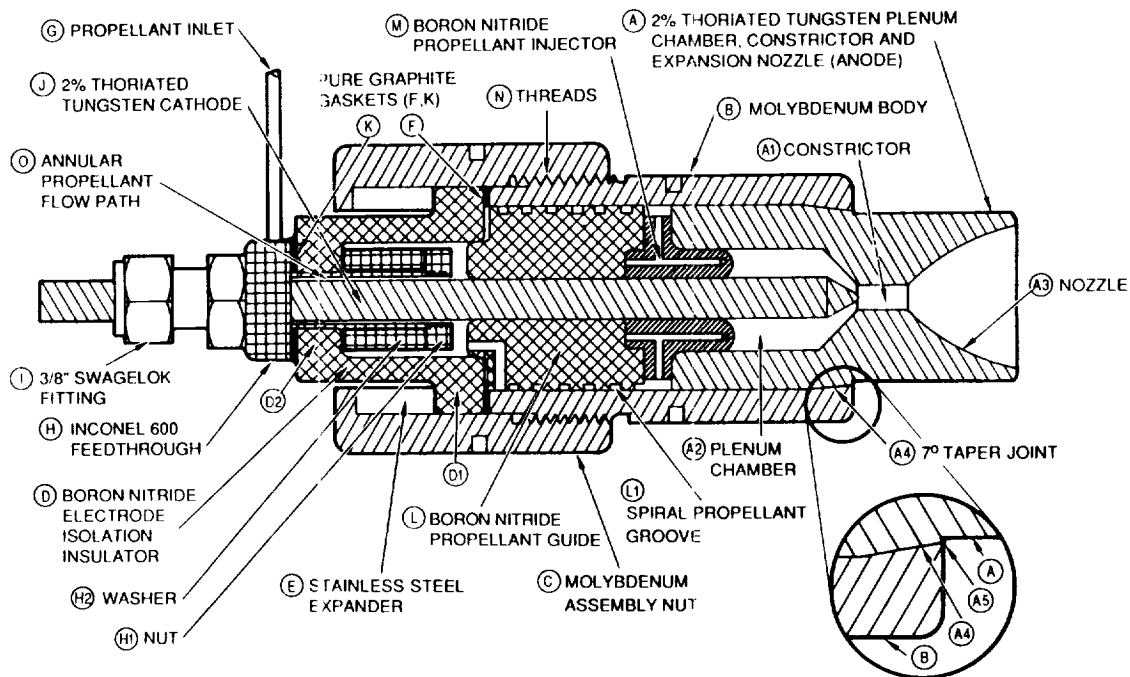


Figure 11-1. The D-1E arcjet engine.

11.1.3 Materials Analysis

The cathode, anode and injector of a 30-kW class arcjet were analyzed. The arcjet had been operated for a total time of 573 hours at power levels between 25 and 30 kW on ammonia, at (uncorrected) flow rates of 0.30 and 0.32 g/s, during a previous Air Force-funded program. The accumulated run time was sufficient to clearly establish erosion patterns and provide indications as to their causes. The cathode, made from 2-percent thoriated tungsten, eroded such that a hemispherical depression was formed on the cathode tip. The depression was surrounded by whiskers, thread-like formations which were apparently formed by vapor deposited tungsten (Fig. 11-2). Energy-dispersive X-ray analysis (EDAX) showed that the whiskers were composed of pure tungsten. The test was terminated at 573 hours when one of these whiskers apparently induced a high-current, reduced-voltage arc between itself and the anode wall. The current rush melted the tungsten and surface tension drew the material into a ball. Control or elimination of whisker growth could significantly enhance engine lifetime since the average erosion rate over 573 hours did not preclude attaining 1500 hours of lifetime. Additionally, the grain size of the cathode material was found to increase several orders of magnitude. The base of the cathode tip crater also showed clear evidence that it was molten during engine operation. No thorium was found in the cathode tip crater surface using EDAX. The concentration increased to 2 percent about 1.0 cm from the base of the crater. Cathode tip erosion appears to result from the convection of tungsten vapor from the molten tip.

The nozzle was found to erode in the region of the constrictor outlet. This material appears to have been redeposited in the outlet region of the nozzle. No erosion was seen in the plenum chamber. The thorium was found, using EDAX, to be depleted in the nozzle about 1 cm downstream of the constrictor exit. This is where the arc is believed to attach in the nozzle. The constrictor erosion appears to result from overheating of the nozzle block.

The propellant injector was badly eroded during the 573-hour test. The injection holes increased in size by a factor of 2.25. The tangential component of propellant injection decreased markedly during the test. Black deposits found on the surface of the injector face were found to be composed of tungsten, thoria and handling contaminants. Gas recirculation in the plenum chamber from the cathode tip region back to the injector face appears responsible for the deposits. The injector erosion was believed to be caused by mechanical erosion of a weak eutectic solid of boron and tungsten which can form at high temperature. Reducing the temperature of the injector could alleviate the erosion.

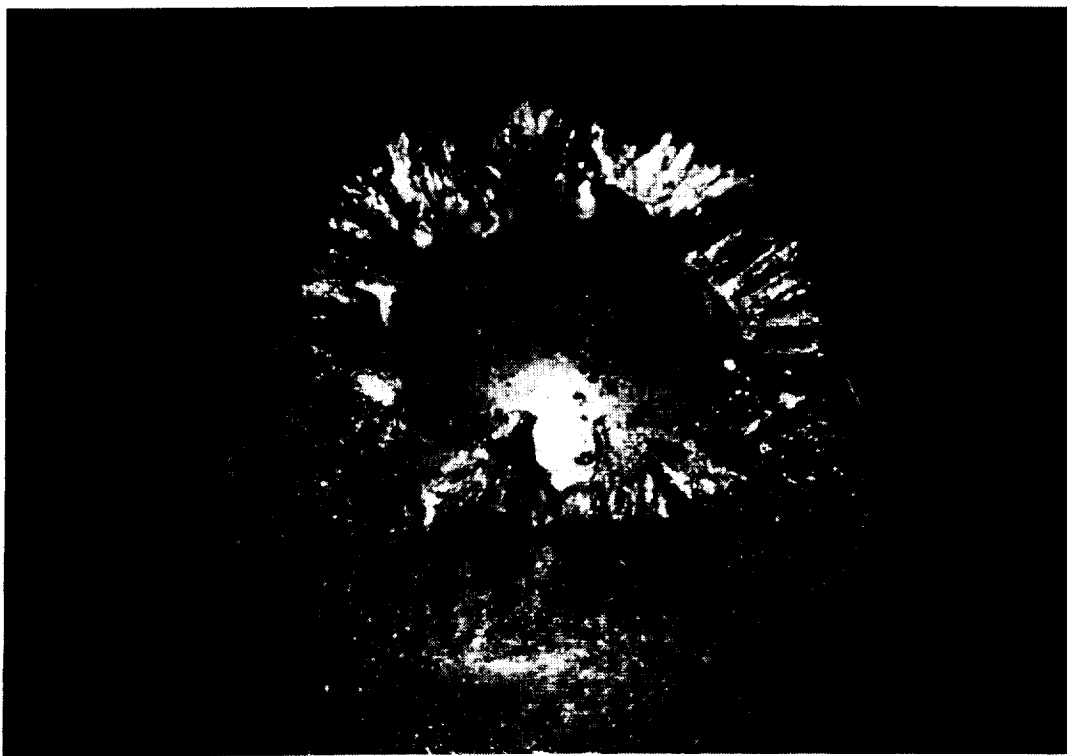


Figure 11-2. Pattern of erosion on a tungsten cathode tip.

One possible way to increase arcjet lifetime is through the use of alternative, high temperature materials. Other tungsten-based materials or carbides could provide enhanced cathode life. Preferentially oriented pure tungsten, tungsten impregnated with other materials (LaB_6 , ThC , ZrN) or tantalum- or zirconium-carbide could operate at lower temperatures, reducing evaporative-convective erosion. Other insulator materials such as alumina, beryllia or ceramic matrix composites could enhance injector life by reducing chemical reactivity.

11.1.4 Performance Testing

Arcjet performance was compared for engines with two different cathode shapes. The first used a baseline cathode with a 60° included angle conical tip (baseline MOD I engine) while the second employed a cathode with a 45° included angle conical tip and a cross section approximately 50 percent smaller than the baseline (baseline MOD II engine). The engines were otherwise identical, including the same cathode-to-anode spacings. The engines were operated at 14.6 and 22.0 kW over a mass flow range of 0.21 to 0.42 g/s. The new cathode tip design and placement led to a 15-percent decrease in the engine operating voltage. However, as shown in Fig. 5-2, there was no significant change in engine performance. This suggests a first-order dependence of performance on power and mass flow rate, with little effect from variation of cathode shape or spacing. Further testing showed that this is true over a wide range of tip shapes, engine operating powers (8 to 30 kW) and cathode spacings.

Additional experiments were conducted to better understand the effects of cathode tip shape and location on the engine electrical characteristics. The electrical behavior of an arcjet was compared for four different cathode shapes. Engine operation was characterized over a range of power levels (20-32 kW), current levels (200-300 A) and cathode-to-anode spacings. A geometric arc length was defined, based on the cathode spacing and constrictor length. The geometric arc length varied in the experiments between 0.85 and 1.81 cm. The cathode tip geometry was found to have no effect on the relation of engine power or arc current to geometric arc length. At fixed power, the arc current appears to asymptotically approach a minimum value as geometric arc length increases, as shown in Fig. 11-3. This result implies a maximum value of arc voltage as the arc length increases. If, at some power level, the arc voltage and current reach asymptotic values, but cathode erosion causes the arc length to increase, an unstable situation may arise. The arc's anode attachment may then migrate upstream from the nozzle to the constrictor, where severe damage is likely. One duration test run during this program showed evidence of this phenomenon. Cathode tip erosion must be anticipated in order to avoid possibly destructive reconfiguration of the arc geometry. The data from geometric experiments of the type conducted for this program can be used to determine an appropriate cathode spacing and define the operating margins for long-duration arcjet tests.

Arcjet performance was compared for engines with a conical nozzle (19° half angle) and area ratio of 22, and engines with an 80 percent bell nozzle with an area ratio of 33. The engines were identical in all other aspects. The engines were operated between 10 and 30 kW, with an uncorrected mass flow range of 0.18 to 0.35 g/s of ammonia. The bell-shaped nozzle was found to provide improved performance over the entire operational envelope. For example, Fig. 11-4 shows the thrust efficiency as a function of engine input power. Thrust improvements of up to 10 percent were found. Gains in thrust efficiency and specific impulse were also noted.

Following the verification of bell-shaped nozzle arcjet performance improvement, a detailed performance mapping was completed. Engine performance was mapped over a power range of 10.6 to 23 kW with an uncorrected mass flow range of 0.18 to 0.35 g/s. The engine performance is shown in Fig. 11-5 over the entire operational envelope.

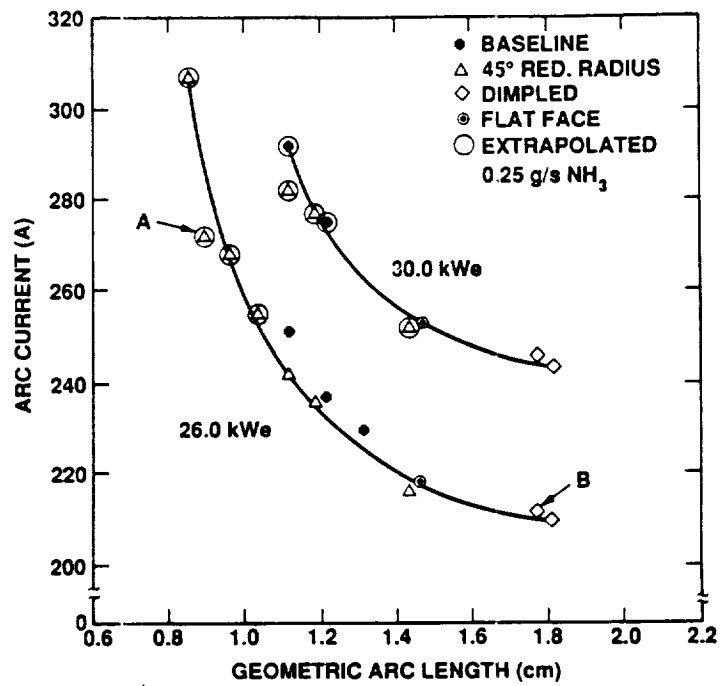


Figure 11-3. Arc current as a function of arc length.

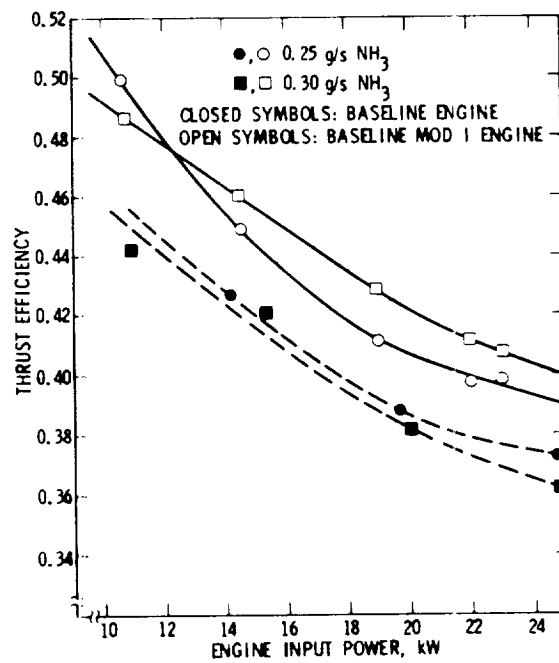


Figure 11-4. Thrust efficiency as a function of input power.
(Data for comparative purposes only; see section 5.6.)

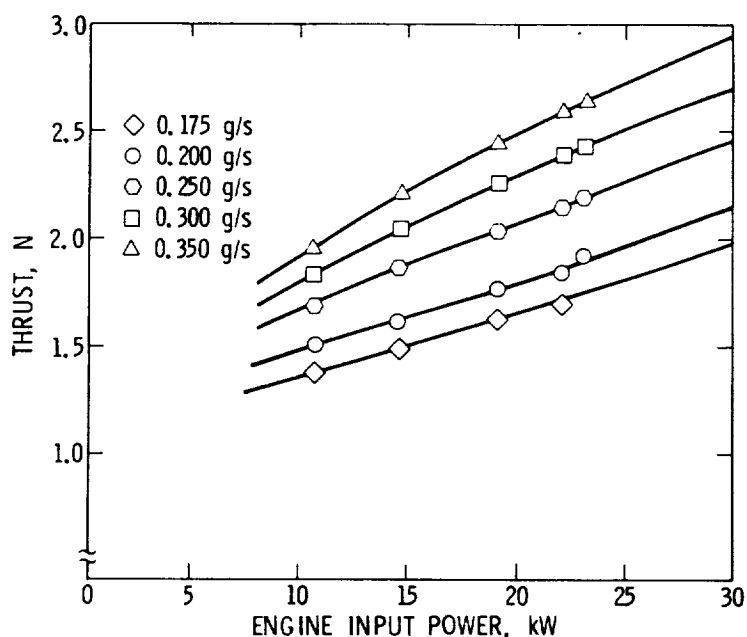


Figure 11-5. Performance of the bell-shaped nozzle.
(Data for comparative purposes only; see section 5.6.)

A series of experiments was conducted in 1989 to examine performance differences between JPL and Rocket Research Company (RRC) arcjet data. These data were generated with arcjets of very similar design. A 20-percent error in the JPL mass flow rate, due to incorrect mass flow controller (MFC) calibration, appears to explain the differences seen between the JPL and RRC data. The engine operating voltages measured in the JPL and RRC facilities agree when the mass flow controller error is accounted for. In addition, the thrust stands used at JPL and RRC agree to within 2 percent when using consistent flow rates. Vacuum effects testing showed that tank background pressure has no effect on engine operating voltage over the range from 0.060 to 10.0 torr and that measured thrust is not affected until the background pressure goes above 0.450 torr. From these indications it can be concluded that the diffuser used at JPL to maintain low background tank pressure has negligible effect on engine electrical or performance characteristics. Data affected by the MFC error have been corrected in this report, where possible, or identified if confident correction is not possible. (See Section 5.6 for a detailed account of the MFC error and the data correction procedure.)

A summary of 30-kW ammonia arcjet performance data is given in Table 11-1. The first column shows data from the original AVCO engine on which subsequent engines were based. The second column shows data from the JPL baseline thruster; these data were quite close to the AVCO data. In the third column are RRC data, showing lower specific impulse and thrust efficiency than the JPL data taken the same year. The fourth column shows data from 1988 performance tests of the D-1E thruster, while the fifth column shows typical data corrected in 1989 for the mass flow controller error. The lower

specific impulse and thrust efficiency of these last data indicate that further arcjet technology development is required in order to achieve the required performance level (>800 s specific impulse, >35-percent thrust efficiency). This development may require the use of alternate propellants (e.g., hydrazine or hydrogen).

Table 11-1. Summary of Reported 30-kW Ammonia Arcjet Performance Data

ENGINE	R-3 ⁵	BASE-LINE ⁸⁵	RRC-2 ¹⁰⁵	D-1E ³⁰	D-1E ⁺
Date	1964	1986	1986	1988	1989
Laboratory	AVCO	JPL	RRC	JPL	JPL
Power, kW	30.0	30.5	29.9	30.5	30.3
Thrust, N	2.50	2.45	2.0	2.50	2.42
Specific Impulse, s	978	967*	850	1018*	754
Efficiency	0.38	0.37*	0.28	0.41*	0.29
Mass Flow, g/s	0.25	0.25*	0.25	0.25*	0.33

* Uncorrected for mass flow error; see Chapter 5.

+ Corrected typical 30-kW operating point.

Gas pulse and capacitive-discharge high-voltage spike techniques have been previously demonstrated for starting low-power and high-power arcjets directly on hydrazine and ammonia. The feasibility of using a glow discharge-arc discharge transition to start directly on ammonia was investigated during this program. The technique was demonstrated in stages. The first stage involved initiating a high voltage, low current discharge on an ammonia flow of less than 0.1 g/s. Breakdown usually occurred at about 900 V. The power and mass flow were increased until engine operation began at about 2 kW. In the second stage, the engine was started on argon and transitioned to ammonia propellant while still operating on the starting power supply. Engine operation was then transitioned from the start supply to the main run supply, allowing the engine to be ramped up to full power. The two stages were never demonstrated consecutively, due to start supply overheating. The technique requires further refinement before it can be implemented as a regular start technique.

11.1.5 Endurance Testing

A series of 100-hour endurance tests was run to evaluate the effect of cathode tip configuration on cathode erosion, as shown in Fig. 11-6. All the cathodes tested were made from 2-percent thoriated tungsten rod stock. The tip configuration did not appear to play a significant role in cathode erosion. However, the tip erosion rate did appear to increase with increasing emitted arc current. The average cathode erosion rate over 100 hours of operation doubled when the nominal engine operating current increased from 235A to 285A. More importantly, the experiments also indicate that the cathode tip erosion rate may increase with time, contrary to previous thought (Fig. 11-7). Melting induced by increased work function, coupled with possible gas dynamic effects, may accelerate the cathode tip erosion rate with time.

The input power to the arcjet was also filtered to determine if low ripple input power reduces whisker growth on the cathode tip. Within the bounds of the test facilities used, it was found that low ripple input power had no significant effect on macroscopic whisker growth for cathodes with a baseline-type tip configuration for 100 hours of continuous operation.

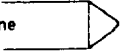

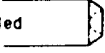
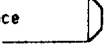

The D-1E engine design shows promise for long-term high-power operation. A 413-hour endurance test was conducted using a flat-face cathode and the D-1E arcjet engine. The test was voluntarily terminated due to test facility problems. The nozzle and propellant injector were in excellent condition at the end of the test: neither part showed evidence of erosion or excessively high temperature operation despite the fact they were operated at a power which was 20 percent higher than the power used in the 1986 test in which these components did show significant wear. This performance was probably due to design improvements, reflecting a more efficiently radiating nozzle. The cathode exhibited a mass loss of 2.16 g over 413 hours for an average mass loss of 5.2 mg/hr. A 252-hour endurance test was run using the same engine geometry as the 413-hour test, but with a 10-percent higher mass flow rate. The higher mass flow rate resulted in a longer arc due to increased propellant pressure. It is believed that the arc reached a maximum sustainable length as the cathode eroded and then pulled back into the constrictor, resulting in engine damage.

11.1.6 Modeling

A modeling effort was performed to quantify the cathode tip heating phenomena. Two separate analyses were combined to achieve an overall solution. The first was a three-species model of the plasma sheath region, and the second was a one-dimensional heat transfer model for the cathode. The plasma sheath model was used to estimate the heat load to the cathode surface.

A test case was examined, using values for the model variables which were based on experimental data. Estimates of plasma number density and temperature at the sheath edge, the sheath fall voltage, and the cathode surface temperature were input to the sheath model. The model then predicted the surface heat flux and total current density. Next, estimates of the cathode base temperature, heat flux at the cathode tip, and total current

(for calculation of ohmic heating) were input to the heat transfer model. This model predicted the temperature distribution in the cathode. The descriptions of cathode tip thermal state predicted by the two models were checked for consistency with each other and agreement with the experimental data. For this test case, the models offered consistent and reasonable results.

	TEST DURATION (hrs)	INPUT CURRENT RIPPLE	GEOMETRIC ARC LENGTH* (cm)	WHISKER GROWTH?	EROSION RATE (mg/hr)	ARC CURRENT (A)
Baseline 	# 13 53	3%	1.11	yes	1.5	265-291
	# 14 100	3%	1.11	yes	4.0	289-303
	# 22 100	0.2%	1.11	yes	3.1	264-289
45° Reduced Radius 	# 4 100	3%	1.43	?	2.1	238-252
Dimpled 	# 15 21	0.2%	1.81	yes	6.2	243-247
Flat Face 	# 20 28	0.2%	1.47	no	1.4	234-252
	# 20 413	0.2%	1.47	yes	5.2	215-251
	# 17 100	0.2%	1.47	no	2.0	246-257
	# 25 252	0.2%	1.44	yes	4.1	229-208
Fat Tip 	# 24 100	3%	1.14	yes	3.3	244-277

* AT START OF TEST

Figure 11-6. Summary of endurance tests.

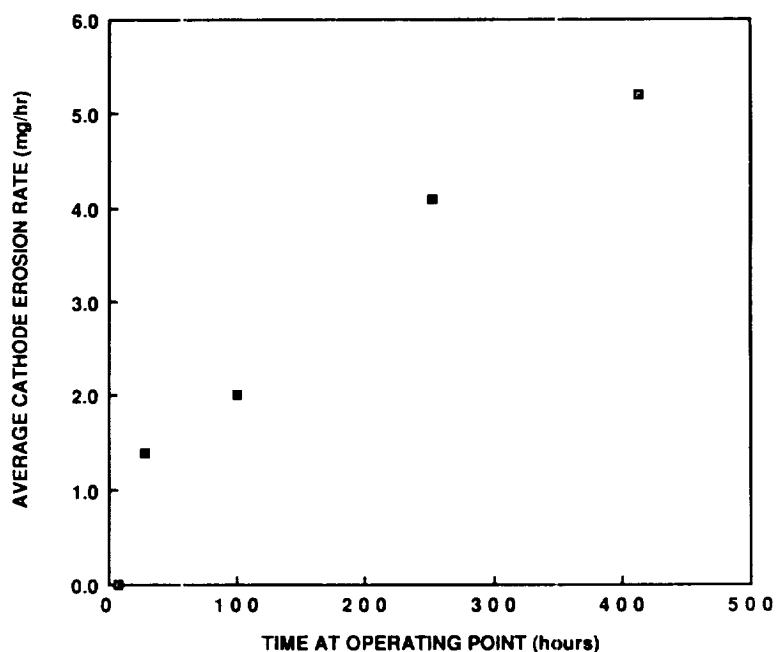


Figure 11-7. Increase of flat-face cathode erosion rate with time.

11.1.7 Diagnostics

Three nonintrusive diagnostic techniques were demonstrated for their applicability to arcjet engines. The techniques were emission spectroscopy, laser-induced fluorescence spectroscopy, and epithermal neutron analysis. Emission spectroscopy involves examining the emission characteristics of an optically thin line resulting from relaxation processes in the plasma plume of an arcjet. The Doppler shift of the line can be used to determine the species velocity. A scanning Fabry-Perot interferometer and spectrometer were used to examine the hydrogen Balmer line at 656.4 nm. The results of a scan with the arcjet operating at 20 kW are shown in Fig. 11-8. An average centerline velocity of 20 km/s was found in this instance.

In laser-induced fluorescence (LIF), the emission characteristics of an optically thin line are also used for species velocity determination. However, in this case a laser is used to excite a specific transition. The LIF signal is obtained when the species de-excites and radiates energy of the desired frequency. This technique provides several advantages over emission spectroscopy. First, it provides accurate point measurements in the plume, limited only by the focus of the laser beam, without using a complicated inversion procedure. Second, the velocity profiles are determined in the direction of the pumping laser beam, allowing the detection optics to remain stationary. This technique was demonstrated using the hydrogen Balmer line at 656.3 nm using a pulsed laser. A velocity profile from an arcjet operating at 14 kW is shown in Fig. 11-9. A centerline velocity of 16 km/s was found, averaged only over the laser beam focus, approximately 3 mm in diameter. The radial extent of this profile is narrow compared to the nozzle exit diameter, indicating that hydrogen atoms are likely only in the center or core portion of the plume at this engine operating condition. Significant Stark broadening of the LIF signal was found, indicating that the electron density is higher than previously thought. A Stark-broadened line profile can be used to determine electron number density.

Epithermal neutron analysis enables real time measurement of surface, bulk material (average) and point temperatures in an operating arcjet. This technique makes use of the highly temperature-dependent resonances which epithermal neutrons have with certain high temperature materials. Surface and point temperatures in an arcjet can be determined by using different materials in different locations which do not have overlapping resonances. Proof-of-principle experiments were carried out at the ISIS Spallation Neutron Source facility at the Rutherford-Appleton Laboratory in England. Figure 11-10 shows epithermal neutron transmission through a material sandwich made of 1-cm-thick molybdenum, 100- μ m-thick rhenium foil and a 1-cm-thick tungsten disk. The resonances (absorptions) are shown as a function of epithermal neutron energy (time-of-flight). The material temperatures are proportional to the absorption line widths and are 484 °C for these proof-of-principle tests.

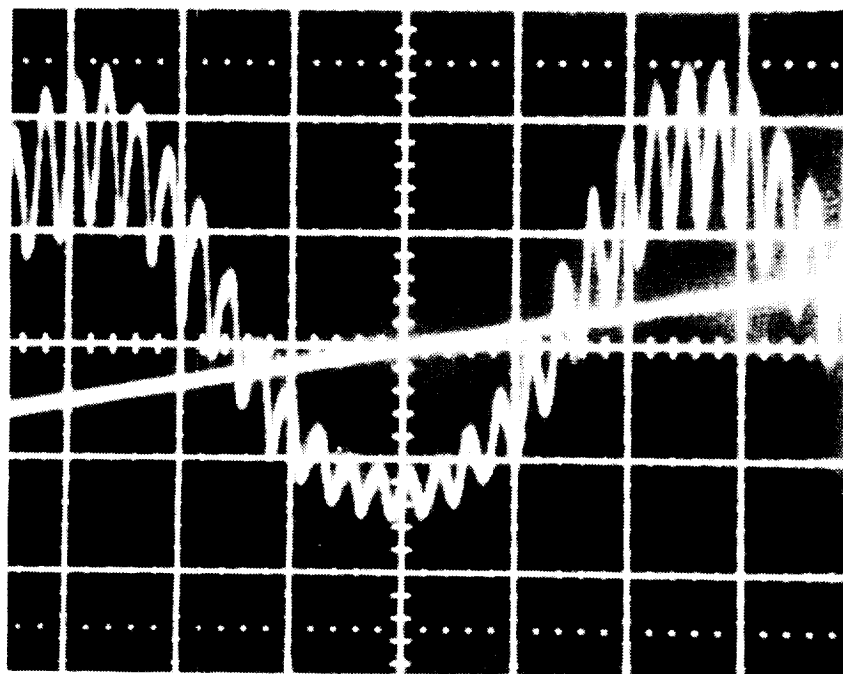


Figure 11-8. The hydrogen Balmer line in a 20-kW arcjet.

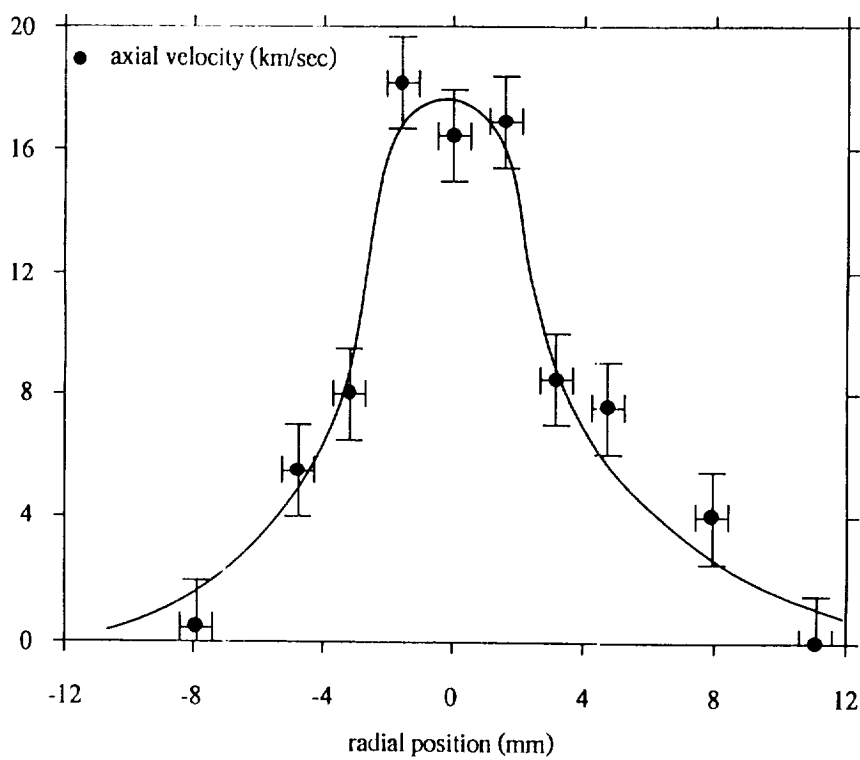


Figure 11-9. Axial velocity profile in a 14-kW arcjet.

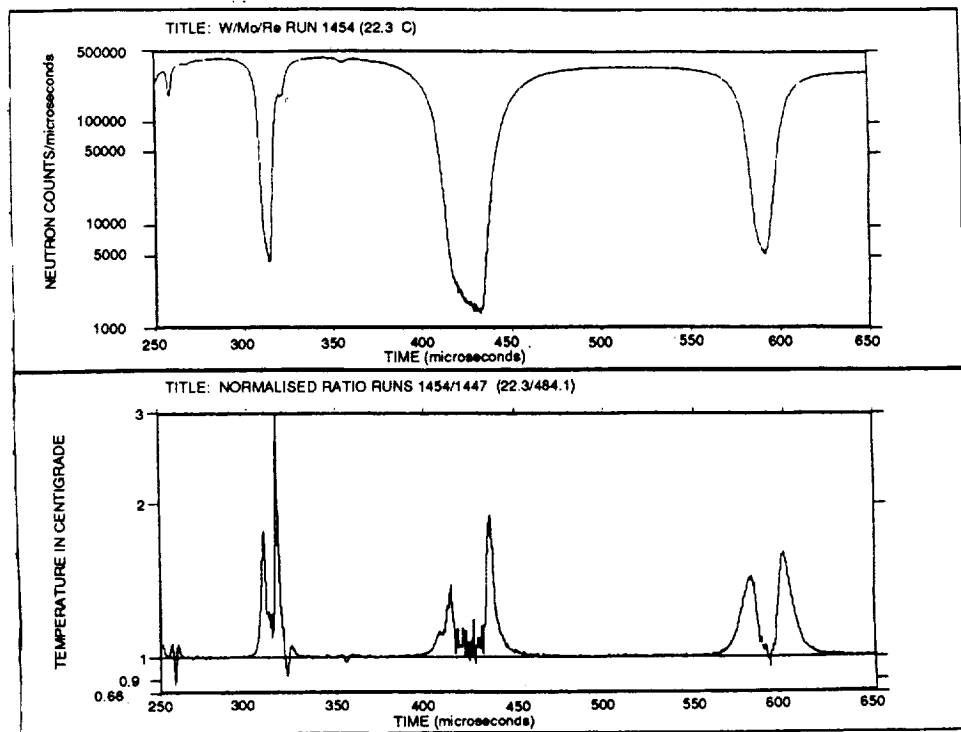


Figure 11-10. Epithermal neutron transmission through a Mo-Re-W material sandwich.

11.1.8 Mission and System Analysis

The design and performance characteristics of an arcjet NEP spacecraft suitable for conducting the SP-100 Flight Experiment were determined. The simplicity of arcjet thrusters and their relatively advanced state of development allow them to meet the SP-100 Flight Experiment constraint of low developmental risk. In addition, they can be scaled up in power into the hundreds of kilowatts regime making them compatible with future SDI power levels. As a result, arcjets are particularly well suited for the SP-100 Flight Experiment. A block diagram of an arcjet NEP system is shown in Fig. 11-11.

A proposed flight experiment vehicle has been outlined and consists of a 100-kW_e SRPS, a spacecraft bus, a radiation/arcjet efflux diagnostics package, and an arcjet propulsion module in an end thrust configuration. The propulsion module consists of three parallel propulsion system assemblies, each of which had four 30-kW_e ammonia arcjets. One arcjet from each assembly can be operated simultaneously. The baseline vehicle mass is 5675 kg, excluding the propellant, tankage and feed system.

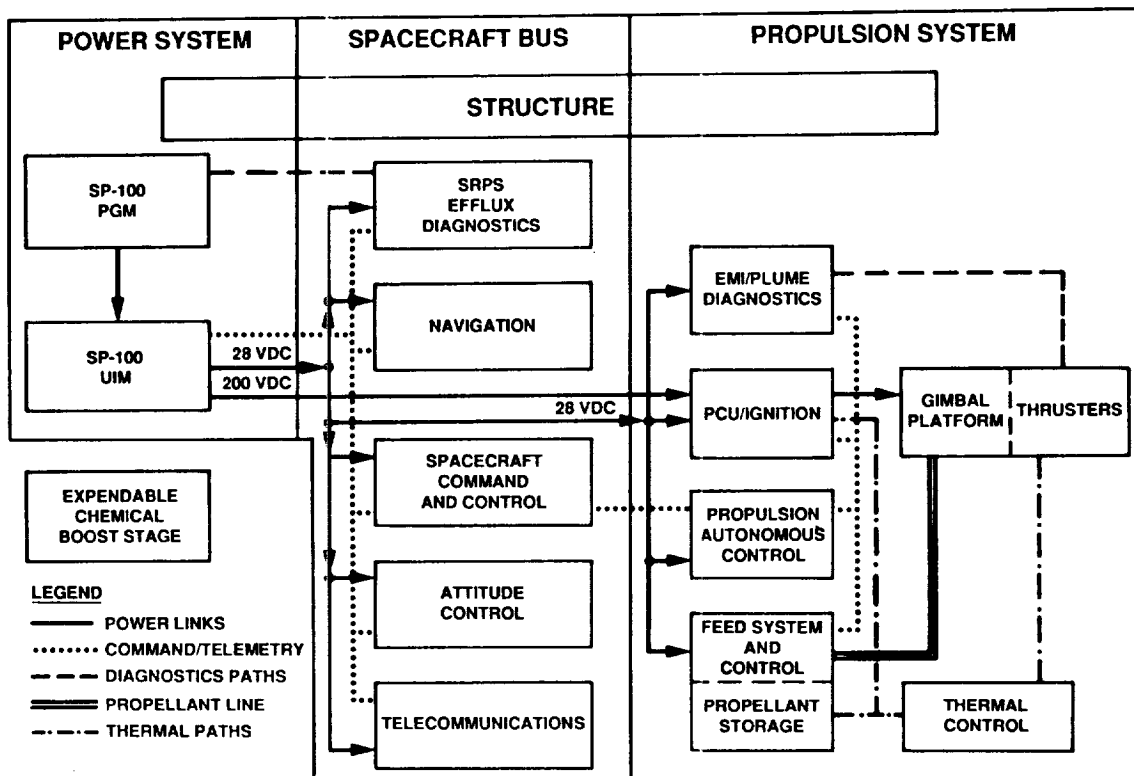


Figure 11-11. Arcjet NEP system block diagram.

Orbital analysis was conducted to evaluate the SP-100 Flight Experiment vehicle performance. A single dedicated Titan IV launch was assumed. A number of candidate missions were proposed. The intent was to present options, any one of which might be representative of future mission deployment requirements. Three specific missions were examined which included power system deployment to possible surveillance platform orbits and a round-trip OTV mission. The analysis showed that this vehicle is capable of mission delta-Vs of approximately 6000 m/s. A propulsion system throttling demonstration would verify the SRPS load-following capabilities.

Additional analysis of the SP-100 mission verified that a 30-kW_e flight demonstration with arcjet propulsion is meaningful using any of the three possible launch vehicles: Titan 4, Titan 3 and Atlas 2AS. The Atlas launch vehicle cannot carry as much ammonia propellant as the Titan vehicles, and thus its missions are limited to a maximum four-month duration with no payload. An alternative and attractive flight demonstration with the Atlas is achieved by reducing arcjet operational time to less than four months, and using the propellant mass savings for payload or additional experiments. For example, if the fuel system was sized for a two-month transfer, 1400 kg of payload could be deployed to a 10,000 km altitude.

Arcjets and other types of electric propulsion were also analyzed for use in SDI constellation deployment and spacecraft maneuvering missions. For typically sized SDI constellations and reasonable launch rates of advanced ground launch systems, the use of electric propulsion upper stages can significantly reduce the number of launches and deployment time compared to those achievable with advanced chemical upper states. It was shown that the number of launch vehicles required to deploy a constellation of 50 10,000-kg platforms could be reduced by up to a factor of two when electric propulsion upper stages were used in place of advanced chemical upper stages. This resulted, primarily, from a reduction in upper stage propellant requirements. In addition, it was found that the total deployment time for a constellation was driven primarily by the number of platforms in the constellation and the launch rate, not the individual upper stage transfer time (Fig. 11-12). Therefore, the reduction in the number of launch vehicles resulted in up to a 40-percent reduction in the constellation deployment time.

Continuous defensive maneuvering using electric propulsion systems can enable lower initial platform masses than chemical maneuvering systems. The number of maneuvers at which electric propulsion becomes mass competitive depends primarily on whether the power supply to drive the electric propulsion system is accounted for in the payload or in the electric propulsion system. For example cases it was shown that when power was considered as part of the payload an arcjet maneuvering system was lighter than a chemical system regardless of the number of maneuvers, and an ion thruster system was lighter if more than 50 maneuvers were needed (Fig. 11-13). When the mass of the power supply was included with the electric propulsion system, arcjet and chemical systems became mass competitive at around 100 maneuvers and an ion system at around 200 maneuvers. The ion system required approximately twice the power of an arcjet system to perform a given number of maneuvers since it has a lower thrust-to-power ratio and a higher dry mass. The ion system required

more than 100 kW_e of power to meet the maneuvering requirements while the arcjet system was able to demonstrate a substantial maneuvering capability with less than 100 kW_e for all of the cases considered.

Finally, technology issues of the arcjet module subsystem were considered. The thruster, power processing, and propellant distribution and storage subsystems are the most critical in terms of validation of the flight system concept. The thruster and power processing unit (PPU) concepts have been validated, while present ammonia propellant system technology is sufficient for the SP-100 Flight Experiment. However, development of a vacuum electronic flow controller would enable engine throttling and should be pursued if a specific-impulse-optimized mission is to be considered. The lifetime of an arcjet engine is limited by the cathode lifetime. The primary power processing concern is attaining a high efficiency in order to reduce the PPU active cooling requirements, which can greatly reduce the overall system mass and complexity.

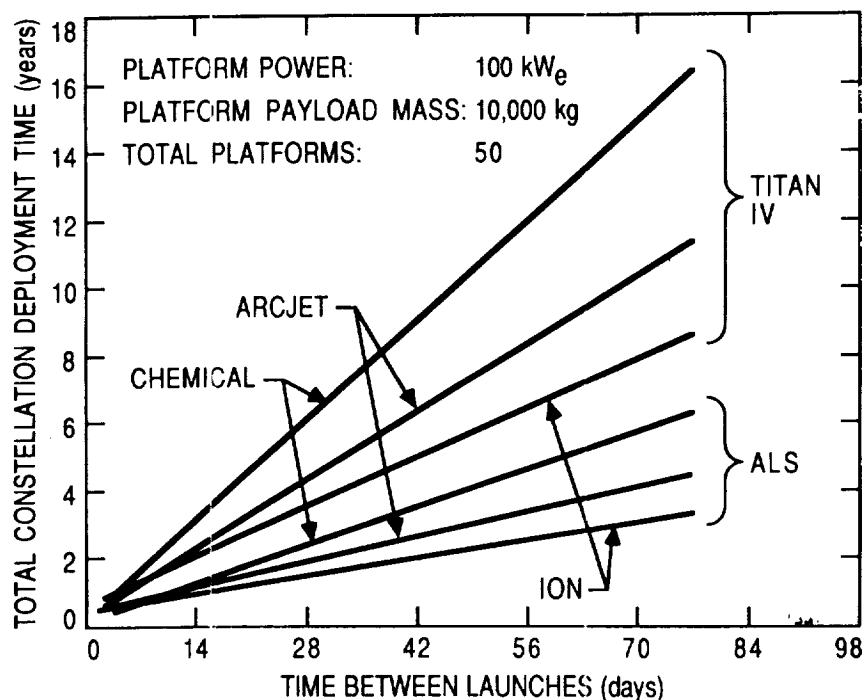


Figure 11-12. Total constellation deployment time as a function of the total time between launches.

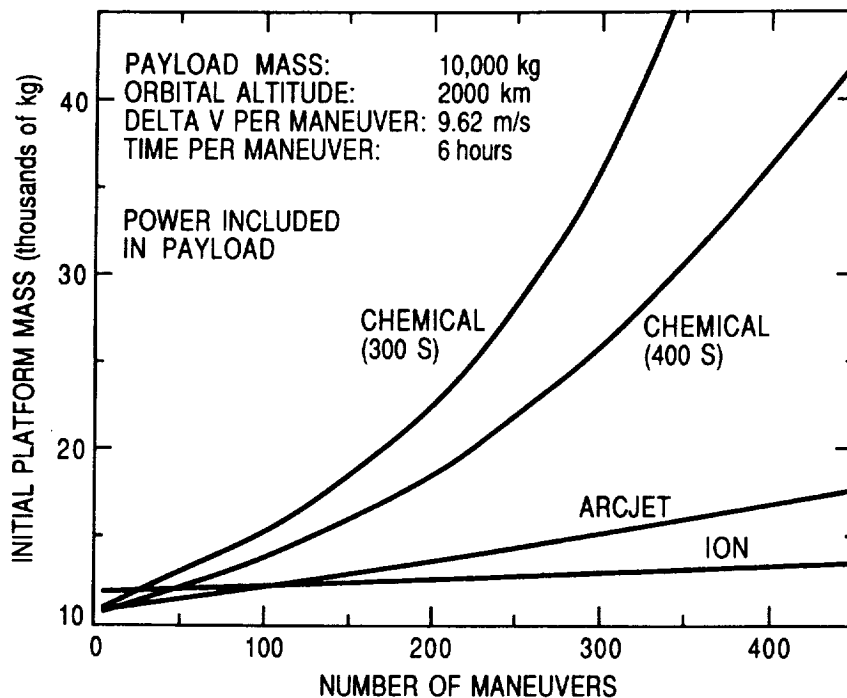


Figure 11-13. Initial platform mass as a function of number of maneuvers. Power included in payload.

The required diagnostics, thermal control, gimbal, and structural subsystems have undergone preliminary development and only require system-specific design and qualification for the flight experiment. The autonomous controller subsystem must face the issue of possibly unknown control dynamics for the continuous thrusting of a large spacecraft; development of artificial intelligence control software may be required.

11.2 RECOMMENDATIONS

In this section, recommendations for future work are made in two areas: engine technology and mission and system design.

11.2.1 Engine Technology

Further examination of the effects of nozzle geometry on engine operation and performance is needed. The preliminary bell-shaped nozzle used during this program led to improved engine performance. Development of predictive analytic codes for arcjet flow conditions is needed to further refine and optimize the nozzle contour. In addition, the effects of nozzle shape on engine electrical characteristics and long-term arc stability need to be examined. During the 1986 endurance test, which was conducted for the previous JPL program, the engine operating voltage increased 11 V over 573 hours. During the 413-hour endurance test conducted during this program, the engine voltage increased in a linear manner by approximately 17 V even

though cathode tip erosion caused the centerline to recede 20 percent less than the amount seen in the 1986 test. These differences are believed to be associated with the nozzle shape. Since the conical nozzle diverged more slowly, the anode arc attachment could have had more freedom of movement to maintain a stable arc configuration resulting in a lower operating voltage. Nozzle shapes which include conical and bell-shaped sections should be investigated.

The effect of propellant swirl on engine operation and performance, including the optimum swirl angle, should be determined. An optimum swirl angle, if it exists, will likely be a function of engine power, mass flow rate and internal geometry. An attempted restart of the endurance test done in 1986 resulted in constrictor damage which is believed to have been caused by diminished propellant swirl. Construction of the D-1E engine allows simple changeout of the injector. Injectors with different gas outlet angles could be used during several different tests to examine the effects of swirl on engine performance. A thrust stand-mounted engine, coupled with optical diagnostics would allow a complete experimental evaluation. The optimum angle could then be machined directly into the tungsten nozzle block at the upstream end of the plenum chamber in the D-1E engine. An endurance test would confirm the design.

Cathode erosion was found to be the chief threat to long engine life. No nozzle or injector erosion was seen following periods of stable engine operation. The experimental results from this program suggest that the cathode tip erosion rate increases with time. This effect should be analyzed to determine if it is gas-dynamically driven, electromagnetically driven, driven by the materials properties of the cathode, or the result of a combination of effects. A basic understanding of this effect could enable the development of a low erosion cathode.

The influence of the electrode work function on erosion needs to be determined. At present, there are groups which advocate either a high or a low work function as optimum. Materials such as preferentially oriented or single crystal tungsten, lanthanum hexaboride, zirconium diboride, tantalum carbide, zirconium carbide and several impregnated tungsten materials may provide enhanced erosion resistance for cathodes. Analysis and follow-up experiments are needed to determine the best alternative.

The mechanisms which drive cathode tip whisker growth should be determined. The results of this program suggest that gas dynamics and the formation of the cathode tip crater promote whisker growth. Understanding and controlling whisker growth is a key to enabling long-life arcjet operation. Appropriate selection of a propellant mixture could reduce whisker growth but might also accelerate erosion. Alternate materials may also provide a solution.

The results of this program have implications for the arc geometry and stability. In particular, studies of the effective arc length suggest that as the arc geometry adjusts in response to an eroding cathode, it eventually reaches a maximum length and associated voltage. Further cathode erosion

then may lead to an unstable situation where the arc can no longer be maintained between the cathode and the nozzle, and the anode current attachment moves into the constrictor with destructive results. The critical condition should depend on mass flow rate, power, and engine internal geometry (including nozzle shape). The conditions at which this unstable condition occurs should be determined.

The realization that 30-kW ammonia arcjet performance is not as high as previously believed should lead to the investigation of other propellants, especially hydrazine and hydrogen. Since 1- to 2-kW arcjets achieve specific impulses of over 500 s on hydrazine, a specific impulse of 800 s at 30 kW would seem to be possible. Such an engine could then be used in present 0.5 to 10 N applications where monopropellant hydrazine engines are currently used.

Additional coating materials should be investigated to increase the emissivity of the nozzle radiating surface. While zirconium diboride works well and exhibits very good long-term wear properties, higher emissivity materials may be available. Materials in the carbide and nitride families are especially promising. However, if the engine runs too much cooler, efficiency losses may result since the heat in the propellant could be soaked up by the anode block and radiated away instead of contributing to propellant acceleration in the nozzle. Analysis of propellant flow heating and of thermal gradients in the anode block may be used to predict the onset of the efficiency loss.

A procedure for starting the arcjet directly on ammonia, and which can be used in a flight system, needs to be developed. The demonstrated direct-start laboratory techniques require massive start circuits due to the use of ballast resistors and large transformers. A high voltage spike technique, similar to those used for 1- to 2-kW arcjets, should be optimized to avoid the need for ballast resistors while causing no electrode damage.

11.2.2 Mission and System Design and Evaluation

An endurance test involving engineering model hardware, including the arcjet engine, power conditioning unit (PCU), and propellant feed system, should be conducted to ensure that no subsystem-level show-stopper issues will prevent the application of this technology.

Applications for 30-kW arcjet engines are likely to involve the use of gimbals on the host spacecraft for attitude control. The power feed of this gimbal mechanism will have to be able to supply up to 300 A of current continuously and handle start transient voltage spikes of up to 1500 V while maintaining its flexibility. Hundreds to thousands of flexing cycles are likely to be needed, depending on the mission and number of engines per gimbal. A power feed meeting these criteria requires development.

In an arcjet propulsion system architecture, the engine is likely to be the component with the shortest life. PCUs should have a large life margin and can probably be used to run several engines in succession. An ability

to operate more than one engine in succession would reduce spacecraft mass (compared to one PCU per engine) and require the use of a switching mechanism. Such a switching mechanism would have to be able to handle 300 A of current steady-state and withstand starting transients of up to 1500 V hundreds to thousands of times. A high-power, radiation-hardened semiconductor switch should be developed for this application.

Certain missions will require engine throttling to accomplish their objectives. Engine thrust can be varied by changing the engine input power requiring the PCU to be power controllable. If the throttling scheme required by the mission planners calls for variable specific impulse, efficiency or maintenance of constant specific impulse or efficiency for variable thrust, active mass flow control over a fairly broad range (e.g., 0.1 to 0.45 g/s) will be required. Accurate (+/- 1 percent) flow control hardware for flight applications does not presently exist and requires development.

A meaningful flight test of a high-power arcjet propulsion system should be conducted to validate this technology for future use. Such a flight test should demonstrate the required attributes of an arcjet propulsion system: appropriate delta-V; the on/off cycling needed for a solar-powered mission; adequate lifetime; EMI characteristics; and particulate contamination levels. A flight demonstration of 30-kW arcjet technology is a required step toward mission application of the technology.

12.0 LIST OF PROGRAM-SUPPORTED PUBLICATIONS

1. W. Deininger and R. Vondra, "Development of an Arcjet Nuclear Electric Propulsion System for a 1993 Flight Demonstration," AIAA 86-1510, 22nd JPC, June 1986.
2. W. D. Deininger, Editor, "Proceedings for the Arcjet Plume Diagnostics Technical Workshop," Pasadena, California, JPL Internal Document D-3623, October 2-3, 1986.
3. W. D. Deininger and R. J. Vondra, "Design and Performance of an Arcjet Nuclear Electric Propulsion System for a Mid-1990s Reference Mission," AIAA 87-1037, 19th IEPC, May 1987.
4. T. J. Pivrotto and W. D. Deininger, "Velocity Measurements in the Plume of an Arcjet Engine," AIAA 87-1063, 19th IEPC, May 1987.
5. W. D. Deininger, T. J. Pivrotto and J. R. Brophy, "The Design and Operating Characteristics of an Advanced 30-kW Ammonia Arcjet Engine," AIAA 87-1082, 19th IEPC, May 1987.
6. W. D. Deininger and R. J. Vondra, "Spacecraft and Mission Design for the Space Nuclear Power Source Reference Mission," AIAA 87-2026, 23rd JPC, July 1987.
7. T. J. Pivrotto and W. D. Deininger, "Velocity Measurements in the Plume of an Arcjet Engine," SPIE Proceedings-Propulsion, Vol. 872, p. 107, 1988.
8. W. D. Deininger and T. J. Pivrotto, "Detailed Operating Characteristics of a 30-kW Ammonia Arcjet Engine with a Contoured Nozzle," SPIE Proceedings - Propulsion, Vol. 872, pp. 108-118, 1988.
9. T. J. Pivrotto and W. D. Deininger, "Analysis of a Used Pair of Arcjet Electrodes," SPIE Proceedings - Propulsion, Vol. 872, pp. 119-126, 1988.
10. W. D. Deininger and T. J. Pivrotto, "High-Power, NH_3 Arcjet Cathode Lifetimes Evaluation, Experiments and Plans," SPIE Proceedings - Propulsion, Vol. 872, pp. 127-134, 1988.
11. W. D. Deininger and R. J. Vondra, "Electric Propulsion for Constellation Deployment and Spacecraft Maneuvering," AIAA 88-2833, 24th JPC, July 1988.
12. W. D. Deininger and R. J. Vondra, "Spacecraft and Mission Design for the SP-100 Flight Experiment," IEPC 88-013, 20th IEPC, October 1988.
13. W. D. Deininger, A. Chopra, D. Q. King and T. J. Pivrotto, "Thermal Design Improvements for 30-kWe Arcjet Engines," IEPC 88-073, 20th IEPC, October 1988.
14. T. J. Pivrotto and W. D. Deininger, "Electrode Erosion in Steady-State Electric Propulsion Engines," IEPC 88-074, 20th IEPC, October 1988.

15. W. D. Deininger and R. J. Vondra, "Arcjet Propulsion System for an SP-100 Flight Experiment," Journal of Spacecraft and Rockets, Vol. 25, No. 6, pp. 427-432, November-December 1988.
16. W. D., Deininger and R. J. Vondra, "Spacecraft and Mission Design for the SP-100 Flight Experiment," Journal of Spacecraft and Rockets, Vol. 26, No. 2, pp. 109-115, March-April 1989.
17. A. Chopra, W. D. Deininger and D. Q. King, "Effect of Cathode Configuration on 30-kWe Arcjet Electrical Characteristics," AIAA 89-2261, 25th JPC, July 1989.
18. W. D. Deininger, A. Chopra and K. D. Goodfellow, "Cathode Erosion Tests for 30-kW Arcjets," AIAA 89-2264, 25th JPC, July 1989.
19. D. Q. King, J. W. Barnett, A. Chopra, W. D. Deininger, C. E. Garner, T. J. Pivrotto and J. C. Sercel, "A Brief Review of JPL's Electric Propulsion Technology Activities," AIAA 89-2493, 25th JPC, July 1989.
20. W. Sokolowski, T. O'Donnell and W. D. Deininger, "Cathode and Insulator Materials for a 30-kW Arcjet Thruster," AIAA 89-2514, 25th JPC, July 1989.
21. W. D. Deininger and R. J. Vondra, "A Baseline Spacecraft and Mission Design for the SP-100 Flight Experiment," AIAA 89-2594, 25th JPC, July 1989.
22. R. Vondra and W. Deininger, "Options for a 30-kW SP-100 Flight Demonstration," AIAA 89-2597, 25th JPC, July 1989.
23. G. Pham-Van-Diep, W. D. Deininger, T. J. Pivrotto and D. A. Erwin, "Velocity Mapping in a 30-kW Arcjet Plume Using Laser-Induced Fluorescence," AIAA 89-2831, 25th JPC, July 1989.
24. P. A. E. Stewart, P. H. Fowler, W. D. Deininger, J. D. Rogers and A. D. Taylor, "Neutron and High-Speed Photogrammetric Arcjet Diagnostics," AIAA 89-2955, 25th JPC, July 1989.
25. W. D. Deininger and R. J. Vondra, "Electric Propulsion for Constellation Deployment and Spacecraft Maneuvering," Journal of Spacecraft and Rockets, Vol. 26, No. 5, pp. 352-357, September-October 1989.
26. W. D. Deininger, T. J. Pivrotto and J. R. Brophy, "Effect of Nozzle and Cathode Configuration on Arcjet Performance," Journal of Propulsion and Power, in press, November-December 1989.
27. D. A. Erwin, G. Pham-Van-Diep, W. D. Deininger and T. J. Pivrotto, "Laser-Induced Fluorescence Measurements of Flow Velocity in High-Power Ammonia Arcjet Plumes," Final Report, University of Southern California, JPL Internal Document D-6873, December 1989.

13.0 REFERENCES

1. AVCO Corporation, "Thirty-Kilowatt Plasmajet Rocket-Engine Development, Second Year Development Program," 1st Quarterly Progress Report, RAD SR-62-182, NASA CR-50849, September 1962.
2. AVCO Corporation, "Thirty-Kilowatt Plasmajet Rocket Engine Development/Second Year Development Program," 2nd Quarterly Progress Report, December 21, 1962.
3. AVCO Corporation, "Thirty-Kilowatt Plasmajet Rocket Engine Development/Third Year Development Program," 1st Quarterly Progress Report, September 1963.
4. AVCO Corporation, "Thirty-Kilowatt Plasmajet Rocket Engine Development/Third Year Development Program," 4th Quarterly Progress Report, RAD SR-64-168, NASA CR-58154, June 1964.
5. AVCO Corporation, "Thirty-Kilowatt Plasmajet Rocket Engine Development," Summary Report, RAD TR-64-6, NASA CR-54044, July 1964.
6. J. R. Beattie, Hughes Research Laboratory, Private Communication, 1988.
7. J. R. Beattie, J. N. Matossian and R. R. Robson, "Status of Xenon Ion Propulsion Technology," 19th International Electric Propulsion Conference, AIAA Paper 87-1003, May 1987.
8. M. Blackburn, Sierra Instruments, Carmel Valley, CA, Private Communication, August 1989.
9. D. Bohm, "Minimum Ionic Kinetic Energy for a Stable Sheath," The Characteristics of Electrical Discharges in Magnetic Plasmas, A. Guthrie and R. K. Wakerling, Editors, McGraw-Hill, New York, 1949, pp. 77-86.
10. W. L. Bohn, "On Spectroscopic Measurements of Velocity Profiles and Non-Equilibrium Radial Temperatures in an Argon Plasma Jet," J. Quantitative Spectroscopy and Radiative Transfer, Vol. 7, pp. 661-676, Pergamon Press Ltd. 1967
11. J. R. Brophy, T. J. Pivrotto and D. Q. King, "Investigation of Arcjet Nozzle Performance," AIAA 85-2016, 18th IEPC, October 1985.
12. A. Bruckner, "Spectroscopic Studies of the Exhaust Plume of a Quasi-Steady MPD Accelerator," Ph.D. diss., Dept. of Aerospace and Mechanical Sciences, Princeton University, Princeton, NJ, May 1972.
13. D. Buden, R. Verga and L. Caveny, "SP-100 Projected Flight Experiments," AIAA 89-2590, 25th JPC, July 1989.
14. D. D. Burgess, et al., Journal of Physics B, 13, 1675, 1980.

15. W. Butler, Rocket Research Company, Redmond, Washington, Private Communication, June 1989.
16. R. J. Cassady, P. G. Lichon and J. C. Andrews, "Arcjet Endurance Test Results," AIAA, 21st International Electric Propulsion Conference, Orlando, Florida, in press, July 1990.
17. R. J. Cassady, P. G. Lichon, J. C. Andrews and W. D. Deininger, Meeting at Rocket Research Company, Redmond, Washington, June 1989.
18. R. J. Cassady and M. S. Hiatt, "Thrust Measurement of a 30-kW Arcjet," Proceedings 1986 JANNAF Propulsion Meeting, Vol. 1, pp. 409-17, August 1986.
19. A. Chopra and W. D. Deininger, "D-1E Arcjet Engine Design, Assembly and Operation," JPL Internal Document D-6738, October 1989.
20. A. Chopra, W. D. Deininger and D. Q. King, "Effect of Cathode Configuration on 30-kW Arcjet Electrical Characteristics," AIAA 89-2261, 25th JPC, July 1989.
21. R. F. Cuffel, "Computer Program Description for Laminar Nozzle Flow Prediction and Global Plume Backflow Estimate," Internal Software Document, Jet Propulsion Laboratory, June 1975.
22. F. M. Curran, NASA Lewis Research Center, Private Communication.
23. F. M. Curran and T. W. Haag, "An Extended Life and Performance Test of a Low-Power Arcjet," AIAA 88-3106, 24th JPC, July 1988.
24. Daalder, "Cathode Spots and Vacuum Arcs," Physica, Vol. 104C, pp. 91-106, 1981.
25. W. D. Deininger and R. J. Vondra, "Arcjet Propulsion System for an SP-100 Flight Experiment," Journal of Spacecraft and Rockets, Vol. 25, No. 6, pp. 427-32, November-December 1988.
26. W. D. Deininger and R. J. Vondra, "A Baseline Spacecraft and Mission Design for the SP-100 Flight Experiment," AIAA 89-2594, 25th JPC, July 1989.
27. W. D. Deininger, A. Chopra and K. D. Goodfellow, "Cathode Erosion Tests for 30-kW Arcjets," AIAA 89-2264, 25th JPC, July 1989.
28. W. D. Deininger, T. J. Pivirotto and J. R. Brophy, "The Design and Operating Characteristics of an Advanced 30-kW Ammonia Arcjet Engine," AIAA 87-1082, 19th IEPC, May 1987.
29. W. D. Deininger and R. J. Vondra, "Design and Performance of an Arcjet Nuclear Electric Propulsion System for a Mid-1990s Reference Mission," AIAA 87-1037, 19th IEPC, May 1987.

30. W. D. Deininger and T. J. Pivirotto, "Detailed Operating Characteristics of a 30-kW Ammonia Arcjet Engine with a Contoured Nozzle," SPIE Proceedings-Propulsion, Vol. 872, 1988, pp. 108-18.
31. W. D. Deininger and R. J. Vondra, "Development of an Arcjet Nuclear Electric Propulsion System for a 1993 Flight Demonstration," AIAA 86-1510, 22nd JPC, June 1986.
32. W. D. Deininger, T. J. Pivirotto and J. R. Brophy, "Effect of Nozzle and Cathode Configuration on Arcjet Performance," Journal of Propulsion and Power, December 1989.
33. W. D. Deininger and R. J. Vondra, "Electric Propulsion for Constellation Deployment and Spacecraft Maneuvering," Journal of Spacecraft and Rockets, Vol. 26, No. 5, pp. 352-57, September-October 1989.
34. W. D. Deininger and T. J. Pivirotto, "High-Power, NH₃ Arcjet Cathode Lifetime Evaluation Experiments and Plans," SPIE Proceedings-Propulsion, Vol. 872, 1988, pp. 127-34.
35. W. D. Deininger, Editor, "Proceedings for the Arcjet Plume Diagnostics Technical Workshop," Pasadena, California, JPL Internal Document D-3623, October 2-3, 1986.
36. W. D. Deininger and R. J. Vondra, "Spacecraft and Mission Design for the SP-100 Flight Experiment," Journal of Spacecraft and Rockets, Vol. 26, No. 2, pp. 109-15, March-April 1989.
37. W. D. Deininger and R. J. Vondra, "Spacecraft and Mission Design for the Space Nuclear Source Reference Mission," AIAA 87-2026, 23rd JPC, July 1987.
38. W. D. Deininger, A. Chopra, D. Q. King, and T. J. Pivirotto, "Thermal Design Improvements for 30-kWe Arcjet Engines," IEPC 88-073, 20th IEPC, October 1988.
39. A. Ducati, et al., "1-kW Arcjet Engine System Performance Test," Journal of Spacecraft and Rockets, Vol. 1, No. 3, pp. 327-32, May-June 1964.
40. Dyubinov, Rakhouskii, "The Cathode Spot of a Vacuum Arc," Soviet Physics Uspekhi 21 (8), 1978.
41. V. Fomenko, Emission Properties of Materials, 3rd Ed., Naukova Dumka, Kiev, 1970.
42. P. H. Fowler, "Temperature Imaging Using Epithermal Neutrons," Rutherford Appleton Laboratory Report RAL-87-056, Rutherford-Appleton Laboratory, England, August 1987.

43. General Electric Corporation, "SP-100 Ground Engineering System (GES) Baseline System Definition and Characterization Study - Thermoelectric Power Conversion Study," Final Report, Vol. 1, Document No. 85SDS 4268, August 1985.
44. P. Gohil et al., Journal of Physics D, Vol. 16, 1983, p. 333.
45. K. D. Goodfellow and S. N. B. Murthy, "Electrode Processes and MPD Thruster Operation," 24th JPC, AIAA 88-3207, July 1988.
46. A. Guile and B. Juttner, "Basic Erosion Processes of Oxidized and Clean Metal Cathodes by Electric Arc," IEEE, Transactions on Plasma Science, Vol. PS-8, No. 3, 1980.
47. T. W. Haag, F. M. Curran, "Arcjet Starting Reliability: A Multi-Start Test on Hydrogen/Nitrogen Mixtures," AIAA 87-1061, 19th IEPC, May 1987.
48. Handbook of Chemistry and Physics, 51st Ed., The Chemical Rubber Co. Press, 1970-71.
49. Handbook of Thermophysical Properties of Solid Materials, Macmillan Company, New York, 1961.
50. R. Havell and F. Holtz, "High-Temperature Electrical Properties of Insulators and Their Compatibility with Refractory Metals," ITT Research Institute, Contract NAS3-4104.
51. K. Hoyer and V. Subramaniam, "Limits on Steady Diffuse Mode Operation of the Cathode in an MPD Thruster," 25th JPC, AIAA 89-2601, July 1989.
52. R. G. Jahn, "Physics of Electric Propulsion," McGraw-Hill Book Company, San Francisco, 1968.
53. R. R. John, S. Bennett and J. F. Connors, "Arcjet Engine Performance: Experiment and Theory," AIAA Journal, #1 (11), 2517-2525, November 1963. See also R. R. John, et al., "Arcjet Engine Performance: Experiment and Theory," ARS Paper 2667-62, 1962.
54. R. R. John, J. F. Connors and S. Bennett, "Thirty-Day Endurance Test of a 30-kW Arcjet Engine," 1963 AIAA Summer Meeting, AIAA Paper 63-274, June 1963.
55. R. R. John, "Thirty-Kilowatt Plasmajet Rocket Engine Development," Summary Report, AVCO Corporation, RAD TR-64-6, NASA CR-54044, July 1964.
56. R. M. Jones, "A Comparison of Potential Electric Propulsion Systems for Orbit Transfer," 16th International Electric Propulsion Conference, AIAA 82-1871, November 1982.

57. C. Kimblin, "Cathode Spot Erosion and Ionization Phenomena in the Transition from Vacuum to Atmospheric Pressure Arcs," Journal of Applied Physics, Vol. 45, No. 12, December 1974.
58. D. Q. King, J. W. Barnett, A. Chopra, W. D. Deininger, C. E. Garner, T. J. Pivrotto and J. C. Sercel, "A Brief Review of JPL's Electric Propulsion Technology Activities," AIAA 89-2493, 25th Joint Propulsion Conference, July 1989.
59. R. W. Klemetson, Jet Propulsion Laboratory, Pvt. Communication, August 1988.
60. R. W. Klemetson, Jet Propulsion Laboratory, Pvt. Communication, May 1988.
61. S. C. Knowles, "Arcjet Thruster Research and Technology," Final Report, Rocket Research Company, NASA CR-182107, September 1987.
62. S. C. Knowles and S. E. Yaro, "Design, Testing and Integration of a Flight-Ready Hydrazine Arcjet System," AIAA 89-2720, 25th Joint Propulsion Conference, July 1989.
63. D. M. Corpi and J. G. Olin, Sierra Instruments, Carmel Valley, CA, Pvt. Communication, August 29, 1989.
64. H. C. Kurtz, M. Auweter-Kurtz, et al., "A 15-kW Experimental Arcjet," IEPC 88-107, 20th IEPC, Federal Republic of Germany, October 1988.
65. J. Lawless, Presentation at Workshop on "Electrode Erosion in Electric Space Propulsion Engines," Tamarron, CO, March 1989.
66. C. C. Limbaugh, "Determination of the Excited-State Density Distribution with a Non-Equilibrium Freely-Expanding Argon Arcjet Plume," Final Report, AEDC-TR-77-23, March 1977.
67. A. C. Malliaris, "Spectroscopic Study of Ion-Neutral Coupling in Plasma Acceleration," AIAA Journal, Vol. 9, No. 1, January 1971.
68. L. H. Malone, "Comparison of Electron-Ion Recombination and Gas-Dynamic Expansion Rates in Freely-Expanding Helium and Argon Plasmas," Interim Report, AEDC-TR-76-34, March 1976.
69. R. Manvi, "Recommendation on SP-100 Survival in the Debris and Meteoroid Environment," JPL Internal Document, IOM 354-SP-100-87-001 to C. Shinbrot, May 18, 1987.
70. Martin Marietta Denver Aerospace, "Space Power Architecture Study," OTV Section, Technical Report MCR-86-613, Task 1; Requirements Definition, September 2, 1986.
71. R. Matlock and J. Fieg, Astronautics Laboratory (AFSC), Pvt. Communication, May 1989.

72. R. Munns, Dick Munns Company, Los Alamitos, CA, Pvt. Communication, March 1985.
73. O. H. Nestor, "Numerical Methods for Reducing Line and Surface Probe Data," SIAM Review, Vol. 2, No. 3, July 1960.
74. R. E. Olgevie, T. R. Egan and J. P. Penn, "Autonomous Flight Control for Low-Thrust Orbit Transfer Vehicles," AIAA Paper 88-2838, July 1988.
75. W. Ohlinger, Ceradyne Electron Sources, Lexington, KY, Pvt. Communication, June 1989.
76. J. G. Olin, "Process Gas Mass Flow Controllers, An Overview," Solid State Technology, PennWell Publishing, April 1988.
77. C. Oshima, M. Aono and T. Tanaka, J. Appl. Phys, 51 (997), 1980.
78. E. M. Passmore, J. E. Boyd, et al., "Investigation of Diffusion Barriers for Refractory Metals," WADC Tech. Rep. 60-343, August 1960.
79. T. J. Pivrotto and W. D. Deininger, "Analysis of a Used Pair of Arcjet Electrodes," SPIE Proceedings-Propulsion, Vol. 872, pp. 119-126, 1988.
80. T. J. Pivrotto, D. Q. King, W. D. Deininger and J. R. Brophy, "The Design and Operating Characteristics of a 30-kW Thermal Arcjet Engine for Space Propulsion," 22nd Joint Propulsion Conference, AIAA Paper 86-1508, June 1986.
81. T. J. Pivrotto, D. Q. King and J. R. Brophy, "Development and Life Testing of 10-kW Class Thermal Arcjet Engines," AIAA 85-2031, 18th IEPC, October 1985.
82. T. J. Pivrotto and W. D. Deininger, "Electrode Erosion in Steady-State Electric Propulsion Engines," IEPC 88-074, 20th IEPC, October 1988.
83. T. J. Pivrotto, D. Q. King and W. D. Deininger, "Long-Duration Test of a 30-kW Class Thermal Arcjet Engine," AIAA 87-1083, 19th IEPC, May 1987.
84. T. J. Pivrotto, D. Q. King and W. D. Deininger, "Long-Duration Test of a 30-kW Class Thermal Arcjet Engine," AIAA 87-1947, 23rd Joint Propulsion Conference, June 1987.
85. T. J. Pivrotto, D. Q. King, J. R. Brophy and W. D. Deininger, "Performance and Long-Duration Test of a 30-kW Class Thermal Arcjet Engine," Final Report, JPL Internal Document D-4643 to Air Force Astronautics Laboratory (AFAL), Edwards AFB, July 1987.
86. T. J. Pivrotto and D. Q. King, "Thermal Arcjet Technology for Space Propulsion," JANNAF Propulsion Meeting, San Diego, CA, Spring 1985.

87. P. D. Prewett and J. E. Allen, "The Double Sheath Associated With a Hot Cathode," Proceedings of the Royal Society of London, Vol. 348, pp. 435-446, 1976.
88. L. L. Price and W. K. McGregor, "Spectral Characteristics of a Low-Density, Arc-Heated Nitrogen Plasma," AEDC-TR-66-139, October 1966.
89. T. Price, "Arcjet Propulsion System Definition Studies," AIAA 89-2593, 25th Joint Propulsion Conference, July 1989.
90. G. T. Radzobarin, et al., Nuclear Fusion, Vol. 19, p. 1439, 1979.
91. Lt. Gen. R. Rankine, Air Force Space Systems Command, Invited Speaker, Comments during Awards Luncheon, 25th Joint Propulsion Conference, July 1989.
92. G. V. R. Rao, "Exhaust Nozzle Contour for Optimum Thrust," Jet Propulsion, Vol. 28, pp. 377-382, November 6, 1958.
93. Raytek, Inc., "Thermalert II Installation and Operation Manual.
94. R. Richter, "Development of a 30-kW Three-Phase AC Arcjet Propulsion System," Report No. R63FPD237, NASA CR-52664, May 1963.
95. T. Riethof, P. D. Acchione and E. R. Branyan, "High-Temperature Spectral Emissivity Studies on Some Refractory Metals and Carbides," Art. 49, Temperature, Vol. 3, pp. 515-522, A. I. Dahl, ed., Reinhold Publishing, New York, 1962.
96. S. Rosen and J. Sloan, "Electric Orbital Transfer Vehicle - A Military Perspective," AIAA 89-2496, 25th Joint Propulsion Conference, July 1989.
97. K. V. Rudolph, "MPD Thruster Definition Study," Final Report, Martin Marietta Denver Aerospace, AFRPL-TR-84-046, July 1984.
98. T. Sanks, Astronautics Laboratory (AFSC), "30-kWe Class Arcjet Advanced Technology Development (ATD)," Request for Proposals, Solicitation No. F04611-89-R-0010, May 16, 1989.
99. M. Schuleer, D. Conley and D. Verrill, "SP-100 Flight Experiment," AIAA 89-2592, 25th Joint Propulsion Conference, July 1989.
100. H. O. Schrade, et al., "Analysis of the Cathode Spot of Metal Vapor Arcs," IEEE Transactions on Plasma Science, Vol. PS-11, No. 3, 1983.
101. H. O. Schrade, M. Anweter-Kurtz and H. L. Kurtz, "Cathode Erosion Studies on MPD Thrusters," AIAA Journal, Vol. 25, No. 8, August 1987.
102. P. T. Shaffer, Handbook of High-Temperature Materials, Plenum Press, New York, No. 1 Material Index, G. V. Samsonov ibid, No. 2 Properties Index.

103. Sierra Instruments, 830-840 Side-Trak Mass Flow Meters and Controllers Instrument Instruction Manual, 1987.
104. M. A. Simon, S. C. Knowles, F. M. Curran and T. L. Hardy, "Low-Power Arcjet Life Issues," 19th OEPC, AIAA 87-1059, May 1987.
105. W. W. Smith and J. R. Cassady, "Arcjet Technology Improvement," Final Report, Rocket Research Company, No. 86-R-1063, AFRPL-TR-86-079, December 1986.
106. C. J. Smithells, "Tungsten - A Treatise on Its Metallurgy, Properties and Application," 3rd Edition, Chapman and Hall LTD, London, 1952.
107. W. Sokolowski, T. O'Donnell and W. Deininger, "Cathode and Insulator Materials for 30-kW Arcjet Thrusters," 25th Joint Propulsion Conference, AIAA 89-2514, July 1989.
108. Stewart, "Neutron and Positron Techniques for Fluid Transfer System Analysis and Remote Temperature and Stress Analysis," ASME 87-GT-219, June 1987.
109. Steward, "Real-Time Neutron Imaging of Gas Turbines," AIAA 87-1762, 23rd Joint Propulsion Conference, July 1987.
110. D. Stull and H. Propheti, JANNAF Thermochemical Tables, 2nd Edition, June 1971.
111. J. J. Sullivan and R. P. Jacobs, Jr., "Flow Measurement and Control in Vacuum Systems for Microelectronics Processing," Solid State Technology, PennWell Publishing, pp. 113-118, October 1986.
112. Martin Marietta Corporation document MCR-86-2541, Titan IV User's Handbook, preliminary, June 1987.
113. J. P. Todd, "30-kW Arcjet Thruster Research," Giannini Scientific Corporation, Santa Ana, CA, Air Force Aero Propulsion Laboratory Report No. APL-TDR-64-58, March 1964.
114. Union Carbide Corporation, Carbon Products Division, Chicago, IL, GRAFOIL^R Catalog G-8816.
115. W. M. VanCamp, et al., "Study of Arcjet Propulsion Devices," Final Report, McDonnell Report No. E368, NASA, CR-54691, March 1966.
116. R. Vondra and W. Deininger, "Options for a 30-kW SP-100 Flight Demonstration, AIAA 89-2597, 25th Joint Propulsion Conference, July 1989.
117. R. Vondra, K. Nock and R. M. Jones, "A Review of Electric Propulsion Systems and Mission Applications," 17th IEPC, IEPC 84-82, July 1984.
118. L. W. Wallner and J. Czika, Jr., "Arcjet Thruster for Space Propulsion," NASA Technical Note TN D-2868, June 1965.

119. J. W. Widhalm and S. A. Eide, "Optimal Continuous Thrust In-Plane Orbital Evasive Maneuvers," 26th Aerospace Sciences Meeting, AIAA Paper 88-0374, January 1988.
120. R. Wiley, "SDIO Space Power and Power Conversion," Nuclear Working Group/MHD Working Group Meeting, Dept. of Energy, Germantown, MD, April 15, 1986.
121. Workshop on Electrode Erosion in Electric Space Propulsion Engines, Durango, CO, March 28-31, 1989.
122. L. M. Zana, "Langmuir Probe Surveys of an Arcjet Exhaust," 23rd Joint Propulsion Conference, AIAA 87-1950, July 1987.
123. W. M. Zelinsky, "SP-100 Reference Mission Integration Study," Final Report, Aerospace Corporation Report No. TOR-0086A (2052-20)-2, Vols. 1-3, November 1986.

